Transport of sulfuric acid in the atmosphere of Venus studied on the basis of radio signal attenuation effects observed in the Venus Express Radio Science Experiment VeRa

Inaugural-Dissertation
zur
Erlangung des Doktorgrades
der Mathematisch-Naturwissenschaftlichen Fakultät
der Universität zu Köln

vorgelegt von
Janusz Oschlisniok
aus Hindenburg
Köln
2020

Berichterstatter: (Gutachter)	Priv. Doz. Dr. Martin Pätzold
	Prof. Dr. Andreas Eckart

Tag der Mündlichen Prüfung: 06.10.2020

Abstract

The most striking features on Venus are the cloud deck, which cover the entire planet at altitudes between about 50 and 70 km and its superrotating atmosphere. With highest zonal wind velocities in excess of 100 m/s at altitudes of about 65 to 70 km the atmosphere circles the planet in about four Earth-days. Until today, the mechanism that supports the superrotation is not understood. It is assumed that atmospheric waves, e.g. thermal tides, as well as meridional circulation may provide the required angular momentum. However, the knowledge about the meridional wind pattern is poor. The latter can be studied by means of their influence on the abundance and spatial distribution of trace gases like sulfuric acid and sulfur dioxide. The influence of atmospheric waves, on the other hand, can be seen for example in temporal temperature and density variations of the trace gases.

While increased abundances of SO_2 exist at altitudes below about 60 km altitude, significant amounts of H_2SO_4(g) can be found in the altitude region below about 50 km altitude. H_2SO_4 is produced in the upper clouds (60 - 70 km) where it predominantly exists in the liquid phase. It is transported to lower altitudes where it evaporates due to increasing temperatures so that a haze layer consisting of H_2SO_4(g) is formed between about 35 and 50 km altitude.

Gaseous sulfuric acid and sulfur dioxide are responsible for the absorption of radio waves. The absorption can be used to derive the abundances of SO_2 and H_2SO_4(g). The radio science experiment VeRa on board the Venus Express spacecraft was used to sound the atmosphere of Venus with X- and S-band radio waves between the years 2006 and 2014. In the present work, X- and S-band absorptivity profiles were derived from these radio soundings. Those were used to derive mean SO_2 values between 51 and 54 km altitude as well as H_2SO_4(g) abundance profiles between about 40 and 55 km altitude. More than 800 profiles could be derived which, thanks to the orbit of Venus Express, cover a large number of latitudes and local times.

Distinct latitudinal variations of SO_2 and H_2SO_4(g) were found. Mean SO_2 values of 90 ppm and 150 - 160 ppm were derived at the equatorial and the polar regions, respectively, while a relatively low mean abundance value of 50 ppm was found at the mid-latitudes. Increased H_2SO_4(g) accumulations with mean values of 13 ppm and 9 - 14 ppm were observed at low and high latitudes, respectively, while lower values of

5 - 7 ppm were derived at the mid-latitudes. Furthermore, a decrease of the topside of the H_2SO_4(g) haze layer was observed at higher latitudes. Long-term variations of SO_2 were found at both polar regions with SO_2 low abundant periods in the years 2006/2007 and 2013 as well as with an SO_2 high abundant period between the years 2008 and 2011. A similar long-term trend was observed in the H_2SO_4(g) abundance at the northern polar latitudes. Lowest values were observed in 2007, while distinctly enhanced values were found between the end of 2008 and middle of 2012. Moreover, a local time dependence was found in the equatorial H_2SO_4(g) abundance, which is likely caused by a semidiurnal tide.

A 2D mass transport model was developed in the present work in order to study the meridional wind pattern in Venus' atmosphere which caused the observed spatial distribution of H_2SO_4(g). It turned out that the H_2SO_4(g) accumulation observed at high latitudes was mainly caused by precipitation of H_2SO_4 droplets at these latitudes. The latter evaporated into gaseous sulfuric acid at lower altitudes and formed the observed gas accumulation. The influence of wind transport on this formation process was minor. The H_2SO_4(g) accumulation observed at equatorial latitudes is the result of opposite directed mass transport by upward winds and sedimentation as well as evaporation and condensation processes. The low H_2SO_4(g) abundance observed at mid-latitudes was reproduced by downward winds in the model calculations. The general assumption on Venus' wind pattern made in the present model is confirmed by the successful reproduction of the observed global H_2SO_4(g) distribution. The assumed wind pattern is also supported by the latitudinal SO_2 distribution observed between 51 and 54 km altitude.

Kurzzusammenfassung

Zu den auffäligsten Merkmalen des Planeten Venus gehören die Wolkendecke, die in einer Höhe von 50 und 70 km den gesamten Planeten überdeckt sowie die superrotierende Atmosphäre. Mit Geschwindigkeiten von mehr als 100 m/s umrundet die Atmosphäre in ungefähr vier Erdtagen den Planeten. Bis heute ist der Mechanismus, der die Superrotation aufrechterhält, nicht verstanden. Es wird davon ausgegangen, dass atmosphärische Wellen wie z.B. thermische Gezeiten, sowie die meridionale Zirkulation den nötigen Impuls liefern. Die Kenntnis über die meridionale Windstruktur ist jedoch gering. Letztere kann anhand des Einflusses der Zirkulation auf die Konzentration und auf die räumliche Verteilung von Spurengasen wie z.B. Schwefelsäure und Schwefeldioxid untersucht werden. Der Einfluss von atmosphärischen Wellen hingegen, kann z.B. in zeitlichen Variationen der Temperatur und der Dichte der Spurengase beobachtet werden.

Während sich größere SO_2 Konzentrationen unterhalb von ungefähr 60 km Höhe befinden, können erhöhte Konzentrationen von H_2SO_4(g) unterhalb von ungefähr 50 km Höhe beobachtet werden. H_2SO_4(g) wird in der oberen Wolkenschicht (60 - 70 km) produziert, wo es sich überwiegend in flüssiger Form befindet. Es nach unten transportiert, wo es aufgrund der steigenden Temperaturen verdampft, so dass sich zwischen ungefähr 35 und 50 km Höhe eine Dunstschicht aus H_2SO_4(g) bildet.

Gasförmige Schwefelsäure und Schwefeldioxid sind verantwortlich für die Absorption von Radio Wellen. Die Absorption kann genutzt werden um die Konzentrationen von H_2SO_4(g) und SO_2 zu bestimmen. Das Radiosondierungsexperiment VeRa an Bord der Raumsonde Venus Express wurde verwendet, um die Atmosphäre der Venus mit X- und S-Band Radio Signalen zwischen 2006 und 2014 zu sondieren. In der vorliegenden Arbeit wurden X- und S-Band Absorptionsprofile aus diesen Messungen berechnet. Diese wurden verwendet, um mittlere SO_2 Werte zwischen 51 und 54 km Höhe zu bestimmen sowie H_2SO_4(g) Konzentrationsprofile zwischen ungefähr 40 und 55 km Höhe zu berechnen. Mehr als 800 Profile konnten berechnet werden, die dank des Orbits von Venus Express eine große Anzahl von planetaren Breiten und lokalen Zeiten abdecken.

Es wurden deutliche latitudinale Variationen von H_2SO_4(g) und SO_2 gefunden. In äquatorialen und polaren Breiten wurden mittlere SO_2 Werte von 90 ppm und 150 - 160 ppm berechnet, während in mittleren Breiten relativ geringe Konzentrationen

von 50 ppm gefunden wurden. In äquatorialen und polaren Breiten wurden erhöhte H_2SO_4(g) Ansammlungen beobachtet, mit mittleren Werten von 13 ppm und 9 - 14 ppm. In mittleren Breiten hingegen, wurden kleinere Werte von 5 - 7 ppm bestimmt. Darüber hinaus wurde bei hohen Breiten eine Absenkung der Oberseite der H_2SO_4(g) Dunstschicht beobachtet. In beiden polaren Regionen wurde eine Langzeitvariation von SO_2 gefunden, mit Perioden geringer SO_2 Konzentration in den Jahren 2006/2007 und 2013 sowie hoher Konzentration zwischen 2008 und 2011. Eine ähnliche Variation der H_2SO_4(g) Konzentration wurde in der nördlichen Polarregion festgestellt. Niedrige Werte wurden im Jahr 2007 beobachtet, während im Zeitraum zwischen Ende 2008 und Mitte 2012 deutlich erhöhte Werte gefunden wurden. Außerdem wurde in der äquatorialen Region eine Abhängigkeit der H_2SO_4(g) Konzentration von der lokalen Zeit festgestellt, welche wahrscheinlich durch thermische Gezeiten verursacht wurde.

Ein 2D Transportmodell wurde in der vorliegenden Arbeit entwickelt um die meridionale Windstruktur in der Venusatmosphäre zu untersuchen, welche die beobachtete räumliche Verteilung von H_2SO_4(g) gebildet hat. Es hat sich herausgestellt, dass die beobachtete H_2SO_4(g) Ansammlung in den hohen Breiten durch den Niederschlag von H_2SO_4 Tropfen verursacht wurde. Letztere verdampften in niedrigeren Höhen zu gasförmiger Schwefelsäure und bildeten die beobachtete Ansammlung von H_2SO_4(g). Der Einfluss von Winden war gering bei diesem Bildungsprozess. Die H_2SO_4(g) Ansammlung in der äquatorialen Region ist das Resultat von entgegengestztem Massentransport, bestehend aus Aufwinden und Sedimentation sowie von Verdampfungs- und Kondensationsprozessen. Die niedrige H_2SO_4(g) Konzentration, welche in den mittleren Breiten beobachtet wurde, konnte in den Modellrechnungen durch abwärts gerichtete Winde rekonstruiert werden. Die im vorliegendem Modell getroffenen Annahmen über die Windstruktur in der Venusatmosphäre werden sowohl durch die erfolgreiche Reproduktion der beobachteten globalen H_2SO_4(g) Konzentration bestätigt, als auch durch die beobachtete globale SO_2 Konzentration bekräftigt.

Contents

1 Introduction **1**

2 The atmosphere of Venus below 80 km altitude **5**
2.1 Thermal structure 5
2.2 Chemical composition 7
2.3 Wind dynamics 17

3 The Venus Express spacecraft, payload and data acquisition **25**
3.1 The Venus Express spacecraft and payload 25
3.1.1 Venus Express Radio Science Experiment VeRa 28
3.1.2 Radio occultation 30
3.2 Data acquisition 32
3.2.1 Signal power and the atmospheric Doppler shift 33
3.2.2 Radio ray parameters as well as temperature, pressure and number density 36
3.2.3 Spatial resolution 40

4 Radio signal attenuation in the Venus atmosphere **43**
4.1 Radio signal attenuation 43
4.1.1 Refractive defocussing 45
4.1.2 Mispointing 47
4.1.3 Absorption 49
4.2 Previous observations 53

5 Two-dimensional mass transport model of the lower and middle Venus atmosphere **61**
5.1 Transport, condensation and evaporation 61
5.2 Numerical solution 71

6 Attenuation of Venus Express radio signals and comparison of closed-loop with open loop data **75**
6.1 Comparison of closed-loop with open loop data 75
6.2 Refractive defocussing 78
6.3 Mispointing 80

7 Absorptivity, SO_2 abundance and H_2SO_4(g) profiles derived from VeRa's open loop data **87**
7.1 Comparison of results derived from S-and X-band radio signals 88
7.2 Upper limits of the SO_2 abundance derived from VeRa's X-band data . 95
7.3 H_2SO_4(g) profiles derived from VeRa's X-band data from the entire Venus Express mission 107
7.3.1 Global H_2SO_4(g) distribution 107
7.3.2 H_2SO_4(g) abundance variations 110

8 Model results and comparison with observations and previous simulations **121**
8.1 Model results and comparison with VeRa 122
8.1.1 Modeled H_2SO_4(g) distribution 122
8.1.2 Comparison with VeRa 129
8.2 Modeled distributions of the clouds and water vapor 135
8.3 Comparison with other model results and previous observations 140

9 Summary and future prospects **151**
9.1 Observation 151
9.2 Modeling 156
9.3 Outlook 160

A Radio signal attenuation in the Earth atmosphere **163**

B Multipath propagation effects occurring in Venus Express radio occultation experiments **171**

C Coefficients for the mass transport equation **175**

D The effect of the antenna mispointing on the Venus Express S-band radio signal **179**

E H_2SO_4(g) profiles derived from VeRa's X- and S-band radio absorptivity in the year 2006. **181**

Bibliography **183**

List of Figures

2.1 Panel a): Zonal and temporal averaged temperature distribution in Venus' atmosphere between 40 and 80 km altitude derived from Venus Express radio occultation data. The southern and northern hemispheres were subdivided into equal latitudinal bins of 5 deg each. Vertical temperature profiles from the years 2006 to 2014 located within each bins were averaged to one profile. The lack of data in the latitude range between about 0°N and 65°N is a consequence of the spacecrafts orbit geometry; Panel b): Static stability in Venus' atmosphere derived by *Ando et al.* (2015) from Venus Express radio occultation data. 6

2.2 Vertical distribution of the number density (panel a)) and mass loading (panel b)) of mode 2 and 3 particles in Venus' atmosphere as observed by the PVO particle size spectrometer. Data were adopted from *Knollenberg and Hunten* (1980). The contribution of the mode 1 particles to the overall mass loading of the Venus clouds is small and is therefore neglected. 10

2.3 Water vapor in Venus' middle and lower atmosphere obtained from airborne, ground based and spacecraft observations as well as from model results (*Fink et al.*, 1972; *Bézard et al.*, 1990; *Bell et al.*, 1991; *Crisp et al.*, 1991; *Bjoraker et al.*, 1992; *Donahue and Hodges*, 1992; *Pollack et al.*, 1993; *Bergh et al.*, 1995; *Meadows and Crisp*, 1996; *Ignatiev et al.*, 1997, 1999; *Fedorova et al.*, 2008; *Marcq et al.*, 2008; *Cottini et al.*, 2012; *Fedorova et al.*, 2016). 12

2.4 Panel a): Sulfur dioxide in Venus' middle and lower atmosphere obtained from ground based and spacecraft observations as well as from model results (*Barker*, 1979; *Hoffman et al.*, 1980; *Oyama et al.*, 1980; *Zasova et al.*, 1993; *Bézard et al.*, 1993; *Pollack et al.*, 1993; *Parisot et al.*, 1986; *Bertaux et al.*, 1996; *Jenkins et al.*, 2002; *Marcq et al.*, 2008; *Belyaev et al.*, 2012; *Krasnopolsky*, 2007, 2012; *Zhang et al.*, 2012). Arrows placed on data samples represent either 'less than' or 'greater than'. Panel b): Temporal evolution of the equatorial SO_2 abundance at cloud top altitudes observed by *Marcq et al.* (2020) in SPICAV-UV measurements from the years 2006 to 2015. The red line represents the moving median value. The Figure was adopted from *Marcq et al.* (2020). 14

2.5 The abundance of a) carbon monoxide around 36 km altitude and b) carbonyl sulfide around 33 km altitude in Venus' atmosphere as derived by *Marcq et al.* (2008) from VEX/VIRTIS measurements (section (3.1)). 16

2.6 a): Zonal wind velocity profiles as measured by the Venera and Pioneer Venus entry probes (*Schubert et al.*, 1980); b): Latitudinal distribution of the zonal wind at three altitude regions, $\sim$ 66 km (blue), $\sim$ 61 km (violet), $\sim$ 47 km (red), derived from Venus Express measurements between the years 2006 and 2007 (*Sánchez-Lavega et al.*, 2008). 18

2.7 Observed meridional wind directions in Venus' atmosphere between 40 and 70 km altitude. Red arrows represent poleward wind, blue arrows represent equator-ward wind. The following observations from the years 1972 to 2017 from the day- and nightside southern and northern hemispheres are presented: a) *Kerzhanovich et al.* (1972), b) *Counselman et al.* (1980), c) *Rossow et al.* (1980), d) *Rossow et al.* (1989), e) *Carlson et al.* (1991), f) *Peralta et al.* (2007), g) *Sánchez-Lavega et al.* (2008), h) *Moissl et al.* (2009), i) *Hueso et al.* (2012), j) *Khatuntsev et al.* (2013), k) *Khatuntsev et al.* (2017), l) *Gonçalves et al.* (2020). 20

2.8 Vertical and latitudinal structure of the mean meridional circulation in Venus' atmosphere proposed by a) *Schubert et al.* (1980), b) *Yamamoto and Tanaka* (1997) and c) *Imamura and Hashimoto* (1998). 21

3.1 Artistic image of the Venus Express spacecraft and its seven scientific instruments (ESA). 26

3.2 Radio occultation geometry during VEX radio science measurements. Due to the refraction of the emitted radio signal in Venus' atmosphere the geometrical signal path ($R_1 + R_2$) is longer compared to the direct line of sight (R_3). The scenario is presented for signal refraction in the neutral atmosphere. In the ionosphere the value of refractive index is less than 1 (see section (3.2.2)) and refraction occurs away from the planet (Figure adopted from *Lipa and Tyler* (1979)) 31

3.3 First three *Fresnel zones* (F_1, F_2 and F_3) centered around the direct signal path between the spacecraft (S/C) and ground station (G/S). Both, the S/C and G/S are located at the focal points of the ellipsoidal cones. F_1 is defined so that the path length difference between the direct and the reflected signal is half the signal period. The first *Fresnel zone* contains the most signal energy. The diameter d_F of the first *Fresnel zone* is a measure for the spatial resolution in radio occultation measurements. The distance between the S/C and the atmospheric reference point as well as between the S/C and G/S is given b_1 and b_2, respectively. . . . 41

4.1 Radiation pattern of the Venus Express HGA1 (a) X-band; b) S-band) and HGA2 (c) X-band) for the azimuth angle of $\xi = 0°$. 48

4.2 Observed signal attenuation as well as absorptivity and H_2SO_4(g) abundance on the equatorial nightside (upper panels; *ingress*) and dayside (lower panels; *egress*) Venus atmosphere derived from Mariner V radio occultation data. Absorptivity profiles on the nightside were derived from the S-band radio signal attenuation using i) the S-band Doppler data and ii) the 423.3 MHz amplitude data for removal of the defocussing loss. On the dayside the S-band Doppler data were used, only. The black profiles shows the saturation abundance (cf. equation (5.13)). Signal level, absorptivity, temperature and pressure data for the creation of the figures were extracted from *Mariner Stanford Group* (1967) and *Fjeldbo et al.* (1971). No information on the uncertainty of the derived values was provided. 54

4.3 S-band radio absorptivity and H_2SO_4(g) abundance in Venus' equatorial atmosphere (red) derived by *Lipa and Tyler* (1979) as well as *Kolodner and Steffes* (1998) from Mariner 10 radio occultation data. The black profile shows the saturation abundance (cf. equation (5.13)). Data were extracted from the corresponding publications. Absorptivity data were interpolated at altitudes from *Kolodner and Steffes* (1998). 55

4.4 S-band radio signal absorptivity profiles in the Venus atmosphere derived by *Cimino* (1982) as well as *Jenkins and Steffes* (1991) from Pioneer Venus radio occultation measurements from the years 1978/1979 (a) - d)) and 1986/1987 (d)) at different latitudinal regions. Note that: $\alpha[\mathrm{dBkm}^{-1}] = 10\log_{10}(e)\alpha[km^{-1}]$ (see equation (4.22)). The dashed line in e) represents the approximate location of the 1 bar pressure level. . . 56

4.5 Panels a) and b): X-and S-band radio signal absorptivity profiles in Venus' nightside atmosphere ($\sim 67°$N) derived by *Jenkins et al.* (1994) from Magellan radio occultation measurements conducted in October 1991 (Orbit 3214). Panel c): Sulfuric acid vapor abundance profiles computed by *Kolodner and Steffes* (1998) from the absorptivity profiles visible in the panels a) and b). The saturation abundance was computed by using equation (5.13). The dashed lines in the panels a) to c) represent the approximate location of the 1 bar pressure level. 58

4.6 Residual attenuation of the 5 cm radio signal derived by *Gubenko et al.* (2001) from the Venera 15/16 radio occultation measurements carried out at two different latitudes. The defocussing loss was removed by using the 32 cm radio signal amplitude. Data were extracted from the corresponding publication and the absorption coefficient was transferred into units of dB/km by using equation (4.22). The value of the mean Venus radius was corrected from 6051 to 6051.8 km. The dashed line represent the approximate location of the 1 bar pressure level. 59

5.1 Mass stream function ψ in units of $kg \cdot m^{-1} \cdot s^{-1}$ in the northern hemisphere used in the simulation run *Test 1* (cf. Table 8.1). In the southern hemisphere the same parameters are used. 64

5.2 a) Meridional and b) vertical wind velocities in the circulation cells shown in Figure 5.1. Positive values represent poleward/upward flow while equatorward/downward wind is represented by negative values. While meridional wind velocity values are in units of m/s, vertical velocity values are in units of mm/s. 65

5.3 Profiles of vertical and horizontal eddy diffusion coefficients used in the present model. No latitudinal variations were considered in the model. In order to simulate the convection layer located between about 50 and 60 km altitude, the values of K_{zz} were increased in this region. 67

5.4 Mean sedimentation velocity at equatorial and polar latitudes used in the model. 69

6.1 Observed decrease of VeRa's X-band radio signal obtained from Closed-Loop (CL) recordings (green) as well as determined from Open-Loop (OL) recordings (blue) as a function of time. Please note the break between 900 and 2500 seconds. Radio ray parameters and atmospheric profiles were derived from the ingress and egress part of the measurement when a clear carrier signal (CS) could be detected, either by the CL receiver at the G/S on Earth or by the FFT based algorithm applied to the OL recordings. 76

6.2 Deepest altitudes in Venus atmospheric profiles achieved from VeRa's X-band CL data (panel a) and OL data (panel b) as a function of the latitude. The red profiles show the mean altitude in latitudinal bins of 5° each. 77

6.3 Attenuation of the X-band radio signal observed in two radio occultation measurements. Left: Ingress measurement conducted on 2006-08-11 at the southern mid-latitudes (52.70°S) (distance of VEX to center of Venus approx. 18535 km); Right: Ingress measurement conducted on 2007-01-03 at the northern polar latitudes (83.27°N) (distance of VEX to center of Venus approx. 8647 km). The green profile shows the contribution of refractive defocussing to the total signal attenuation (black). The blue profile presents the absorption of the signal in Venus' atmosphere. The horizontal dashed line shows the approximate altitude of the 1 bar pressure level. 78

6.4 Upper panel: Distance of Venus Express to the center of Venus while sounding the altitude region between 40 and 80 km at the southern and northern hemisphere. Lower panel: Contribution of the refractive loss to the observed attenuation of the X-Band radio signal between 40 and 80 km altitude at the southern and northern hemisphere. The hemispheres were subdivided into equal latitudinal bins of 5° each. Measurements located within each bin were averaged to one profile. No measurements are available in the northern mid-latitudinal region between about 20 and 60°N below 50 km altitude due to the orbit geometry of Venus Express. 80

6.5 The effect of pointing inaccuracies on Venus Express' X-Band radio signals occurred during the occultation measurements between the years 2006 and 2013 as a function of sounded altitude (left panel: HGA1; right panel: HGA2). The horizontal axes were subdivided into equal bins of 0.015 dB each and measurements located within each bin were counted. The color code gives the number of measurements located within each bin. The white profiles represent maximal pointing inaccuracies occurred between 2006 and 2014. The smaller image section in the right panel shows the zoomed area of the HGA2 pointing errors in the range from 0 to 2 dB between 40 and 100 km altitude. 81

6.6 Impact of pointing errors of the HGA1 (panel a) and b)) and HGA2 (panel d) and e)) on the derived H_2SO_4(g) abundance visible in the panels c) and f), respectively. The saturation vapor abundance was computed by using equation (5.13). 83

6.7 Sulfuric acid vapor abundance derived from Venera's 5 cm (6 GHz) radio absorptivity data visible in panel b) of Figure 4.6 by using equation (4.20d). Temperature and pressure data were adopted from VeRa's radio occultation measurements between the years 2006 and 2014 from the corresponding latitudes. Error bars, which were calculated by applying the standard error propagation, represent the variation of the temperature and pressure between the years 2006 and 2014. No information on the uncertainty of the absorptivity is included. The black profile represent the saturation vapor abundance (cf. equation (5.13)). 85

7.1 Absorptivity of VeRa's X- and S-band radio signals derived from egress measurements carried out in the year 2006 at northern cold collar latitudes (panels a) and b)) and polar region (panels d) and e)). The absorptivity profiles contain contributions mainly from CO_2, N_2 and H_2SO_4(g). The corresponding sulfuric acid vapor profiles are presented in the panels c) and f) for the collar and polar latitudes, respectively. The saturation abundance (black profiles in the panels c) and f)) was computed by using equation (5.13). 89

7.2 Mean absorptivity profiles from the Venus northern hemisphere derived from VeRa's X-Band (blue) and S-Band (red) radio signals from the year 2006. The profiles contain contributions mainly from CO_2, N_2 and H_2SO_4(g). The upper panel shows the latitudinal region between 60° and 74°, the lower panel shows the polar region between 78° and 90°. Narrow figures attached to the absorptivity profiles represent the number of data samples used for averaging. 91

7.3 Mean sulfuric acid vapor profiles from the Venus northern hemisphere derived from VeRa's S-and X-band radio signal absorption observed in 2006 (see Figure 7.2). The saturation abundance was computed by using equation (5.13). 92

7.4 Sulfur dioxide in Venus' middle and lower atmosphere obtained from ground based and spacecraft observations as well as from model results (cf. Figure 2.4.a)). The black square represent the SO_2 abundance derived from Magellan radio occultation S-and X-band data obtained from the orbit 3212. The blue square shows the SO_2 abundance calculated from Magellan data from the orbit 3214. The error bars represent the SO_2 abundance range derived from the uncertainty of the H_2SO_4(g) profiles. 94

7.5 Sulfuric acid vapor profiles derived from VeRa's X-band data calculated without (green) and with (blue) the SO_2 contribution to the total X-band radio signal absorption (cf. equation (4.21)). For the blue profile an SO_2 mixing ratio of 200 ± 80 ppm was used to correct for the contribution of sulfur dioxide to the total signal absorption. The black profile shows the H_2SO_4(g) saturation abundance calculated using the saturation vapor pressure over a H_2SO_4-H_2O solution of about 98% by weight (cf. equation (5.13)). 96

7.6 Upper limits of the sulfur dioxide abundance in the altitude region between 51 and 54 km derived from VeRa's X-band data between the years 2006 and 2015. The measurement uncertainties vary between 30 and 80 ppm. The red line represent the average abundance. The hemispheres were subdivided into equal latitudinal bins of 5° each. SO_2 values located within each bin were averaged to one mean value. Due to the low number of measurements, SO_2 values located in the latitude region between 25°N and 60°N were not considered for averaging. 98

7.7 Upper limits of the sulfur dioxide abundance in the altitude region between 51 and 54 km derived from VeRa's X-band absorptivity data between the years 2006 and 2015. Panel a) shows the abundance at southern and northern polar latitudes ($\geq 75°$), panel b) shows the abundance at the equatorial region (25°S - 25°N). The measurement uncertainties vary between 30 and 70 ppm. The red and blue data represent averaged abundances computed from measurements, which were obtained from different occultation seasons. 99

7.8 Mean atmospheric temperature as a function of the year at altitudes levels between 55 and 42 km at the northern polar region ($\geq 75°$) (panel a) to e)) as well as its annual difference (panel f)) derived from VeRa's X-band radio occultation data. 100

7.9 Averaged abundance of SO_2 at the equatorial and polar region derived from VeRa's X-band absorptivity/H_2SO_4(g) data (cf. Figure 7.7) incorporated into Figure 2.4. 102

7.10 Panel a): Latitudinal distribution of SO_2 at 70 km altitude as observed by *Marcq et al.* (2020) using SPICAV-UV data. Panel b): The mean SO_2 abundance adopted from panel a) (blue) along with that between 51 and 54 km altitude derived from radio occultation measurements (red) (cf. Figure 7.6). 103

7.11 Long-term evolution of SO_2 in the equatorial region at 70 km altitude (panel a)) extracted from Figure 2.4.b) as well as between 51 and 54 km altitude (panel b)) extracted from Figure 7.7.b). Panel c) shows the long-term trend in Venus' 365 nm albedo observed by *Lee et al.* (2019) at equatorial and mid-latitudes. Panel d) represents the temporal SO_2 evolution between 51 and 54 km altitude at both polar regions extracted from Figure 7.7.a). Error bars in the panels b) and d) represent the variability of the SO_2 abundance values observed in the corresponding years. 105

7.12 Zonally and time-averaged H_2SO_4(g) distribution in Venus' lower atmosphere at the southern and northern hemispheres derived from VeRa's radio occultation data from the years 2006 to 2014 (lower panel). The hemispheres were subdivided into equal latitudinal bins of 5° each. H_2SO_4(g) profiles located within each bin were averaged to one sulfuric acid vapor profile. The number of data samples used for averaging is shown in the upper panel. The white dashed line in the lower panel shows the isotherm of T = 340 K derived from VeRa's X-band radio occultation data from the same period of time. 108

7.13 Upper panel: H_2SO_4(g) column density computed between 42 and 47 km altitude in the northern polar region (75° - 90°) between 2006 and 2013. Red data represent averaged values computed from measurements obtained from different occultation seasons. Error bars (0.01 - $0.2{\cdot}10^{30}$ km^{-2}) were calculated using the standard error propagation; Lower panel: Temporal evolution of the mean temperature at 44 km altitude in the northern polar region (75° - 90°) between 2006 and 2014. The lower panel was adopted from Figure 7.8.d). 111

7.14 Mean H_2SO_4(g) profiles (blue straight line) and observed variation (blue dashed lines) at the northern polar latitudes between the years 2006 and 2007 (panel a)) as well as between end of 2008 and 2013 (panel b)). Error bars were calculated using the standard error propagation. The mean saturation abundance (black straight line) was computed using equation (5.13). Narrow figures attached to the mean H_2SO_4(g) profiles represent the number of data used for averaging. 112

7.15 Upper panel: H_2SO_4(g) column density computed between 46 and 50 km altitude in the equatorial region (25°S - 25°N) between the years 2006 and 2014. Error bars, in the order of 0.01 - $0.1{\cdot}10^{30}$ km^{-2}, were calculated using the standard error propagation; Lower panel: Temperature at 47 km altitude in the same latitudinal region derived from VeRa's radio occultation data from the years 2006 to 2014. Red data represent mean values resulting from averaging over a time period of 6 hours. 114

7.16 Mean H_2SO_4(g) profiles (blue straight line) and observed variation (blue dashed lines) between 0 and 3 h local time (panel a)) as well as between 6 and 10 h local time (panel b)). Error bars were calculated using the standard error propagation. The mean saturation abundance (black straight line) was computed using equation (5.13). Narrow figures attached to the mean H_2SO_4(g) profiles represent the number of data used for averaging. 115

7.17 Sulfuric acid vapor abundance profiles obtained from Mariner, Magellan and Venus Express radio occultation measurements at different latitudinal regions: a) equatorial latitudes, b) 65 - 70°S/N, c) polar region. Profiles from the Mariner observations were adopted from Figure 4.2 and Figure 4.3. While the Magellan profile in panel b) was adopted from Figure 4.5, that in panel c) was adopted from *Kolodner and Steffes* (1998). 116

8.1 H_2SO_4(g) distribution in Venus' northern hemisphere obtained from the simulation runs *Test 0*a), *Test 0*b) and *Test 1*a). The white dashed lines mark the altitude of the highest H_2SO_4(g) abundance. 124

8.2 Vertical profiles of H_2SO_4(g) in Venus' equatorial and polar atmosphere (panel a) and b), respectively) obtained from the simulation run *Test 1*a) performed with different circulation velocities of the Hadley and polar cells. The horizontal dashed lines show the approximate altitude of the 1 bar pressure level. 126

8.3 H_2SO_4(g) distribution in Venus' northern hemisphere obtained from the simulation runs *Test 2*a) and b) as well as from *Test 3*a) and b). The white dashed lines in *Test 2*b) and *Test 3*b) mark the altitude of the highest H_2SO_4(g) abundance. 127

8.4 H_2SO_4(g) distribution in Venus' atmosphere obtained from the simulation runs *Test 1*a) (upper panel), *Test 2*a) (middle panel) as well as derived from VeRa's radio occultation observations (lower panel) adopted from Figure 7.12. 130

8.5 Vertical profiles of H_2SO_4(g) at equatorial latitudes obtained from VeRa's observations as well as from the simulation runs *Test 1*a) and *Test 2*a). For the run *Test 1*a)* the global temperature was decreased by 10 K. Test The horizontal dashed lines show the approximate altitude of the 1 bar pressure level. 131

8.6 Vertical profiles of H_2SO_4(g) in Venus' northern polar atmosphere obtained from the simulation runs *Test 1*a) and *Test 2*a) as well as obtained from VeRa's observations. The horizontal dashed line show the approximate altitude of the 1 bar pressure level. 133

8.7 Mean SO_2 abundance in the altitude region between 51 and 54 km derived from VeRa's X-band data between the years 2006 and 2015 (data from the southern and northern hemisphere were adopted from Figure 7.6) superimposed on the mass stream function ψ in the northern hemisphere used in the simulation run *Test 1* (adopted from Figure 5.1). . . 135

8.8 Bulk density of the Venus clouds consisting of H_2SO_4-H_2O droplets obtained from the simulation run *Test 1a)* in the northern hemisphere. . . 137

8.9 Vertical profiles of H_2SO_4(g) and H_2SO_4-H_2O cloud droplets at equatorial (panel a)), mid- (panel b)), and polar (panel c)) latitudes obtained from the simulation run *Test 1*a). The horizontal dashed line shows the approximate altitude of the 1 bar pressure level. 138

8.10 Spatial distribution of water vapor obtained from the simulation run *Test 1a)* in the northern hemisphere. 139

8.11 Spatial distribution of sulfuric acid vapor obtained from the simulation run *Test 1a)* (panel a)) as well as obtained by *Imamura and Hashimoto* (1998) from a 2D model (panel b)) and by *Ando et al.* (2020) from a 3D model (panel c)). 141

8.12 Sulfuric acid vapor profiles in the equatorial region obtained from the simulation run *Test 1a)* (panel a) as well as calculated by *Imamura and Hashimoto* (2001) (panel b) and by *Parkinson et al.* (2015) (panel c) using 1D models. Explanation of the legend in panel b) can be found in *Imamura and Hashimoto* (2001). Black dots in panel c) represent H_2SO_4(g) values derived by *Kolodner and Steffes* (1998) from Mariner 10 radio occultation data. 143

8.13 Vertical profiles of the Venus clouds bulk density observed by *Knollenberg and Hunten* (1980) (cf. Figure 2.2b)) as well as obtained from the simulation run *Test 1a)*. 145

8.14 Spatial distribution of the cloud density obtained from the simulation run *Test 1a)* (panel a)) as well as obtained by *Imamura and Hashimoto* (1998) from a 2D model (panel b)) and by *Ando et al.* (2020) from a 3D model (panel c)). 146

8.15 Profiles of the cloud density at different latitudinal regions obtained from the simulation run *Test 1a)* (panel a)) as well as obtained by *McGouldrick* (2017) from a 1D model (panel b)). LCPS data in panel b) represent measurements from the Pioneer Venus Large probe Cloud Particle size Spectrometer. The legend in panel b) was adjusted according to the caption in *McGouldrick* (2017). 147

8.16 Water vapor concentration in Venus' middle and lower atmosphere obtained from observations and model calculations adopted from Figure 2.3 along with H_2O(g) profiles at the equatorial and polar latitudes obtained from the simulation run *Test 1a)*. 148

8.17 Spatial distribution of water vapor obtained from the simulation run *Test 1a)* (panel a)) as well as obtained by *Imamura and Hashimoto* (1998) from a 2D model (panel b)) and by *Ando et al.* (2020) from a 3D model (panel c)). 149

A.1 Receiving antenna pointing angle distribution. The elevation angle is represented by ϑ. 164

A.2 Path attenuation in the Earth atmosphere due to oxygen and water vapor for the elevation angles $\vartheta = 5°$ and $\vartheta = 90°$. 165

A.3 Path attenuation in the Earth atmosphere due to clouds/fog and rain for the elevation angles $\vartheta = 5°$ and $\vartheta = 90°$. For the cloud/fog attenuation it was set: $L_c = 2$ kg/m^2; exceedance probability: 0.1%. For the rain attenuation it was set: $R = 25$ mm/h; exceedance probability: 0.01%; rain height: 3.9 km. 168

B.1 Sketch of multipath propagation in the atmosphere. Radio rays, emitted by the transmitter, traverse the atmospheric region where inhomogeneities of the refractive index occur. The refractive index doesn't increase monotonically with depth and causes therefore a variation of the radio ray refraction in a narrow altitude range. This implies that several different radio rays arrive at the receiver at the same time. The sketch of the *multipath* geometry was adopted from *Lauritsen and Lohmann* (2004) who depicted the occurrence of *multipath propagation* in radio occultation measurements conducted on the Earth atmosphere. 172

B.2 Power spectra of VeRa's X-band radio signals computed when the *multipath* region in Venus' atmosphere was sounded. The signals were down converted to base-band. The Doppler shift induced by the relative motion between the S/C and G/S was removed. Additionally a predicted atmospheric Doppler shift was removed. The down mixing of the base-band signal by using the predicted Doppler shift results either in positive or in negative frequencies of the residual signal. The black dots show the residual frequency f_{res} computed by using the standard FFT-based algorithm outlined in section 3.2.1. Panel a) shows the latitudinal region around 73°S, panel b) shows the region around 65°S. The white dashed lines represent the sounded altitude corresponding to the ground station received time visible on the abscissa. 173

B.3 Panel a): Power spectra of VeRa's X-band radio signal adopted from Figure B.2.a). Panel b): Power spectra of VeRa's S-band radio signal from the same measurement as presented in panel a). 174

D.1 The effect of pointing inaccuracies on Venus Express' S-Band radio signals occurred during the occultation measurements in the year 2006 as a function of the sounded altitude. The horizontal axes were subdivided into equal bins of 0.0015 dB each and measurements located within each bin were counted. The color code gives the number of measurements located within each bin. The white profile represents maximal pointing inaccuracies occurred in 2006. 179

E.1 Sulfuric acid vapor profiles at the northern cold collar latitudes in Venus atmosphere derived from VeRa's X- and S-band radio signal absorption in the year 2006. 181

E.2 Sulfuric acid vapor profiles at the northern polar region in Venus atmosphere derived from VeRa's X- and S-band radio signal absorption in the year 2006. 182

Acronyms

AGC Automatic Gain Control

ASPERA Analyzer of Space Plasmas and Energetic Atoms

CHAMP Challenging Minisatellite Payload

CL Closed-Loop

D/L downlink

EIRP Equivalent Isotropically Radiated Power

ESA European Space Agency

FORMOSAT-3/COSMIC Constellation Observing System for Meteorology, Ionosphere and Climate

FFT Fast Fourier Transform

GCM General Circulation Model

GPS Global Positioning System

GRACE Gravity Recovery And Climate Experiment

G/S ground station

HGA1 high gain antenna 1

HGA2 high gain antenna 2

JAXA Japan Aerospace Exploration Agency

LCP Left Hand Circular Polarization

LO Local Oscillator

LOS line-of-sight

MAG Magnetometer

NASA National Aeronautics and Space Administration

OL Open-Loop

ONED one-way dual frequency

PVO Pioneer Venus Orbiter

PFS Planetary Fourier Spectrometer

PLL Phase-Locked Loop

RF Radio Frequency

RCP Right Hand Circular Polarization

RSS Radio Science Simulator

ROMAP Rosetta Magnetometer and Plasmamonitor

S/C spacecraft

SPICAV Spectrometer for Investigation of Characteristics of the Atmosphere of Venus

TWOD two-way dual frequency

TDB Barycentric Dynamical Time

U/L uplink

USO Ultra Stable Oscillator

UTC Coordinated Universal Time

VeRa Venus Express Radio Science Experiment

VEX Venus Express spacecraft

VIRTIS Visible and Infrared Thermal Imaging Spectrometer

VMC Venus Monitoring Camera

VME2000 Venus Mean Equator of Date J2000 frame

List of Symbols

a	Impact parameter
c	Speed of light in vacuum
d_a	Antenna diameter
d_F	Diameter of the first Fresnel zone
e	Elementary charge
$e_{\vec{R}_3}$	Unity vector along the line of sight between S/C and G/S
$e_{\vec{R}_1}$	Unity vector of the radio ray asymptote R_1 in Figure (3.2)
$e_{\vec{R}_2}$	Unity vector of the radio ray asymptote R_2 in Figure (3.2)
f_{DL}	Down Link Frequency
f_{res}	Residual frequency after correcting for straight-line and atmospheric Doppler shift
f_{sky}	Sky Frequency
f_{sky}^{prd}	Predicted Sky Frequency
G	Antenna gain
g	Gravitational acceleration
g_r	Focussing of a radio beam perpendicular to the plane of refraction
$\underline{K}$	Eddy diffusion tensor
k_B	Boltzmann constant
L	Refractive defocussing
l_r	Defocussing of a radio beam in the plane of refraction
$\overline{m}$	Mean molecular mass in the atmosphere of Venus below 100 km altitude
m_e	Mass of an electron
N	Refractivity
N_L	Loschmidt's number
n	Number density
p	Pressure
q	Number mixing ratio
r	Venus radius
r_0	Closest approach of the refracted ray to the planetary center of mass
r_p	Particle radius

T	Temperature
$\vec{v}$	Wind and sedimentation velocity vector
$v_{\vec{GS}}$	Velocity vector of the G/S
$v_{\vec{SC}}$	Velocity vector of the S/C
x_s	Size Parameter for scattering
α	Absorption
γ	Elevation angle of the antenna radiation pattern
Δf_{atm}	Atmospheric Doppler shift
Δf_{atm}^{RS}	Atmospheric Doppler shift computed by the RSS
Δf_E	Earth ionospheric/atmospheric influence on the radio signals
Δf_{str}	Straight-Line Doppler shift
Δf_{str}^{LO}	Straight-Line Doppler shift generated by Local Oscillator
δ	Bending angle of a radio ray
ϵ_0	Vacuum permittivity
η	Dynamical viscosity of CO_2
$\vartheta_{3\text{dB}}$	Half power beam width
$\overline{\kappa}$	Refractive volume
λ	Wavelength of a radio signal
μ	Index of refraction
μ^*	Chemical potential in the H_2SO_4-H_2O solution
ξ	Azimuth angle of the antenna radiation pattern
ρ_p	Particle density
σ	Cross section of a spherical particle
τ	Path absorption
ϕ_{res}	Residual Signal Phase
ψ	Mass stream function
ω	Angular frequency of an electromagnetic wave
ω_0	Resonant frequency (angular) of an electron bound in an atom
ω_p	Plasma frequency (angular)

Chapter 1

Introduction

Despite the proximity of Venus to Earth as well as its similar physical character, Earth's sister planet has evolved differently. Venus' atmosphere consists to a large extent of carbon dioxide ($\sim 96.5\%$) with a surface temperature exceeding 730 K and a pressure of 92 bar. The extreme conditions are most probably the result of a large runaway greenhouse effect which was triggered in Venus' early evolution by the smaller distance to the Sun compared to the Earth-Sun distance (e.g. *Ingersoll*, 1969; *Kasting and Pollack*, 1983; *Kasting*, 1988; *Goldblatt and Watson*, 2012). It is believed that oceans, which were probably present on the early Venus, evaporated as a result of the high solar flux. The resulting water vapor condensed at higher altitudes and formed a cloud deck which, along with water vapor and carbon dioxide, increased the greenhouse effect.

Today, among the depth of the atmosphere, CO_2 and the cloud deck are the main reasons for the high surface temperatures (e.g. *Bengtsson et al.*, 2013). Venus' present atmosphere is dry and water vapor is a trace gas with mixing ratios of approx. 30 ppm below about 40 km altitude and less than 15 ppm above 60 km (e.g. *Marcq et al.*, 2008; *Fedorova et al.*, 2016). Liquid H_2O exists mainly in the cloud deck which is located between about 50 and 70 km altitude. Along with sulfuric acid, it forms H_2SO_4-H_2O aerosols whose H_2SO_4 concentration is believed to increase from more than 75% around 70 km altitude to about 98% around 50 km altitude (e.g. *Hashimoto and Abe*, 2001). Observations of the vertical distribution of the clouds obtained by *Knollenberg and Hunten* (1980) revealed mainly a three layered structure at the equatorial region. Similar observations from the higher latitudes are missing so that information about the latitudinal distribution of the clouds are mainly based on model calculations (e.g. *Imamura and Hashimoto*, 1998; *Parkinson et al.*, 2015; *McGouldrick*, 2017; *Ando et al.*, 2020).

Sulfuric acid is produced in the altitude region between 60 and 70 km altitude (upper clouds). Here, sulfur dioxide reacts with oxygen and forms sulfur trioxide which then

reacts with H_2O(g) to form sulfuric acid vapor. Due to the low temperatures, H_2SO_4(g) condensates into liquid sulfuric acid and forms with water the above mentioned H_2SO_4-H_2O aerosols (e.g. *Krasnopolsky*, 2012). It is likely that volcanic eruptions were the source for SO_2 (e.g. *Bengtsson et al.*, 2013) which today is the most abundant trace gas in Venus' atmosphere. Mixing ratios of more than 100 ppm were observed below the clouds (e.g. *Marcq et al.*, 2008). In contrast to this, SO_2 abundances of a few tens of parts per billion were observed at cloud deck altitudes (e.g. *Marcq et al.*, 2020). The process causing the decrease of SO_2 between the lower and upper cloud region is not well understood due to the low number of SO_2 observations at these altitudes.

It is assumed that SO_2 is transported from lower to higher altitudes by diffusion and upward directed winds (e.g. *Marcq et al.*, 2012; *Vandaele et al.*, 2017). The latter may be part of circulation cells (e.g. Hadley cell, polar cell) which, among atmospheric waves, are thought to play a crucial role in the maintenance of the superrotation observed in Venus atmosphere (e.g. *Yamamoto and Takahashi*, 2006). This zonal wind flow is a well known fact. Wind velocities in excess of 100 m/s were observed between 60 and 70 km altitude in the latitudinal region between 0° and 50° in both hemispheres (e.g. *Schubert et al.*, 1980; *Sánchez-Lavega et al.*, 2008). Although it is assumed that meridional circulation plays an important role in the evolution and maintenance of Venus' atmospheric superrotation, the knowledge about the meridional wind pattern is poor. The latter can be studied by means of its influence on the abundances and the global distributions of SO_2, H_2O(g) and H_2SO_4(g). Particularly, spatial and temporal variations of these species may result from the predominant wind dynamics as well as from its variations.

The abundances of SO_2 and H_2O(g) were acquired from spectroscopic measurements. While no clear meridional variations could be observed below the clouds, a latitudinal trend was found at cloud top altitudes (e.g. *Marcq et al.*, 2008; *Cottini et al.*, 2012; *Fedorova et al.*, 2016; *Marcq et al.*, 2020). Spectroscopic measurements were also used by *Jenkins et al.* (2002) who observed a latitudinal variation in the sulfuric acid vapor abundance below the clouds. They detected increased H_2SO_4(g) amounts at mid- and polar latitudes and no significant H_2SO_4(g) content at the equatorial region. In general, the vertical resolution of spectroscopic measurements, however, is limited to values of the order of 2 - 12 km (e.g. *Jenkins et al.*, 2002; *Grassi et al.*, 2008; *Limaye et al.*, 2018). A much better vertical resolution is achieved by radio occultation measurements. Those provide atmospheric profiles with a vertical resolution of a few hundred meters. Radio occultation studies at Venus were carried out with the Mariner V (*Fjeldbo et al.*, 1971), Mariner 10 (*Lipa and Tyler*, 1979), Venera (*Gubenko et al.*, 2001), Pioneer Venus (*Cimino*, 1982; *Jenkins and Steffes*, 1991) and the Magellan (*Jenkins et al.*, 1994) spacecraft. As H_2SO_4(g) is the most opaque constituent

in Venus' atmosphere at radio wavelengths (*Steffes and Eshleman*, 1981), a strong absorption of radio signals was observed in these measurements. The absorption can be used to derive the abundance of sulfuric acid vapor. First reliable H_2SO_4(g) profiles were provided by *Kolodner and Steffes* (1998), who transferred the absorptivity data acquired from the Mariner 10 and the Magellan radio occultation measurements into H_2SO_4(g) profiles. These measurements, however, were locally constrained so that latitudinal and temporal variations couldn't be studied. Indications for those variations were found by *Cimino* (1982) as well as by *Jenkins and Steffes* (1991) in the absorptivity data derived from the Pioneer Venus radio occultation measurements. They observed a distinct latitudinal dependance of the S-band absorption below 50 km altitude as well as a decrease of the latter between 70° and 80°N between the years 1978 and 1987.

The Venus Express spacecraft (VEX) probed the atmosphere of Venus' between the years 2006 and 2014 with radio signals at 13 cm (S-band) and 3.6 cm (X-band) wavelengths. The orbit of VEX allowed to sound the atmosphere over a wide range of latitudes and local times. This way, latitudinal and temporal variations of the SO_2 and H_2SO_4(g) abundances below about 55 km altitude could be studied. Latitudinal variations of H_2SO_4(g) were observed by *Oschlisniok et al.* (2012) around 50 km altitude using Closed-Loop (CL) data acquired from the Venus Express Radio Science Experiment (VeRa). CL-data are not suited to study Venus' deep atmosphere below about 50 km altitude, where the signal exhibits strong attenuation effects. In the present work, VeRa's Open-Loop (OL) data are used. In contrast to the CL-receiving system, in the OL-system the incoming radio signals are heterodyned to base band and recorded for later processing. This way, a signal which was lost in the CL-receiver may be recovered using OL-data so that the atmospheric region below 50 km altitude can be studied. More than 800 radio occultation measurements obtained from VeRa are used in the present work to study the radio signal absorption which occurred in Venus' atmosphere. The latter is used to derive the global distributions of the SO_2 and H_2SO_4(g) abundances as well as their variations below 55 km altitude. Additionally, a two-dimensional mass transport model is developed in order to study the influence of wind transport on the derived H_2SO_4(g) abundance.

Chapter 2 provides an overview of the thermal structure and chemical composition of the Venusian atmosphere below 80 km altitude. Moreover, a summary of wind observations is presented.

Chapter 3 contains a brief description of the Venus Express spacecraft and its payload. Furthermore, a description of the data acquisition and data processing is presented.

Chapter 4 describes attenuation effects which may occur in radio occultation measurements. Additionally, a presentation of absorption and H_2SO_4(g) observations derived from previous radio occultation measurements is given.

Chapter 5 presents the two-dimensional mass transport model which is developed in the present work to study wind transport mechanisms in Venus' atmosphere.

Chapter 6 presents attenuation effects which occurred in VeRa's X- and S-band radio signals during the radio occultation measurements.

Chapter 7 shows the computed absorption of VeRa's X- and S-band radio signals in Venus' atmosphere. Subsequently, the spatial distributions and variations of the SO_2 and H_2SO_4(g) abundances below 55 km altitude derived from the X-band radio signal absorption are presented.

Chapter 8 presents the modeled spatial distributions of the H_2SO_4(g) and H_2O(g) abundances as well as that of the Venus clouds. The results are compared with the results derived from VeRa's measurements as well as with previous results.

Chapter 9 summarizes the observations derived from VeRa's measurements as well as the modeled results obtained from the 2D transport model. Furthermore, suggestions for future observation and modeling studies are given.

Chapter 2

The atmosphere of Venus below 80 km altitude

The following chapter provides an overview about Venus' neutral atmosphere below 80 km altitude. The presented results were obtained from previous measurements and other experiments on board VEX. Section 2.1 outlines the structure of the atmosphere based on the vertical temperature distribution. In section 2.2 the chemical composition is presented by means of the most abundant trace gases. Their global distributions as well as their temporal variations are thought to be the result of the wind system and its variation in the atmosphere. Observations and simulations of Venus' wind dynamics are presented in section 2.3.

2.1 Thermal structure

Measurements of the temperature in the atmosphere of Venus were conducted by ground based, in situ and spacecraft observations (e.g. *Sagan*, 1962; *Avduevsky et al.*, 1971; *Kliore and Patel*, 1982). They revealed a temperature of about 735 K at the planets surface with small spatial and diurnal variations (e.g. *Seiff et al.*, 1985). While the latter remain small in the deep atmosphere ($<$ 30 km), they increase significantly with altitude. The planets exosphere ($>$ 100 km), for example, shows the highest temperature variations. Here, values of approx. 300 K were observed on the dayside (thermosphere), while on the nightside 100 K were measured (cryosphere) (e.g. *Keating et al.*, 1980).

The knowledge about the spatial temperature distribution in the altitude range between about 35 and 90 km was mainly achieved from radio occultation measurements. Those were conducted with the Mariner, Pioneer Venus, Venera, Magellan and Venus Express spacecraft (sections 3.1.2 and 3.2.2). Panel a) in Figure 2.1 shows the

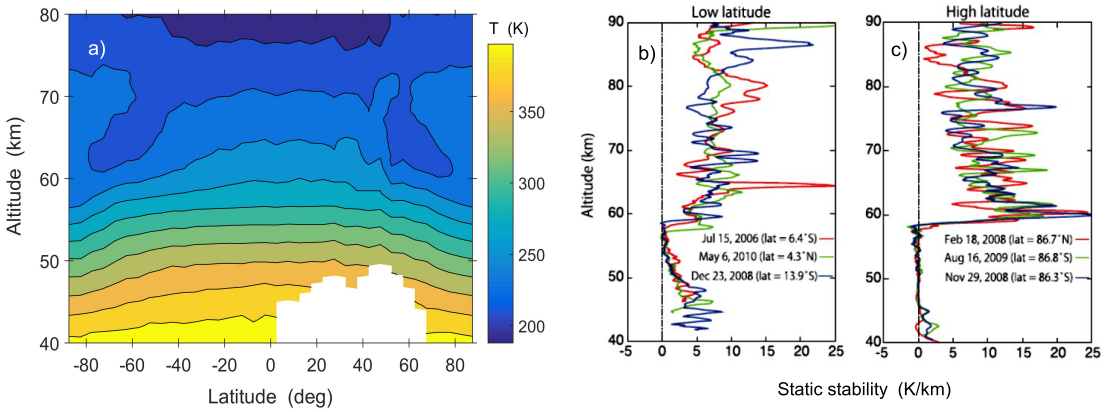

Figure 2.1: *Panel a): Zonal and temporal averaged temperature distribution in Venus' atmosphere between 40 and 80 km altitude derived from Venus Express radio occultation data. The southern and northern hemispheres were subdivided into equal latitudinal bins of 5 deg each. Vertical temperature profiles from the years 2006 to 2014 located within each bins were averaged to one profile. The lack of data in the latitude range between about* $0°N$ *and* $65°N$ *is a consequence of the spacecrafts orbit geometry; Panel b): Static stability in Venus' atmosphere derived by Ando et al. (2015) from Venus Express radio occultation data.*

zonal and temporal averaged temperature distribution in Venus' southern and northern hemispheres between 40 and 80 km altitude. The temperature map was derived from Venus Express radio occultation data achieved between the years 2006 and 2014.

It shows a monotonically decreasing temperature from almost 400 K at 40 km to less than 200 K at 80 km altitude. An exception to this is the altitude region between 60 and 70 km around the planetary latitude of 60° on both hemispheres. Here, a clear depression of the temperature is visible, the so-called *cold collar*. It surrounds the polar regions at both hemispheres.

Based on the vertical temperature distribution, the Venusian atmosphere is divided into two altitude regions, i.e., the troposphere (lower atmosphere) and the mesosphere (middle atmosphere).

The troposphere extends from the surface to an altitude of about 60 km. Within this altitude range an almost constant temperature lapse rate of about 10 K/km was found (e.g. *Pätzold et al.*, 2007). The latitudinal temperature distribution reveals a clear trend. The almost constant temperature at each altitude between about 40°S and 40°N decreases rapidly poleward of approx. 50° latitude. The upper boundary, i.e., the tropopause, shows a distinct latitudinal variation (e.g. *Tellmann et al.*, 2009). While the altitude of the tropopause is lowest at the equatorial ($\sim$ 59 km) and highest

at the *cold collar* region ($\sim$ 62 km), its temperature shows the opposite behavior (270 K at low latitudes; 215 K at *cold collar* latitudes). Superimposed on the latter values are local time variations. The mesosphere is located above the tropopause and extends to altitudes of up to 100 km. In contrast to the troposphere, the temperature lapse rate in the mesosphere reveals a series of sign changes between about 60 and 75 km altitude (e.g. *Pätzold et al.*, 2007; *Tellmann et al.*, 2009). This altitude range depends strongly on the planetary latitude with the largest extension at *cold collar* and polar regions.

The vertical temperature distribution is used to study the static stability of the atmosphere (e.g. *Tellmann et al.*, 2009). While increased stability values support enhanced wave activity, low values may indicate convective mixing. The panels b) and c) in Figure 2.1 show the derived static stability in the lower and middle Venus atmosphere at two latitudinal regions derived by *Ando et al.* (2015) from Venus Express radio occultation measurements.

The highest values can be found at altitudes above 60 km indicating high atmospheric static stability. At these altitudes, an increased level of atmospheric wave activity was reported by various authors (e.g *Seiff et al.*, 1985; *Hinson and Jenkins*, 1995; *Tellmann et al.*, 2009; *Ando et al.*, 2015). *Tellmann et al.* (2012) have found a clear latitudinal and local time variation of gravity waves in this region based on Venus Express radio occultation measurements. They observed the highest values at the *cold collar* and polar regions as well as during daytime at equatorial latitudes.

Below that altitude range the lowest values can be found indicating instability of the atmosphere against convective overturning. According to *Baker et al.* (2000*b*,*a*) this convection layer may serve as a source mechanism for the atmospheric waves observed above 60 km altitude. By comparing the panels b) and c) in Figure 2.1 it can be seen that the vertical extension of the convection layer shows a clear latitudinal variation. It has the largest extension at high latitudes. According to *Imamura et al.* (2014), enhanced convective mixing at high latitudes may lead to increased wave activity at these regions as observed by *Tellmann et al.* (2012).

2.2 Chemical composition

Since carbon dioxide was first detected by *Adams and Dunham* (1932) in the IR spectrum of Venus, the knowledge of the CO_2 abundance and that of other gases in Venus' atmosphere was increased by further observations (e.g. *Adel*, 1937; *Herzberg*, 1951; *Reese and Swan*, 1968; *Prinn*, 1978). Today CO_2 is known to be the main constituent in Venus' atmosphere (96.5%) followed by nitrogen (N_2) (3.5%). Less abundant species

are carbon monoxide (CO), water vapor (H_2O) and the sulfur gases sulfur dioxide (SO_2), sulfuric acid (H_2SO_4) and carbonyl sulfide (OCS). These trace gases, with mixing ratios in the order of parts per million (ppm), are among the most important constituents in the middle and lower Venus' atmosphere. Their global distribution as well as vertical and temporal variation is a consequence of the predominant atmospheric conditions as well as chemical and dynamical processes. In the following the occurrence of the trace gases in Venus' atmosphere is briefly described based on ground based and spacecraft observations as well as one-dimensional chemical model results.

H_2SO_4

Sulfuric acid is the main constituent of Venus's main cloud deck between approx. 50 and 70 km altitude (e.g. *Young*, 1973; *Hansen and Hovenier*, 1974; *Palmer and Williams*, 1975). Due to the low temperatures within this altitude range (350 - 230 K) it predominantly exists in the liquid state and forms along with water H_2SO_4-H_2O aerosols. A low concentration of the latter can also be found in the upper haze located above the main clouds between 70 and 90 km altitude (*Kawabata et al.*, 1980). Due to the higher temperatures below the main clouds H_2SO_4 exists in the gaseous state between about 30 and 50 km altitude. Here, it is part of a haze layer which most probably extends to altitudes as deep as 30 km (*Knollenberg and Hunten*, 1980; *Esposito et al.*, 1983).

On the basis of PVO particle size spectrometer and photopolarimeter measurements *Knollenberg and Hunten* (1980) as well as *Kawabata et al.* (1980) and *Lane and Opstbaum* (1983) have deduced a bimodal/trimodal size distribution of the particles in the altitude range between about 30 and 90 km. Table 2.1 summarizes the vertical occurrence of these particles along with their mean diameter between 30 and 90 km altitude.

The smallest particles, mode 1, could be detected within the entire altitude range between 30 and 90 km. They are thought to consist mainly of elemental sulfur (e.g. *James et al.*, 1997). Only a small number of mode 1 sized H_2SO_4-H_2O aerosols may exist above about 50 km altitude whose concentration is believed to be 75% H_2SO_4 by weight in the upper haze region (*Kawabata et al.*, 1980). Due to the small mass of the mode 1 particles, however, the contribution of the latter to the overall bulk density of the cloud can be neglected.

The larger mode 2 particles, located in the main clouds between about 48 and 70 km altitude, are most likely H_2SO_4-H_2O aerosols (*Knollenberg and Hunten*, 1980). In

	Altitude Range (km)	Mean Diameter (μm)		
		Mode 1	Mode 2	Mode 3
Upper Haze	70 - 90	0.4		
Upper Clouds	56.5 - 70	0.4	2.0	
Middle Clouds	50.5 - 56.5	0.3	2.5	7.0
Lower Clouds	47.5 - 50.5	0.4	2.0	8.0
Lower Haze	31 - 47.5	0.2		

Table 2.1: *The occurrence of the mode 1, 2 and 3 particles in the altitude range between 30 and 90 km in Venus' atmosphere as measured by the PVO particle size spectrometer and photopolarimeter (Knollenberg and Hunten, 1980; Kawabata et al., 1980; Lane and Opstbaum, 1983).*

contrast to the mode 1 aerosols, however, the concentration of the mode 2 particles is believed to be higher, ranging from 75% to 85% (*Esposito et al.*, 1983). Here, *Cottini et al.* (2012) found indications for a latitudinal variation after which the concentration reveals a more narrow range in the polar latitudes (80-83%).

The composition of the large mode 3 particles, located mainly in the lower and middle clouds, is still a highly controversial issue. While *Knollenberg and Hunten* (1980) argued that those are crystalline particles, *Cimino* (1982) proposed a solid dielectric core coated by a thin highly concentrated H_2SO_4-H_2O solution ($>$ 95% of H_2SO_4). *Esposito et al.* (1983) suggested that the particles could be a mis-identified tail of the mode 2 particles. Re-examining PVO particle size spectrometer data, *Toon et al.* (1984) concluded that the mode 3 particles may be composed of liquid sulfuric acid, which was confirmed by *Grinspoon* (1993) using Galileo Near-Infrared Mapping Spectrometer (NIMS) data.

Knollenberg and Hunten (1980) derived the vertical distribution of the number densities of the mode 1, 2 and 3 particles from PVO particle size spectrometer measurements. The results are shown in panel a) of Figure 2.2 for the mode 2 and 3 particles. Assuming a density of $2 \cdot 10^6$ gm^{-3}, panel b) in Figure 2.2 shows the corresponding mass loading (*Knollenberg and Hunten*, 1980).

It is clearly visible, that although the number density of the mode 2 particles exceeds that of mode 3 particles, the bulk mass in the lower and middle clouds is dominated by the mode 3 particles. This is a consequence of their larger size compared to the

mode 2 particles (cf. table 2.1). The latter make up the bulk mass in the upper clouds between about 57 and 70 km altitude.

The different sizes and vertical distributions of the mode 1, 2 and 3 particles may be explained by their different phases, growth history as well as the impact of dynamical transport processes on the particles (*Knollenberg and Hunten*, 1980). At least the mode 2 particles are produced in a narrow altitude range around 66 km altitude (*Knollenberg and Hunten*, 1980; *Krasnopolsky*, 2012; *Zhang et al.*, 2012). Here, SO_2 is oxidized into SO_3, which in turn rapidly reacts with water and this way produces sulfuric acid vapor

$$\begin{aligned} SO_2 + O + M &\longrightarrow SO_3 + M \\ SO_3 + H_2O + H_2O &\longrightarrow H_2SO_4 + H_2O. \end{aligned} \tag{2.1}$$

According to one-dimensional photochemical models the column integrated production rate of H_2SO_4 is in the order of 10^{11} - 10^{13} $cm^{-2}s^{-1}$ (*Yung and Demore*, 1982; *Krasnopolsky and Pollack*, 1994; *Krasnopolsky*, 2012). The oxygen atoms, O, are produced photochemically above the main clouds ($\geq$ 70 km) and are transported to lower altitudes (*Krasnopolsky*, 2012). *James et al.* (1997) have shown that gaseous H_2SO_4

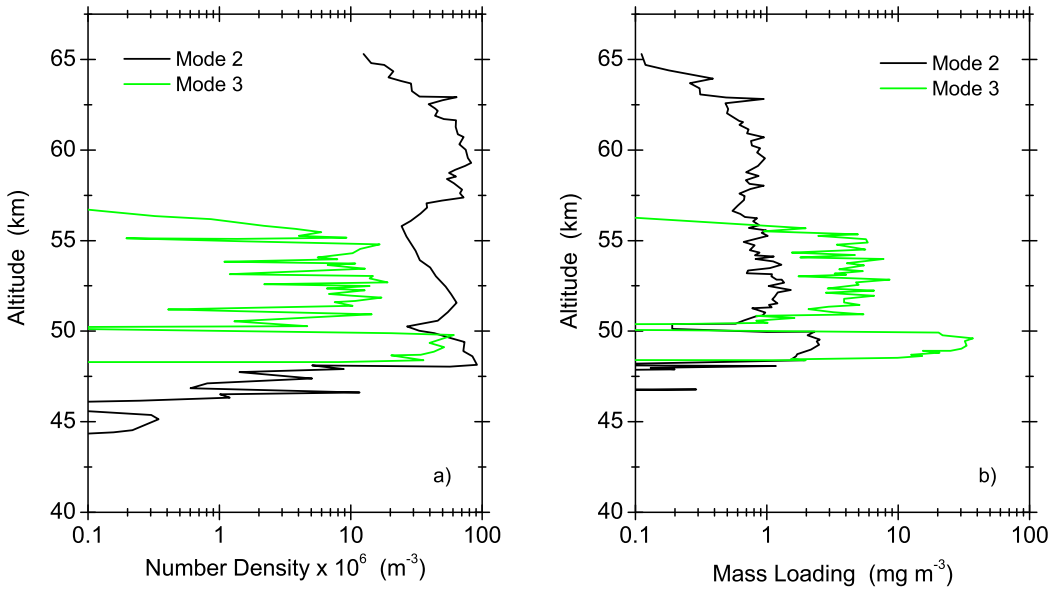

Figure 2.2: *Vertical distribution of the number density (panel a)) and mass loading (panel b)) of mode 2 and 3 particles in Venus' atmosphere as observed by the PVO particle size spectrometer. Data were adopted from Knollenberg and Hunten (1980). The contribution of the mode 1 particles to the overall mass loading of the Venus clouds is small and is therefore neglected.*

produced by the net reaction (2.1) may condensate onto mode 1 particles at cloud temperatures and pressures and this way produce H_2SO_4 droplets. The absorption of H_2SO_4(g) in those droplets leads to a growth of the aerosols, i.e., mode 2 particles.

The mode 2 aerosols are transported downward by wind dynamics (section 2.3) as well as by sedimentation. Evaporation of the aerosols at higher temperatures produces gaseous sulfuric acid below about 50 km altitude. In contrast to the upper clouds, where the abundance of H_2SO_4(g) is small due to rapid absorption in droplets, the H_2SO_4(g) abundance below the main clouds is found to be in the order of parts per million (*Jenkins et al.*, 1994; *Kolodner and Steffes*, 1998; *Jenkins et al.*, 2002; *Oschlisniok et al.*, 2012). A presentation of sulfuric acid vapor profiles from the lower Venus atmosphere derived from previous radio occultation measurements is given in section 4.2.

Due to the high temperatures below about 40 km altitude gaseous sulfuric acid is thermally decomposed into SO_3 and H_2O

$$H_2SO_4 + H_2O \longrightarrow SO_3 + H_2O + H_2O \tag{2.2}$$

and subsequently, sulfur trioxide reacts with carbon monoxide and carbonyl sulfide producing sulfur oxides and carbon dioxide

$$\begin{aligned} SO_3 + CO &\longrightarrow SO_2 + CO_2 \\ SO_3 + OCS &\longrightarrow (SO)_2 + CO_2. \end{aligned} \tag{2.3}$$

The rapid reaction of sulfur trioxide with carbon monoxide represents a production of sulfur dioxide and loss of CO in Venus' lower atmosphere (*Krasnopolsky and Pollack*, 1994; *Krasnopolsky*, 2007).

H_2O

Water exists in the liquid and gaseous states in Venus' middle and lower atmosphere. Along with liquid sulfuric acid, liquid water forms H_2SO_4-H_2O aerosols which were identified as mode 2 and probably mode 3 particles in Venus' main clouds (e.g. *Knollenberg and Hunten*, 1980; *Toon et al.*, 1984; *Grinspoon*, 1993). Their vertical distributions are presented in the table 2.1 and Figure 2.2.

Water vapor was detected within the entire middle and lower atmosphere by airborne, ground based and spacecraft observations. Examples of results are shown in Figure 2.3 along with model results.

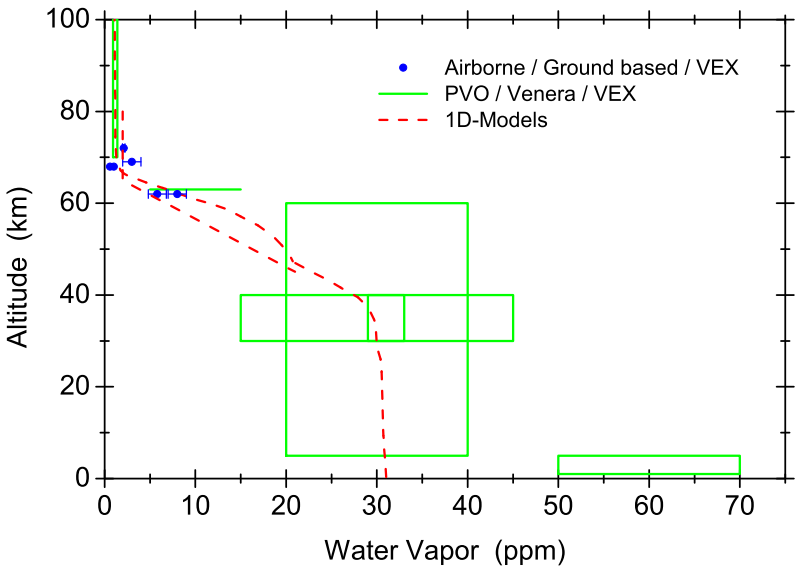

Figure 2.3: *Water vapor in Venus' middle and lower atmosphere obtained from airborne, ground based and spacecraft observations as well as from model results (Fink et al., 1972; Bézard et al., 1990; Bell et al., 1991; Crisp et al., 1991; Bjoraker et al., 1992; Donahue and Hodges, 1992; Pollack et al., 1993; Bergh et al., 1995; Meadows and Crisp, 1996; Ignatiev et al., 1997, 1999; Fedorova et al., 2008; Marcq et al., 2008; Cottini et al., 2012; Fedorova et al., 2016).*

Obviously the amount of water vapor was found to be highest below the main clouds. Maximal H_2O(g) mixing ratio values ranging between 50 and 70 ppm near Venus' surface were derived by *Ignatiev et al.* (1997) from optical sunlight spectra measured by the Venera 11, 13 and 14 entry probes. They also derived an almost constant water vapor content of 30 ± 10 ppm between 5 and 60 km altitude, which is consistent with H_2O(g) mixing ratio values observed by *Marcq et al.* (2008) who used Venus Express/VIRTIS-H (section 3.1) measurements. The increase of the H_2O content in the lowest 5 km would imply a source for water near the surface, which could be provided by volcanic outgassing as proposed for example by *Grinspoon* (1993).

The consumption of H_2O(g) in the upper clouds, described by equation (2.1), leads to a decrease of the water vapor content at cloud altitudes. Above the main clouds only small values of less than 10 ppm were measured by airborne, ground based and spacecraft observations.

In contrast to the lower atmosphere, where no latitudinal variations could be measured (*Marcq et al.*, 2008), *Cottini et al.* (2012) found indications for a latitudinal

trend at cloud top altitudes. In Venus Express/VIRTIS (section 3.1) dayside data they observed minimal H_2O(g) mixing ratio values of 3 ± 1 ppm at 40° latitude at both hemispheres and maximal values of 5 ppm at the polar regions around ±80°. *Fedorova et al.* (2016) confirmed the observed latitudinal variation by using Venus Express/SPICAV (section 3.1) measurements. They observed highest H_2O(g) values of 7.2 ± 1.4 ppm between 70° and 80° at both hemispheres and minimal abundances of 5.4 ± 1.0 ppm between 30° and 50°. The authors also reported on indications for a topographical influence at the equatorial region where the *Aphrodite Terra* highlands may influence the vertical transport of H_2O(g).

SO_2

Sulfur dioxide is the most abundant trace gas in Venus' middle and lower atmosphere. It's mixing ratio ranges from a few tens of parts per billion (ppb) above about 60 km altitude to several hundreds of ppm below 55 km. It is believed that the SO_2 high abundant region below 55 km altitude serves as a source for the sulfur dioxide observed at higher atmospheric regions. It is transported from lower to higher altitudes by means of the upward directed branch of the global Hadley circulation (section 2.3). Panel a) in Figure 2.4 summarizes SO_2 abundance values achieved from ground based and spacecraft observations as well as model results of SO_2 between 0 and 100 km altitude.

The low SO_2 abundance values above about 60 km altitude were obtained from ground based as well as from spacecraft observations. Highest values of 0.1 - 1 ppm were derived by *Zasova et al.* (1993) at altitudes around 69 km from Venera-15 IR spectrometer measurements. They also observed a clear latitudinal variation with lowest SO_2 abundance values at equatorial and highest values at polar latitudes. A similar trend was observed by *Marcq et al.* (2012) on the basis of Venus Express SPICAV measurements (section (3.1)). They also detected the opposite trend which emphasizes the high variability of the SO_2 abundance at the cloud tops. The latter trend was also reported by *Marcq et al.* (2020). Based on ground based and spacecraft observations *Esposito et al.* (1988) have reported a long-term trend in the equatorial SO_2 abundance at cloud top altitudes with highest values around the year 1978 and a smooth decrease in the following years. A long-term variation in the equatorial cloud top SO_2 abundance was also observed by *Marcq et al.* (2012, 2020) in SPICAV-UV measurements (section 3.1). The results are presented in panel b) of Figure 2.4 along with Hubble Space Telescope and ground based observation carried out by *Jessup et al.* (2015) and *Encrenaz et al.* (2016), respectively. Distinctly increased values are visible in the years 2007 and 2009. Additionally, a general decrease of SO_2 accompanied by oscillations on shorter

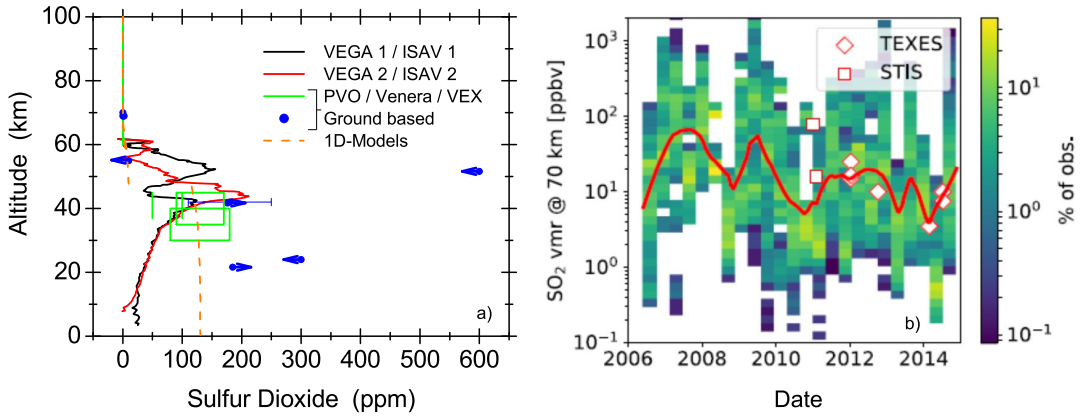

Figure 2.4: *Panel a): Sulfur dioxide in Venus' middle and lower atmosphere obtained from ground based and spacecraft observations as well as from model results (Barker, 1979; Hoffman et al., 1980; Oyama et al., 1980; Zasova et al., 1993; Bézard et al., 1993; Pollack et al., 1993; Parisot et al., 1986; Bertaux et al., 1996; Jenkins et al., 2002; Marcq et al., 2008; Belyaev et al., 2012; Krasnopolsky, 2007, 2012; Zhang et al., 2012). Arrows placed on data samples represent either 'less than' or 'greater than'. Panel b): Temporal evolution of the equatorial SO_2 abundance at cloud top altitudes observed by Marcq et al. (2020) in SPICAV-UV measurements from the years 2006 to 2015. The red line represents the moving median value. The Figure was adopted from Marcq et al. (2020).*

time scales is visible during this period of time. Enhanced SO_2 abundances may result from injections from the deep atmosphere which are a consequence of upward transport variations of the global Hadley circulation (*Esposito*, 1984; *Jessup et al.*, 2015; *Marcq et al.*, 2012, 2020). *Vandaele et al.* (2017) as well as *Marcq et al.* (2020) have detected a distinct local time variation of the SO_2 abundance between 70 and 80 km altitude using SPICAV-UV observations (section (3.1)). While increased values were observed at the morning and evening terminator, lowest SO_2 values were measured at the local noon. *Vandaele et al.* (2017) also reported short-term SO_2 variations (in the order of a few Earth days) ranging over several orders of magnitude.

It can be seen from Figure 2.4.a) that below about 60 km the SO_2 abundance increases with decreasing altitude. Maximal values are visible between 30 and 55 km. Enhanced values of > 176 ppm around 42 km altitude were obtained by *Oyama et al.* (1980) from in situ measurements of the gas chromatograph mounted on the PVO large probe. Similar SO_2 values (180 ± 70 ppm) at 42 km altitude on the nightside of Venus were achieved by *Pollack et al.* (1993) from ground based spectroscopic measurements. Ground based observations were also conducted by *Bézard et al.* (1993) as well as by *Jenkins et al.* (2002). They derived SO_2 abundance values of 130 ± 70 ppm between

35 and 45 km altitude as well as $<$ 100 ppm (equatorial latitudes) and $<$ 50 ppm (polar latitudes) between 37 and 45 km altitude, respectively. *Marcq et al.* (2008) have derived SO_2 abundance values of 130 ± 50 ppm between 30 and 40 km altitude from VIRTIS-H measurements (section (3.1)) from a wide range of southern and northern latitudes. Due to the large error bars, however, a latitudinal variation, similar to that observed at the cloud tops, couldn't be observed. The largest SO_2 abundance values were obtained by *Oyama et al.* (1980) as well as by *Hoffman et al.* (1980) from early Pioneer Venus observations. They detected enhanced values of $<$ 600 ppm around the cloud base and $<$ 300 ppm at 24 km altitude at equatorial latitudes. The only SO_2 abundance profiles were derived in the equatorial region by the spectrometers on board the VEGA 1 and 2 entry probes in 1985 (*Bertaux et al.*, 1996). The probes entered Venus' atmosphere separated by four days and reached the surface at similar geolocations. The obtained profiles show increased values between 30 and 60 km altitude with highest values of more than 200 ppm between 40 and 45 km. Both profiles show a clear disagreement between 40 and 60 km altitude emphasizing the high SO_2 variation below the main clouds within this period of time. Below 40 km altitude, both profiles monotonically decrease with decreasing altitude reaching minimal values of less than 25 ppm below 10 km.

Krasnopolsky (2012) as well as *Zhang et al.* (2012) have successfully reproduced the SO_2 abundance observations above about 60 km altitude using one-dimensional photochemical models. The highly variable SO_2 abundance in the altitude range between 30 and 60 km, however, is difficult to reproduce. Especially the transition from the SO_2 high abundant altitude region below the main clouds to SO_2 low abundant altitudes above about 60 km is not fully understood. The latter altitude region is thought to be steadily supplied with SO_2 from the lower atmosphere (e.g. *Marcq et al.*, 2012). Processes which deplete the SO_2 abundance in the transition region between about 50 and 60 km altitude, however, are missing in current chemical one-dimensional models. This leads to unreliable SO_2 abundance values at these altitudes (*Krasnopolsky*, 2012; *Zhang et al.*, 2012). Observations of SO_2 between 50 and 60 km altitude would help to constrain the model parameter and this way help to understand the unresolved chemical processes in this altitude region.

CO and OCS

Carbon monoxide is mainly produced by photodissociation of carbon dioxide at altitudes above 80 km (e.g. *Krasnopolsky*, 2012). The CO abundance exhibits a high variability at these altitudes ranging between 4 and 1000 ppm (e.g. *Clancy et al.*, 2003; *Svedhem et al.*, 2007). Using microwave spectra *Clancy and Muhleman* (1985) have

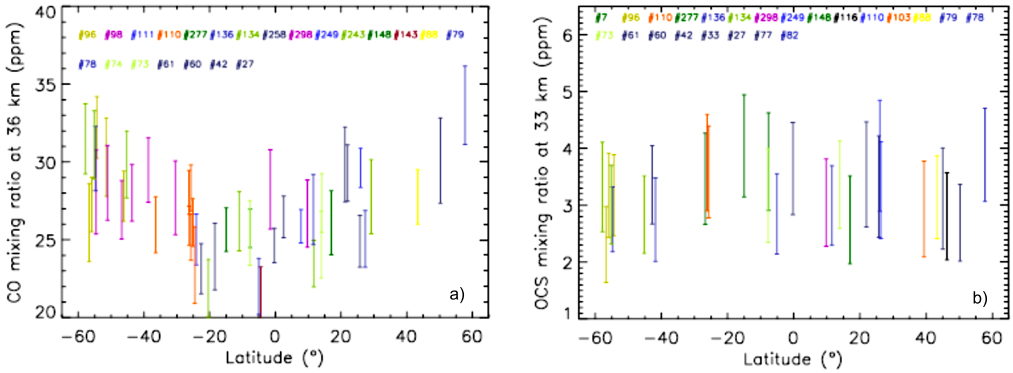

Figure 2.5: *The abundance of a) carbon monoxide around 36 km altitude and b) carbonyl sulfide around 33 km altitude in Venus' atmosphere as derived by Marcq et al. (2008) from VEX/VIRTIS measurements (section (3.1)).*

observed a diurnal variation of the CO values with highest abundances on the night side of Venus. The latter variation was confirmed by *Clancy et al.* (2003) using ground based measurements. *Irwin et al.* (2008) have found indications for a weak latitudinal gradient of CO in VIRTIS observations (section (3.1)) with a slight CO enhancement toward the poles. At lower regions, the abundance of CO decreases with decreasing altitude reaching values in the order of tens of ppm within and below the main clouds (e.g. *Young*, 1972; *Oyama et al.*, 1980).

Marcq et al. (2005, 2006, 2008) have observed a clear latitudinal variation of the CO abundance below the main clouds using ground based and VIRTIS measurements (section (3.1)). The left panel in Figure 2.5 shows the zonally averaged mixing ratio of carbon monoxide as a function of the planetary latitude. It shows a clear CO increase toward the polar regions.

Although there are no reliable measurements of OCS near Venus' surface, one-dimensional chemical models indicate that carbonyl sulfide is formed in the lowest altitudes of Venus' atmosphere (e.g. *Hong and Fegley*, 1997; *Krasnopolsky*, 2007; *Zhang et al.*, 2010). In the range between 25 and 40 km altitude the OCS abundance values vary between 5 and 20 ppm (e.g. *Marcq et al.*, 2006). The chemical consumption of carbonyl sulfide at higher altitudes lets the OCS abundance decrease to values less than 1 ppm (e.g. *Krasnopolsky*, 2007).

Among the latitudinal CO trend observed by *Marcq et al.* (2005, 2006, 2008) (Figure 2.5.a)), they also measured a latitudinal variation of the OCS abundance. Panel b) in Figure 2.5 shows the zonally averaged latitudinal distribution of OCS around 33

km altitude. In contrast to the poleward increase of the CO abundance, however, the highest OCS values can be found at equatorial latitudes.

2.3 Wind dynamics

The global wind system in the atmosphere of Venus below 80 km altitude consists mainly of large-scale **zonal** and **meridional** winds as well as **vortices** at both polar regions. The first mentioned form a retrograde wind flow which was first detected in Earth based observations of Venus (e.g. *Boyer and Camichel*, 1961; *Smith*, 1967). Maximal wind velocities of around 100 m/s in the upper cloud region (60 - 70 km) (e.g *Schubert et al.*, 1980) lead to an atmospheric rotation that is about 60 times faster than the planetary body - a phenomenon called superrotation. The second mentioned belong to a system of global scale circulation cells. Highest wind velocities were observed at cloud top altitudes (65 - 70 km) and are one order of magnitude smaller than those of the zonal winds (e.g. *Sánchez-Lavega et al.*, 2008; *Gonçalves et al.*, 2020). The meridional circulation cells are thought to be one of the key mechanisms which maintain the zonal superrotation. The third mentioned are permanent features in Venus' atmosphere and were observed at both, the southern and northern polar regions (e.g. *Taylor et al.*, 1980; *Luz et al.*, 2011). The polar vortices have an irregular structure and change their shape from a single pole over a S-shaped structure to a dipole on timescales of one to several days (e.g. *Garate-Lopez et al.*, 2013). In the following the zonal and meridional winds as well as the polar vortices are discussed with respect to spatial and temporal variations.

Zonal winds

Earth based observations of Venus' atmospheric retrograde rotation in the 1960s provided indications about the zonal wind velocities at cloud top altitudes (e.g. *Boyer and Camichel*, 1961; *Smith*, 1967). A measured atmospheric rotation period of 4 - 5 days implied values of around 100 m/s. Later measurements of the Venera and Pioneer Venus entry probes confirmed the high wind velocity. Additionally, they allow to measure the wind velocities at deeper atmospheric regions (e.g. *Keldysh*, 1977; *Counselman et al.*, 1980). Panel a) in Figure 2.6 shows the vertical distribution of the zonal wind velocity below 70 km altitude as measured by the Venera and Pioneer Venus entry probes (*Schubert et al.*, 1980). The highest variation can be found within the main clouds ($\geq$ 50 km) with maximal values between 60 and 70 km altitude. Above that altitude range the wind speed decreases due to the smaller pressure gradient at this region (*Taylor*, 2006). Below the main clouds ($\leq$ 50 km) all profiles show a gradual

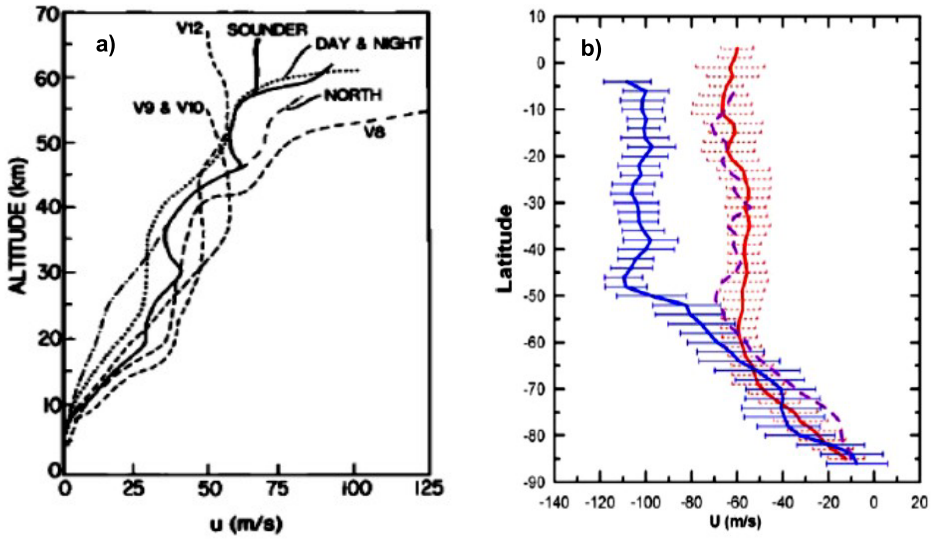

Figure 2.6: *a): Zonal wind velocity profiles as measured by the Venera and Pioneer Venus entry probes (Schubert et al., 1980); b): Latitudinal distribution of the zonal wind at three altitude regions,* $\sim$ *66 km (blue),* $\sim$ *61 km (violet),* $\sim$ *47 km (red), derived from Venus Express measurements between the years 2006 and 2007 (Sánchez-Lavega et al., 2008).*

decrease of the wind velocity. The high density of the atmosphere decelerates the wind to minimal velocities of less than 10 m/s around 10 km altitude.

Among the wind measurements conducted by the entry probes, the tracking of cloud features, which are observed in UV and IR images of Venus' clouds, is used to derive the wind velocity [1)]. For UV images the solar radiation is used, which is reflected by the upper clouds. Those images show mostly the upper cloud region (60 - 70 km) on the dayside of the planets. For IR images the thermal radiation is used, which originates at deeper atmospheric regions. Those images show mostly the nightside of the planet. By applying cloud tracking methods to UV and IR images obtained from Pioneer Venus and Venus Express *Rossow et al.* (1980) as well as *Sánchez-Lavega et al.* (2008) observed a clear latitudinal dependance of the zonal wind. Panel b) in Figure 2.6 shows the latitudinal distribution of the zonal wind at three altitude regions in Venus' southern hemisphere derived by *Sánchez-Lavega et al.* (2008) from VIRTIS measurements (section (3.1)). An almost constant wind speed of about 100 m/s is visible around 66 km altitude at low and mid-latitudes ($\leq$ 50°S). It may be one of

[1)] The determination of the altitude of the IR cloud features requires the usage of a radiative transfer model. The assigned altitude depends therefore strongly on the spatial structure of the model (*Khatuntsev et al.*, 2013).

the driving mechanisms which form the *Y-feature* observed in UV images of the Venus upper clouds (e.g. *Rossow et al.*, 1980). At higher latitudes a quasi-linearly decrease of the velocity can be seen with minimal values of less than 10 m/s at polar latitudes. Such a velocity distribution is similar to a solid body rotation and is consistent with the structure of a *Rankine vortex* (e.g. *Limaye and Rengel*, 2013).

Further observations of the zonal wind velocity revealed small-scale spatial variations as well as local time and long-term variations (e.g. *Kouyama et al.*, 2013; *Horinouchi et al.*, 2018). Additionally, a superposition of the zonal wind by jet streams was found. They accelerate the zonal wind to velocities of more than 110 m/s at the mid-latitudes (e.g. *Rossow et al.*, 1980; *Limaye and Suomi*, 1981) and more than 80 m/s at the equatorial region below 60 km altitude (*Horinouchi et al.*, 2017).

Meridional winds

Similar to the zonal wind, the meridional wind was also studied using the Venera and Pioneer Venus entry probes as well as cloud tracking methods. Depending on the observed altitude region in Venus' atmosphere the measurements revealed both, equator-ward and poleward directed winds. Figure 2.7 represents the wind directions observed between the years 1972 and 2017 in the altitude range between 40 and 70 km.

A poleward directed wind was found in the upper clouds (60 - 70 km) by various authors using Pioneer Venus, Galileo, Venus Express and Akatsuki data. Highest wind velocities of more than 10 m/s were observed at latitudes between 30° and 60° (e.g. *Sánchez-Lavega et al.*, 2008; *Hueso et al.*, 2012; *Gonçalves et al.*, 2020). Below the upper clouds, an equator-ward wind flow was detected between about 50 and 55 km altitude. *Counselman et al.* (1980) as well as *Khatuntsev et al.* (2017) have observed wind velocities ranging between 5 and 10 m/s. The wind directions in the main clouds (50 - 70 km) are interpreted as the poleward and equator-ward paths of a Hadley cell.

As can be seen from Figure 2.7, the observed wind directions below the main clouds indicate the presence of a second smaller convection cell located between about 40 and 50 km altitude. *Counselman et al.* (1980) as well as *Carlson et al.* (1991) have observed poleward winds with velocities of 5 to 10 m/s between 45 and 50 km altitude. At lower altitudes, *Counselman et al.* (1980) and *Sánchez-Lavega et al.* (2008) detected equator-ward directed winds with maximal velocities of about 5 m/s.

The observed wind velocities between 50 and 70 km altitude obviously reveal local-time and spatial variations. In the poleward branch of the upper Hadley cell *Hueso*

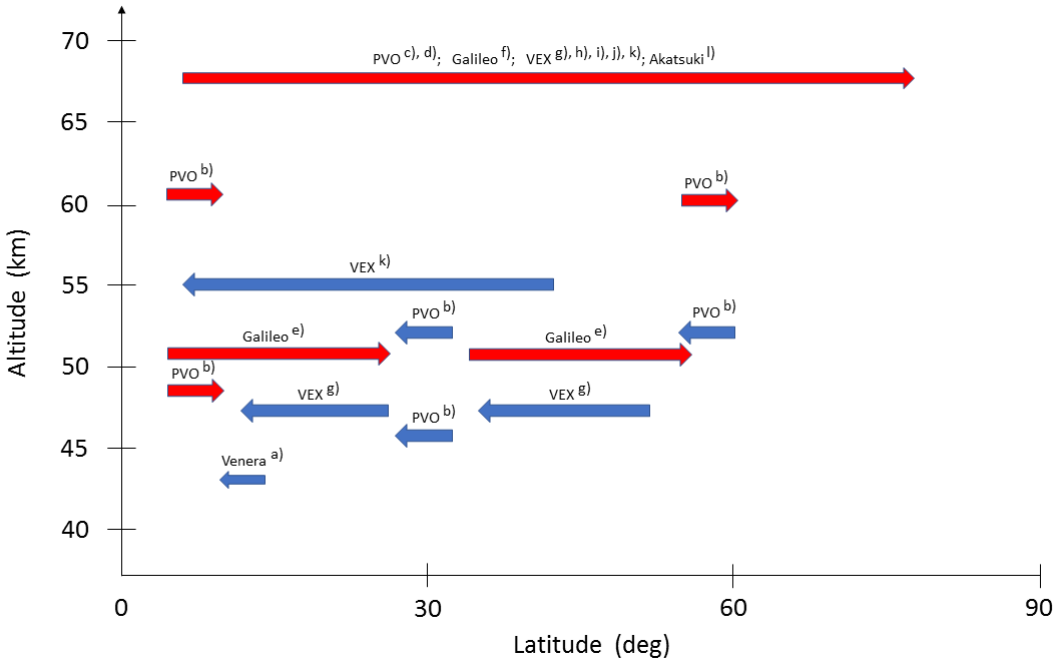

Figure 2.7: *Observed meridional wind directions in Venus' atmosphere between 40 and 70 km altitude. Red arrows represent poleward wind, blue arrows represent equator-ward wind. The following observations from the years 1972 to 2017 from the day- and nightside southern and northern hemispheres are presented: a) Kerzhanovich et al. (1972), b) Counselman et al. (1980), c) Rossow et al. (1980), d) Rossow et al. (1989), e) Carlson et al. (1991), f) Peralta et al. (2007), g) Sánchez-Lavega et al. (2008), h) Moissl et al. (2009), i) Hueso et al. (2012), j) Khatuntsev et al. (2013), k) Khatuntsev et al. (2017), l) Gonçalves et al. (2020).*

et al. (2012) have observed the highest wind velocities on the dayside of the planet after 12 h. In the equator-ward branch of the Hadley cell *Khatuntsev et al.* (2017) have found indications for a topographic influence on the wind speed with maximal velocities above the *Aphrodite Terra* highlands. The latter represents an elevated region at the equatorial latitudes between about 50°E and 150°E (*Rappaport et al.*, 1999). The observed wind directions in the upper and lower branches of the upper level Hadley cell were constantly poleward and equator-ward, respectively. In contrast to this, in the lower branch of the lower level convection cell *Hueso et al.* (2012) found equator-ward winds between 18 and 24 h and indications for poleward winds between 0 and 6 h.

Vertical wind velocities of the upward and downward branches of the convection cells were not measured. The latitudinal extension of the cells is therefore unknown. Lowest values of the meridional wind velocities found at equatorial and *cold collar* lat-

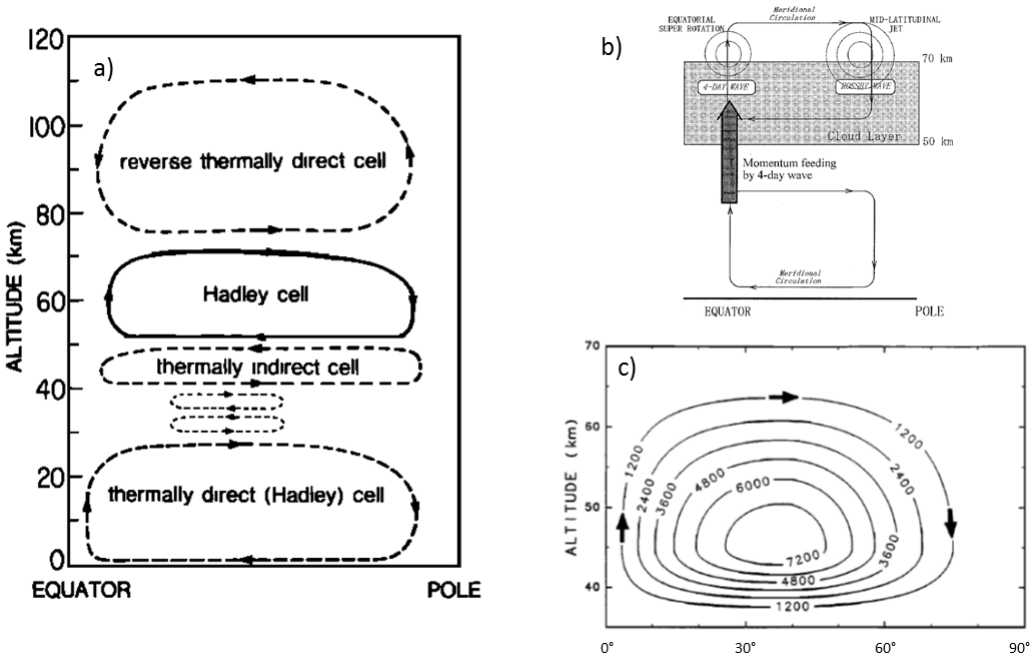

Figure 2.8: *Vertical and latitudinal structure of the mean meridional circulation in Venus' atmosphere proposed by a) Schubert et al. (1980), b) Yamamoto and Tanaka (1997) and c) Imamura and Hashimoto (1998).*

itudes (e.g. *Sánchez-Lavega et al.*, 2008; *Gonçalves et al.*, 2020) indicate, however, that the meridional circulation may occur between these latitudes.

Based on the observed meridional wind, various authors proposed a spatial structure of the convection cells. Figure 2.8 shows three examples.

Schubert et al. (1980) assumed a system of thermally direct and indirect cells in the altitude range between the surface and 120 km altitude (panel a)). In accordance with observations, they consider poleward directed transport in the upper clouds (60 - 70 km). The return path of the cell is located below 60 km altitude, while the 1 bar pressure level ($\sim$ 50 km) marks the bottom of the Hadley cell. The upward and downward branches of the cell are located at the equatorial and polar latitudes, respectively. Below the cloud level convection a narrower indirect cell is located between 40 and 50 km altitude. The cell transports cloud material from polar to equatorial latitudes, so that at equatorial latitudes the material is transported downward. The upward branch is located at the polar regions.

In their circulation model *Yamamoto and Tanaka* (1997) have assumed a Hadley cell that is generated by cloud heating at equatorial latitudes (panel b)). In agreement with observations there is poleward transport in the upper clouds (60 - 70 km) and equator-ward transport around the cloud bottom. This is similar to the Hadley cell proposed by *Schubert et al.* (1980) in the main clouds (50 - 70 km). In contrast to *Schubert et al.* (1980), however, *Yamamoto and Tanaka* (1997) have proposed a single direct cell in the lower atmosphere instead of stacked direct and indirect cells. The highest meridional wind velocity of about 1 m/s was obtained in the upper clouds between 30° and 60° latitude. Maximal vertical velocities of more than 2 mm/s and more than 4 mm/s were achieved above 60 km altitude at equatorial and polar latitudes, respectively.

Imamura and Hashimoto (1998) have waived the multiple-cell structure in their 2D-transport model and assumed a single convection cell between 35 and 70 km altitude (panel c)). Poleward directed wind was considered above 45 km altitude and the return flow below 45 km. Similar to the meridional circulation presented by *Yamamoto and Tanaka* (1997), the upward and downward transport is located at equatorial and polar latitudes, respectively. A maximal meridional velocity of 2 m/s and vertical velocity of more than 1.6 mm/s at low and more than 4 mm/s at high latitudes were used.

Polar vortices

The polar vortices, which are located poleward of about 70° latitude at both hemispheres, are believed to be located in an altitude range between about 42 and 65 km (e.g. *Titov et al.*, 2008; *Ignatiev et al.*, 2009; *Garate-Lopez et al.*, 2013). Consequently the upper boundary of the vortices is located approx. 5 km deeper than that of the main clouds at equatorial and mid-latitudes. UV images of the upper clouds indicate that the polar vortices are tied to the retrograde zonal wind flow (e.g. *Limaye and Rengel*, 2013). Zonal wind velocities range between 20 and 30 m/s between 70 and 85° in the upper cloud layer, while decreasing rapidly beyond that region (e.g. *Luz et al.*, 2011). The meridional wind component was found to be nearly zero between 70 and 90°.

UV and IR measurements revealed that the polar vortices represent highly irregular features (e.g. *Schofield and Diner*, 1983; *Titov et al.*, 2008; *Garate-Lopez et al.*, 2013). A clear displacement from the geographic pole by about 2 to 4° as well as a dipole structure was discovered from Pioneer Venus observations (e.g. *Taylor et al.*, 1980; *Taylor*, 1992). *Luz et al.* (2011) as well as *Garate-Lopez et al.* (2013) have observed the evolution of the vortex shape from a single pole over an S-form to a dipole on time scales ranging from one to several days. *Garate-Lopez et al.* (2013) observed the

mass flow during this period of time using VIRTIS IR (section 3.1) measurements. Among a clear closed circulation around the pole they also observed divergent (mass outflow) and convergent (mass inflow) motions with vertical velocities of 0.16 ± 0.01 and 0.05 ± 0.01 m/s, respectively.

Chapter 3

The Venus Express spacecraft, payload and data acquisition

The following chapter describes the Venus Express spacecraft, measurement technique and derivation of atmospheric profiles. While section 3.1 provides information about Venus Express, scientific instruments on-board the S/C and the radio occultation measurement technique, section 3.2 is dedicated to the used signal recording techniques as well as to the derivation of radio ray parameters and atmospheric profiles of temperature, pressure and neutral number density.

3.1 The Venus Express spacecraft and payload

After numerous US and Russian spacecraft missions to Venus (Venera, Mariner, Pioneer Venus, Vega, Magellan) on 9 November 2005 the European Space Agency (ESA) launched its first orbiter on a Soyuz-Fregat rocket from the Baikonur Cosmodrome in Kazakhstan to our neighbor planet. After a flight period of 153 days Venus Express was put into an elliptical 24h orbit on 7 Mai 2006. Between May 2006 and December 2014 the spacecraft delivered insights into the thick Venus atmosphere, circumplanetary plasma and surface of the planet (*Titov et al.*, 2006).

Figure 3.1 shows the Venus Express S/C and the payload on board consisting of seven scientific instruments. The design of Venus Express was based on the European Mars orbiter Mars Express, which was launched almost 2.5 years before Venus Express. Because of the harsher Venus environment and configuration of planets, however, some modifications mainly related to the thermal control system and communication system had to be made. One of them was an additional smaller high gain antenna 2 (HGA2) mounted on the top floor of the spacecraft behind the larger high gain antenna 1 (HGA1). From Figure 3.1 it can be seen that both antennas were pointing

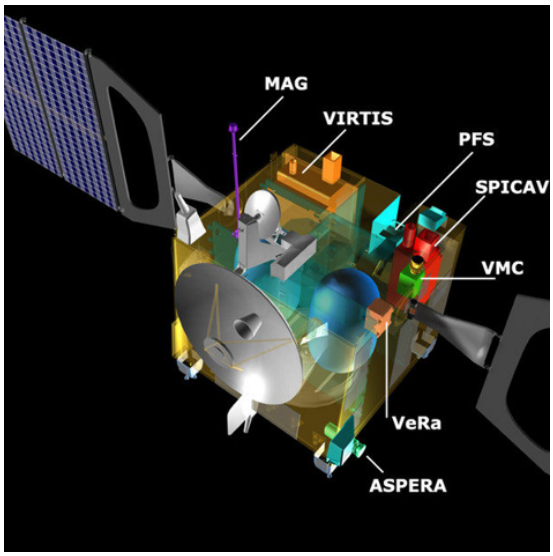

Figure 3.1: *Artistic image of the Venus Express spacecraft and its seven scientific instruments (ESA).*

in opposite directions. While the HGA1 was the main antenna used for Earth communication the HGA2 was used for communication during quadrature (time periods during which the Sun-spacecraft-Earth angle is between 75 and 95 degrees). During this period sensitive cooling components of the spacecraft would be exposed to a strong illumination if the HGA1 would be used. Table 3.1 summarizes the basic parameters of both antennas which were operated by a 65-W X-band and a 5-W S-band transmitter. More information on the design of Venus Express as well as differences between Venus Express and Mars Express can be found in *Sivac and Schirmann* (2007).

Both antennas were used for the Venus Express Radio Science Experiment (**VeRa**), which will be described later in the text and in section (3.1.1). In addition to the radio science experiment, six further scientific instruments belonged to the payload of VEX. The Analyzer of Space Plasmas and Energetic Atoms (**ASPERA**) studied the interaction of the solar wind with the ionosphere/atmosphere of Venus, the near planet space and the composition of the matter escaping the planet (e.g. *Barabash et al.*, 2007; *Whittaker et al.*, 2010). Using a wavelength interval between 0.9 and 45μm the Planetary Fourier Spectrometer (**PFS**) was supposed to investigate the abundance of H_2O, SO_2, CO and CO_2 in the upper part of the clouds and the mesosphere. Observations of thermal emission and reflected solar radiation were planned to study the radiation balance of the planet as well as to map thermal winds in the mesosphere. Due to a defect, however, the instrument couldn't be used during the entire Venus Express mission (e.g. *Formisano et al.*, 2006; *Svedhem et al.*, 2009). The composition of the mesosphere was

Parameter	Unit	Frequency	Antenna HGA1	Antenna HGA2
Diameter	m		1.3	0.3
Minimum Gain	dBi	X-band S-band	37.0 25.7	26.0
3 dB beamwidth	deg	X-band S-band	1.6 6	8
EIRP	dBW	X-band S-band	55 32	44

Table 3.1: *Parameter of the Venus Express antennas HGA1 and HGA2. The antenna gain is given for the downlink.*

investigated by the Spectrometer for Investigation of Characteristics of the Atmosphere of Venus (**SPICAV**). The instrument, consisting of three spectrometers, was designed to study the mesosphere and upper part of the thermosphere of Venus. Operating in three wavelength ranges (110 - 320nm; 0.7 - 1.7μm; 2.2 - 4.4μm) it provided information about the temperature between 70 and 180 km altitude and studied the abundance of HDO, SO_2, SO, OCS, CO, HCl and HF in the upper atmosphere. Further goals of SPICAV were the search for new molecules, like hydrocarbonates, nitrogen oxides or chlorine-bearing gases as well as the study of the composition of the lower atmosphere and surface temperature on the night side of the planet (e.g. *Bertaux et al.*, 2007; *Belyaev et al.*, 2012; *Mahieux et al.*, 2012; *Piccialli et al.*, 2015). The task of the Visible and Infrared Thermal Imaging Spectrometer (**VIRTIS**), observing in the wavelengths of 0.25 to 5μm and 2 to 5μm, was to investigate the abundance of H_2O, SO_2, CO and OCS in the lower atmosphere between 30 and 40 km altitude on the night side of the planet as well as to study the composition of the atmosphere and aerosols at cloud top altitudes on the dayside. Additionally, ultraviolet and infrared images of cloud layer details provided information on wind velocities between 50 and 70 km altitude (e.g. *Drossart et al.*, 2007; *Marcq et al.*, 2008; *Grassi et al.*, 2010; *Gilli et al.*, 2015). Wind field measurements at cloud top altitudes were also performed by the Venus Monitoring Camera (**VMC**). It was a wide angle camera with 17.5° field of view, taking images of Venus in narrow band filters of 365, 513, 965 and 1000nm. Furthermore, observation of the unknown UV absorber as well as thermal mapping of the surface on the night side of the planet were performed (e.g. *Markiewicz et al.*, 2007; *Titov et al.*,

2008, 2012; *Molaverdikhani et al.*, 2012). Magnetic field measurements of the plasma environment of Venus were carried out by the Magnetometer (**MAG**), which was a further development of the Rosetta Magnetometer and Plasmamonitor (ROMAP) (e.g. *Zhang et al.*, 2006; *Dubinin et al.*, 2013). The Venus Express Radio Science Experiment (**VeRa**) provided ionospheric/atmospheric parameter measurements (number density, temperature, pressure, sulfuric acid vapor) with higher vertical resolution compared to the spectrometers on board. Furthermore, it was designed to investigate gravity field anomalies and surface properties of Venus as well as to sound the solar corona. Since the data from VeRa's atmospheric measurements build the basis for this study it shall be discussed in more detail below.

3.1.1 Venus Express Radio Science Experiment VeRa

VeRa used the radio communication subsystem of the spacecraft to investigate the atmosphere, surface and gravity field of Venus as well as the solar corona (*Häusler et al.*, 2006). For this purpose the spacecraft (S/C) emitted radio signals (X-band; 3.6cm and S-band; 13cm) toward the ground station (G/S) on Earth while the investigated object was on the radio ray path between the S/C and the G/S [1)]. Since the influence of the objects on the signals was observed as a phase/frequency shift (**Doppler shift**) and amplitude variation of the Radio Frequency (RF) carrier signals the desired information about the objects were derived from the variations of the radio signal along the radio ray path. Therefore it was necessary to guarantee a high amplitude stability as well as a phase stability/coherency of the radio signals. While the signal amplitude was stabilized internally, the phase stability/coherency was ensured either by an coherent transponder on board which received an uplink (U/L) signal or by an on board Ultra Stable Oscillator (USO). The X-band U/L radio signal, which was generated at the G/S by a H_2-Maser, was part of the two-way dual frequency (TWOD) transmission mode, which was applied for solar corona and gravity field measurements. On board the U/L signal was used by the transponder to generate coherent X- and S-band downlink (D/L) signals at a frequency ratio of 11/3 [2)]. For investigations of the Venus atmosphere and surface the one-way dual frequency (ONED) transmission mode was applied, in which the USO provided the reference frequency for the X- and S-band D/L signals (*Häusler et al.*, 2006).

The usage of the dual-frequency D/L allowed to separate influences caused by the investigated objects from those caused by indeterminable S/C movements. It turned

[1)] During gravity field measurements the investigated object was not directly located between the S/C and the G/S. Here, gravitational forces affected the S/C. In contrast to this, the investigated objects affected the propagation of the radio signals in case of Venus atmosphere and surface as well as solar corona measurements.

[2)] The U/L signal was multiplied by the ratios 880/749 and 240/749 to generate the X-band and S-band D/L signal, respectively.

out that those S/C movements caused Doppler shifts in the order of mHz. Solar coronal and planetary ionospheric plasma as well as anomalies in Venus' gravity field caused Doppler shifts in the order of mHz to Hz. Both frequency shifts are comparable. In order to avoid misinterpretations in these measurements a dual-frequency D/L was therefore advantageous (*Häusler et al.*, 2003; *Peter et al.*, 2014). Additionally, the influence of the interplanetary plasma on the D/L signals could be determined by using two frequencies. A further advantage of the dual-frequency D/L was the possibility of comparison of results simultaneously derived from both signals, which increased their reliability (*Häusler et al.*, 2006).

Each of VeRa's investigation targets required a particular geometrical constellation between the S/C, target and G/S.

- Gravity field measurements were carried out around the pericenter of VEX's orbit, mostly above the northern polar region *Atalanta Planitia*, which was already observed by the Magellan spacecraft (*Häusler et al.*, 2006; *Leftwich et al.*, 1999). For these observations the radio ray path between the S/C and G/S was not occulted by Venus' atmosphere, ionosphere or planetary disc. The S/C moved over the target and emitted constantly radio signals toward the G/S. Anomalies in the gravity field disturbed the orbit of VEX, which was observed as a phase shift in the D/L signals. These Doppler shifts were used to calculate the line-of-sight (LOS) velocity disturbances, which then could be used to derive information on the lithospheric and crustal density. More information on the measurement technique can be found in (e.g. *Remus*, 2004; *Häusler et al.*, 2006; *Mattei and Häusler*, 2011).

- Solar corona measurements were conducted during superior solar conjunction when the elongation angle between the Sun and the S/C was equal or less 10 deg as seen from the G/S. In this constellation the solar coronal plasma was sounded. Its influence on the radio signals was observed as a phase shift and time delay, which was used to derive information on the electron density and the solar wind speed. More information on the measurement technique can be found in (e.g. *Tyler et al.*, 1977; *Bird et al.*, 1994; *Hahn*, 2008).

- For measurements of the surface characteristics (*Bistatic Radar* experiment) the HGA1 was pointing toward a selected target on Venus' surface. The reflected radio signals from the specular point were received at the G/S on Earth. The reflection process converts the right hand circular polarized (RCP) X- and S-band signals to echoes containing RCP and left hand circular polarized (LCP) components. The power of the echoes was used to derive values of surface dielectric constants at the *Maxwell Montes* region, a mountain massif in the northern

Venus hemisphere which was also investigated by the Magellan spacecraft. Further targets were the highlands of *Beta Regio* and *Atla Regio* at lower latitudes (e.g. *Pettengill et al.*, 1996; *Häusler et al.*, 2006; *Simpson et al.*, 2009).

- Atmospheric/Ionospheric parameter were obtained by sounding the atmosphere with radio waves. The orbit of Venus Express allowed to study the atmosphere/ionosphere over a wide range of latitudes and local times. This way a global picture of the temperature, pressure and sulfuric acid vapor in the lower and middle atmosphere as well as of the electron density in the ionosphere could be obtained. For this purpose the **radio occultation** method was applied. Since the data from this experiment are the basis for this work, section 3.1.2 is dedicated to the explanation of the measurement technique, following by the description of the data acquisition and analysis in section 3.2.

3.1.2 Radio occultation

For radio occultation measurements the S/C moves behind the planet as seen from the Earth. Prior to the start of the occultation of the S/C by the planet the spacecraft emits continuously radio waves through the planets atmosphere and ionosphere toward the G/S on Earth. In addition to these *ingress* measurements, *egress* measurements can be performed, in which the planets atmosphere is sounded while the S/C emerges from behind the planet [3)]. While traversing through the planets atmosphere the signals are refracted leading to an increased geometrical signal path length (Figure 3.2). At the ground station this can be observed as a signal phase/frequency shift ($\boldsymbol{\Delta f_{atm}}$). In addition to this Doppler shift, a decrease of the X- and S-band signal power was observed when Venus Express sounded Venus' atmosphere below approx. 100 km altitude. The attenuation was caused by absorption, refractive defocussing effects and pointing inaccuracies of the spacecraft antenna (see chapters 4 and 6). Additional *intensity scintillations* and *multipath effects* were observed especially when Venus' cloud region was sounded. The signal amplitude and phase/frequency are the observables of a radio occultation measurement. While the signal amplitude may provide insights on the absorbing gases, the Doppler shift computed using the observed signal phase/frequency, the so-called *sky-frequency* ($\boldsymbol{f_{sky}}$), contains information about the refractivity field of the atmosphere/ionosphere. The refractivity of the atmosphere depends on the predominant atmospheric composition, density, temperature and pressure and can therefore be used to determine these atmospheric parameters (see section 3.2).

[3)] For *egress* measurements the phase stability can't be ensured fast enough by an U/L signal. An USO was used on VEX to ensure a high signal phase stability making *ingress* and *egress* measurements possible. In contrast to VEX the oscillator used on the Mariner V and 10 provided a poor signal stability increasing the uncertainty of the *egress* measurements.

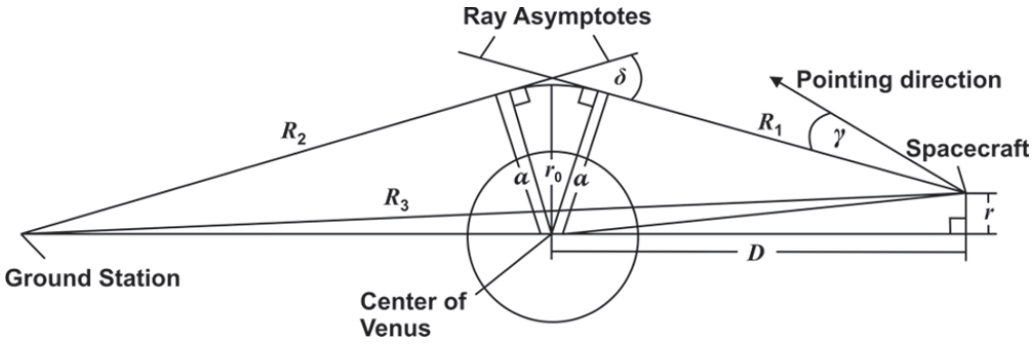

Figure 3.2: *Radio occultation geometry during VEX radio science measurements. Due to the refraction of the emitted radio signal in Venus' atmosphere the geometrical signal path ($R_1 + R_2$) is longer compared to the direct line of sight (R_3). The scenario is presented for signal refraction in the neutral atmosphere. In the ionosphere the value of refractive index is less than 1 (see section (3.2.2)) and refraction occurs away from the planet (Figure adopted from Lipa and Tyler (1979))*

The radio occultation technique was first applied during the Mariner IV flyby at Mars in 1965 (*Kliore et al.*, 1965) using a single-frequency S-band D/L. A reference signal phase was provided by an U/L. On Venus the first radio occultation measurements were performed with the Mariner V spacecraft in 1967. A one-way dual frequency U/L (49.8 and 423.3 MHz) was chosen to sound Venus' neutral atmosphere and ionosphere. The signal characteristics were stored on board the spacecraft for later transmission to Earth (*Mariner Stanford Group*, 1967). In addition to the uplink experiment, a single-frequency S-band D/L experiment was performed providing improved results of the neutral Venus atmosphere (*Kliore et al.*, 1967). A coherent transponder receiving an S-band U/L as well as an auxiliary oscillator on board ensured the phase coherency of the D/L signals of the Mariner 10 radio occultation experiment in 1974 on its Venus flyby. The D/L comprised S-band and for the first time X-band radio signals (*Howard et al.*, 1974). The measurements of the Russian spacecraft Venera 9 and 10 (1975) present the first extensive radio occultation studies at Venus. An U/L signal in the decimeter range and a dual-frequency D/L (centimeter and decimeter bands) were applied (*Keldysh*, 1977; *Savich*, 1981; *Gringauz et al.*, 1979). The Pioneer Venus orbiter sounded the atmosphere of Venus with radio waves at S- and X-band between the years 1978 and 1992 (e.g. *Kliore and Patel*, 1980). Phase coherency was achieved by an coherent transponder operating at S-band in the U/L and an on board oscillator for the cases when coherency was not available (egress) (*Colin and Hall*, 1977). During the Pioneer Venus mission the Venera 15 and 16 spacecrafts performed radio occultation measurements at Venus between 1983 and 1984. Similar to Venera 9 and 10 a centimeter band U/L and dual-frequency D/L (centimeter and decimeter bands) was applied (*Yakovlev et al.*, 1991; *Gubenko et al.*, 2008). The Magellan spacecraft (1990 - 1994), so

far the most recent US mission to Venus, conducted radio occultation measurements in the TWOD transmission mode with an S-band U/L and S/X-band D/L (*Steffes et al.*, 1994). During the Venus Express mission (2006 - 2014), the Japan Aerospace Exploration Agency (JAXA) launched in 2010 its first orbiter to explore Venus. Since 2016 the Akatsuki spacecraft conducts radio occultation measurements using an X-band D/L signal [4]. Phase stability is ensured by an USO on board (*Imamura et al.*, 2011).

Radio occultation measurements have also been conducted at the outer planets Jupiter (e.g. *Lindal et al.*, 1981), Saturn (e.g. *Lindal et al.*, 1985), Uranus (e.g. *Lindal et al.*, 1987) and Neptune (e.g. *Lindal*, 1992) with the Voyager 1 and 2 spacecraft between the years 1979 and 1989. An oscillator on board guaranteed phase coherency of the dual-frequency S/X-band D/L.

The radio occultation technique, which was originally developed to study the atmosphere of planets was adopted to investigate also the atmosphere of the Earth. For this purpose at least two satellites in Earth's orbit are required (transmitter and receiver). This can be achieved by using Global Positioning System (GPS) and geoscience satellites like the Challenging Minisatellite Payload (CHAMP), Gravity Recovery And Climate Experiment (GRACE) and Constellation Observing System for Meteorology, Ionosphere and Climate (FORMOSAT-3/COSMIC) (e.g. *Wickert et al.*, 2001; *Schmidt et al.*, 2008; *Wickert et al.*, 2009).

3.2 Data acquisition

The radio signals transmitted by the spacecraft through the planets atmosphere are recorded at different ground stations on Earth [5], where the data are digitized and provided for signal power, Doppler shift, radio ray parameter and atmospheric profile calculations. While the Coordinated Universal Time (UTC) was used in the ground stations, the Venus Mean Equator of Date J2000 frame (VME2000) was used for radio ray parameter and atmospheric profile calculations, where J2000 stands for 12h 1 January 2000 Barycentric Dynamical Time (TDB). Descriptions about reference systems and time basis can be found in *NAIF* (2020). In the following sections the calculations for Venus Express radio occultation measurements are presented.

[4] The first attempt of orbit insertion in 2010 failed.

[5] For Earth radio occultation measurements, one of the satellites in Earth's orbit serves as a receiver instead of a ground station on Earth.

3.2.1 Signal power and the atmospheric Doppler shift

Considering the Doppler shift induced by the Venus atmosphere Δf_{atm} and by the relative motion between the S/C and G/S Δf_{str} as well as Earth ionospheric/atmospheric influences on the radio signals Δf_E, the observed frequency of the D/L radio signals at G/S receiving time (*sky-frequency*) can be described as

$$f_{sky} = f_{DL} + \Delta f_{str} + \Delta f_{atm} + \Delta f_E, \tag{3.1}$$

where f_{DL} represents the frequency of the D/L radio signals at emitting time by the S/C. The X- and S-band signals were recorded at ESA [6)] and NASA [7)] ground stations. Both ground segments used the Closed-Loop (CL) and Open-Loop (OL) receiving technique.

In the **CL-system** the signal phase was determined by using a Phase-Locked Loop (PLL) scheme, in which an incoming radio signal was compared with a reference signal. The latter was generated by the H_2-Maser in the G/S feeding a local oscillator with the carrier frequency of the incoming signal. Additionally, the oscillator was provided with the expected Doppler shift Δf_{str}^{LO} to reduce the signal dynamics. From the difference signal a residual phase ϕ_{res} was extracted which contained also the contribution from the atmospheric Doppler shift and influences of the Earth ionosphere/atmosphere. The phase ϕ_{res} was subsequently stored for later processing. It was also used to adjust the local oscillator frequency and this way to track the incoming radio signal. Detailed information on the operation of PLL circuits can be found in (e.g. *Best*, 2011). The signal power was determined by using an Automatic Gain Control (AGC) circuit. It maintained the signal amplitude at a constant level by increasing it when the signal power decreased. The amplification corresponded to the signal attenuation in Venus' atmosphere and served also as a feedback for the gain amplifier of the AGC. Detailed information on the operation of AGC circuits can be found in (e.g. *Alegre Pérez et al.*, 2011). The derived parameters were recorded with a sampling frequency of 10 Hz throughout the occultation measurement providing a time series of phase and signal power. Using the feedback loops PLL and AGC the CL receiving system provides a fast way to extract parameters from incoming radio signals. However, both circuits cannot adopt to rapid phase and amplitude changes. In the lower Venus atmosphere increased signal attenuation and atmospheric dynamics caused Doppler shift and amplitude variations in the order of tens of Hz/s and tens of dB/s. Those increased variations caused the PLL and AGC to lose lock to the incoming signal. The sensibility of the circuits against high signal dynamics makes therefore the CL receiving technique unsuitable for radio soundings of the lower Venus atmosphere.

[6)] New Norcia, Australia, diameter: 35 m.

[7)] Canberra, Australia, diameter: 34 m and 70 m.

In general, the CL receiver lost the lock to the signal when altitudes below 44 km were sounded (cf. Figure 6.2). The CL receiving technique also failed when Venus' cloud region was sounded where increased phase variations and *intensity scintillations* caused the CL receiver to lose lock. Furthermore, it was not possible for the receiver to cope with *multipath effects* which occur when sounding Venus' cloud region.

In the **OL-system** the incoming RF signals are heterodyned to base band by feeding the Local Oscillator (LO) in the G/S with the nominal carrier frequency and prediction of the expected motion-induced frequency shift Δf_{str}^{LO}. This way the bandwidth of the signals was reduced to values lower than 50 kHz. According to the Nyquist-Shannon sampling theorem, the base band signal could then be sampled with a rate of 100 kHz [8]. Subsequently, the real and imaginary part $I(t)$ and $Q(t)$ [9] of the signals were stored for determination of the atmospheric Doppler shift Δf_{atm} and signal amplitude (e.g. *Abello*, 2003; *Mattei and Häusler*, 2011; *Mattei*, 2011). This way the OL technique allowed to apply digital signal processing tools to the recorded voltage samples $I(t)$ and $Q(t)$ in later processing steps. Therefore, in contrast to CL, using the OL technique the atmospheric Doppler shift and amplitude of the received signals could be determined even at high signal dynamics and increased noise. At northern polar latitudes the signal parameters were derived to altitudes as deep as 38 km (sometimes deeper). Due to the orbit geometry and increased H_2SO_4(g) accumulation at equatorial latitudes, (e.g. Figure 7.12), these altitudes could only be reached in a small number of measurements at this region. In general the signal parameters were derived to altitudes as deep as 45 km. A discussion about VeRa's deepest sounded altitudes with respect to the signal frequency, signal strength and attenuation in Venus' atmosphere can be found in the sections 4.1, 6.1 and 7.3.1. In contrast to CL, the OL receiving technique also provides the opportunity to analyze *multipath effects* occurring in Venus' atmosphere (*Imamura et al.*, 2018). The analysis will support the *intensity scintillation* study as well as provide more reliable atmospheric profiles in Venus' cloud region compared to those derived from CL data.

The AGC circuit provided the signal strength of the CL recordings. From OL recordings the amplitude was determined by applying digital signal processing tools. The process of derivation of the atmospheric Doppler shift Δf_{atm}, however, was based on the same principle for both, the CL and OL recordings: 1) Recovery of the *sky*

[8] At NASA OL-receivers an additional expected atmospheric Doppler shift was removed. This process reduced the sample rate applied to the signal and reduced therefore the size of the provided data files.

[9] The base band signal can be presented in the complex form consisting of the analogue components $I(t)$ (*in-phase*) and $Q(t)$ (*quadrature*) of the signal at the time t.

frequency f_{sky} [10] and 2) subtraction of a predicted *sky frequency* f_{sky}^{prd} based on the assumption that the induced Doppler shift is caused by the relative motion between the S/C and G/S Δf_{str} only.

$$\begin{aligned}\Delta f_{atm} &= f_{sky} - f_{sky}^{prd} \\ &= (f_{DL} + \Delta f_{str} + \Delta f_{atm} + \Delta f_E) - (f_{DL} + \Delta f_{str} + \Delta f_E).\end{aligned} \tag{3.2}$$

The predicted *sky frequency* f_{sky}^{prd} was computed by using the Radio Science Simulator (RSS). It is a software package developed at the Institute of Space Technology at the German Armed Force University in Neubiberg (Munich). Based on orbit data of VEX and those of celestial bodies, both provided by ESA, it is possible to compute the straight-line Doppler shift Δf_{str} (*Häusler et al.*, 2003; *Selle*, 2005).

The recovery of the *sky frequency* from CL recordings f_{sky}^{CL} was achieved by computing the sum of (i) the D/L frequency f_{DL} and (ii) the time derivative of the residual phase ϕ_{res}

$$f_{sky}^{CL} = f_{DL} + \frac{d\phi_{res}}{dt}. \tag{3.3}$$

For the recovery of the *sky frequency* from OL recordings f_{sky}^{OL}, the removal of the expected Doppler shift Δf_{str}^{LO} applied in the G/S receiver was corrected by the improved Doppler shift Δf_{str}. Additionally, a coarse atmospheric Doppler shift Δf_{atm}^{RS} was removed from the $I(t)$ and $Q(t)$ voltage samples in order to further reduce the signal dynamics. Δf_{atm}^{RS} was also computed by using the RSS, which uses a model atmosphere to predict the bending of a radio ray traversing the medium. Subsequently, a Fast Fourier Transform (FFT) was applied to the residual signal providing the signal strength and a residual frequency f_{res}. The *sky frequency* f_{sky}^{OL} was computed as the sum of (i) the D/L frequency value f_{DL}, (ii) the straight-line Doppler shift Δf_{str}, (iii) the coarse atmospheric Doppler shift Δf_{atm}^{RS} and (iv) the residual frequency f_{res}

$$f_{sky}^{OL} = f_{DL} + \Delta f_{str} + \Delta f_{atm}^{RS} + f_{res}. \tag{3.4}$$

The predicted *sky frequency* f_{sky}^{prd} as well as the achieved *sky frequencies* f_{sky}^{CL} and f_{sky}^{OL} were then used to compute the atmospheric Doppler shift Δf_{atm} following equation (3.2).

While at ionospheric regions maximal Δf_{atm} values don't exceeded 2 Hz, a strong increase was detected when the middle and lower atmosphere was sounded. Doppler shift values of more than 4 and 10 kHz were observed in the S-and X-band radio signals below 40 km altitude. In addition, an attenuation of more than 20 dB in the S-band

[10] The necessity to recover the *sky frequency* was the correction for Δf_E and $\Delta f_{str} - \Delta f_{str}^{LO}$ which among the desired Doppler shift Δf_{atm} were still contained in the the CL and OL receiver outputs.

signal and more than 40 dB in the X-band signal could be seen in this altitude region. A more detailed discussion on the signal attenuation can be found in chapter 4 and 7.

3.2.2 Radio ray parameters as well as temperature, pressure and number density

The atmospheric Doppler shift Δf_{atm} was used to compute radio ray parameters like the bending angle δ and the impact parameter a (Figure 3.2). Both parameters uniquely define the refracted radio ray path $R_1 + R_2$ in Figure 3.2. By using the velocity vectors $v_{\vec{SC,GS}}$ of the S/C and G/S, respectively, as well as the unity vectors $e_{\vec{R_{1,2,3}}}$ of the ray asymptotes R_1 and R_2 and of the line of side R_3, respectively, the atmospheric Doppler shift can be written as (*Ahmad*, 1998)

$$\Delta f_{atm} = \frac{f_{DL}}{c}[(v_{\vec{SC}} \cdot e_{\vec{R_1}} + v_{\vec{GS}} \cdot e_{\vec{R_2}}) - (v_{\vec{SC}} \cdot e_{\vec{R_3}} - v_{\vec{GS}} \cdot e_{\vec{R_3}})], \tag{3.5}$$

where c is the speed of light in vacuum. The velocity vectors of the S/C and G/S as well as the unity vector $e_{\vec{R_3}}$ were computed using ephemeris data for the VEX spacecraft and celestial bodies provided by ESA. The unity vectors $e_{\vec{R_1}}$ and $e_{\vec{R_2}}$, however, were unknown and must be approached by making a geometrical simplification. A spherical symmetric Venus atmosphere was assumed constraining the radio ray path to remain in the so-called *occultation plane*, which is defined by the S/C, planet and G/S. In this frame $e_{\vec{R_1}}$ and $e_{\vec{R_2}}$ could be expressed by trigonometric functions. Additionally, Snell's low was used which provided along with equation (3.5) a system of linear equations for the derivation of the bending angle δ and impact parameter a. The calculation was performed iteratively beginning at the top of the highest measured altitudes and proceeding to lower altitudes (*Fjeldbo et al.*, 1971; *Schaa*, 2005).

The computed bending angles reveal values in the order of $0.0001° - 0.001°$ in the ionospheric region with higher refraction of the S-band signal compared to the X-band signal. In contrast to the ionosphere, in the neutral atmosphere the refraction is identical for X-and S-band radio signals (see equations (3.9) and (3.11)). Here, the bending angles increase from $\delta < 0.1°$ at cloud top altitudes (65 - 70 km) to $\delta > 6°$ below 40 km altitude. At lower altitudes the dense Venus atmosphere leads to a *critical refraction* of the radio rays [11]. This limits the sounding of the deep Venus atmosphere to altitudes around 33 km (e.g. *Fjeldbo et al.*, 1971; *Steffes et al.*, 1994).

The calculated bending angles δ were used to compute the corresponding index of refraction μ and refractivity N which were then used to derive the atmospheric

[11] Critical refraction occurs when the radius of the curvature of a horizontal ray is equal to the distance to the planetary center of mass (*Fjeldbo et al.*, 1971).

parameters temperature (T), pressure (p) and number density (n). The assumption of a spherical symmetric atmosphere simplifies the relation between δ and μ. In this case it can be shown that δ is related to μ via an *Abel transform*, which provides the projection of the spherical symmetric index of refraction along the line of sight between the S/C and G/S at the sounded altitude

$$\delta(a) = -2a \int_{r_0}^{\infty} \frac{1}{\mu} \frac{d\mu}{dr} \frac{dr}{\sqrt{(\mu r)^2 - a^2}}, \tag{3.6}$$

where $r_0 = a(r_0)/\mu(r_0)$ is the closest approach of the refracted ray to the planetary center of mass (Figure 3.2). Inverting the *Abel transform* yields the index of refraction (*Fjeldbo et al.*, 1971; *Schaa*, 2005)

$$\ln(\mu(r_0)) = \frac{1}{\pi} \int_{a(r_0)}^{\infty} \frac{\delta(a)da}{\sqrt{a^2 - a(r_0)^2}}. \tag{3.7}$$

It should be emphasized that μ represents the real part of the complex refractive index $\widetilde{\mu} = \mu + i\alpha$. The imaginary part of $\widetilde{\mu}$ refers to the signal attenuation. Atmospheric attenuation is mainly caused by absorption in VeRa's radio occultation measurements and is discussed in chapter 4.1.3.

The contribution of the ionosphere to μ can be distinguished from the contribution of the neutral atmosphere, so that the total refractive index can be written as the sum of both contributions

$$\mu = \mu_A + \mu_I, \tag{3.8}$$

with the refractive index of the neutral atmosphere μ_A and ionosphere μ_I. It is possible to determine both from a single radio occultation measurement by considering the dominant part only. The ionospheric term dominates above 100 km, the atmospheric below 100 km (e.g. *Pätzold et al.*, 2007; *Tellmann et al.*, 2009). In the case of two coherent frequencies, both effects can also be separated even more effectivelly.

For radio waves traversing an ionospheric/atmospheric gas it can be shown that the refractive index μ can be related to the number density n via the *refractive volume* $\overline{\kappa}$ (e.g. *Feynman et al.*, 1964; *Eshleman*, 1973; *Hinson et al.*, 1999; *Schaa*, 2005; *Feynman et al.*, 2011).

For the neutral atmosphere is

$$\begin{aligned} \mu_A &= 1 + n_A \cdot \overline{\kappa}_A \\ &= 1 + n_A \cdot \frac{e^2}{2\epsilon_0 m_e} \cdot \frac{1}{\omega_0^2 - \omega^2}, \end{aligned} \tag{3.9}$$

where e represents the charge of an bounded electron in an atom with the mass m_e and the natural frequency ω_0. The frequency of the incident wave is given by ω. ϵ_0 is the permittivity in vacuum. The values of the natural frequency for the most gases in Venus' atmosphere are much larger than the used signal frequency for the radio occultation experiment (X-and S-band). The term $(\omega_0^2 - \omega^2)$ in the denominator of equation (3.9) is therefore similar for both, the X-and S-band radio signals. Consequently, the refractive index computed for the X-and S-band signal show similar values. The derived radio ray parameters, bending angle δ and impact parameter a which are related to the refractive index via the *Abel transform* (equation (3.6)), reveal therefore identical values in the neutral atmosphere.

In practice, the *refractive volume* $\overline{\kappa}_A = \sum_i q_i \cdot \kappa_i$ can be computed for non-polar gases using the Loschmidt's number $N_L = 2.6867811 \cdot 10^{25}$ m^{-3} and the number mixing ratios q_i of the i components of the gas mixture

$$\kappa_i = \frac{\mu_i - 1}{N_L}. \tag{3.10}$$

Adopting measurements of the refractive index of carbon dioxide and nitrogen made by *L Essen and K D Froome* (1951) the values $\kappa_{CO_2} \approx 1.84 \cdot 10^{-29}$ m^3 and $\kappa_{N_2} \approx 1.10 \cdot 10^{-29}$ m^3 were obtained assuming gas concentrations of $CO_2 = 96.5\%$ and $N_2 = 3.5\%$.

In the ionosphere the free electrons have no restoring forces ($\omega_0 = 0$). The derived refractive index reduces therefore to (cf. equation (3.9))

$$\begin{aligned} \mu_I &= 1 + n_I \cdot \overline{\kappa}_I \\ &= 1 + n_I \cdot \left(-\frac{e^2}{2\epsilon_0 m_e} \frac{1}{\omega^2} \right), \end{aligned} \tag{3.11}$$

revealing negative values of μ_I. It can be seen from equation (3.11) that the refractive index of the ionosphere is frequency-dependent, which is in contrast to the neutral atmosphere (for X- and S-band radio signals). The dispersive effect leads to a stronger refraction of the S-band signals compared to the X-band signals. Using the *plasma frequency* [12)]

$$\omega_p = \frac{n_I e^2}{\epsilon_0 m_e} \tag{3.12}$$

the refractive index of the ionosphere can be written as

$$\mu_I = 1 - \frac{40.31 \cdot n_I}{f_{DL}^2}. \tag{3.13}$$

[12)] The plasma frequency is a fundamental quantity in plasma physics. Plasma gas reflects electromagnetic waves with $\omega < \omega_p$, while for $\omega > \omega_p$ it is transparent.

Since the values of μ_A and μ_I are close to unity in the atmosphere/ionosphere, the refractivity

$$N = (1 - \mu) \cdot 10^6 \tag{3.14}$$

was introduced (e.g. *Fjeldbo and Eshleman*, 1968), providing the equations for the refractivity in the atmosphere N_A and ionosphere N_I

$$N_A = n_A \cdot \overline{\kappa}_A \cdot 10^6 \tag{3.15}$$

$$N_I = -n_I \cdot \frac{40.31 \cdot 10^6}{f_{DL}^2}. \tag{3.16}$$

Equations (3.15) and (3.16) were used to derive the number density of the neutral gas in the atmosphere n_A and electron density in the ionosphere n_I of Venus.

From the number density of the neutral atmosphere n_A the temperature T and pressure p were derived assuming the atmosphere to be in hydrostatic equilibrium. This assumption is valid for a well-mixed atmosphere, the homosphere. The boundary of the homosphere, the homopause, was located between 120 and 132 km altitude (e.g. *Mahieux et al.*, 2010). Atmospheric profiles of temperature and pressure were derived for the region below 100 km altitude by applying the equations of an ideal gas and hydrostatic equilibrium (e.g. *Fjeldbo and Eshleman*, 1968; *Jakovlev*, 2002; *Tellmann et al.*, 2009)

$$p(r_0) = k_B \cdot n_A(r_0) \cdot T(r_0) \tag{3.17}$$

$$\frac{\partial p}{\partial r} = -n_A(r) \cdot \overline{m} \cdot g(r), \tag{3.18}$$

where k_B is the Boltzmann constant. The mean molecular mass $\overline{m}$ was computed for an atmospheric composition of $CO_2 = 96.5\%$ and $N_2 = 3.5\%$. The gravitational acceleration g was calculated using a gravity field model. Substituting the number density in equation (3.15) into expression (3.17) provides

$$T(r_0) = \frac{\overline{\kappa}_A}{k_B} \cdot 10^6 \cdot \frac{p(r_0)}{N_A(r_0)}. \tag{3.19}$$

Integrating equation (3.18) and substituting the number density by equation (3.15) provides the expression for the pressure

$$p(r_0) = p(r_{up}) - \frac{\overline{m}}{\overline{\kappa}_A} \cdot 10^{-6} \cdot \int_{r_0}^{r_{up}} N_A(r^{'}) g(r^{'}) dr^{'}, \tag{3.20}$$

with $p(r_{up}) = k_B n_A(r_{up}) T(r_{up})$, where $T(r_{up})$ is the temperature at the upper boundary of the detectable atmosphere (e.g. *Jenkins et al.*, 1994; *Pätzold et al.*, 2007; *Tellmann*

et al., 2009). Substituting equation (3.20) into equation (3.19) provides the expression used to calculate temperature and pressure profiles

$$T(r_0) = \frac{N_A(r_{up})}{N_A(r_0)} T(r_{up}) - \frac{\overline{m}}{k_B} \frac{1}{N_A(r_0)} \int_{r_0}^{r_{up}} N_A(r') g(r') dr' \tag{3.21}$$

$$p(r_0) = k_B \cdot \frac{N_A(r_0)}{\overline{\kappa}_A} \cdot 10^{-6} \cdot T(r_0). \tag{3.22}$$

Values of $T(r_{up}) = 170, 200$ and $230K$ were applied for the temperature at the upper boundary. The three retrieved profiles reveal a convergence to the same vertical temperature distribution below 90 km altitude (*Pätzold et al.*, 2007; *Tellmann et al.*, 2009).

3.2.3 Spatial resolution

The spatial resolution of atmospheric profiles derived from radio occultation measurements is limited by diffraction effects which are ignored when methods of geometrical optics are applied. Because of the antenna beam width, radio rays are emitted at different angles from the S/C and reach the G/S receiver on Earth through different paths. Among the direct signal, further radio rays, which travel along different ways, are captured by the receiver. Those signals arrive at the G/S either 'out of phase' or 'in phase' with the direct signal. Depending on the phase difference, the interference of the signals may either decrease or increase the signal power. Destructive and constructive interference depends on the difference in path length. Based on this quantity, the area between the S/C and G/S can be divided into so-called *Fresnel zones* (e.g. *Born et al.*, 2000). These are ellipsoidal shaped regions centered around the direct signal path with the S/C and G/S located at the focal points. Figure 3.3 shows the first three *Fresnel zones*. The first zone F_1 contains signals with path length differences to the direct signal ranging between 0° and 180°. The largest value would be achieved by a reflected signal. Signals from F_1 are 'in phase' with the direct signal and may increase the signal power. The second zone F_2 contains signals with path length differences between 180° and 360°. Those signals are 'out of phase' with the direct signal and may decrease the signal power. In general, signals from odd-numbered zones potentially increase the signal power, while signals from even-numbered zones potentially decrease it.

The signal power of a radio beam decreases with increasing distance from the antenna boresight (cf. Figure 4.1). Therefore, higher numbered *Fresnel zones* can be neglected in radio occultation measurements. In practice, the first *Fresnel zone* contains the most signal energy and all captured radio signals from F_1 contribute to the observed values of the atmospheric profiles. The diameter of the cross section of F_1 at

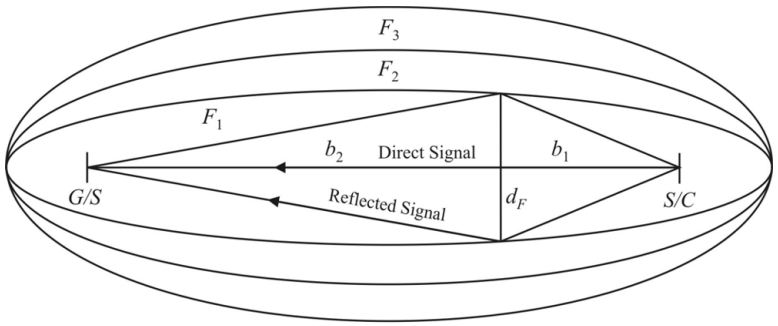

Figure 3.3: *First three Fresnel zones (F_1, F_2 and F_3) centered around the direct signal path between the S/C and G/S. Both, the S/C and G/S are located at the focal points of the ellipsoidal cones. F_1 is defined so that the path length difference between the direct and the reflected signal is half the signal period. The first Fresnel zone contains the most signal energy. The diameter d_F of the first Fresnel zone is a measure for the spatial resolution in radio occultation measurements. The distance between the S/C and the atmospheric reference point as well as between the S/C and G/S is given b_1 and b_2, respectively.*

the atmospheric reference point is therefore a measure for the spatial resolution of the profiles. It can be calculated with

$$d_F = 2\sqrt{\frac{\lambda b_1 b_2}{b_1 + b_2}}, \tag{3.23}$$

where λ is the signal wavelength, b_1 is the S/C-limb distance and b_2 is the distance between the S/C and G/S (e.g. *Häusler et al.*, 2006). Due to the vertical refractivity gradient, which causes a defocussing of the radio beam (section 4.1.1), the *Fresnel zones* are compressed in the vertical direction and elongated in the horizontal direction. The shape of the cross section of F_1 changes from circular to elliptic (e.g. *Fjeldbo and Eshleman*, 1969; *E. T. Karayel and D. P. Hinson*, 1997). The minor axis of the ellipse d_F^V decreases to

$$\begin{aligned} d_F^V &= 2\sqrt{\lambda b_1} \cdot \sqrt{l_r} \\ &= 2\sqrt{\frac{\lambda b_1}{1 - R_1 \frac{d\delta}{da}}}, \end{aligned} \tag{3.24}$$

which increases the vertical resolution of the atmospheric profiles (*Eshleman et al.*, 1979). l_r is the defocussing of the radio beam that occurs in the plane of refraction caused by the vertical refractivity gradient (section 4.1.1). Additionally it was assumed that $b_2 >> b_1$.

The vertical resolution of atmospheric profiles derived from VeRa measurements is in the order of 10^2 m. The values of d_F^V decrease with decreasing altitude.

Chapter 4

Radio signal attenuation in the Venus atmosphere

The refraction of radio signals in Venus' atmosphere was used to derive the temperature, pressure and number density of the atmospheric gas. The absorption was used to derive the abundance of sulfuric acid vapor. The latter is the main absorber of radio waves in the Venus lower atmosphere, so that the amount of absorption can be transferred into H_2SO_4(g) abundance. For this purpose the contributions of antenna mispointing as well as refractive defocussing to the observed total signal attenuation must be removed. Section 4.1 describes important parameters defining VeRa's radio downlink and introduces attenuation factors which affected the occultation measurements. Section 4.2 presents results from previous missions, which are used for comparison with VeRa observations in the section 6 and 7.

4.1 Radio signal attenuation

Influences on the radio signal power during occultation measurements result from unknown and known factors. The first mentioned are pointing inaccuracies (section 4.1.2) of the S/C antenna and mainly the effects of refractive defocussing (section 4.1.1) and absorption (section 4.1.3) in Venus' atmosphere. The latter is used to derive information about the absorber. Known factors result from the transmitter and receiver designs as well as from the distance between them. They must be calculated prior to the start of the observations and are used to define the *link-budget*. The latter is an appropriate measure for the quality of the transmission. The calculations shall guarantee a measurable amplitude of the carrier signal at the tracking station on Earth. The *link-budget* is used to calculate the expected *signal-to-noise ratio* (SNR). Using the power of the transmitted signal P_T as well as the gains of the transmitting and

receiving antennas G_T and G_R, respectively, the SNR can be written as [1)]

$$\mathrm{SNR} = \frac{P_T G_T G_R}{L_{FS} N_0 B}. \tag{4.1}$$

The quantity $N_0 = k_B T_{sys}$ is called the *noise power spectral density*, with the Boltzmann constant k_B and the system temperature of the receiving system T_{sys}. B represents the received frequency bandwidth. For equation (4.1) it was assumed that the receiving antenna is oriented for maximum response without any ohmic losses.

The product $P_T \cdot G_T$ in equation (4.1) is called the *Equivalent Isotropically Radiated Power* (EIRP). It is the transmit power of a hypothetical antenna radiating equally in all directions (*isotropic radiator*) so as to have the same power flux density over the coverage area as the actual antenna (*Maral and Bousquet*, 2011). Since the value of G_T is a function of the elevation angle γ and azimuth angle ξ (cf. Figure 4.1), the EIRP value strongly depends on γ and ξ. It decreases with increasing elevation angle. An inaccuracy of the HGA pointing direction reduces therefore the EIRP, which is observed as a signal decrease at the G/S. High EIRP values were required to withstand the absorbing effects in Venus' lower atmosphere below approx. 50 km altitude. Values of EIRP for the HGA1 and HGA2 of VEX are given in table 3.1 for the antenna boresight, i.e., the axis of the maximum gain ($\gamma = \xi = 0°$). High X-band EIRP values as well as limb tracking maneuvers (section 4.1.2) allowed to maintain a measurable carrier signal at the G/S even when Venus' deep absorbing atmosphere was probed. In most cases, altitudes as deep as 40 to 42 km at the northern polar region and 45 km at the equatorial latitudes could be achieved with the X-band downlink. The S-band soundings reached similar altitudes in the first occultation season (2006-07-11 to 2006-08-30). A decrease of the S-band EIRP by approx. 14 dB after the first occultation season, however, increased the lowest sounded altitude to the vicinity of Venus' main cloud deck (65 - 70 km).

The quantity $L_{FS} = ((4\pi R_{S/C-G/S})/\lambda)^2$ in equation (4.1) represents the *free-space path loss* with the S/C to G/S distance $R_{S/C-G/S}$ and the signal wavelength λ. Due to the enormous distances between the S/C and the G/S, L_{FS} was the main attenuation factor of radio signals in VeRa's occultation measurements. Table 4.1 presents values of L_{FS} for the X-and S-band downlink signals for minimal and maximal values of $R_{S/C-G/S}$ during VeRa's occultation measurements. The high L_{FS} values indicate that only a small fraction of the transmitted signal power was captured by the G/S. Sufficient high SNR values could still be obtained by choosing appropriate large S/C and G/S antennas for the measurements. Since $G_{T,R} \sim d_a^2$, where d_a is the antenna

[1)] Here, the SNR is considered for the carrier signal, only. If a data signal modulates the carrier signal, Bessel's functions must be considered for the calculations of the SNR.

	$R_{S/C-G/S}$ (km)·10^6	
	40	254
L_{FS}^{X-band} (dB)	263	279
L_{FS}^{S-band} (dB)	252	268

Table 4.1: *Values of free space path loss L_{FS} for minimal and maximal S/C - G/S distances for VeRa's X-and S-band downlink signals.*

diameter, large antennas increase the SNR. On the other hand, they decrease the half power beam width, which may be of disadvantage in case of pointing inaccuracies (section 4.1.2). For Venus Express mainly a 35-m diameter G/S antenna at New Norcia, Australia, was used providing a gain of 55.8 dBi at S-band and 68.2 dBi at X-band (*Häusler et al.*, 2006). In addition to the ESA G/S, NASA tracking stations with diameters ranging between 34 and 70 m could be used. The diameter and gain values of the S/C antennas are given in table 3.1.

Without any atmospheric influences, SNR values of 50 - 65 dB/Hz could be achieved for VeRa's X-band radio signals. For the S-band signals SNR values around 35 dB/Hz were achieved, dropping to 20 dB/Hz after the first occultation season due to a degradation of the S-band antenna feeder system. The SNR of both radio signals decreased, however, when Venus' dense middle and lower atmosphere was sounded. Pointing inaccuracies of the S/C antenna as well as Refractive defocussing and absorption effects decreased the received signal power and therefore the SNR value to

$$\mathrm{SNR} = \frac{P_T G_T G_R}{L_{FS} L_A N_0 B}. \tag{4.2}$$

$L_A = L + \Delta G_T + \alpha$ represents the attenuation due to refractive defocussing L, antenna mispointing ΔG_T and atmospheric absorption α. Attenuation in the Earth atmosphere could be neglected for the X-and S-band radio signals (see appendix A).

4.1.1 Refractive defocussing

When radio waves penetrate Venus' atmosphere, the latter's vertical refractivity gradient leads to a differential refraction of the radio rays and therefore to a widening of the spherical surface of the radio beam. Consequently, the signals power flux density over the surface of the G/S receiving antenna is decreased when the radio waves reach

the G/S. The effect increases with decreasing altitude probed in Venus' atmosphere. This can be observed as a decrease/increase of the time series of the signal amplitude in *ingress/egress* occultation measurements. According to equation (3.9), the effect is identical for a large range of radio waves. The amount of the refractive signal decrease can be determined in two ways:

i) Using radio ray parameters a and δ, derived from Doppler data.

ii) Using amplitude data of a second radio signal which is not affected by any frequency dependent influences.

VeRa has used X-and S-band radio signals to sound Venus' atmosphere. Since both signals are differently affected by absorption effects in lower atmospheric regions (see section 4.1.3), Doppler data were used to determine the refractive loss (method i)). *Eshleman et al.* (1979) have provided a simplified procedure to compute the refractive signal decrease using a and δ. It must be mentioned that the effect of defocussing loss is independent of the signal propagation direction. It is equal for both, from G/S to S/C, and vise versa. The following derivation is depicted for the case of an uplink signal from the G/S to the S/C. Referring to Figure 3.2, in this scenario two parallel radio rays, separated by a vertical distance da before refraction, penetrate Venus' atmosphere. After refraction the energy contained between these two rays is spread out to a width of $\cos\delta \cdot dr$. The reciprocal value of the received signal energy at the G/S normalized by the signal energy without refractive influences provides the amount of refractive loss. It is

$$l_r = \left(\cos\delta \cdot \frac{dr}{da}\right)^{-1}. \tag{4.3}$$

With

$$r = a\sec\delta - D\tan\delta \tag{4.4}$$

it follows

$$l_r = \left(1 - (D\sec\delta - a\tan\delta)\,\frac{d\delta}{da}\right)^{-1}. \tag{4.5}$$

For two adjacent radio rays, the time-variable distance of the S/C behind the planet D (see Figure 3.2) was treated as constant. For S/C to planet distances much smaller than S/C to G/S distances and small bending angles δ, equation (4.5) reduces to

$$l_r = \left(1 - R_1\frac{d\delta}{da}\right)^{-1}. \tag{4.6}$$

(*Lipa and Tyler*, 1979; *Eshleman et al.*, 1980). Additional to the defocussing effect described by equation (4.3), the curved limb of the atmosphere has a focussing effect

on the radio signal amplitude occurring normal to the plane of refraction depicted in Figure 3.2. It is described by

$$g_r = \left(\frac{r}{a}\right)^{-1} \tag{4.7}$$

and is a multiplicative factor in the net effect, called refractive defocussing

$$L = \left[\frac{r}{a}\left(1 - R_1\frac{d\delta}{da}\right)\right]^{-1} \tag{4.8}$$

(e.g. *Eshleman et al.*, 1979; *Lipa and Tyler*, 1979; *Eshleman et al.*, 1980). In decibels is

$$L[dB] = -10\log_{10}(L). \tag{4.9}$$

4.1.2 Mispointing

Radio occultation measurements performed with the Venus Express spacecraft were mainly carried out by using the HGA1, with a diameter of 1.3 m and a half power beam width value of $\vartheta_{3\text{dB}}^{\text{X-band}} \approx 1.6°$ at X-Band and $\vartheta_{3\text{dB}}^{\text{S-band}} \approx 6°$ at S-band (cf. Table 3.1). The half power beam width represents the width of the antennas main lobe at which the signal power is half the maximum power, i.e., the antennas boresight. It can be estimated by

$$\vartheta_{3\text{dB}} \approx 58.8\frac{\lambda}{d_a}, \tag{4.10}$$

with the antenna diameter d_a and the signals wavelength λ. It was known from previous measurements that the ray bending in the atmosphere of Venus would exceed the 3-dB beam width of the signals. In order to avoid significant degradation of the signal amplitude due to mispointing, predetermined spacecraft slews were performed during the measurements [2)]. This way, the antenna boresight was oriented toward the refracted ray path from the spacecraft to the tracking station on Earth (R_1 and R_2 in Figure 3.2). The adjustments of the spacecraft attitude ensured an optimal antenna pointing so that signal power variations could be linked to atmospheric effects rather than pointing inaccuracies. These limb tracking maneuvers were based on a model atmosphere and predicted orbital trajectory of VEX. Deviations of the model atmosphere from the real Venus' refractivity field as well as uncertainties in the S/C position vectors, however, led to pointing inaccuracies.

Pointing errors are described by the elevation angle γ and azimuth angle ξ. Both describe the deviation of the ray asymptote R_1 (cf. Figure 3.2) from the antenna boresight, i.e., the S/C pointing direction. Both angles were computed using the radio

[2)] Without limb tracking maneuvers of the HGA1 a X-band signal power degradation of 3 dB would occur when Venus' atmospheric region between 55 - 60 km altitude was sounded. In this region is $\delta \approx 0.5 \cdot \vartheta_{3\text{dB}}^{\text{X-band}}$.

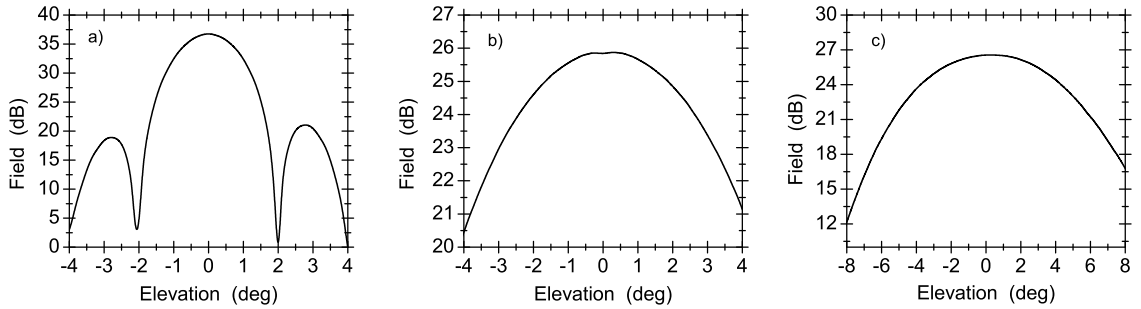

Figure 4.1: *Radiation pattern of the Venus Express HGA1 (a) X-band; b) S-band) and HGA2 (c) X-band) for the azimuth angle of* $\xi = 0°$.

ray parameters δ and a derived from VeRa's Doppler data. Additionally, ephemeris data for the VEX spacecraft and celestial bodies as well as reconstructed S/C attitude information were used. The latter were derived from the star trackers on board Venus Express (*Geiger*, 2011). For the calculation of γ and ξ the unity vector of R_1 and that of the antenna boresight were transferred from the *occultation plane* into spherical coordinates. The antenna gain value at the corresponding angles γ and ξ was obtained from the antenna radiation pattern. The panels a) and b) in Figure 4.1 show the radiation pattern of the HGA1 for the X-and S-band radio signals, respectively. Both radiation patterns are presented for the azimuth angle $\xi = 0°$.

The smaller high gain antenna (HGA2) was used during quadrature (time periods during which the Sun - S/C - G/S angle is between 75 and 95 degrees) in the years 2007, 2012, 2013 and 2014. The parabolic antenna with a diameter of 0.3 m was capable of transmitting at X-band with a half power beam width value of $\vartheta_{3\mathrm{dB}}^{\text{X-band}} \approx 8°$ (cf. Table 3.1). In contrast to measurements carried out with the HGA1, no limb tracking maneuvers were performed during quadrature soundings. The antenna boresight was constantly oriented toward the Earth line of sight (R_3 in Figure 3.2). It can easily be seen from Figure 3.2 that in this case the expected angle γ is in the order of the bending angle δ. The corresponding radiation pattern (for $\xi = 0°$) can be seen in panel c) of Figure 4.1.

With the antenna gain values at the computed elevation and azimuth angles, the HGA pointing errors were simply achieved from

$$\Delta G_T = G_T^{\gamma=0°,\xi} - G_T^{\gamma,\xi}. \tag{4.11}$$

4.1.3 Absorption

As mentioned in section 3.2.2, the imaginary part of the complex refractive index $\widetilde{\mu} = \mu + i\alpha$ refers to the signal attenuation. The latter is used in *Beer-Lambert's law* to describe the power decrease of a radiation which traverses an attenuating medium

$$dP = -\alpha P dx. \tag{4.12}$$

P represents the power and dP the incremental power reduction of the radiation and dx the traversed distance. When applying to radio occultation measurements, the integration over the radio ray path leads to

$$\tau = \ln \frac{P(x)}{P_0} = -\int_{\text{Ray path}} \alpha dx', \tag{4.13}$$

where P_0 is the undisturbed signal power. $\tau = \tau_\text{V} + \tau_\text{E}$ is the integrated attenuation along the radio radio path, the so-called path absorption, with contributions from the Venus τ_V and Earth τ_E atmospheres, respectively. In general, τ is caused by the atmospheric gas, clouds and precipitation resulting from absorption and scattering (*Battan*, 1973), so that

$$\alpha = (\alpha_\text{g} + \alpha_\text{c} + \alpha_\text{p})_\text{abs} + (\alpha_\text{g} + \alpha_\text{c} + \alpha_\text{p})_\text{scat}\,. \tag{4.14}$$

A typical Venus Express radio occultation measurement, *ingress* or *egress*, took several minutes. The weather conditions on Earth can be considered as constant during this period of time. Earth atmospheric influences on the signal amplitude were therefore not considered in the present study. Those are outlined in appendix A.

In order to attribute the specific attenuation α to the atmosphere of Venus as a function of altitude, Snell's low is applied. The path absorption in equation (4.13) can then be expressed as an integral over radius and rewritten in form of the inverse Abel transform (*Jenkins and Steffes*, 1991)

$$\alpha\left(r_0\right) = -\frac{\mu(r_0)}{\pi a\left(r_0\right)} \frac{d}{da} \left(\int_{a(r_0)}^{\infty} \frac{\tau\left(a\right) \cdot a \cdot da}{\sqrt{a^2 - a\left(r_0\right)}} \right). \tag{4.15}$$

Here, it was used that $da \approx \mu \cdot dr$. The inverse Abel integral was calculated by using the Gaussian quadrature, which ensures an exact integration (*Brzeziński and Ostalczyk*, 2014; *Krüger*, 2008; *Oschlisniok*, 2010). When extremely noisy data are used, however, the exact integration as well as the derivation of the integral in equation (4.15) can have an adverse effect. A resultant amplification of the noise may lead to misinterpretations of the obtained absorptivity and H_2SO_4(g) results. In order to decrease the effect of noise amplification, downsampling methods and filtering tools were

applied in the process of absorptivity and sulfuric acid vapor calculations. Residual noise, however, may still affect the results.

In the following, the contribution factors to the attenuation coefficient α (see equation (4.14)) shall be discussed. Since the radio signal attenuation is only attributed to the atmosphere of Venus, the attenuation factors due to precipitation can be removed ($\alpha_{\mathrm{p,\,abs}} = \alpha_{\mathrm{p,\,scat}} = 0$). Furthermore, scattering effects of radio waves caused by atmospheric gases can be neglected ($\alpha_{\mathrm{g,\,scat}} = 0$). The size of the molecules is too small compared to radio wavelengths, so that no significant power reduction is expected. Signal attenuation caused by particles of the Venus clouds can be estimated by applying the theory of scattering and absorption of electromagnetic waves by colloids. Lord Rayleigh (1842 - 1919) provided a formalism, which describes the scattering of electromagnetic waves by spherical non-absorbing particles with diameters smaller than the wavelength. A generalized theory, without limitations to the size of the particles (non-absorbing and absorbing), was given by Gustav Mie (1868 - 1957) (*Mie*, 1908). Mie theory is therefore used for most scattering systems and includes the theory provided by Rayleigh. Both theories make use of the extinction cross section σ_{ext}, the area which, when multiplied by the incident radiation, provides the total signal power abstracted from the incident wave. Since the attenuation is caused by scattering and absorption effects, the extinction cross section can be written as

$$\sigma_{\mathrm{ext}} = \sigma_{\mathrm{abs}} + \sigma_{\mathrm{scat}}. \tag{4.16}$$

When the particles are small with respect to the wavelength, both theories provide similar results (e.g. *Gunn and East*, 1954). In this case the absorption and scattering cross sections can be written as

$$\sigma_{\mathrm{abs}} = \frac{2\lambda^2}{3\pi} x_s^6 \left| \frac{\epsilon - 1}{\epsilon + 2} \right|^2 \tag{4.17a}$$

$$\sigma_{\mathrm{scat}} = \frac{\lambda^2}{\pi} x_s^3 \cdot \mathrm{Im}\left(-\frac{\epsilon - 1}{\epsilon + 2} \right), \tag{4.17b}$$

with the dimensionless *size parameter* $x_s = 2\pi a_p/\lambda$, particle radius a_p and permittivity (or dielectric constant) $\epsilon = \epsilon' - i\epsilon''$ (e.g. *Gunn and East*, 1954). The so-called *Rayleigh approximation* for σ_{abs} and σ_{scat} presented by the equations 4.17a and 4.17b can be applied for sufficient small *size parameter* values ($x_s << 1$ or $a_p << \lambda$) (e.g. *Gunn and East*, 1954; *Battan*, 1973). Values in the order of 10^{-3} are obtained for X-and S-band radio signals, so that equations (4.17a) and (4.17b) can be used for scattering and absorption calculations at theses wavelengths. Here, particle size results derived by *Knollenberg and Hunten* (1980) from the cloud particle size spectrometer (LCPS) on board Pioneer Venus were used with a maximal particle diameter of 25 µm. Along

with permittivity measurements for different H_2SO_4-H_2O solutions, provided by *Cimino* (1982), maximal values of the ratio $\sigma_{\text{scat}}/\sigma_{\text{abs}}$ of $8.8 \cdot 10^{-7}$ for the X-band and $5.3 \cdot 10^{-8}$ for the S-band are obtained. The small values indicate that signal attenuation due to scattering in the Venus clouds can be neglected at these wavelengths ($\alpha_{\text{c, scat}} = 0$).

Equation (4.17a) can be used to find an expression for the absorption caused by the cloud particles. Since all particles located in the ray path contribute to the signal absorption, their cross sections must be summed up. An estimation of the drop size distribution along the radio ray path, however, is not possible. Instead, the bulk density M is introduced, leading to an expression for the absorption of radio waves by cloud particles (*Battan*, 1973)

$$\begin{aligned} \alpha_{\text{c, abs}} &= K \cdot M \\ &= \frac{246}{\rho\lambda} \frac{\epsilon''}{(\epsilon' + 2)^2 + \epsilon''^2} \cdot M. \end{aligned} \tag{4.18}$$

For X- and S-band radio signals maximal values of $2.7 \cdot 10^{-3}$ dB/km and $2.6 \cdot 10^{-4}$ dB/km, respectively, are achieved. Mass loading measurements were obtained from *Knollenberg and Hunten* (1980) and permittivity values of the H_2SO_4-H_2O solution are provided by *Cimino* (1982). Additionally, a particle density of $\rho = 1.8 \cdot 10^3$ kg/m^3 was used. Since the obtained values are much lower than the expected absorptivity values caused by the atmospheric gas (see section 4.2), absorption due to the Venus clouds can be neglected at these wavelengths ($\alpha_{\text{c, abs}} = 0$).

The attenuation coefficient α for radio waves at X- and S-band presented in equation (4.14) can finally be reduced to the absorption by the atmospheric gas

$$\alpha = \alpha_{\text{g, abs}}. \tag{4.19}$$

Here, energy is abstracted from the incident wave by molecules having a permanent or induced electric or magnetic dipole moment. Those molecules are exited to vibrate or rotate as the wave passes over the particles, extracting this way energy from the radio signal. A formalism to describe pressure induced absorption by molecules was provided, for example, by Hendrik Antoon Lorentz (1853 - 1928) for electromagnetic waves in the optical range (*Lorentz*, 2011). It was modified by *van Vleck and Weisskopf* (1945) for the application to the microwave region and used by *van Vleck* (1947) to describe the absorption of microwaves by oxygen.

Microwave absorbing gases in Venus' atmosphere are sulfuric acid (H_2SO_4), sulfur dioxide (SO_2), carbon dioxide (CO_2) and nitrogen (N_2). Small absorption effects are caused by argon (Ar) and water vapor (H_2O). *Ho et al.* (1966) have used the Van

Vleck-Weisskopf theory to calculate the microwave absorption caused by H_2O under simulated Venus' lower atmospheric conditions. The absorption coefficient, however, was found to provide too low values when fitted to the absorptivity data. Instead, a power low expression was used. The latter was also applied to derive an expression for the microwave absorptivity of CO_2, N_2 and Ar. *Steffes and Eshleman* (1982) as well as *Steffes* (1985) have identified sulfuric acid vapor to be the main absorber of microwaves in Venus' atmosphere. Absorption coefficients were obtained by *Kolodner and Steffes* (1998) by fitting power low expressions to experimental absorptivity data. Centimeter wave opacity measurements of sulfur dioxide under simulated Venus atmospheric conditions were performed by *Steffes and Eshleman* (1981). New measurements were conducted by *Fahd and Steffes* (1992) as well as by *Suleiman et al.* (1996). The following equations present the absorption coefficient as a function of temperature and pressure derived by *Ho et al.* (1966) for CO_2 and N_2 (equation (4.20a)) as well as by *Kolodner and Steffes* (1998) for H_2SO_4(g) (equations (4.20b) and (4.20c)). Additionally, *Kolodner and Steffes* (1998) have provided a model for the absorption coefficient in the frequency range between S- and K-band (equation (4.20d)). Equation (4.20e) presents the SO_2 absorption coefficient adjusted by *Oschlisniok et al.* (2012) based on results provided by *Fahd and Steffes* (1992) as well as by *Suleiman et al.* (1996).

$$\alpha_{CO_2,N_2}[\mathrm{dB/km}] = 1.15 \cdot 10^8 \left(q_{CO_2}^2 + 0.25 q_{CO_2} q_{N_2} + 0.0054 q_{N_2}^2\right) \cdot f^2 p^2 T^{-5} \tag{4.20a}$$

$$\alpha_{H_2SO_4}^{\text{X-band}}[\mathrm{dB/km}] = 443.570 p^{1.302} \left(\frac{553}{T}\right)^{3.0} q_{H_2SO_4} \tag{4.20b}$$

$$\alpha_{H_2SO_4}^{\text{S-band}}[\mathrm{dB/km}] = 103.587 p^{1.356} \left(\frac{553}{T}\right)^{3.2} q_{H_2SO_4} \tag{4.20c}$$

$$\alpha_{H_2SO_4}^{\text{S,X,Ku,K-band}}[\mathrm{dB/km}] = 53.601 p^{1.11} \cdot f^{1.15} \left(\frac{553}{T}\right)^{3.2\pm0.2} q_{H_2SO_4} \tag{4.20d}$$

$$\alpha_{SO_2}[\mathrm{dB/km}] = 4.3 \cdot 10^6 \cdot f^2 \cdot q_{SO_2} \cdot p^{1.28} \cdot T^{-2.91}. \tag{4.20e}$$

The number mixing ratio is denoted by q, the pressure and temperature by p[atm.] and T[K], respectively, and f is the wave frequency in GHz. Contributions by H_2O and Ar to the absorption of VeRa's X- and S-band radio signals are small and could be neglected. Considering the absorption contribution of CO_2, N_2, SO_2 and H_2SO_4(g), equation (4.19) can be written as

$$\alpha = \alpha_{CO_2,N_2} + \alpha_{H_2SO_4} + \alpha_{SO_2}. \tag{4.21}$$

The above expression was used to derive the sulfuric acid vapor abundance from VeRa's radio occultation measurements after removing the contribution by CO_2, N_2 and SO_2.

It should be noted, that the discussed absorption coefficient α is given in units of dB/km. The conversion between dB/km and 1/km is

$$\alpha[\mathrm{dB/km}] = 10 \log_{10}(e)\, \alpha[1/\mathrm{km}], \tag{4.22}$$

where e is the Euler's number.

4.2 Previous observations

First analysis of radio signal attenuation effects were performed on the basis of the **Mariner V** radio occultation measurements (e.g. *Mariner Stanford Group*, 1967; *Kliore et al.*, 1967; *Fjeldbo and Eshleman*, 1969; *Fjeldbo et al.*, 1971). The two radio sounding measurements, performed on 19 October 1967 during the *ingress* and *egress* part of the occultation, consisted of a one-way dual-frequency U/L (49.8 and 423.3 MHz) and a one-way single-frequency D/L (S-band) experiment. While the uplink signals were recorded by a phase-locked receiver on board, CL and OL receivers were used at the 63-m diameter G/S antenna for recordings of the S-band downlink. Using the HGA of the spacecraft (the reflector was a paraboloid with an elliptic aperture; major axis 1.17 m; minor axis 0.53 m; (*Imbriale*, 2006)), the atmosphere was sounded to altitudes as deep as 35 km at the southern and northern equatorial regions. Figure 4.2 shows the observed decrease of the radio signal power as well as the derived absorptivity and H_2SO_4(g) abundance profiles. The shown signal power was already corrected for signal degradation effects due to pointing inaccuracies, which occurred since no limb tracking maneuvers were performed with Mariner V. The decrease of the signal power, visible in both experiments, reveals clear frequency dependent effects. While ionospheric contributions to the attenuation are barely visible in the S-band signal, the uplink signals show distinct defocussing, *scintillations* and *multipath* influences when the ionospheric region was sounded (*Mariner Stanford Group*, 1967; *Fjeldbo and Eshleman*, 1969). In the neutral atmosphere the total attenuation of the downlink signal shows clear absorption contributions, while the attenuation of the uplink signals was caused by defocussing effects, only. Defocussing contributions to the attenuation of the S-band radio signal could therefore be removed by using i) the S-band Doppler data and ii) the 423.3 MHz radio signal attenuation [3)] (see section 4.1.1). The absorptivity profiles computed this way show distinct disagreements (Figure 4.2.b)), which most probably result from the combination of uplink and downlink signals (method ii)). Both signals traversed Venus' atmosphere separated by approx. 9 minutes at slightly different atmospheric regions, which led to a different attenuation. The almost constant absorptivity values of $4 - 5 \cdot 10^{-3}$ dB/km below 47 - 48 km altitude were

[3)] The amplitude of the 49.8 MHz radio signal revealed increased oscillations in the neutral atmosphere and was therefore not used for defocussing correction of the S-band downlink signal.

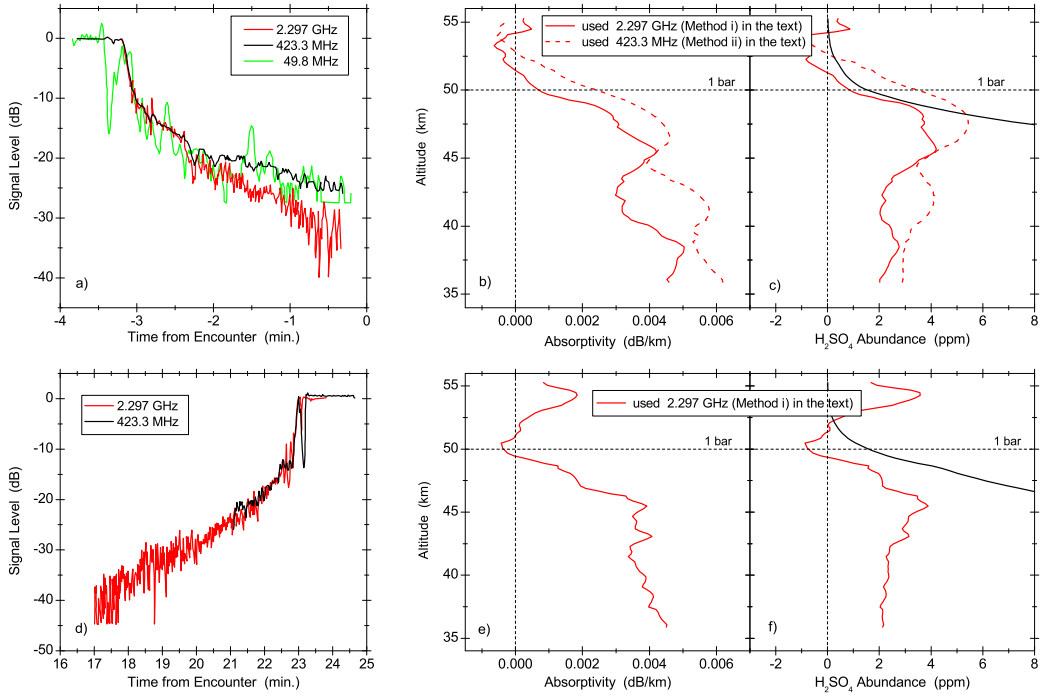

Figure 4.2: *Observed signal attenuation as well as absorptivity and $H_2SO_4(g)$ abundance on the equatorial nightside (upper panels; ingress) and dayside (lower panels; egress) Venus atmosphere derived from Mariner V radio occultation data. Absorptivity profiles on the nightside were derived from the S-band radio signal attenuation using i) the S-band Doppler data and ii) the 423.3 MHz amplitude data for removal of the defocussing loss. On the dayside the S-band Doppler data were used, only. The black profiles shows the saturation abundance (cf. equation (5.13)). Signal level, absorptivity, temperature and pressure data for the creation of the figures were extracted from Mariner Stanford Group (1967) and Fjeldbo et al. (1971). No information on the uncertainty of the derived values was provided.*

used to compute the $H_2SO_4(g)$ abundance, which reveals maximal values of 4 - 6 ppm around 47 km altitude when using equation (4.20c). Below this altitude the sulfuric acid vapor abundance decreases to values of 2 - 3 ppm between 35 and 43 km altitude.

Increased sulfuric acid vapor values right below the main cloud deck at equatorial latitudes were also observed by *Kolodner and Steffes* (1998). They used S-band radio absorptivity data derived by *Lipa and Tyler* (1979) from the **Mariner 10** radio occultation measurement. The measurement was conducted during the Venus flyby on the way to Mercury on 5 February 1974. In contrast to Mariner V, the 1.37-m diameter HGA of Mariner 10 continuously pointed toward the virtual image of the Earth when Venus' atmosphere was sounded. Thanks to the S/C attitude adjustments as well as a

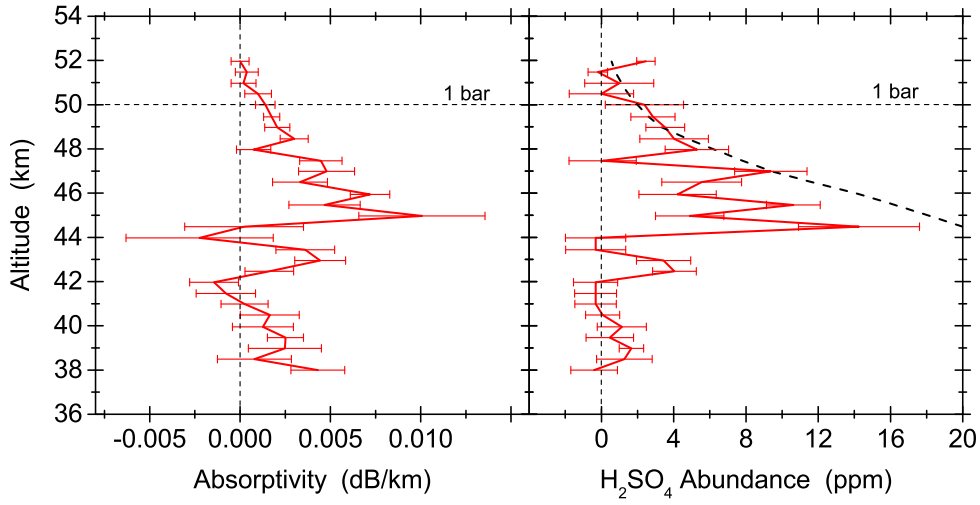

Figure 4.3: *S-band radio absorptivity and $H_2SO_4(g)$ abundance in Venus' equatorial atmosphere (red) derived by Lipa and Tyler (1979) as well as Kolodner and Steffes (1998) from Mariner 10 radio occultation data. The black profile shows the saturation abundance (cf. equation (5.13)). Data were extracted from the corresponding publications. Absorptivity data were interpolated at altitudes from Kolodner and Steffes (1998).*

large half power beam width value ($\vartheta_{3\text{dB}}^{\text{S-band}} \approx 6°$) the S-band signal amplitude was only marginal influenced by pointing inaccuracies. A constant pointing error of 0.25 dB was included in the error analysis. While the deepest sounded altitude by the S-band radio signal was located around 42 km, the weaker X-band signal ($\text{EIRP}_{\text{X-band}} \approx 32$ dBW; $\text{EIRP}_{\text{S-band}} \approx 41$ dBW (*Imbriale*, 2006)) was much more rapidly attenuated. The atmospheric region above 51 km was sounded before no measurable X-band signal could be detected by the G/S receiving system. The latter consisted of a 70-m diameter antenna as well as CL and OL receivers. It turned out that results derived from CL data, which were used as a cross check, agree quite well with those derived from OL data (*Howard et al.*, 1974; *Nicholson and Muhleman*, 1978; *Lipa and Tyler*, 1979). The contribution of the defocussing of the radio beam was removed from the observed total signal attenuation by using the Doppler data before the absorptivity could be calculated. Both, the S-band OL absorptivity and sulfuric acid vapor profiles acquired from the *ingress* [4)] measurement are given in Figure 4.3. The $H_2SO_4(g)$ abundance was computed by using equation (4.20c). The increased absorptivity and $H_2SO_4(g)$ values right below the main cloud deck derived from Mariner 10 data are distinctly

[4)] Mariner 10 radio occultation measurements were mainly performed in the two-way dual-frequency transmission mode during *ingress* measurements. An auxiliary oscillator on board was switched on when deeper altitudes were sounded. For egress measurements the oscillator didn't provide the required phase stability.

higher than those observed by Mariner V (Figure 4.2). Maximal absorptivity and H_2SO_4(g) values of around 0.005 - 0.01 dB/km and 8 - 14 ppm, respectively, are visible between 44 and 46 km altitude, before sharply decreasing below this altitude range.

Radio signal attenuation studies extended to a wide range of planetary latitudes were performed by *Cimino* (1982) as well as by *Jenkins and Steffes* (1991). They used radio occultation measurements conducted by the **Pioneer Venus Orbiter (PVO)** between the years 1978 and 1992. PVO used X-and S-band radio signals and a 1.09-m diameter HGA to sound Venus' atmosphere during so-called *occultation seasons*. Similar to Mariner 10, limb tracking maneuvers were performed in the earlier PVO *seasons*. Due to the applied S/C attitude adjustments and a large half power beam width value ($\vartheta_{3\mathrm{dB}}^{\text{S-band}} \approx 7.6°$) the S-band signal amplitude was barely affected by pointing inaccuracies. Additionally, an EIRP of about 36 dBW allowed to detect a measurable S-band carrier signal at the 70-m diameter G/S even when Venus' lower atmosphere was sounded. Deepest probed altitudes were located around 37 km. The weaker X-band transmitter (750 mW) allowed to sound altitudes above approx. 45 km, before the carrier signal wasn't detectable anymore (*Colin and Hall*, 1977; *Cimino*, 1982). In later *occultation seasons*, the attitude of the S/C was only adjusted once per orbit so that it pointed towards the G/S at the orbit periapsis (*Jenkins and Steffes*, 1991). The mispointing caused a significant decrease of the S-band signal amplitude. Additionally, a severe continuous degradation of the solar panel power output caused a decrease of the EIRP to a value of about 33 dBW (e.g. *Goldhammer et al.*, 1987; *Steffes et al.*, 1994). As a consequence, the deepest sounded altitudes by the S-band radio signal were located above 40 km. The contributions of the mispointing and defocussing loss to the

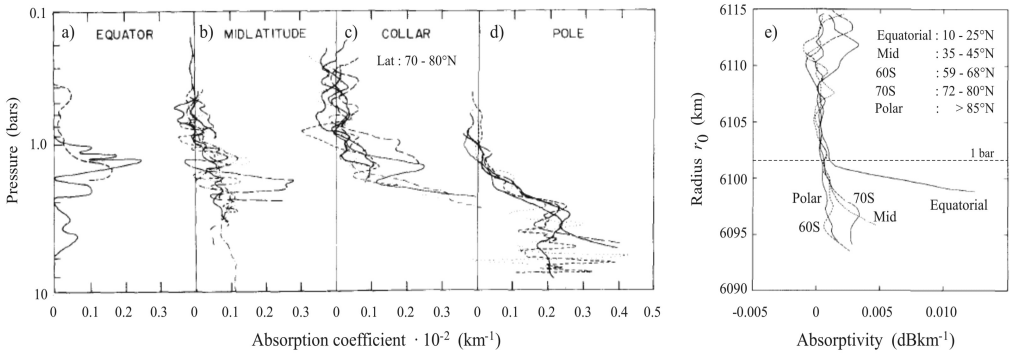

Figure 4.4: *S-band radio signal absorptivity profiles in the Venus atmosphere derived by Cimino (1982) as well as Jenkins and Steffes (1991) from Pioneer Venus radio occultation measurements from the years 1978/1979 (a) - d)) and 1986/1987 (d)) at different latitudinal regions. Note that:* $\alpha[dBkm^{-1}] = 10\log_{10}(e)\alpha[km^{-1}]$ *(see equation (4.22)). The dashed line in e) represents the approximate location of the 1 bar pressure level.*

total signal decrease were removed by using Doppler data before deriving absorptivity profiles. Figure 4.4 shows the absorptivity of the S-band radio signal derived from the first two *occultation seasons* (1978/1979) (panels a) to d)) as well as from *occultation season* 10 (1986/1987) (panel e)) [5]. Both, the earlier and later radio soundings show a distinct latitudinal variation. Increased absorption at polar latitudes is located at lower altitudes when compared to the equatorial region. Furthermore, an indication for a long-term variation can be observed between 70 and 80°N when comparing the measurements from the *seasons* 1 and 2 with those from *season* 10. Increased absorptivity values can be observed in the earlier observations implying a decrease of sulfuric acid vapor from 1978 to 1987 at this latitudinal region.

Radio absorptivity profiles from the deep Venus atmosphere simultaneously achieved from S-and X-band radio signals were derived by *Jenkins et al.* (1994). They used radio occultation *ingress* measurements conducted by the **Magellan** spacecraft during three consecutive orbits on 5 - 6 October 1991. Similar to Mariner 10 and PVO, limb tracking maneuvers were performed during Magellan's occultation measurements. The adjustments of the S/C attitude inhibited any significant mispointing effects on the S-band radio signal amplitude. Due to a small value of the half power beam width ($\vartheta_{3\mathrm{dB}}^{\text{X-band}} \approx 0.6°$), however, the X-band radio signal was severely affected by pointing inaccuracies (maximal pointing error $\sim 0.4°$ resulted in a signal degradation of up to 7 dB; (*Steffes et al.*, 1994)). In contrast to previous missions, a large 3.7-m diameter HGA fed by 5-W and 20-W S-and X-band transmitters, respectively, radiated an EIRP with values of 44 dBW (S-band) and 61.4 dBW (X-band). This way, the carrier signals could be detected at the 70-m diameter G/S receiving system even when Venus' atmosphere was probed to altitudes as deep as 33 - 35 km. The signal decrease due to mispointing (in case of X-band) and defocussing loss was removed from the total attenuation by using the OL Doppler data. Subsequently, X-and S-band absorptivity and H_2SO_4(g) abundance profiles could be derived. The panels a) and b) in Figure 4.5 show the absorptivity profiles in Venus' nightside atmosphere ($\sim 67°$N) derived by *Jenkins et al.* (1994) from Magellan's orbit 3214. Panel c) shows the corresponding sulfuric acid vapor abundance profiles computed using the equations (4.20c) and (4.20b). It is clearly visible that above about 50 km altitude no absorption/H_2SO_4(g) was detected. Maximal sulfuric acid vapor values of 4 - 6 ppm are located around 46 km altitude. Those values are comparable to the H_2SO_4(g) abundance values derived from the Mariner V radio soundings at equatorial latitudes (cf. Figure 4.2). The H_2SO_4(g) abundance profiles derived from Magellan soundings, however, show a supersaturation at the topside of the sulfuric acid haze layer, which is more pronounced at the S- than at the X-band data. This is not visible in the profiles derived from the Mariner V and

[5] Since the temperature and pressure values were not provided in the corresponding publications, the absorptivity profiles could not be transferred into H_2SO_4(g) abundance values.

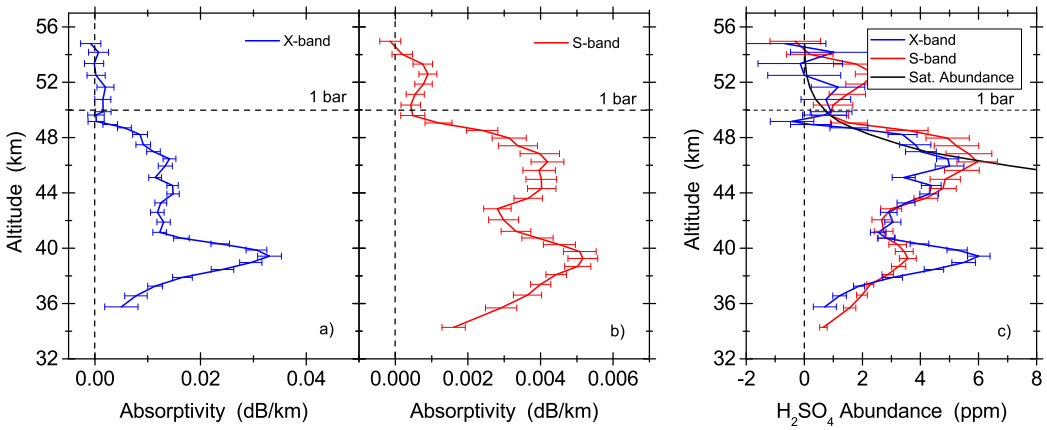

Figure 4.5: *Panels a) and b): X-and S-band radio signal absorptivity profiles in Venus' nightside atmosphere (∼ 67°N) derived by Jenkins et al. (1994) from Magellan radio occultation measurements conducted in October 1991 (Orbit 3214). Panel c): Sulfuric acid vapor abundance profiles computed by Kolodner and Steffes (1998) from the absorptivity profiles visible in the panels a) and b). The saturation abundance was computed by using equation (5.13). The dashed lines in the panels a) to c) represent the approximate location of the 1 bar pressure level.*

Mariner 10 measurements. In general, the H_2SO_4(g) profiles derived from the Magellan S-and X-band soundings show a clear agreement within the presented altitude range. The only significant difference appears right below 40 km altitude. Here, the H_2SO_4(g) profile derived from the X-band data shows distinctly increased abundance values. According to *Kolodner and Steffes* (1998), the disagreement might be caused by an increased abundance of sulfur dioxide at these altitudes. The contribution of SO_2 to the total absorption of the signals was not removed when transferring the absorptivity into H_2SO_4(g) profiles. As can be seen from equation (4.20e), the SO_2 radio signal absorptivity at these wavelengths shows a frequency-squared dependance. The absorption effect is therefore stronger at X-band than at S-band.

The absorptivity and sulfuric acid vapor values retrieved from the Mariner, Pioneer Venus and Magellan missions generally agree with each other. No significant absorption of the radio signals was observed above about 50 km altitude. Increased H_2SO_4(g) values were detected between 33 and 50 km altitude with indications for latitudinal and temporal variations.

Distinctly increased absorption values, however, have been observed by *Gubenko et al.* (2001) at the mid-latitudinal (around 50°N) and *cold collar* (71 - 76°N) regions. They analyzed the attenuation of 5 and 32 cm radio waves used in radio occultation

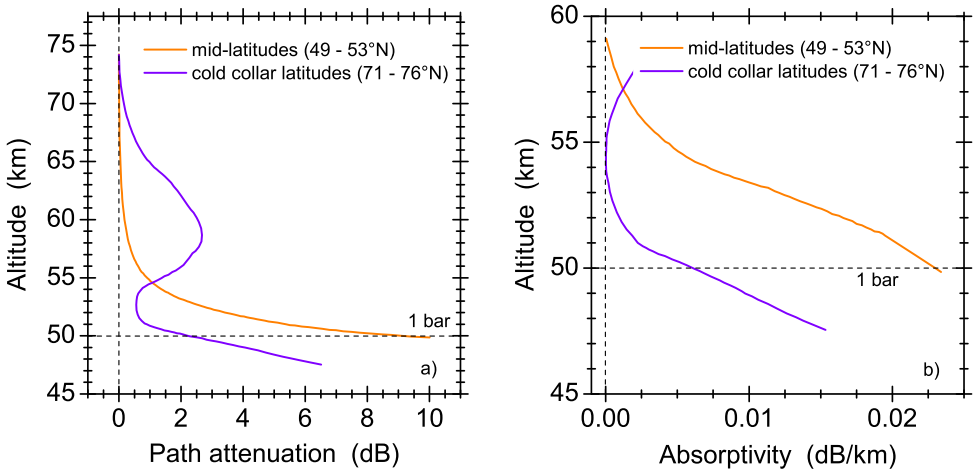

Figure 4.6: *Residual attenuation of the 5 cm radio signal derived by Gubenko et al. (2001) from the Venera 15/16 radio occultation measurements carried out at two different latitudes. The defocussing loss was removed by using the 32 cm radio signal amplitude. Data were extracted from the corresponding publication and the absorption coefficient was transferred into units of dB/km by using equation (4.22). The value of the mean Venus radius was corrected from 6051 to 6051.8 km. The dashed line represent the approximate location of the 1 bar pressure level.*

measurements carried out with the **Venera 15/16** spacecrafts in 1983/1984. The spacecrafts used 2.6-m diameter high gain antennas to sound Venus' atmosphere. On Earth, the centimeter and decimeter radio waves were recorded at 64-m and 70-m diameter G/S receiving systems. Similar to Mariner V, no adjustments of the S/C attitude were performed during the measurements. Considering the small value of the half power beam width ($\vartheta^{5\,\mathrm{cm}}_{3\mathrm{dB}} \approx 1.2°$), at least the 5 cm radio signal was significantly affected by resulting pointing inaccuracies. Those were corrected by using the bending angles δ of the radio rays (cf. Figure 3.2). According to *Gubenko et al.* (2001), the amplitude of the decimeter radio signal was not affected by any absorption effects in Venus' atmosphere. It was therefore used to remove the defocussing loss contribution from the observed total attenuation of the 5 cm radio signal. The residual attenuation is presented in panel a) of Figure 4.6. It shows a layer of increased attenuation with values ranging between 2 and 3 dB around 60 km altitude at the *cold collar* region. Near the 1 bar pressure level a strong increase is visible to maximal attenuation values of more than 6 dB around 47 km altitude. A comparable strong increase can be observed at the mid-latitudes. Here, the attenuation increases from 0.5 dB at 57 km to maximal values of almost 10 dB around 50 km altitude. Panel b) shows the corresponding absorptivity in the altitude range between 45 and 60 km altitude. Equation (4.22) was used in order to transfer the absorption coefficient from units of 1/km into dB/km.

Chapter 5

Two-dimensional mass transport model of the lower and middle Venus atmosphere

The global distribution of H_2SO_4(g) in Venus' lower atmosphere computed from the observed absorption of VeRa's X-band radio signals will be used to derive information about the wind dynamics in this altitude region. For this purpose a two-dimensional zonally averaged mass transport model was developed in the present work, which is used to reproduce the observations. Conclusions about the global wind transport can be drawn from the comparison of the observed with the modeled H_2SO_4(g) distribution. Section 5.1 presents the included transport mechanisms as well as the condensation and evaporation processes while the implementation of the numerical solution is described in section 5.2.

5.1 Transport, condensation and evaporation

Since sulfuric acid exists in the liquid and in the gaseous phases within the considered altitude range, both parts must be considered in the model calculations. The latter part consists of a H_2SO_4-H_2O solution (cf. section 2.2), so that in addition to sulfuric acid, the abundance of water must be simulated. The H_2SO_4 concentration in the solution is believed to be 75 - 85% by weight in the upper cloud region increasing to values of more than 90% in the lower clouds (*Young*, 1973; *Krasnopolsky*, 2012). For the present work a modeled concentration profile presented by *Hashimoto and Abe* (2001) was adopted showing the lowest value of 79% at 70 km altitude and more than 99 % around 47 km altitude. The abundances of H_2SO_4 and H_2O shall be modeled in the altitude region between 35 and 80 km at both hemispheres. Therefore, the

concentration profile was linearly extrapolated to higher and lower altitudes resulting in a concentration of approx. 75% at 80 km altitude and almost 100 % at 30 km. A background atmosphere consisting of temperature T, pressure p and number density n_0 was available from VeRa's radio occultation observations (cf. section 3.2.2). Additionally, data from the *Venus International Reference Atmosphere* (VIRA) were used for atmospheric regions which were not covered by the VeRa measurements.

The present model shall mainly simulate the meridional and vertical transport of the number density $n_l = n_l^{\text{gas}} + n_l^{\text{liq}}$ of sulfuric acid $l = H_2SO_4$ and water $l = H_2O$ in the above mentioned spatial region. Besides the chemical production and loss processes of H_2SO_4 in the upper and lower atmosphere, respectively, which are presented in section 2.2, the transport of gaseous and liquid H_2SO_4 and that of H_2O is realized by **wind**, **eddy diffusion** (turbulent diffusion) and **sedimentation**.

Wind transport

The temporal variation of the number density in a particular volume caused by the change of the mass flux $\vec{F}_{\text{circ.},l} = n_l \cdot \vec{v}$ through that volume is described by the continuity equation

$$\left(\frac{\partial n_l}{\partial t}\right)_{\text{circ.}} = -\vec{\nabla}\vec{F}_{\text{circ.},l} = -\vec{\nabla}(n_l\vec{v}), \tag{5.1}$$

where $\vec{v}$ is the wind velocity vector. The wind field in each hemisphere is realized on the basis of the observations presented in section 2.3. They indicate the presence of a number of circulations cells located in different altitude ranges. The number of circulation cells as well as their spatial extension can be varied in the model in order to particularly match the observed H_2SO_4(g) distribution. This allows to draw conclusions about the geometry of the cells.

The transport of the gas and liquid species by the circulation cells shall be treated as mass conservative, so that

$$\vec{\nabla} \cdot \vec{v} = 0. \tag{5.2}$$

In this case the wind stream may be depicted by a mass stream function ψ $[kg{\cdot}m^{-1}{\cdot}s^{-1}]$, whose streamlines $\psi = \text{const.}$ represent the trajectories of the particles (e.g. *Batchelor*, 2012; *White*, 2016). At any given instant, the tangent of a streamline $\psi = \text{const.}$ is parallel to the wind velocity vector $\vec{v}$ (e.g. *Etling*, 2013; *Hantel*, 2013), which is perpendicular to the gradient of the streamfunction ψ. In the (y, z)-plane the required meridional and vertical wind velocity components v_y and v_z can be derived by using

the unit vector $\vec{k}$, which is orthogonal to the (y, z)-plane

$$\vec{v} = \vec{k} \times \vec{\nabla}\psi \tag{5.3}$$

or in components

$$v_y = -\frac{\partial\psi}{\partial z} \qquad v_z = \frac{\partial\psi}{\partial y}. \tag{5.4}$$

In the present model, the zonally averaged transport shall be simulated in geofluid coordinates (*Hantel and Mayer*, 2006), so that equation (5.1) can be written as

$$\left(\frac{\partial n_l}{\partial t}\right)_{\text{circ.}} = -\frac{\partial(\cos\phi n_l v_\phi)}{r\cos\phi\partial\phi} - \frac{\partial(v_h n_l)}{\partial h}, \tag{5.5}$$

with the meridional and vertical wind velocities

$$v_\phi = -\frac{1}{\rho\cos\phi}\frac{\partial\psi}{\partial h} \qquad v_h = \frac{1}{\rho r\cos\phi}\frac{\partial\psi}{\partial\phi}, \tag{5.6}$$

where ϕ and r represent the planetary latitude and radius, respectively, h is the altitude and ρ is the atmospheric density. It can easily be seen that the velocities in equation (5.6) satisfy the incompressibility condition described by equation (5.2).

The circulation cells were created using the drawing software *CorelDRAW*. The color code of the images was turned into values which correspond to the mass stream function ψ. A two-dimensional fit to those values ensured that neighboring values of ψ differ from each other so that $v_\phi \neq 0$ and $v_h \neq 0$. A variety of those cells were created and tested in the model. The configuration that best matched the observed H_2SO_4(g) values is presented below.

In order to simulate meridional wind transport in Venus' atmosphere, it is common to use circulation cells whose poleward and equatorward branches are simply vertically layered. As can be seen from Figure 2.8 those circulation cells extend from the equatorial to the polar latitudes. As for the upper clouds (60 - 70 km), this assumption is consistent with a large number of wind velocity observations which continuously show a poleward wind direction in this altitude region (cf. Figure 2.7). In the deeper atmosphere, only a small number of wind measurements exists. Those indicate a more complicated wind structure.

In the present model, a system of two cells, i.e. a Hadley and a polar cell, is implemented in the altitude range between 35 and 80 km altitude. Figure 5.1 shows the mass stream function ψ of those circulation cells in the northern hemisphere. In the southern hemisphere the same circulation cells are present. While the flow direction

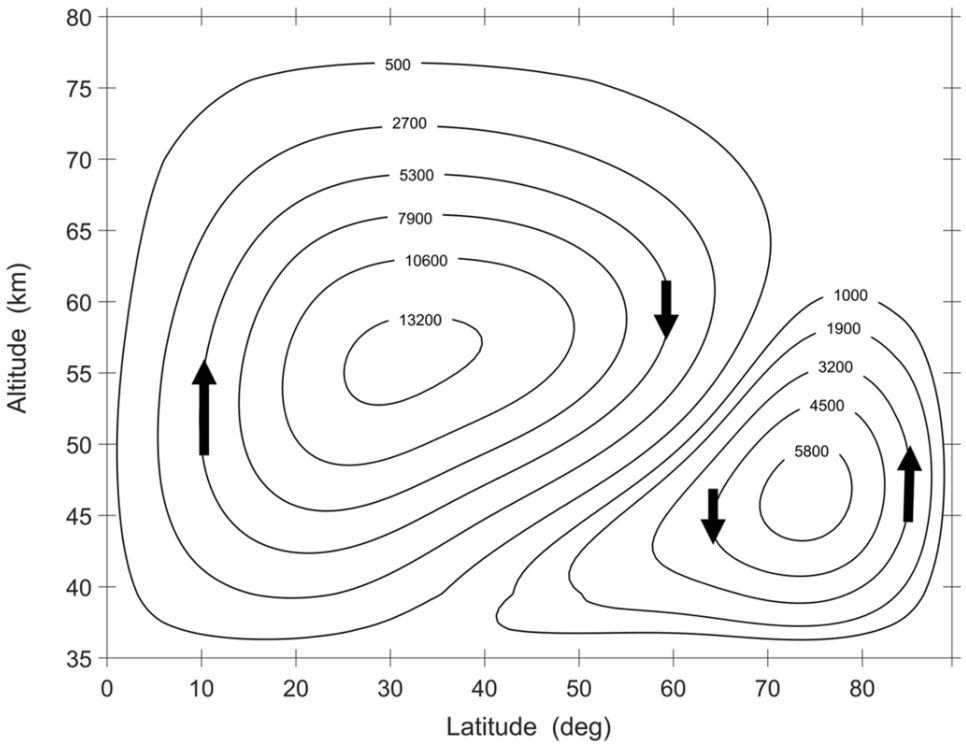

Figure 5.1: *Mass stream function ψ in units of $kg \cdot m^{-1} \cdot s^{-1}$ in the northern hemisphere used in the simulation run Test 1 (cf. Table 8.1). In the southern hemisphere the same parameters are used.*

is depicted by the black arrows, the numbers visible on the streamlines represent the values of ψ. In order keep the poleward flow in the upper cloud region consistent with observations, the upper branch of the Hadley cell extends in the model from the equatorial to the polar latitudes. A continuous poleward flow at these altitudes was confirmed by a large number of measurements (cf. Figure 2.7) and is therefore present in the model calculations. This is also in agreement with previous atmospheric simulations (cf. Figure 2.8). In contrast to previous transport models, however, the downward directed branch of the Hadley cell is tilted. The tilted branch transports gas constituents and cloud material from the upper mid- and high latitudes to the lower equatorial region. Additionally, a polar cell is implemented at the high latitudes which is tilted towards the mid-latitudes. The rotation direction of the latter is reversed compared to the Hadley cell. The meridional and vertical wind velocities in both circulation cells were calculated by using the equations (5.6). Panel a) in Figure 5.2 shows the meridional component, while panel b) represents the vertical velocity.

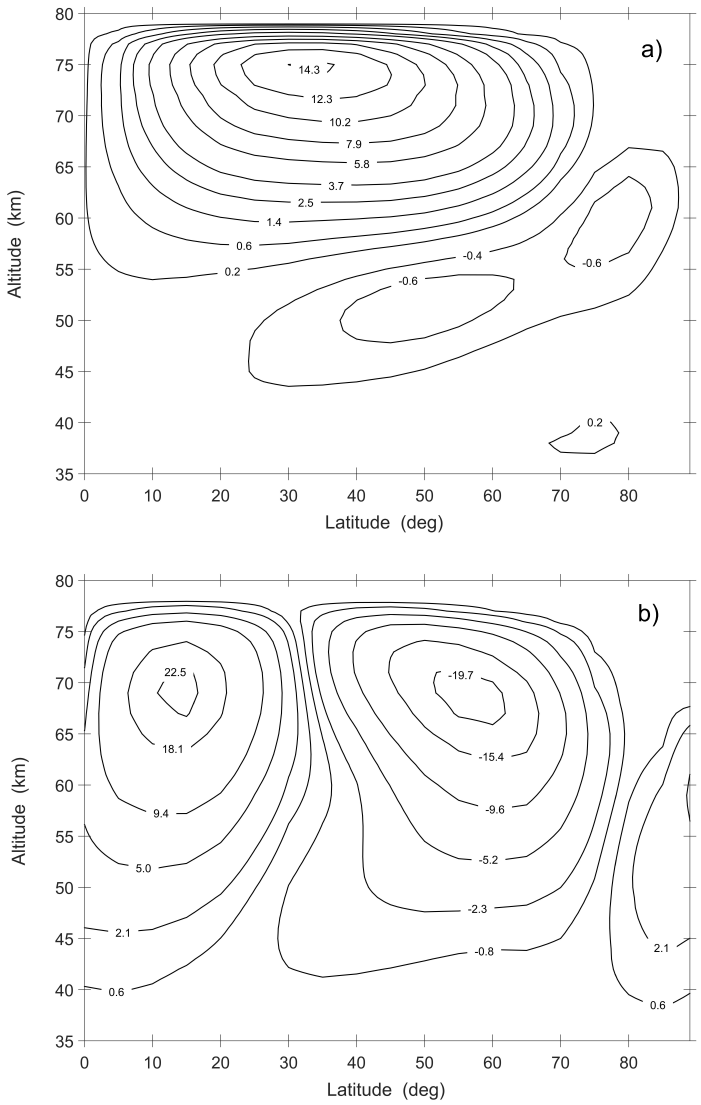

Figure 5.2: *a) Meridional and b) vertical wind velocities in the circulation cells shown in Figure 5.1. Positive values represent poleward/upward flow while equatorward/downward wind is represented by negative values. While meridional wind velocity values are in units of m/s, vertical velocity values are in units of mm/s.*

Highest meridional wind speeds of more than 14 m/s are visible around 75 km altitude at latitudes between 30° and 40°. This is in general agreement with observations. Poleward wind velocities at cloud top altitudes (65 - 75 km) were observed to vary between 10 and more than 30 m/s in the latitude range between 30° and 60° (e.g. *Sánchez-Lavega et al.*, 2008; *Hueso et al.*, 2012; *Gonçalves et al.*, 2020). In the present

model the characteristic time scale of the horizontal winds at these altitudes are in the order of 13 to 5 days. The meridional wind speed decreases with decreasing altitude which is a consequence of the increased atmospheric density. Values of less than 1 m/s can be found below about 60 km altitude with time scales in the order of 90 to 200 days. Meridional wind speeds associated with the polar cell don't exceed 1 m/s due to lower values of ψ compared to those of the Hadley cell.

In contrast to meridional wind velocities, the vertical wind speeds are in the order of mm/s. Highest values are visible at cloud top altitudes with upward and downward wind velocities of about 20 mm/s between 10° and 20° and between 50° and 60°, respectively. As previously stated for example by *Imamura and Hashimoto* (1998), vertical transport may play a crucial role in the formation process of the enhanced H_2SO_4(g) accumulation in the equatorial region below about 50 km altitude. Figure 5.2b) shows here upward wind velocities of 0.5 - 3.0 mm/s between 40 and 50 km altitude and values between 0.8 and 4 mm/s at polar latitudes. Observations of vertical winds at equatorial latitudes are missing. At the southern polar region, *Garate-Lopez et al.* (2013) derived upward wind speeds of 50 ± 10 mm/s around 63 km altitude from VIRTIS (section 3.1) measurements.

Diffusion

In addition to the mass transport by the Hadley and polar cells, the transport by diffusion is implemented in the model. In general, the diffusive transport can be divided into eddy and molecular diffusion. While eddy diffusion dominates below the homopause, molecular diffusion dominates above that altitude level (e.g. *Pater and Lissauer*, 2015). *Mahieux et al.* (2012) found that the homopause in Venus' atmosphere is located above 120 km altitude. This is far above the upper boundary of the present model, so that molecular diffusion can be neglected.

The diffusive mass flux per surface area is given by $\vec{F}_{\text{diff.},l} = -\underline{K} n_0 \vec{\nabla} \left(\frac{n_l}{n_0} \right)$, where $\underline{K}$ represents the tensor of the eddy diffusion and n_0 is the total number density of the atmosphere (e.g. *Prölss*, 2001). The temporal variation of the number density in a particular volume caused by the alteration of the diffusive flux is given by

$$\left(\frac{\partial n_l}{\partial t} \right)_{\text{diff.}} = -\vec{\nabla} \vec{F}_{\text{diff.},l} = \vec{\nabla} \left(\underline{K} n_0 \vec{\nabla} \left(\frac{n_l}{n_0} \right) \right) \tag{5.7}$$

and in zonally averaged geofluid coordinates as

$$\left(\frac{\partial n_l}{\partial t} \right)_{\text{diff.}} = \frac{1}{r^2 \cos\phi} \frac{\partial}{\partial \phi} \left(\cos\phi K_{yy} n_0 \frac{\partial}{\partial \phi} \left(\frac{n_l}{n_0} \right) \right) + \frac{\partial}{\partial h} \left(K_{zz} n_0 \frac{\partial}{\partial h} \left(\frac{n_l}{n_0} \right) \right). \tag{5.8}$$

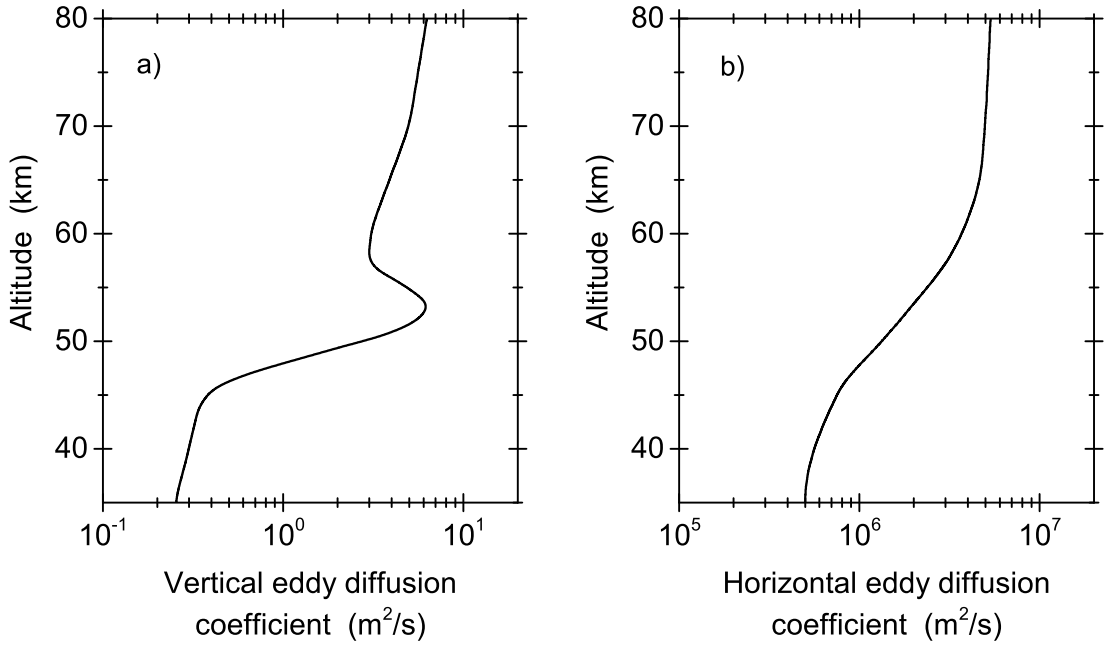

Figure 5.3: *Profiles of vertical and horizontal eddy diffusion coefficients used in the present model. No latitudinal variations were considered in the model. In order to simulate the convection layer located between about 50 and 60 km altitude, the values of K_{zz} were increased in this region.*

Only the diagonal elements K_{yy} and K_{zz} of the eddy diffusion tensor $\underline{K}$ are considered in the present model. Values of the vertical eddy diffusion K_{zz} were derived by *Woo and Ishimaru* (1981) as well as by *Woo et al.* (1982) from Pioneer Venus radio occultation measurements. Based on the assumption that observed intensity scintillations of radio waves were caused by turbulence which was generated by wind shear in thin atmospheric layers, they computed eddy diffusion values ranging between 0.2 and 4 m^2/s. *Hinson and Jenkins* (1995) as well as *Leroy and Ingersoll* (1996) showed, however, that intensity scintillations are most probably generated by freely propagating gravity waves, so that the eddy diffusion values derived by *Woo and Ishimaru* (1981) as well as by *Woo et al.* (1982) remain highly debatable. *Krasnopolsky* (2012) presented an altitude dependent eddy diffusion which ranges between 1 m^2/s at cloud base altitudes ($\sim$ 50 km) and about 10 m^2/s around 80 km. *Ando et al.* (2015) have estimated turbulent diffusion coefficient values (2.7 - 31 m^2/s) on the assumption that saturation of gravity waves occurs between 65 and 80 km altitude. In terrestrial atmospheres the horizontal eddy diffusion coefficient K_{yy} is expected to be larger than K_{zz} by several orders of magnitude (e.g. *Moore et al.*, 1954; *Shia et al.*, 1989; *Zellner*, 2011).

In the present model, profiles of K_{zz} and K_{yy} are chosen so as to agree with those used in previous models (e.g. *Imamura and Hashimoto*, 1998; *Krasnopolsky*, 2007, 2012). Figure 5.3 represents the corresponding eddy diffusion coefficient profiles used in all simulation runs. The increased values of K_{zz} in the altitude region between about 50 and 60 km simulate the convection layer located in this spatial region (cf. *Imamura and Hashimoto* (1998, 2001)). No latitudinal variation is implemented. The characteristic time of vertical (horizontal) diffusion increases from 90 - 60 (90 - 80) days between 65 and 75 km altitude to 3000 - 350 (560 - 300) days between 45 and 50 km altitude, respectively.

Sedimentation

Similar to the mass flux associated with the Hadley and polar circulation, that associated with sedimentation can be described by $\vec{F}_{\text{sed.},l} = n_l \cdot \vec{v}_{\text{sed.}}$. Since sedimentation occurs only in the vertical direction, the continuity equation reduces to

$$\left(\frac{\partial n_l}{\partial t}\right)_{\text{sed.}} = -\vec{\nabla}\vec{F}_{\text{sed.},l} = -\frac{\partial\left(v_{\text{sed.}} n_l\right)}{\partial h}. \tag{5.9}$$

The sedimentation velocity $v_{\text{sed.}}$ can be obtained from *Stokes' law*

$$v_{\text{sed.}} = \frac{2}{9}\frac{r_p^2 g\left(\rho_p - \rho_{\text{CO}_2}\right)}{\eta}, \tag{5.10}$$

where

r_p : Radius of the spherical particle in m (cf. table 2.1)

g : Gravitational acceleration in $\frac{\text{m}}{\text{s}^2}$

ρ_p : Density of the particle in $\frac{\text{kg}}{\text{m}^3}$

ρ_{CO_2} : Density of the background gas CO_2 in $\frac{\text{kg}}{\text{m}^3}$

η : Dynamical viscosity of CO_2 in $\frac{\text{kg}}{\text{ms}}$.

The gravitational acceleration g is adopted from VIRA, while the particle density of H_2SO_4 is set to $\rho_p = 2 \cdot 10^3 \ \frac{\text{kg}}{\text{m}^3}$. The density of the background gas CO_2 is derived from the ideal gas law

$$\rho_{\text{CO}_2} = \frac{p}{R_S T}, \tag{5.11}$$

where $R_S = 191.8 \frac{\text{J}}{\text{kgK}}$ is the averaged specific gas constant adopted from VIRA. The dynamical viscosity η of the background gas CO_2 is computed by using *Sutherland's*

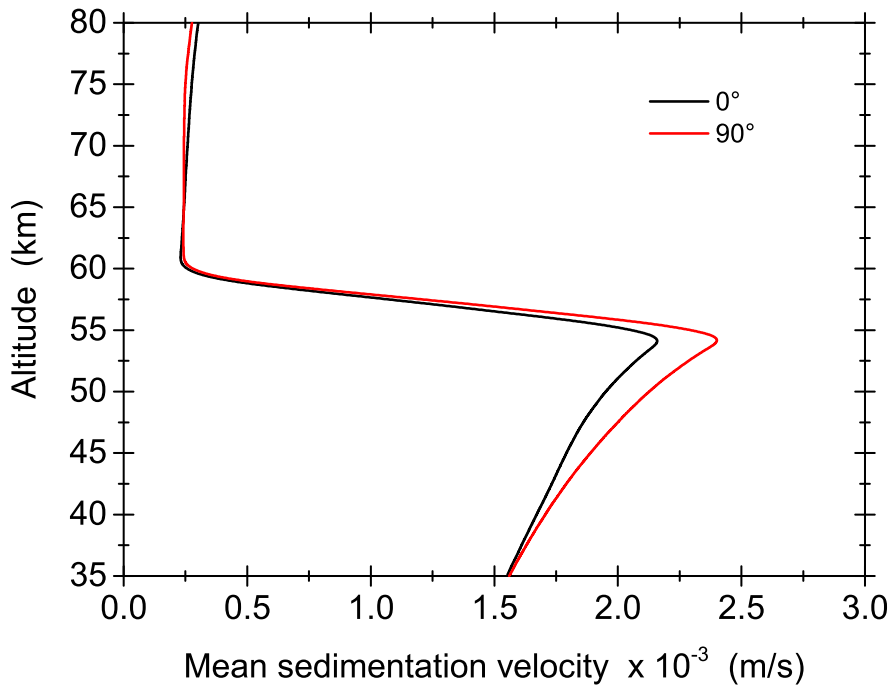

Figure 5.4: *Mean sedimentation velocity at equatorial and polar latitudes used in the model.*

model

$$\eta = \eta_0 \frac{T_0 + C}{T + C} \left(\frac{T}{T_0} \right)^{\frac{3}{2}}, \tag{5.12}$$

with $\eta_0 = 14.80 \cdot 10^{-6} \frac{\text{kg}}{\text{ms}}$, $T_0 = 293.15$ K and $C = 240$ K, where

η_0 : Reference viscosity at a reference temperature T_0
T_0 : Reference temperature
C : Sutherland constant.

The dynamical viscosity η may be considered as independent of the atmospheric pressure below values of approx. 10 bar, which corresponds to an altitude of approx. 30 km. Below this altitude the influence of the pressure on the viscosity can not be neglected and the uncertainty in equation (5.12) increases.

In the present model a mean sedimentation velocity shall be applied. The diameter of the particles is adopted from table 2.1. Here, the presence of Mode 2 and Mode 3 particles will be extended to altitudes below the lower cloud boundary (< 47.5 km). Figure 5.4 shows the mean sedimentation velocity at equatorial and polar latitudes.

The lowest velocities can be found in the upper cloud region, which is a consequence of missing Mode 3 particles at these altitudes. The characteristic time of sedimentation at these altitudes is in the order of 150 to 300 days. This is in contrast to the altitude region below about 60 km, where the sedimentation velocity is dominated by the Mode 3 particles. Here, the sedimentation time is in the order of 40 to 70 days. The small difference in the velocity values below 60 km altitude is a consequence of the latitudinal temperature variation, which mainly affects the viscosity of the background gas (cf. equation 5.12).

Condensation and evaporation

Sulfuric acid is believed to be produced in a thin layer around 66 km altitude (e.g. *Krasnopolsky*, 2012). The corresponding main chemical reaction is described by equation (2.1). Due to the low saturation vapor pressures of H_2SO_4 and H_2O at these altitudes, both gas species condensate into H_2SO_4-H_2O droplets. The saturation vapor pressure of H_2SO_4 and that of H_2O can be determined from the ambient temperature T and the concentration of the H_2SO_4-H_2O solution (*Ayers et al.*, 1980; *Kulmala and Laaksonen*, 1990; *Krasnopolsky and Pollack*, 1994)

$$\begin{aligned} \ln p^{\mathrm{sat}}_{\mathrm{H_2SO_4}}(T,x) &= 16.259 - \frac{10156}{T} + 7.42\left(1 + \ln\frac{T_0}{T} - \frac{T_0}{T}\right) \\ &\quad + \frac{\mu^*_{\mathrm{H_2SO_4}}(T,x) - \mu^*_{\mathrm{H_2SO_4}}(T,1)}{RT}, \\ \ln p^{\mathrm{sat}}_{\mathrm{H_2O}}(T,x) &= \ln p^{\mathrm{sat}}_{\mathrm{H_2O}}(T,0) \\ &\quad + \frac{\mu^*_{\mathrm{H_2O}}(T,x) - \mu^*_{\mathrm{H_2O}}(T,0)}{RT}. \end{aligned} \tag{5.13}$$

where $T_0 = 385$ K, μ^* represents the chemical potential in the H_2SO_4-H_2O solution, $R = 8.31441$ J/mol·K is the gas constant and x is the mole fraction of H_2SO_4. Values of the ratio μ^*/RT are provided by *Zeleznik* (1991) for the temperature range between 200 and 350 K. Those were linearly extrapolated to lower and higher temperatures which are present in the upper and lower atmosphere, respectively. The approximation of the saturation vapor pressure of pure water $p^{\mathrm{sat}}_{\mathrm{H_2O}}(T,0)$ was adopted from *Wagner and Pruß* (2002) as well as from *Smithsonian* (2015).

The decreasing temperature with increasing altitude reduces the saturation vapor pressure of both species, so that only small amounts of the gaseous part can be found at higher altitudes (cf section 2.2) while the bulk of the species condensate into droplets. It is assumed that mode 1 particles (cf. table 2.1), which are believed to consist of elemental sulfur, may serve as condensation nuclei (e.g. *James et al.*, 1997). The above

presented dynamical processes transport the H_2SO_4-H_2O droplets to lower altitudes where they evaporate due to higher temperatures. The abundance of gaseous sulfuric acid and that of water vapor increases therefore below about 50 km altitude (cf. Figure 2.3; Figures 4.2 - 4.5). In particular sulfuric acid vapor forms a haze layer below the main cloud deck whose topside is often saturated/supersaturated (cf. Figures 4.2.c) and 4.5.c)).

Mass balance equation

Along with the production P and loss L processes of H_2SO_4 and H_2O (cf. equations (2.1), (2.2), (2.3)), the above presented transport processes in Venus' atmosphere can be summarized into the following mass balance equation

$$\left(\frac{\partial n_l}{\partial t}\right) = P_l - L_l + \left(\frac{\partial n_l}{\partial t}\right)_{\text{circ.}} + \left(\frac{\partial n_l}{\partial t}\right)_{\text{diff.}} + \left(\frac{\partial n_l}{\partial t}\right)_{\text{sed.}} . \tag{5.14}$$

5.2 Numerical solution

For each time step of the numerical simulation procedure, the calculations of the mass transport are decoupled from the production and loss calculations. Similarly, the calculation of saturation and condensation of the gas species are calculated separately.

Mass transport

A various number of methods exists for the numerical solution of the transport term of the mass balance equation. The following one is mainly based on the methods provided by *Rausch et al.* (2002), *Haußer and Luchko* (2011) as well as by *Gerya* (2019).

The transport term of equation (5.14) is solved by discretizing the equation on an equidistant grid consisting of latitudes ϕ_i and altitudes h_j using the time discretization t_k, with

$$\begin{aligned} \phi_i &= i\Delta\phi \quad ; i = 0, ..., m_\phi + 1 \quad ; m_\phi \Delta\phi = L \\ h_j &= j\Delta h \quad ; j = 0, ..., m_h + 1 \quad ; m_h \Delta h = Z \\ t_k &= k\Delta t \quad ; k = 0, ..., m_t \qquad ; m_t \Delta t = T. \end{aligned} \tag{5.15}$$

Here, $\Delta\phi$, Δh and Δt are the horizontal, vertical and temporal resolutions, respectively, with the latitudinal and vertical ranges $L = [0°, 90°]$ and $Z = [35$ km, 80 km$]$. The temporal range is [0,T].

The transport term of equation (5.14) shall be solved by using the implicit Euler method, where the spatial derivatives are computed at the times $t = t_{k+1}$. This is in contrast to the explicit method, where the spatial derivatives are computed at the times $t = t_k$. The computational effort of the implicit method is therefore higher than that of the explicit method. However, the first mentioned method is stable for any temporal resolutions, so that Δt can be arbitrary increased without affecting the stability.

The derivatives in equation (5.14) are approximated by difference quotients (finite-difference method). According to the direction of the mass flow, either the left or the right difference quotient is used to approximate the spatial derivatives. Arising numerical uncertainties are corrected by using the method presented by *Smolarkiewicz* (1983, 1984); *Smolarkiewicz and Clark* (1986); *Smolarkiewicz and Grabowski* (1990).

Substituting the temporal and spatial derivatives in equation (5.14) by difference quotients leads to the following linear equation

$$n_{i,j}^{k} = C_1 n_{i,j}^{k+1} + C_2 n_{i-1,j}^{k+1} + C_3 n_{i+1,j}^{k+1} + C_4 n_{i,j-1}^{k+1} + C_5 n_{i,j+1}^{k+1}, \tag{5.16}$$

with $i = 1, ..., m_\phi$, $j = 1, ..., m_h$ and $k = 1, ..., m_t$. The coefficient C_1 represents the meridional and vertical mass outflow from the cell (i, j). The meridional and vertical mass inflow is described by the coefficients C_2 and C_3 as well as by C_4 and C_5, respectively. It must be mentioned that the transport parameters of the cell (i, j) are used for the mass outflow calculations while those of the neighboring cells are used for the mass inflow calculations. Analytical expressions for $C_1, ..., C_5$ can be found in Appendix C for different cases of the wind direction. The number density $n = n(\phi_i, h_j, t_k)$ is represented by

$$n_{i,j}^{k} = n\left(\phi_i, h_j, t_k\right). \tag{5.17}$$

Rewriting equation (5.16) into matrix notation yields

$$AN^{k+1} = B^k \tag{5.18}$$

where vector B contains the known number densities $n_{i,j}^{k}$ while vector N contains the unknowns $n_{i,j}^{k+1}$. The coefficients $C_1, ..., C_5$ form the sparse matrix A.

The system of linear equations presented in equation (5.18) is solved for $k = 1, ..., m_t$ with the initial and boundary conditions

$$\begin{aligned} n_{i,j}^{0} &= n\left(\phi_i, h_j, t_0\right) \\ n_{0,j}^{k} &= n\left(\phi_0, h_j, t_k\right) \\ n_{m_\phi+1,j}^{k} &= n\left(\phi_{m_\phi+1}, h_j, t_k\right) \\ n_{i,0}^{k} &= n\left(\phi_i, h_0, t_k\right) \\ n_{i,m_h+1}^{k} &= n\left(\phi_i, h_{m_h+1}, t_k\right). \end{aligned} \tag{5.19}$$

While the initial conditions for sulfuric acid and those for liquid water are set to $n^0_{i,j} = 0$, $\forall i \in L, \forall j \in Z$, those for water vapor are given by its saturation vapor abundance between 30 and 80 km altitude. The boundary conditions are set to

$$\frac{\partial n^k_l}{\partial z} = 0, \qquad \frac{\partial n^k_l}{\partial \phi} = 0. \tag{5.20}$$

An exception is the lower boundary for water vapor. Here is $q^k_{i,j} = 30$ ppm, $\forall i \in L, \forall j \in Z, \forall k \in$ [0,T], owing to a possible source of H_2O in the deep atmosphere and the observed constant number mixing ratio q (cf. section 2.2).

Chemical kinetics

The implementation of the H_2SO_4 production and H_2O loss processes in Venus' upper clouds is adopted from *Imamura and Hashimoto* (1998). They used an analytical expression of the form

$$P_{H_2SO_4}(\phi, z) = \Phi_{H_2SO_4}(\phi) f(z) \cos\phi, \tag{5.21}$$

where $\Phi_{H_2SO_4}(\phi)$ represents the column integrated production rate of H_2SO_4(g). Here, it is set to 10^{16} $m^{-2}s^{-1}$ which is in accordance with one-dimensional photochemical models (cf. section 2.2). The production rate is weighted by a Gaussian probability function $f(z)$. In the present model the latter is centered at 66 km altitude, which is believed to be the altitude of the highest H_2SO_4(g) production (cf. section 2.2). This is different to the model presented by *Imamura and Hashimoto* (1998) who centered $f(z)$ at 62 km altitude. The influence of the solar zenith angle on the production $P_{H_2SO_4}(\phi, z)$ is approximated by the cosine of the planetary latitude ϕ. The production rate of H_2SO_4(g) is assumed to be the loss rate of H_2O(g) at these altitudes ($P_{H_2SO_4}(\phi, z) = L_{H_2O}(\phi, z)$).

The loss of H_2SO_4(g) is calculated using the chemical reaction equation (2.2), which describes the decomposition of H_2SO_4(g) into H_2O(g) and SO_3. This process is reversible, leading to a loss of H_2O(g) and production of H_2SO_4(g). Obviously, the production of sulfuric acid vapor via the reversed reaction (2.2) depends on the H_2O and SO_3 abundances. A decay of the abundances would therefore reduce the production of H_2SO_4(g). While loss processes of water other than that via the reversed reaction (2.2) are neglected, the decomposition of SO_3 can be significant and may therefore reduce the production of H_2SO_4(g). In order to take this into account, *Imamura and Hashimoto* (1998) calculated the number density of SO_3 from that of H_2SO_4(g) and H_2O(g) using the equilibrium constant provided by *Barin and Sauert* (1989) as well as by *Krasnopolsky and Pollack* (1994). In contrast to this, in the present model Venus

Express observations of CO and OCS (cf. section 2.2) as well as their latitudinal variations are used to calculate the decomposition of SO_3 via the reaction equations (2.3).

The kinetic equations (2.2) and (2.3) form the following system of ordinary differential equations

$$\begin{aligned}
\frac{dn_{H_2SO_4}}{dt} &= -k_1 \cdot n_{H_2SO_4} \cdot n_{H_2O} + k_2 \cdot n_{SO_3} \cdot n_{H_2O} \cdot n_{H_2O} \\
\frac{dn_{H_2O}}{dt} &= -k_2 \cdot n_{SO_3} \cdot n_{H_2O} \cdot n_{H_2O} + k_1 \cdot n_{H_2SO_4} \cdot n_{H_2O} \\
\frac{dn_{SO_3}}{dt} &= -k_3 \cdot n_{SO_3} \cdot n_{CO} - k_4 \cdot n_{SO_3} \cdot n_{OCS} + k_1 \cdot n_{H_2SO_4} \cdot n_{H_2O}
\end{aligned} \tag{5.22}$$

with the reaction rate coefficients $k_1 = 7 \cdot 10^{-14} \mathrm{e}^{-5170/T}$, $k_2 = 2.3 \cdot 10^{-43} T \mathrm{e}^{-6540/T}$, $k_3 = 10^{-11} \mathrm{e}^{-13000/T}$, $k_4 = 10^{-11} \mathrm{e}^{-10000/T}$. Those are adopted from *Krasnopolsky* (2007) and *Zhang et al.* (2012).

The system of equations (5.22) is solved by using the ordinary differential equations (ODE) toolbox of the MATLAB software. MATLAB solvers for ODE's are provided for stiff and non-stiff problems. While various mathematical definitions for stiffness of ODE's can be found for example in *Lambert* (1997) as well as in *Hairer and Wanner* (2010), a presentation of the MATLAB ODE solvers is given for example by *Shampine and Reichelt* (1997). It turned out, that for the system of equations (5.22) most of the solvers provide similar results, however, differing in computational time. Solvers for stiff problems revealed a faster performance than those for non-stiff problems. The first mentioned solvers are therefore used in the present model.

Condensation/Evaporation

Similar to the implementation of the H_2SO_4(g) production in the upper cloud region, the implementation of the condensation and evaporation processes into the model is adopted from *Imamura and Hashimoto* (1998). While in the upper cloud region sulfuric acid and water vapor condensate into H_2SO_4-H_2O droplets, they evaporate at lower altitudes due to the high temperatures. Assuming thermochemical equilibrium between n_l^{gas} and n_l^{liq}, the fraction of gaseous and liquid components is computed from the saturation vapor pressure of both gases $p^{\mathrm{sat}}_{H_2SO_4}(T,x)$ and $p^{\mathrm{sat}}_{H_2O}(T,x)$ (cf. equation (5.13)) as well as from the ideal gas law $p_l^{\mathrm{sat}}(T,x) = n_l^{\mathrm{gas}} k_B T$. Here, $k_B = 1.381 \cdot 10^{-23}$J/K is the Boltzmann constant. Condensation occurs for the fraction of the number density with $n_l^{\mathrm{tot}} = n_l^{\mathrm{gas}} + n_l^{\mathrm{liq}} > {}^{p_l^{\mathrm{sat}}(T,x)}/_{k_B T}$. Consequently, the fraction of the number density with $n_l^{\mathrm{tot}} \leq {}^{p_l^{\mathrm{sat}}(T,x)}/_{k_B T}$ remains in the gaseous phase.

Chapter 6

Attenuation of Venus Express radio signals and comparison of closed-loop with open loop data

The following chapter presents the observed attenuation of VeRa's radio signals during the occultation measurements. A short comparison between CL and OL data is given in section 6.1. Section 6.2 shows the contribution of refractive defocussing to the total signal decrease while section 6.3 presents the effect of mispointing of the spacecraft antenna on the signal level. The results shown in the sections 6.2 and 6.3 are based on OL data.

6.1 Comparison of closed-loop with open loop data

As described in section 3.2.1, the advantage of the OL recording technique over the CL technique lies in the possibility of post-recording analysis of the radio signals. By applying digital signal processing tools, this possibility allows to determine the frequency and amplitude of the signals even when Venus' deep atmosphere was sounded. Due to attenuation effects at these altitudes, the SNR values (cf. equation 4.2) were too low and the signal dynamics (dB/sec; Hz/sec) were too high for the CL receiver to track the incoming RF carrier signals.

As an example Figure 6.1 shows the signal power of VeRa's X-band radio signal obtained from CL recordings (green) as well as determined from OL recordings (blue). The decrease of the signal power is visible in both data beginning approx. 180 seconds after the start of the measurement. The CL receiver, which was able to track the incoming signal for the next 230 seconds, lost lock to the signal about 410 seconds after beginning of the measurement (*ingress*). This corresponds to a sounded altitude

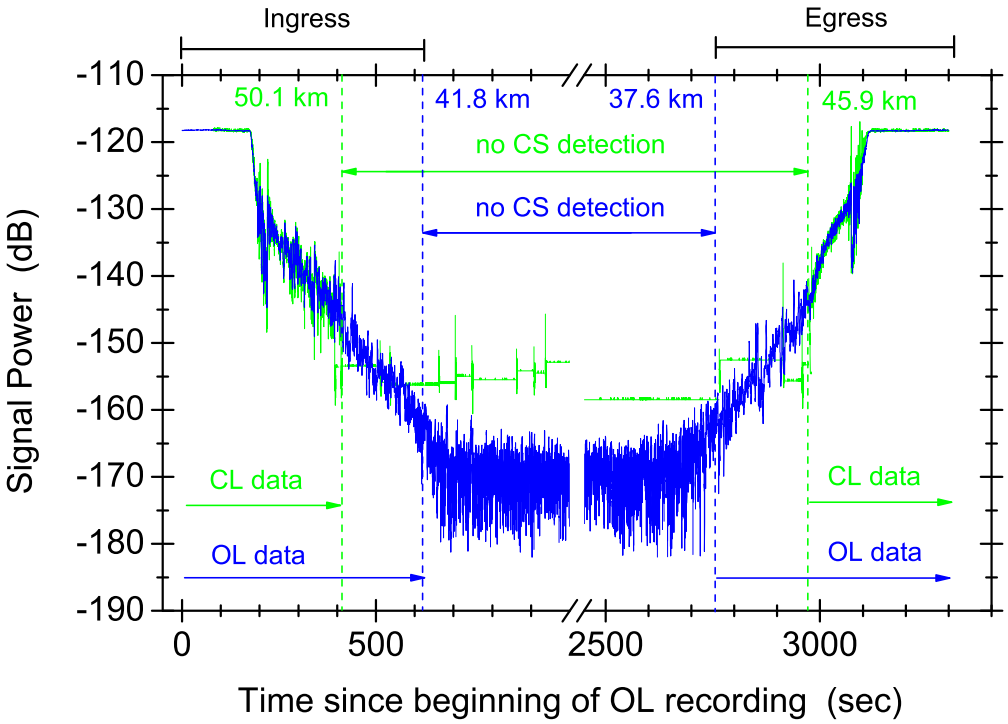

Figure 6.1: *Observed decrease of VeRa's X-band radio signal obtained from CL recordings (green) as well as determined from OL recordings (blue) as a function of time. Please note the break between 900 and 2500 seconds. Radio ray parameters and atmospheric profiles were derived from the ingress and egress part of the measurement when a clear carrier signal (CS) could be detected, either by the CL receiver at the G/S on Earth or by the FFT based algorithm applied to the OL recordings.*

of about 50.1 km. In contrast to this, by applying the FFT based algorithm to the OL recordings as outlined in section 3.2 it was possible to detect a clear carrier signal (CS) when Venus' atmosphere was sounded to altitudes as deep as 41.8 km. In the following time interval the spacecraft was completely behind Venus so that no carrier signal reached the G/S on Earth. A clear carrier signal could be detected in the OL recordings around 2750 seconds after the start of the measurement. The radio signal traversed Venus' atmosphere at an altitude of 37.6 km. The CL receiver was able to lock to the incoming radio signal only approx. 490 seconds later when the altitude of 45.9 km was sounded.

The measurement presented in Figure 6.1 is a typical example that illustrates the advantage of OL over CL data. The lower altitudes of Venus' atmosphere can only be analyzed when OL recordings are used. Figure 6.2 shows the deepest resolved altitudes

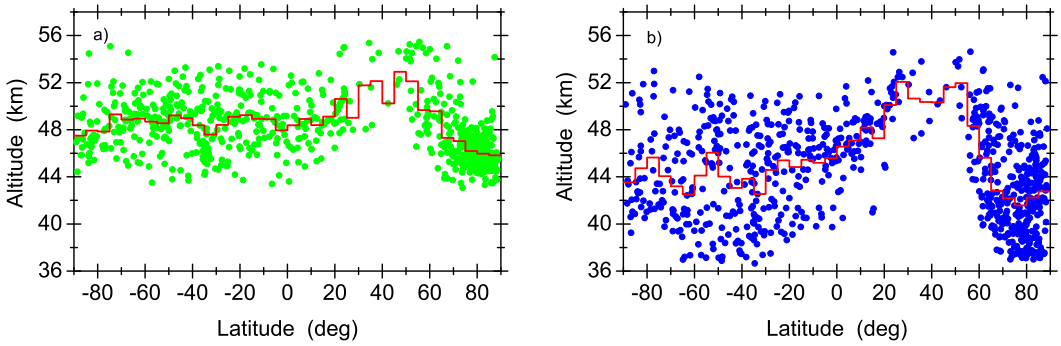

Figure 6.2: *Deepest altitudes in Venus atmospheric profiles achieved from VeRa's X-band CL data (panel a) and OL data (panel b) as a function of the latitude. The red profiles show the mean altitude in latitudinal bins of 5° each.*

in atmospheric profiles derived from VeRa's X-band CL (panel a)) and OL data (panel b)) as a function of the planetary latitude.

The deepest altitudes obtained from the CL recordings are obviously located in the altitude range between about 44 and 52 km with a mean altitude around 49 km. An exception to this is the northern polar region, where most of the values can be found in a narrower range between 44 and 48 km altitude. Here, the mean values are located around 45 km altitude. Due to the orbit geometry of Venus Express the northern mid latitudes reveal a poor coverage. Only a small number of atmospheric profiles are obtained from this region whose deepest altitudes are located mainly above 49 km.

In contrast to this, the range of the deepest altitudes in OL atmospheric profiles is much larger. The deepest altitudes can be found right above 36 km, which are achieved at southern mid and northern polar latitudes. Mean altitude values of about 44 km are obtained at the southern hemisphere and 43 km at the northern polar region.

The upper boundary of the altitude distribution is located around 52 km in both, CL and OL profiles. Those short atmospheric profiles result from the orbit geometry of Venus Express rather than attenuation effects in Venus' atmosphere. The lowered altitude values at the northern polar region must also be attributed to the spacecrafts orbit geometry. The spacecraft to Venus distance was smallest when these latitudes were sounded (see section 6.2). Therefore, the resulting signal decrease due to refractive defocussing was small compared to that at the southern latitudes (cf. Figure 6.4) leading to enhanced SNR values of the received radio signals.

Figure 6.2 shows that VeRa's OL data are well suited to study latitudinal variations of atmospheric parameters in the lower Venus atmosphere to altitudes as deep as 40 km. For the present study VeRa's OL data were used. CL recordings were only used in case no OL data were available.

6.2 Refractive defocussing

Due to the radial gradient of the refractivity in the atmosphere of Venus the radio beam was spread in the plane of refraction (defocussing) and compressed in the perpendicular plane (focussing). For Venus Express measurements, both effects are described by the equations (4.6) and (4.7), respectively. The effect of defocussing is much larger than the focussing effect and the net effect is called refractive defocussing. According to equation (3.9), it is identical for both, the S- and X-band radio signals.

The green profiles in the left and right panels of Figure 6.3 show the contribution of refractive defocussing to the total observed attenuation of the X-band radio signal

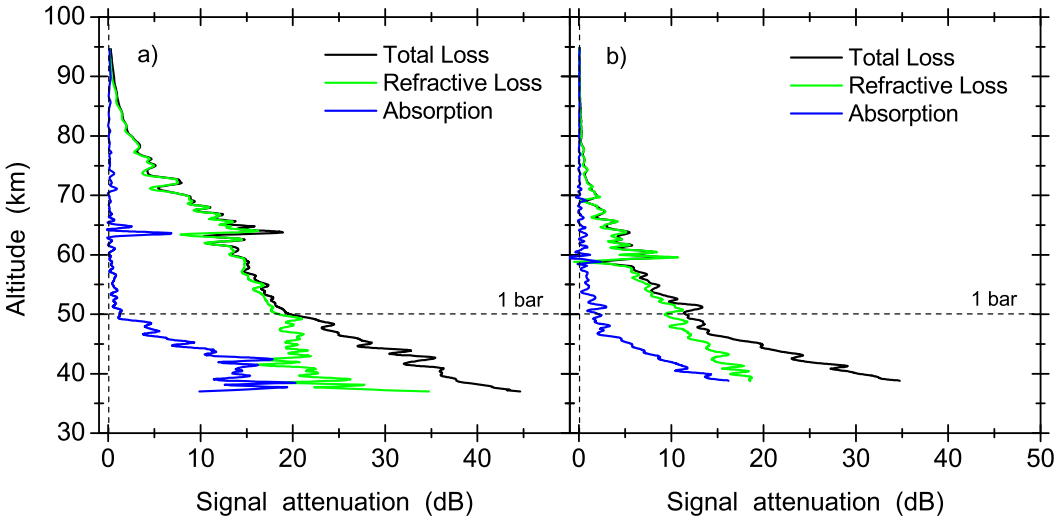

Figure 6.3: *Attenuation of the X-band radio signal observed in two radio occultation measurements. Left: Ingress measurement conducted on 2006-08-11 at the southern mid-latitudes (52.70° S) (distance of VEX to center of Venus approx. 18535 km); Right: Ingress measurement conducted on 2007-01-03 at the northern polar latitudes (83.27° N) (distance of VEX to center of Venus approx. 8647 km). The green profile shows the contribution of refractive defocussing to the total signal attenuation (black). The blue profile presents the absorption of the signal in Venus' atmosphere. The horizontal dashed line shows the approximate altitude of the 1 bar pressure level.*

(black) as a function of the sounded altitude. While Figure 6.3.a) shows the southern mid-latitudinal region (52.70°S), Figure 6.3.b) presents the northern polar region (83.27°N). It is clearly visible that significant attenuation of the radio signals begins below approximately 100 km altitude. Refractive defocussing is the main attenuation factor. Values of more than 20 dB at the mid-latitudes and more than 15 dB at the polar latitudes are reached around 40 km altitude.

The difference of about 5 dB between the signal loss at the southern mid- and northern polar latitudes is a consequence of the distance between Venus Express and Venus. Due to the orbit geometry of VEX, the southern hemisphere was sounded from a further distance compared to the northern latitudes leading to a larger amount of refractive defocussing (cf. equation 4.8). The geometry was kept for the entire Venus Express mission so that the observed signal strength at the ground station was constantly weaker when Venus' southern polar latitudes were sounded.

The upper panel of Figure 6.4 shows the distance of VEX to the center of Venus as a function of the planetary latitude during the radio occultation measurements between the years 2006 and 2014. It is clearly visible that the VEX-Venus distance was largest at the southern collar/polar latitudes varying between 13000 and 22000 km. Highest values are reached around 70°S. The distance decreased northward reaching smallest values of less than 10000 km at the northern polar latitudes. The lower panel of Figure 6.4 shows the resulting contribution of refractive defocussing to the total signal loss between 40 and 80 km altitude as a function of the latitude. Here, the southern and northern hemispheres were subdivided into equal latitudinal bins of 5°. Measurements located within each bin were averaged to one refractive defocussing profile. No measurements are available in the northern mid-latitudinal region between about 20°N and 60°N below approx. 50 km altitude due to the orbit geometry of Venus Express.

It is obvious, that the contribution of refractive defocussing to the total signal loss was highest at the southern hemisphere. Maximal values of almost 25 dB are visible poleward of 40°S around 40 km altitude. The values decreased constantly as the sounded altitude moved to the northern latitudes. Maximal values of about 18 dB were reached at the northern polar region. In contrast to the southern polar region, the refractive defocussing contribution northward of 60 °N remained almost constant below about 45 km altitude. Here, lowest VEX-Venus distances of sometimes less than 6250 km were reached. The difference of refractive defocussing values between the southern and northern polar latitudes decreases with increasing altitude. While a difference of almost 7 dB is visible around 40 km altitude, values of less than 4 dB can be seen at cloud top altitudes.

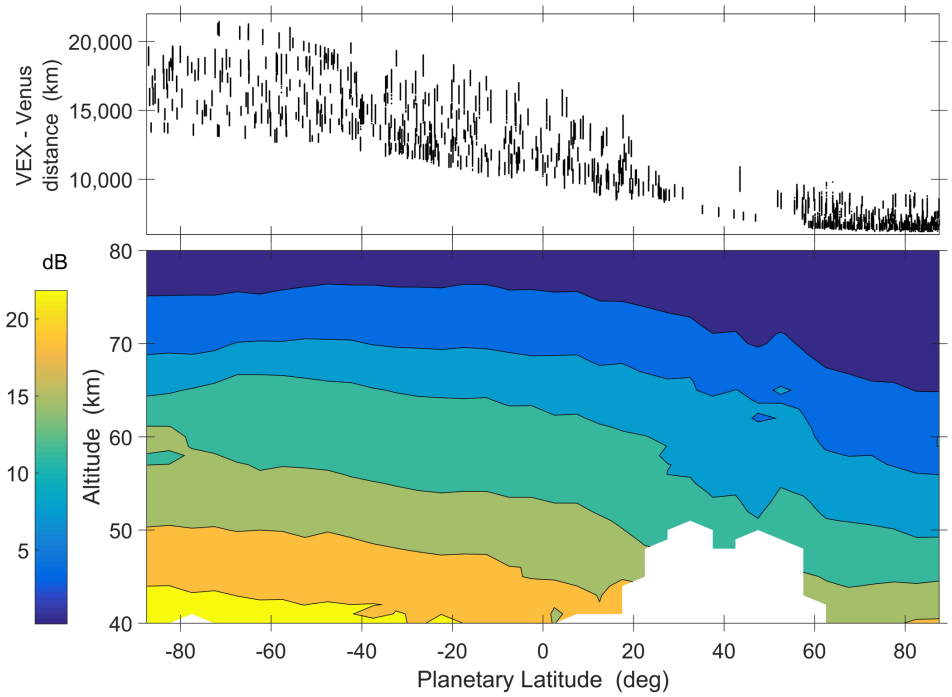

Figure 6.4: *Upper panel: Distance of Venus Express to the center of Venus while sounding the altitude region between 40 and 80 km at the southern and northern hemisphere. Lower panel: Contribution of the refractive loss to the observed attenuation of the X-Band radio signal between 40 and 80 km altitude at the southern and northern hemisphere. The hemispheres were subdivided into equal latitudinal bins of 5° each. Measurements located within each bin were averaged to one profile. No measurements are available in the northern mid-latitudinal region between about 20 and 60°N below 50 km altitude due to the orbit geometry of Venus Express.*

The decreased values of refractive defocussing at the northern polar latitudes, supported by the small VEX-Venus distances, led to enhanced SNR values of the received radio signals compared to those obtained from the southern polar region. This explains why the deepest altitudes of CL and OL atmospheric profiles, presented in Figure 6.2, can be found in northern polar measurements.

6.3 Mispointing

Venus Express used the main High Gain Antenna 1 (HGA1) for the majority of the radio occultation measurements. It had a half power beam width value of $\vartheta_{3\mathrm{dB}}^{\mathrm{X\text{-}band}} \approx 1.6°$ at X-Band and $\vartheta_{3\mathrm{dB}}^{\mathrm{S\text{-}band}} \approx 6°$ at S-band (cf. Table 3.1). The bending angle of the ra-

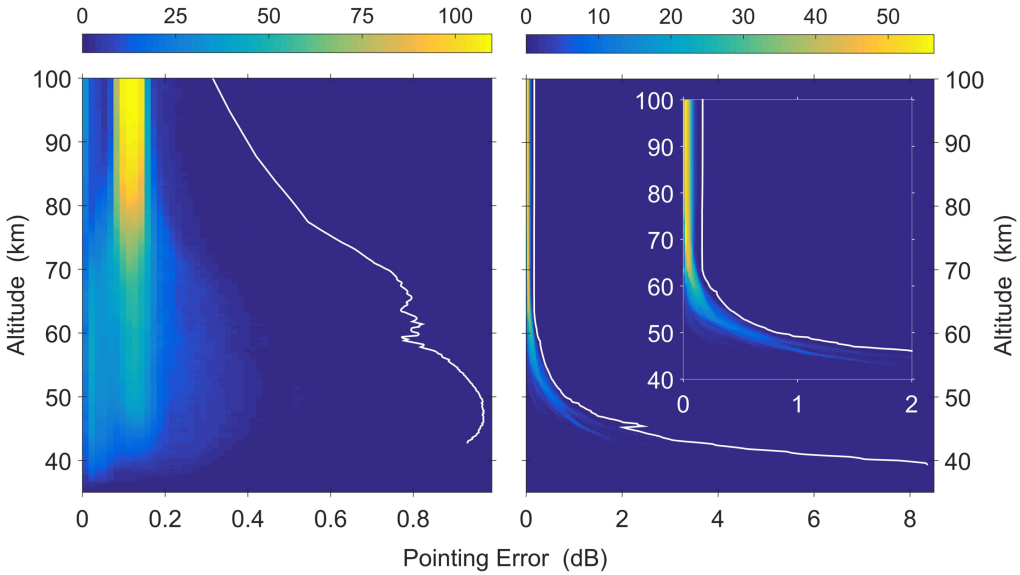

Figure 6.5: *The effect of pointing inaccuracies on Venus Express' X-Band radio signals occurred during the occultation measurements between the years 2006 and 2013 as a function of sounded altitude (left panel: HGA1; right panel: HGA2). The horizontal axes were subdivided into equal bins of 0.015 dB each and measurements located within each bin were counted. The color code gives the number of measurements located within each bin. The white profiles represent maximal pointing inaccuracies occurred between 2006 and 2014. The smaller image section in the right panel shows the zoomed area of the HGA2 pointing errors in the range from 0 to 2 dB between 40 and 100 km altitude.*

dio signals in Venus' deep atmosphere exceeds the values of $\vartheta_{3\mathrm{dB}}/2$. A severe signal decrease would be caused by refraction if the measurements were carried out in the Earth pointing mode. In order to counteract the refraction of the radio rays, predetermined limb tracking maneuvers were performed during the measurements. This way, the antenna boresight was oriented toward the refracted ray path from the spacecraft to the tracking station on earth (R1 and R2 in Figure 3.2). Uncertainties in the slew maneuvers caused a degradation of the signal amplitude which, however, turned out to be small in most measurements.

The left panel in Figure 6.5 shows the effect of mispointing on the X-band radio signals during measurements carried out with the HGA1 between the years 2006 and 2013. The horizontal axes were subdivided into equal bins of 0.015 dB each and measurements located within each bin were counted. The color code gives the number of measurements located within each bin. The white profile represents maximal pointing inaccuracy values observed during the entire Venus Express mission.

It can be clearly seen that most of the measurements reveal a pointing error of 0.1 to 0.2 dB between about 75 and 100 km altitude. The range increases to values located between less than 0.1 and 0.4 dB below 75 km altitude. Pointing inaccuracies exceeding 0.4 dB were found for a small number of measurements, only, showing maximal values of almost 0.9 dB below 50 km altitude (white line). The moderately increased pointing errors within the cloud and sub-cloud region are most probably a consequence of uncertainties in the model atmosphere at these altitudes. Although uncertainties in the performance of the spacecraft slew maneuvers can not be excluded, their contributions are expected to be insignificant.

The effect of pointing inaccuracies on the S-Band radio signals during measurements in the year 2006 are one order of magnitude smaller than those on the X-band signals. The pointing errors didn't exceed 0.1 dB. A graphical representation can be found in the appendix D.

In contrast to the HGA1, no limb tracking maneuvers were performed when the smaller High Gain Antenna 2 (HGA2) was used during quadrature (time periods during which the Sun-spacecraft-Earth angle is between 75 and 95 degrees). It was used in the years 2007, 2012, 2013 and 2014 providing a total number of 250 measurements. The antenna boresight was constantly oriented toward the Earth line of sight (R3 in Figure 3.2). As a consequence, the pointing error is almost identical to the bending angle. The right panel in Figure 6.5 shows the effect of the HGA2 pointing errors on the X-Band radio signals as a function of the sounded altitude between 35 and 100 km. As was expected the effect of the pointing errors increases with decreasing altitude reaching approx. 1 dB around 50 km and more than 2 dB around 45 km altitude. For a few deep occultation measurements the pointing error exceeded 8 dB below 40 km altitude (white line). Although the half power beam width value of $\vartheta_{3\mathrm{dB}}^{\text{X-band}} \approx 8^\circ$ was large compared to that of the HGA1, an enhanced degradation of the signal power due to the mispointing could not be avoided. The bending of the radio ray exceeded the value of $\vartheta_{3\mathrm{dB}}/2 \approx 4^\circ$ between 40 and 45 km altitude so that the power of the received radio signal was reduced by more than 3 dB when these altitudes were sounded.

Measurements carried out with the HGA2 needed to be corrected for the arose pointing errors. This way the observed residual signal decrease could be unambiguously attributed to atmospheric absorption and an overestimation of the derived H_2SO_4(g) abundance could be avoided. Figure 6.6 illustrates the impact of pointing errors on the derived sulfuric acid vapor abundance.

While the upper panels show a measurement carried out with the HGA1, the lower panels represent a measurement with the HGA2. The pointing errors are depicted in

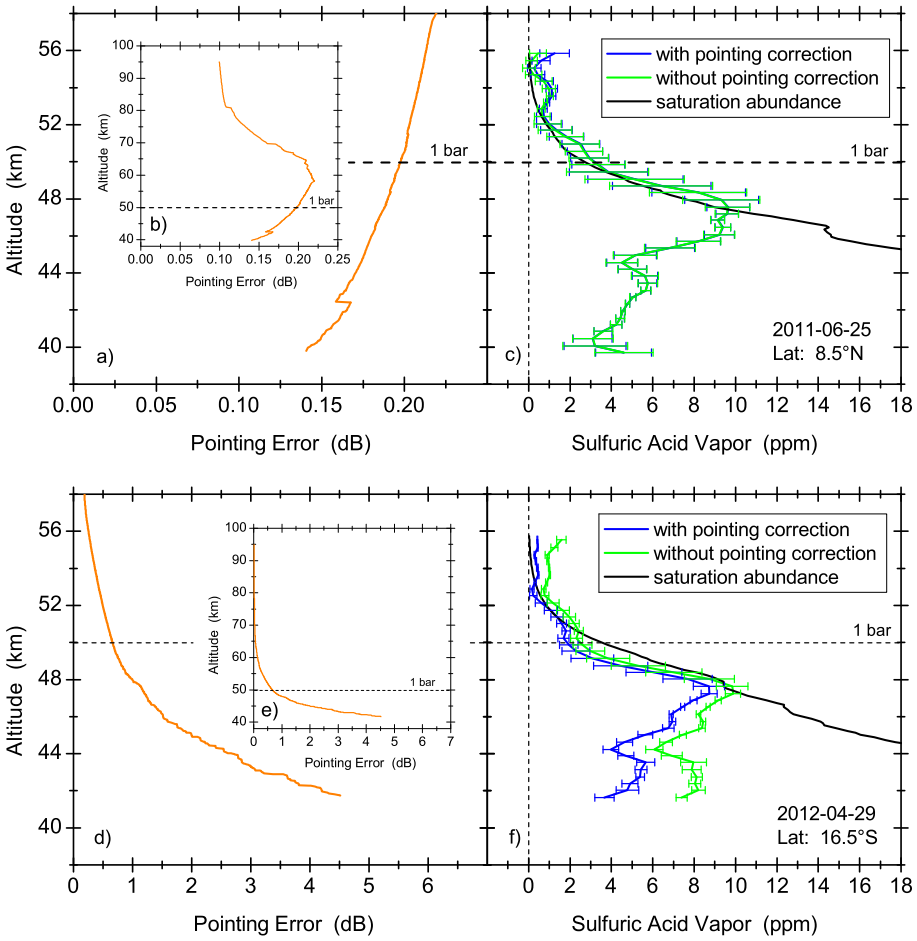

Figure 6.6: *Impact of pointing errors of the HGA1 (panel a) and b)) and HGA2 (panel d) and e)) on the derived $H_2SO_4(g)$ abundance visible in the panels c) and f), respectively. The saturation vapor abundance was computed by using equation (5.13).*

the panels a) and b) as well as d) and e) for the HGA1 and HGA2, respectively. The HGA1 shows the largest mispointing values of more than 0.2 dB between 55 and 60 km decreasing with altitude. The overall small pointing inaccuracy barely affects the derived $H_2SO_4(g)$ profiles visible in panel c). In contrast to this, the increasing pointing error of the HGA2 from less than 1 dB above 48 km altitude to maximal values of approx. 4.5 dB around 42 km altitude would lead to a significant overestimation of the derived $H_2SO_4(g)$ abundance if a correction wouldn't be made. While the overestimation remains constant with a value of less than 1 ppm above 49 km altitude, it monotonically increases from 1 ppm at 49 km altitude to approx. 4 ppm around 42 km.

The example visible in the lower panels of Figure 6.6 shows that the contribution of the antenna mispointing may have a large influence on the H_2SO_4(g) profiles. All H_2SO_4(g) profiles derived from VeRa's CL and OL data between the years 2006 and 2014 were therefore corrected for pointing inaccuracies independent of the used antenna. The correction calculations were based on derived radio ray parameters (section 3.2.2) a well as on spacecraft attitude information and ephemeris data for the celestial bodies provided by the ESA. Uncertainties in the spacecraft attitude and ephemeris data are believed to be small so that errors in the calculated pointing correction are neglected.

Previous measurements

Severe signal degradation due to antenna mispointing may also be responsible for the enhanced attenuation of Venera's 5 cm radio signal at the mid-latitudes represented in Figure 4.6 (orange curve). The observed path attenuation increases from 0.5 dB at 57 km altitude to almost 10 dB around 50 km. The corresponding absorptivity α visible in panel b) was transferred into sulfuric acid vapor abundance $q_{H_2SO_4}$ by using equation (4.20d). Since no information on the temperature T and pressure p was provided by *Gubenko et al.* (2001), data from VeRa's observations between the years 2006 and 2014 at these latitudes were adopted. Figure 6.7 shows the calculated sulfuric acid vapor abundance profile. The error bars on the H_2SO_4(g) values reflect the variation of T and p between the years 2006 and 2014.

Obviously the calculated H_2SO_4(g) abundance profile reveals distinctly higher values when compared to those presented in the Figures 4.2, 4.3 and 4.5 as well as presented by *Oschlisniok et al.* (2012) in the considered altitude range. Additionally, a large degree of supersaturation can be observed above the 1 bar pressure level. Both aspects indicate that the absorptivity and H_2SO_4(g) values derived from Venera's radio occultation data are overestimated. Increased uncontrollable antenna pointing inaccuracies may serve as an alternative explanation for the enhanced radio signal attenuation visible in Figure 4.6.a) and the resultant absorptivity and sulfuric acid vapor values presented in the Figures 4.6.b) and 6.7, respectively.

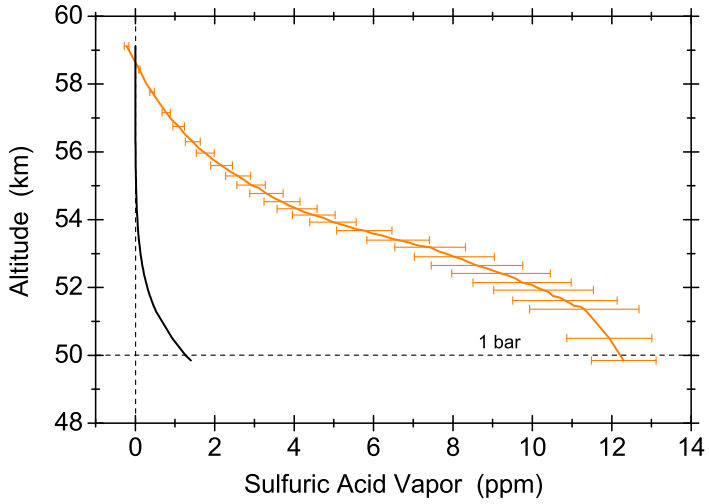

Figure 6.7: *Sulfuric acid vapor abundance derived from Venera's 5 cm (6 GHz) radio absorptivity data visible in panel b) of Figure 4.6 by using equation (4.20d). Temperature and pressure data were adopted from VeRa's radio occultation measurements between the years 2006 and 2014 from the corresponding latitudes. Error bars, which were calculated by applying the standard error propagation, represent the variation of the temperature and pressure between the years 2006 and 2014. No information on the uncertainty of the absorptivity is included. The black profile represent the saturation vapor abundance (cf. equation (5.13)).*

Chapter 7

Absorptivity, SO_2 abundance and H_2SO_4(g) profiles derived from VeRa's open loop data

The derivation of absorptivity profiles as well as SO_2 and H_2SO_4(g) abundances from VeRa's S- and X-band radio science data is described in the sections 3.2 and 4.1. As can be seen from Figure 6.3, significant absorption of VeRa's X-band radio signal begins below about 55 km altitude. Therefore, only this altitude region is considered for the absorptivity, sulfur dioxide and sulfuric acid vapor calculations which are based on VeRa's OL data.

Previous measurements have shown that the SO_2 abundance below 55 km altitude varies between 50 and 200 ppm (cf. Figure 2.4.a)). Distintcly higher SO_2 amounts ($\gg$ 200 ppm) would absorb VeRa's X-band signal significantly stronger than its S-band signal (cf. equation (4.20e)). The comparison of H_2SO_4(g) profiles derived from the absorption of VeRa's S- and X-band radio signals may therefore reveal weather or not enhanced SO_2 abundances were present in Venus's atmosphere during VeRa's measurements. The comparison is shown in section 7.1. The contribution of H_2SO_4(g) to the total signal absorption above about 51 km altitude is small (e.g. *Oschlisniok et al.*, 2012). Here, VeRa's X-band radio signals are used to derive upper limits of the SO_2 abundance at these altitudes. This analysis presented in section 7.2. Section 7.3 presents the global distribution of H_2SO_4(g) (section 7.3.1) and it's variation (section 7.3.2) as observed by VeRa during the entire Venus Express mission. All sections contain comparisons with results derived from ground based observations, previous missions and other experiments on board Venus Express.

Small scale fluctuations with a vertical extension of few hundred meters randomly distributed around a mean value were treated as noise in the data. Those fluctu-

ations, increasing with decreasing altitude, could introduce unwanted noise into the absorptivity and sulfuric acid vapor profiles. In order to decrease the effect of noise amplification, downsampling and filtering tools were applied in the process of absorptivity and H_2SO_4(g) calculations. A residual noise, which may still affect the results, dominates the calculated error bars placed on the atmospheric profiles. Those were calculated using the standard error propagation (e.g. *Jenkins and Steffes*, 1991).

7.1 Comparison of results derived from S-and X-band radio signals

The comparison of sulfuric acid vapor profiles derived simultaneously from S- and X-band radio signals increases the reliability of the H_2SO_4(g) values on the one hand, on the other hand significant differences may give indications for enhanced SO_2 amounts. In order to emphasize a possible contribution of sulfur dioxide to the total absorptivity (cf. equations (4.20e) and (4.21)) the SO_2 contribution was not removed when transferring absorptivity into S-and X-band H_2SO_4(g) profiles.

While VeRa's X-band radio signal was available during the entire Venus Express mission, VeRa's S-band signal could only be used during the first occultation season (2006-07-11 to 2006-08-30) to study Venus' neutral atmosphere. A total number of 30 atmospheric profiles derived from the S-band signals were obtained from the southern (13 profiles) and northern (17 profiles) hemisphere in 2006. A measurable S-band carrier signal could be maintained to altitudes as deep as 45 km when sounding Venus' southern hemisphere. At the northern hemisphere the deepest sounded altitudes reached almost 40 km. The main reason for the difference was the higher signal decrease due to refractive defocussing when sounding the southern hemisphere (cf. Figure 6.4). The latter contribution to the total signal attenuation is identical for both, the X- and S-band radio signals (cf. equation 3.9). As the expected sulfuric acid vapor abundance above 45 km altitude is low, particularly at higher latitudes (*Kolodner and Steffes*, 1998; *Oschlisniok et al.*, 2012), the here presented comparison is reduced to profiles obtained from the northern hemisphere. A total number of 10 out of 17 absorptivity and sulfuric acid vapor profiles obtained from the northern hemisphere could be used for a X-/S-band comparison (in three measurements no X-band signal was recorded; in four cases the occultation geometry at the end of the occultation season didn't allow to sound Venus' deeper atmosphere). The available measurements cover the latitudinal regions located between 60° and 74° as well as between 78° and 90°. While the first mentioned latitudes correspond to the cold collar region, at the last mentioned the northern polar vortex can be found.

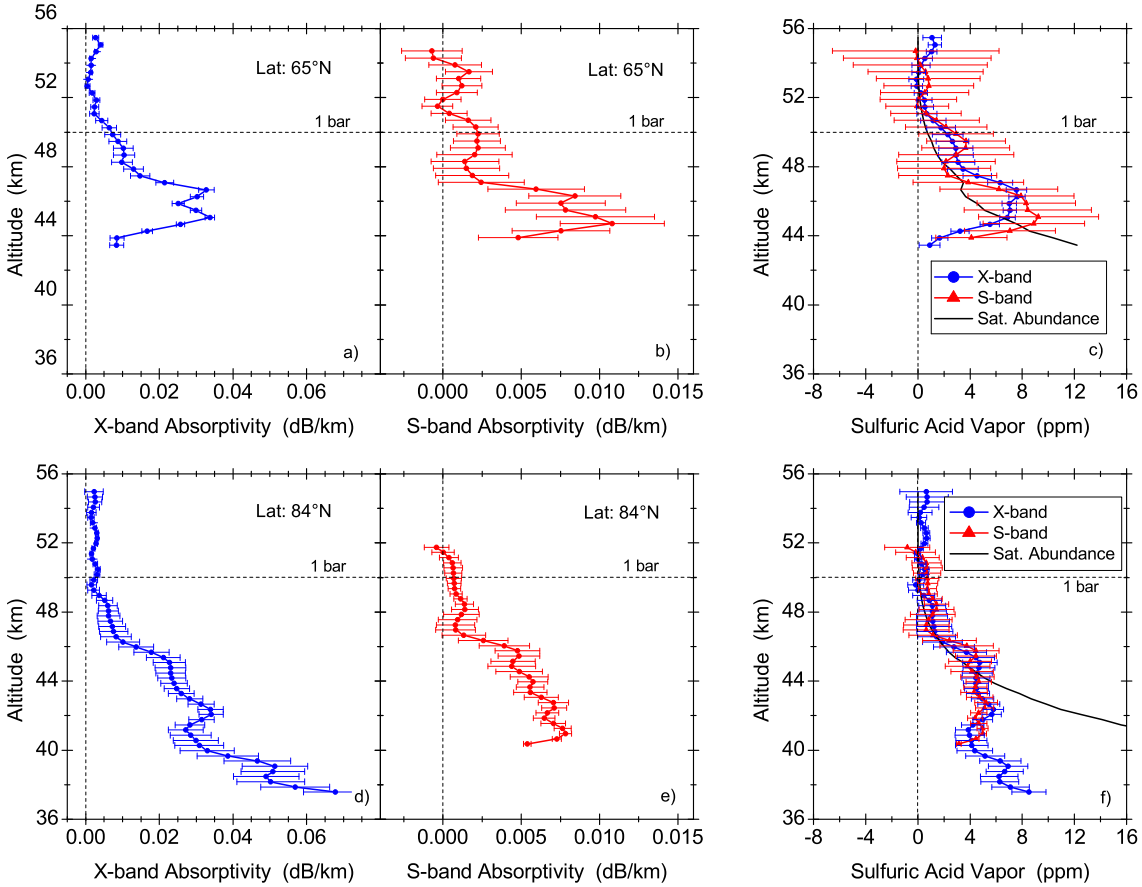

Figure 7.1: *Absorptivity of VeRa's X- and S-band radio signals derived from egress measurements carried out in the year 2006 at northern cold collar latitudes (panels a) and b)) and polar region (panels d) and e)). The absorptivity profiles contain contributions mainly from CO_2, N_2 and $H_2SO_4(g)$. The corresponding sulfuric acid vapor profiles are presented in the panels c) and f) for the collar and polar latitudes, respectively. The saturation abundance (black profiles in the panels c) and f)) was computed by using equation (5.13).*

The upper panels in Figure 7.1 show an example of the X- and S-band radio signal absorptivity as well as the corresponding sulfuric acid vapor abundance derived from the egress measurement at cold collar latitudes. Both absorptivity profiles reveal relatively low values above 48 km and enhanced values between 44 and 48 km altitude. In the latter altitude region the highest sulfuric acid vapor abundance can be observed with maximal values ranging between 6 and 10 ppm. Additionally, both profiles reveal an enhanced degree of supersaturation between 44 and 48 km altitude. Although both H_2SO_4(g) profiles in general agree with each other, the increased error bars on the S-band data prevents to draw any conclusions about additional absorbers like SO_2.

The enhanced error bars form a striking difference between both absorptivity profiles. Those result from the aforementioned small scale fluctuations, which are in most measurements larger in the S-Band signal amplitude data than in the X-band data. Particularly in the deep atmosphere the S-Band signal power fluctuations exceed the X-Band fluctuations by more than 1 dB. Those enhanced fluctuations lead to enlarged uncertainties of the S-Band H_2SO_4(g) values ($\Delta q_{H_2SO_4}^{\text{S-band}} = 1.0 - 4.0$ ppm, sometimes more than 6.0 ppm; $\Delta q_{H_2SO_4}^{\text{X-band}} = 0.5 - 2.0$ ppm, sometimes more than 5.0 ppm).

The lower panels in Figure 7.1 represent an example of the X- and S-band radio absorptivity along with the corresponding H_2SO_4(g) abundance achieved from the polar region. In contrast to the cold collar latitudes, deeper altitudes are resolved at the polar region. This is a consequence of high SNR values when the higher northern latitudes were sounded (section 6.2). Enhanced absorptivity values are visible below approx. 47 km altitude increasing with decreasing altitude in both profiles. Similar to the upper panel, oscillations visible in both profiles are the consequence of several factors, i.e., H_2SO_4(g) accumulations on small vertical scales, influence of atmospheric dynamics and residual noise on the used data.

Similar to the cold collar latitudes, the H_2SO_4(g) abundances derived from the X- and S-band absorptivity profiles show a good agreement in the altitude range between 40 and 52 km. Enhanced values are visible only below approx. 46 km altitude with a stable abundance of 4 to 6 ppm between 40 and 46 km altitude. Significant differences, indicating enhanced accumulations of additional absorbers, are not visible. Consequently, CO_2 and H_2SO_4(g) must be considered as the main absorbing gases at these wavelengths whose influence could be detected by VeRa measurements. The contribution by SO_2 is obviously negligible.

Figure 7.2 shows averaged absorptivity profiles derived from VeRa's X-band (blue) and S-band (red) radio signals from the year 2006. While the upper row presents the latitudinal region between 60° and 74° the lower row shows the polar region between 78° and 90°. The number of data samples used for averaging is presented in the right figures attached to the absorptivity profiles revealing that the deepest absorptivity profiles can be found at the polar region (cf. Figure 6.2). It is also visible that the number of data samples used for averaging decreases with decreasing altitude which influences the calculated error bars. The smaller the number of data samples the higher the uncertainty of the mean profiles. It can be clearly seen that above the altitude range from about 50 km to 52 km no absorption was observed, neither of the S-band nor of the X-band radio signals. Below that altitude range the absorption of both signals increases with decreasing altitude. Maximal X-band absorptivity values ranging between 0.03 dB/km and 0.09 dB/km below 42 km altitude can be observed in Figure 7.2.a). These

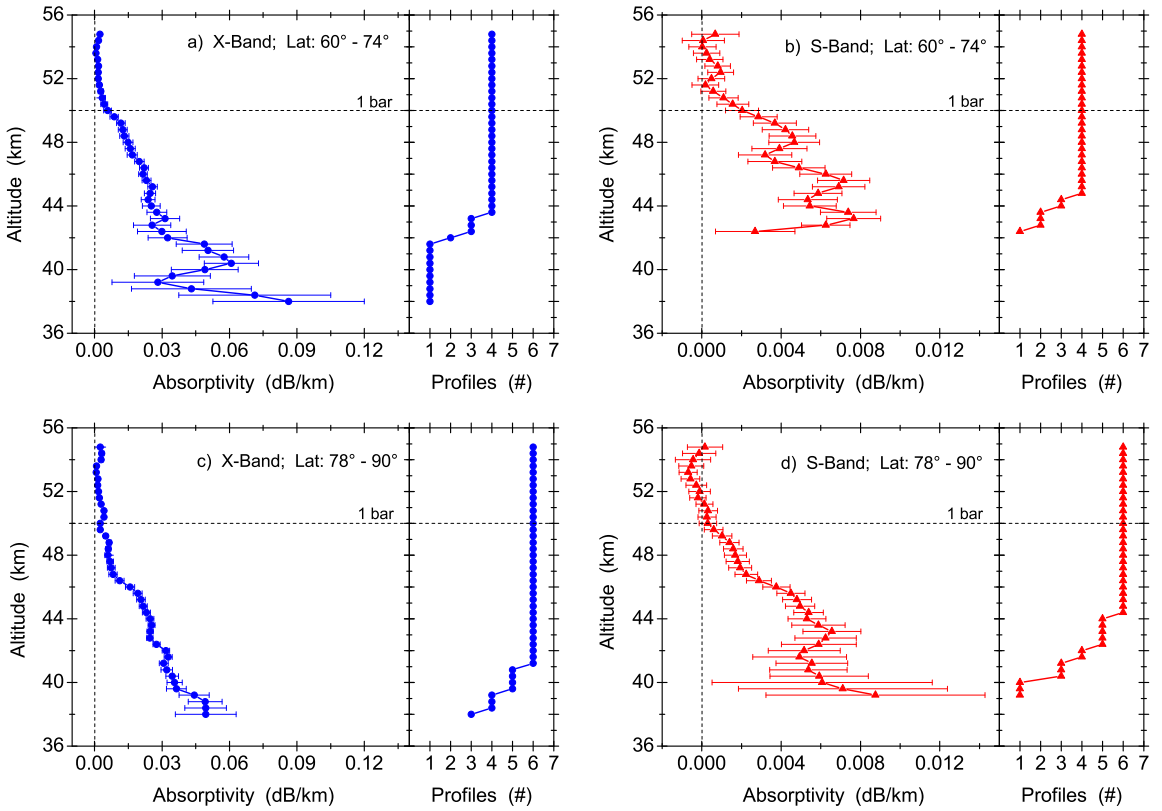

Figure 7.2: *Mean absorptivity profiles from the Venus northern hemisphere derived from VeRa's X-Band (blue) and S-Band (red) radio signals from the year 2006. The profiles contain contributions mainly from CO_2, N_2 and $H_2SO_4(g)$. The upper panel shows the latitudinal region between 60° and 74°, the lower panel shows the polar region between 78° and 90°. Narrow figures attached to the absorptivity profiles represent the number of data samples used for averaging.*

high values, however, are accompanied by large error bars and could not be confirmed in 2006 by further X-band absorptivity profiles from this latitudinal region. The corresponding S-band absorptivity profiles (Figure 7.2.b)) don't cover the altitude region below 42 km altitude. A comparison of the sulfuric acid vapor abundance derived from the S-and X-band absorptivity profiles is therefore not possible in this altitude range.

After removing the CO_2 and N_2 contribution from the total absorptivity the remaining sulfuric acid vapor absorptivity was used to compute the mean H_2SO_4(g) abundance. The results are presented in Figure 7.3. The corresponding individual H_2SO_4(g) profiles can be found in appendix E.

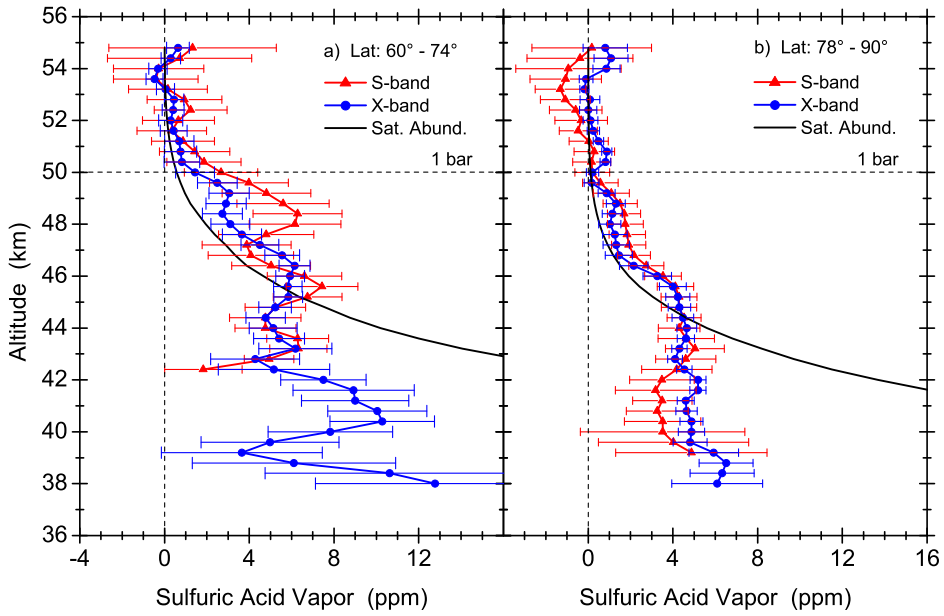

Figure 7.3: *Mean sulfuric acid vapor profiles from the Venus northern hemisphere derived from VeRa's S-and X-band radio signal absorption observed in 2006 (see Figure 7.2). The saturation abundance was computed by using equation (5.13).*

Within the error bars a general agreement between the sulfuric acid vapor profiles derived from VeRa's S-and X-band radio signal absorption can be seen at both latitudinal regions. No enhanced SO_2 contribution is visible. No H_2SO_4(g) can be observed above about 51 km at the *cold collar* region and above about 49 km altitude at the polar latitudes. In the deeper atmosphere the H_2SO_4(g) abundance increases to maximal values ranging from 4 to 8 ppm between 42 and 48 km at the *cold collar* region as well as from 3 to 6 ppm between 39 and 46 km at the polar latitudes. The increased oscillation of the X-band radio signal absorptivity below 42 km altitude at *cold collar* latitudes lead to an oscillation of the H_2SO_4(g) abundance which ranges between 4 ppm and 13 ppm. The corresponding error bars range from about 2 ppm around 42 km altitude to almost 6 ppm around 38 km altitude. In contrast to this, the altitude range below 42 km at the polar latitudes is resolved by a higher number of X- and S-band profiles. Here, the sulfuric acid vapor abundance ranges between 3 and 7 ppm with maximal error bars of 2 ppm on the X-band profiles and less than 4 ppm on the S-band data.

It is clearly visible that the region between about 45 and 50 km altitude reveals a saturation of H_2SO_4 at both latitudinal regions. Even small vertical sections of supersaturation at the topside of the H_2SO_4(g) layer can be observed. Saturation plays an

important role in one-dimensional numerical microphysical models (e.g. *James et al.*, 1997; *Krasnopolsky*, 2015). It's degree and altitude range, however, is debatable. Although H_2SO_4 saturation and even supersaturation at the topside of the haze layer is possible, at least the pronounced supersaturation at the cold collar latitudes, which is visible in the S-band data, may be overestimated. Possible explanations for enhanced supersaturation values in the derived sulfuric acid vapor profiles are discussed in the sections 7.2 and 7.3.2.

Comparison with previous measurements

A comparison of sulfuric acid vapor profiles derived simultaneously from radio signals at different frequencies was only possible with Magellan radio occultation measurements (see section 4.2). S-and X-band radio absorptivity profiles, derived by *Jenkins et al.* (1994), were transferred by *Kolodner and Steffes* (1998) into sulfuric acid vapor abundance profiles (cf. equations (4.20b) and (4.20c)). Figure 4.5.c) shows the acquired H_2SO_4(g) profiles from the orbit 3214. Both profiles agree within the entire altitude range except for the altitudes between 38 and 41 km. Here, the X-band profile shows significant higher values, indicating that an additional frequency dependent absorber contributed much stronger to the absorption of the X-band radio signal. Such a striking difference could not been observed in the VEX radio occultation measurements in the year 2006. The absorption of VeRa's radio signals can be therefore mainly addressed to H_2SO_4(g) and CO_2 during this period of time. The abundance of sulfur dioxide was too small to contribute significantly to the absorption of VeRa's S-and X-band radio signals, so that no clear differences in the corresponding H_2SO_4(g) profiles are visible.

According to *Kolodner and Steffes* (1998), SO_2 is the most likely candidate which is responsible for the aforementioned difference in the H_2SO_4(g) abundance profiles derived from the Magellan data. Using the equations (4.20b) and (4.20e), an upper limit of the SO_2 abundance of 390 ± 100 ppm is calculated for the region around 40 km altitude. Figure 7.4 shows the calculated SO_2 abundance value (blue square) incorporated into Figure 2.4.a). The error bar placed on the Magellan measurement represents the possible range of the SO_2 abundance calculated from the uncertainty of the S-and X-band H_2SO_4(g) profiles provided by *Kolodner and Steffes* (1998).

Obviously the achieved sulfur dioxide value is significantly larger than most of the measured SO_2 values. The enhanced abundance is a consequence of the large difference between the S-and X-band H_2SO_4(g) values around 40 km altitude (≥ 2.5 ppm). According to the equations (4.20b), (4.20c) and (4.20e), the sensitivity of S-and X-band radio signals to SO_2 is small compared to their H_2SO_4(g) sensitivity. Enlarged

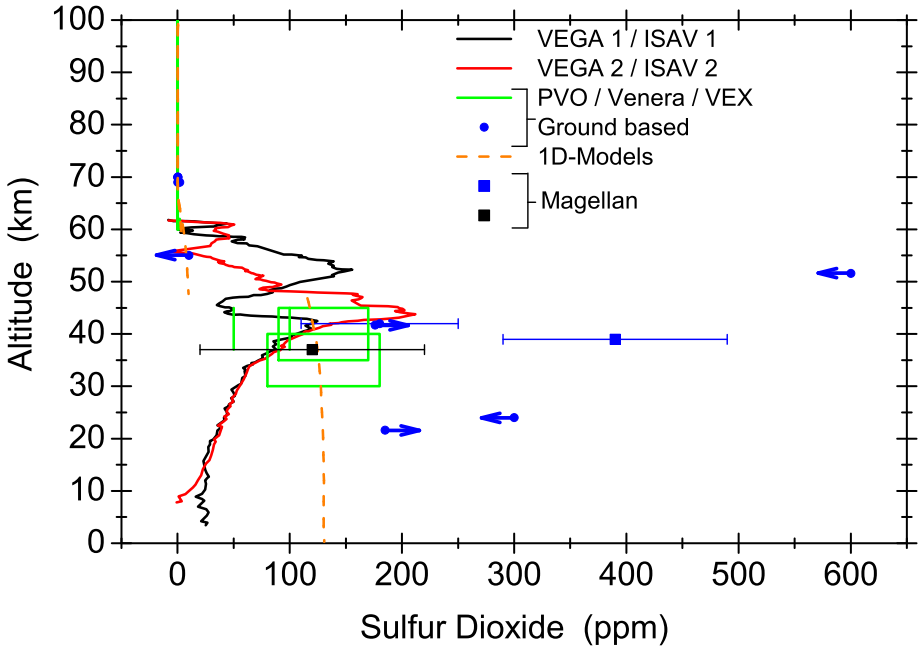

Figure 7.4: *Sulfur dioxide in Venus' middle and lower atmosphere obtained from ground based and spacecraft observations as well as from model results (cf. Figure 2.4.a)). The black square represent the SO_2 abundance derived from Magellan radio occultation S-and X-band data obtained from the orbit 3212. The blue square shows the SO_2 abundance calculated from Magellan data from the orbit 3214. The error bars represent the SO_2 abundance range derived from the uncertainty of the H_2SO_4(g) profiles.*

amounts of sulfur dioxide are needed to absorb the radio signals, while small SO_2 abundances wouldn't cause a detectable absorption at these wavelengths. Ignoring the SO_2 contribution to the total absorption in the latter case wouldn't produce large differences in the derived S-and X-band H_2SO_4(g) profiles. As an example for this, the black square in Figure 7.4 shows the SO_2 abundance derived from Magellan's S-and X-band H_2SO_4(g) data from the orbit 3212. In general the profiles are identical to each other. The largest difference of the profiles is smaller than 1 ppm and is located around 37 km altitude (*Jenkins et al.*, 1994; *Kolodner and Steffes*, 1998). Here, an SO_2 abundance of about 120 ± 100 ppm was derived using the equations (4.20b) and (4.20e).

The weak sensitivity of the S-and X-band radio signals to SO_2 is also responsible for the enhanced error bars placed on the Magellan measurements from the orbits 3212 and 3214. A variation of the S-and X-band H_2SO_4(g) abundance profiles within their error bars leads to a maximal SO_2 variation of around 100 ppm in both measurements.

Similar to VeRa's H_2SO_4(g) abundance profiles, those derived from the Magellan data also reveal saturated and supersaturated altitude regions at the topside of the H_2SO_4 haze layer. The degree of supersaturation, however, is smaller than that presented in the left panel of Figure 7.3. This is most probably a consequence of the atmospheric dynamics at this atmospheric region.

7.2 Upper limits of the SO_2 abundance derived from VeRa's X-band data

In this section H_2SO_4(g) profiles derived from VeRa's X-band radio signals as well as the corresponding saturation abundance profiles are used to compute upper limits of the SO_2 mixing ratio. The derivation of SO_2 by using a single radio frequency is limited to a narrow altitude range above the H_2SO_4 haze layer, i.e., 51 - 54 km. Here, low or no absorption of VeRa's X-band radio signals due to H_2SO_4(g) is expected (e.g. *Oschlisniok et al.*, 2012), so that enhanced absorption/H_2SO_4(g) values can be addressed to SO_2. The upper boundary was set to 54 km because multipath effects (Appendix B) may affect the results negatively above that altitude. Below the lower boundary of 51 km, the dependance of the H_2SO_4 saturation vapor pressure on the concentration of the H_2SO_4-H_2O solution increases, which would significantly enhance the uncertainty of the computed SO_2 values. In the present analysis a saturation vapor pressure of about 98% by weight was used to compute the H_2SO_4 saturation abundance (cf. equation (5.13)).

It is assumed that the concentration of the solution increases from about 90% around 55 km altitude to about 98% near the cloud base (e.g. *Hashimoto and Abe*, 2001; *Imamura and Hashimoto*, 2001; *Krasnopolsky*, 2012). Using the data of the ratio μ^*/RT provided by *Zeleznik* (1991) (μ^* : chemical potential in the H_2SO_4-H_2O solution; R = 8.31441 J/mol·K gas constant) it can easily be shown that a solution of 90% by weight would lead to an H_2SO_4(g) saturation abundance which differs only by 0.2 ppm from that calculated from a 98% solution in the altitude range between 51 and 54 km. The contribution of this difference to the total uncertainty of the computed SO_2 values in this section is less than 30 ppm.

Similar to the analysis conducted in section 7.1, the SO_2 contribution was not removed from the total absorption when transferring absorptivity data into H_2SO_4(g) data (cf. equations (4.20b) and (4.21)). Increased H_2SO_4(g) values between 51 and 54 km altitude indicate an enhanced SO_2 content within this altitude range. A mean abundance of SO_2 was calculated by minimizing the difference between the H_2SO_4(g) and saturation vapor abundance values. Figure 7.5 shows a typical example.

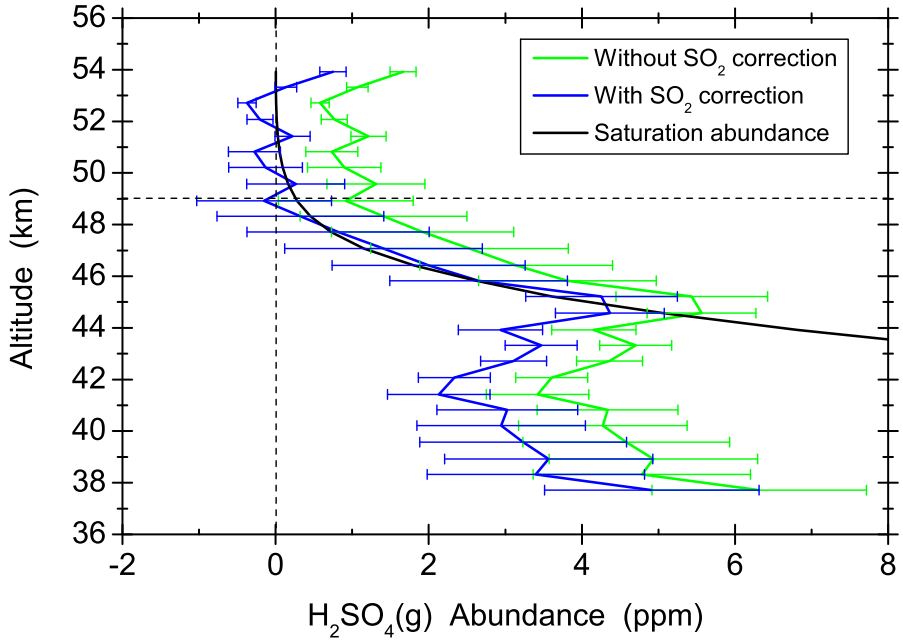

Figure 7.5: *Sulfuric acid vapor profiles derived from VeRa's X-band data calculated without (green) and with (blue) the SO_2 contribution to the total X-band radio signal absorption (cf. equation (4.21)). For the blue profile an SO_2 mixing ratio of* 200 ± 80 *ppm was used to correct for the contribution of sulfur dioxide to the total signal absorption. The black profile shows the H_2SO_4(g) saturation abundance calculated using the saturation vapor pressure over a H_2SO_4-H_2O solution of about 98% by weight (cf. equation (5.13)).*

The green profile shows the calculated H_2SO_4(g) abundance computed using the equations (4.20b) and (4.21) without considering the contribution of SO_2 to the total signal absorption. The black profile shows the H_2SO_4 saturation abundance. A clear difference between both profiles of about 1 ppm can be seen above 49 km altitude (horizontal dashed line). It was used to determine the mean SO_2 abundance in this altitude range. For this purpose the difference between both profiles was decreased by applying an iterative process in which the H_2SO_4(g) profile was repeatedly computed. Here, the SO_2 contribution to the total absorption was removed by gradually increasing the SO_2 abundance. The difference between both profiles turned out to be smallest when an SO_2 value of 200 ppm was used. The corresponding vertical H_2SO_4(g) distribution is represented by the blue profile.

The uncertainty of the H_2SO_4(g) profile was used to compute that of the derived sulfur dioxide abundance value. For this purpose, the '*error profile*' $q_{H_2SO_4} + \Delta q_{H_2SO_4}$ was used to compute the SO_2 abundance, leading to a value of 200 ppm. Considering

the error contribution of the saturation abundance of 30 ppm, the resulting uncertainty of the derived SO_2 abundance is 80 ppm.

It has to be mentioned that the above presented method applied to derive the SO_2 mixing ratio yields upper limits of the gas. It is assumed that after removing the contributions of CO_2 and N_2, sulfur dioxide is the only gas that is responsible for a residual absorption of VeRa's X-band radio signal above the topside of the H_2SO_4 haze layer.

The procedure described above was applied to VeRa's X-band absorptivity and H_2SO_4(g) data from the entire Venus Express mission. About 600 atmospheric profiles were used to derive the mean SO_2 abundance between 51 and 54 km altitude at the southern and northern hemispheres. No dependence on local time was found at any latitudinal region. Figure 7.6 shows the latitudinal distribution of the derived mean SO_2 values (black) along with a 5°-averaged SO_2 abundance (red).

Obviously the derived SO_2 values show an increased level of dispersion, which represents the high variability of sulfur dioxide below the clouds. The latter was also observed in previous measurements as well as by other experiments on board Venus Express (cf. Figure 2.4). The enhanced error bars on the derived SO_2 values are a consequence of the weak sensitivity of X-band radio waves to sulfur dioxide (cf. equation (4.20e)). While enlarged amounts of SO_2 contribute significantly to the signal absorption, small amounts are barely detectable. The latter may therefore lead to unreliable SO_2 values with uncertainties of more than 100%.

Despite the increased dispersion and enlarged error bars, a clear latitudinal dependance of sulfur dioxide is visible in Figure 7.6. Highest SO_2 abundances can be found at both polar regions ($\geq 75°$) with mean values of 150 ± 50 ppm at the south pole and 160 ± 50 ppm at the north pole. In contrast to this, the mid-latitudinal region around 40°S reveals the lowest values of 50 ± 40 ppm, before they increase at equatorial latitudes (25°S - 25°N) to mean values of 90 ± 60 ppm. Though at the latter region, the southern latitudes show lower values than the northern latitudes.

The enhanced sulfur dioxide abundance at the equatorial region is most probably a consequence of the upward transport of SO_2 from the deeper atmosphere by the upwelling branch of the Hadley cell. Small intensity variations of the latter may lead to the increased dispersion of the SO_2 values. Upward directed winds are most probably missing at the mid-latitudes, which may be the reason for the low SO_2 abundance values. Similar to the equatorial region, upward transport of SO_2 may be responsible for the increased abundance values at the polar latitudes. Here, updrafts in the polar

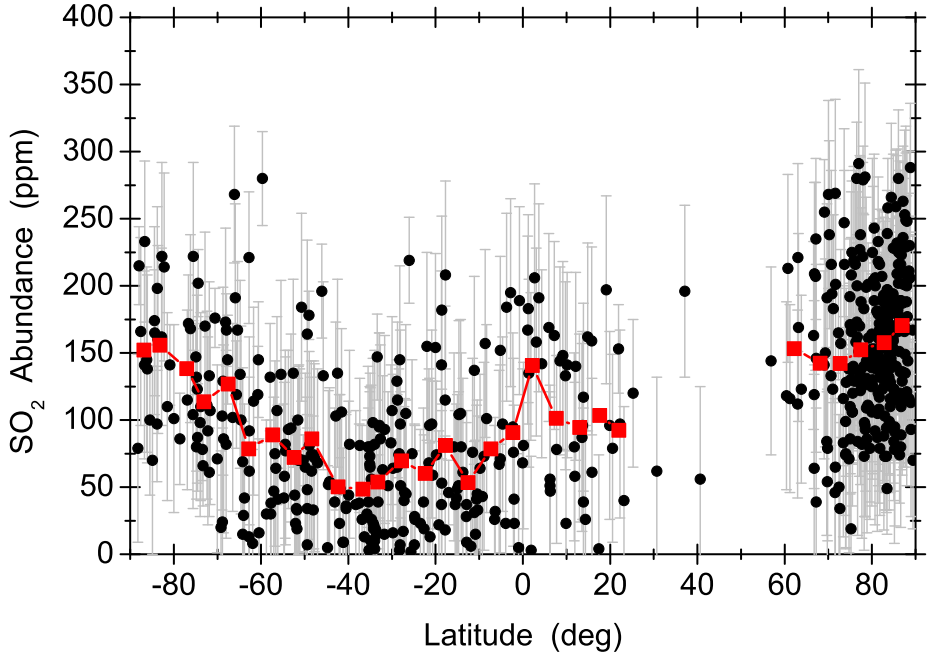

Figure 7.6: *Upper limits of the sulfur dioxide abundance in the altitude region between 51 and 54 km derived from VeRa's X-band data between the years 2006 and 2015. The measurement uncertainties vary between 30 and 80 ppm. The red line represent the average abundance. The hemispheres were subdivided into equal latitudinal bins of 5° each. SO_2 values located within each bin were averaged to one mean value. Due to the low number of measurements, SO_2 values located in the latitude region between 25°N and 60°N were not considered for averaging.*

vortices ensure most probably a steady supply of SO_2 from the deeper atmosphere, while their intensity variations cause the observed dispersion of the SO_2 abundance values.

Long-term variations

In the following, the long-term evolution of the computed sulfur dioxide abundance is presented. Since most of the southern mid-latitudinal SO_2 values are accompanied by enlarged relative errors, observations from this spatial region were not considered for the analysis. Furthermore, the low number of measurements at the northern mid-latitudes precludes an analysis in this region. More than 350 observations from the equatorial (25°S - 25°N) and the polar regions ($\geq$ 75°) were left. Figure 7.7 shows the

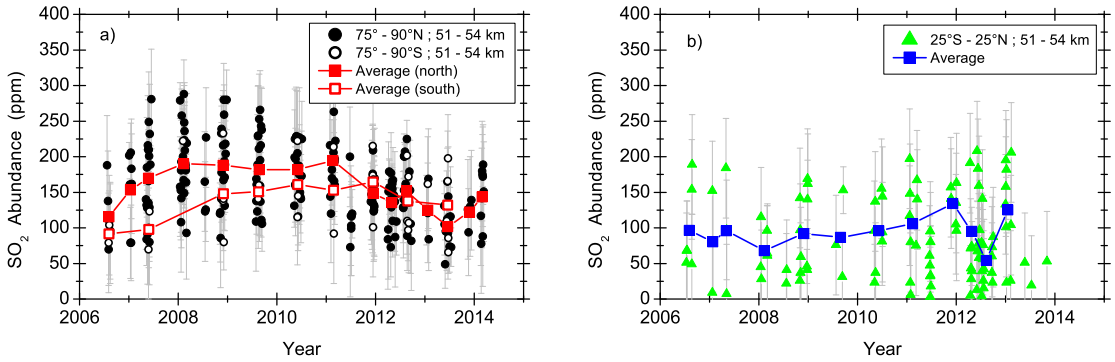

Figure 7.7: *Upper limits of the sulfur dioxide abundance in the altitude region between 51 and 54 km derived from VeRa's X-band absorptivity data between the years 2006 and 2015. Panel a) shows the abundance at southern and northern polar latitudes ($\geq 75°$), panel b) shows the abundance at the equatorial region ($25°S$ - $25°N$). The measurement uncertainties vary between 30 and 70 ppm. The red and blue data represent averaged abundances computed from measurements, which were obtained from different occultation seasons.*

annual variation of the SO_2 abundance at the southern and northern (panel a)) as well as at the equatorial region (panel b)).

A clear long-term trend of SO_2 at the polar latitudes is visible in panel a) with relatively low SO_2 abundance values in the year 2006. Those are consistent with the low SO_2 abundance concluded from the comparison of the S-and X-band H_2SO_4(g) profiles presented in section 7.1. After the year 2006, the abundance increases rapidly to a mean value of 180 ± 50 ppm at the north pole between the years 2008 and 2011. A similar increase of SO_2 at the southern pole seems to be delayed compared to that at the north pole. An enhanced mean abundance value of 140 ± 30 ppm is visible from the year 2009 onwards. The low number of measurements before 2009, however, prevents from drawing any conclusions on the SO_2 abundance at the south pole during this period of time. After the years 2011/2012, a gradual decrease is visible with lowest mixing ratios in the year 2013. Here, mean abundances of 130 ± 50 ppm at the southern pole and 100 ± 30 ppm at the northern polar region can be observed.

The long-term trend is most probably a consequence of temperature variations at the polar region. Those may influence the transport mechanisms as well as the sulfur chemistry at these latitudes and this way affect the mixing ratio of SO_2. Figure 7.8 shows the long-term evolution of the temperature at the northern polar region[1)]

[1)] Only a small number of profiles from the southern polar latitudes show the atmospheric region at altitudes below 44 km (c.f. Figure 6.2). Therefore, the temperature at these latitudes is not shown here.

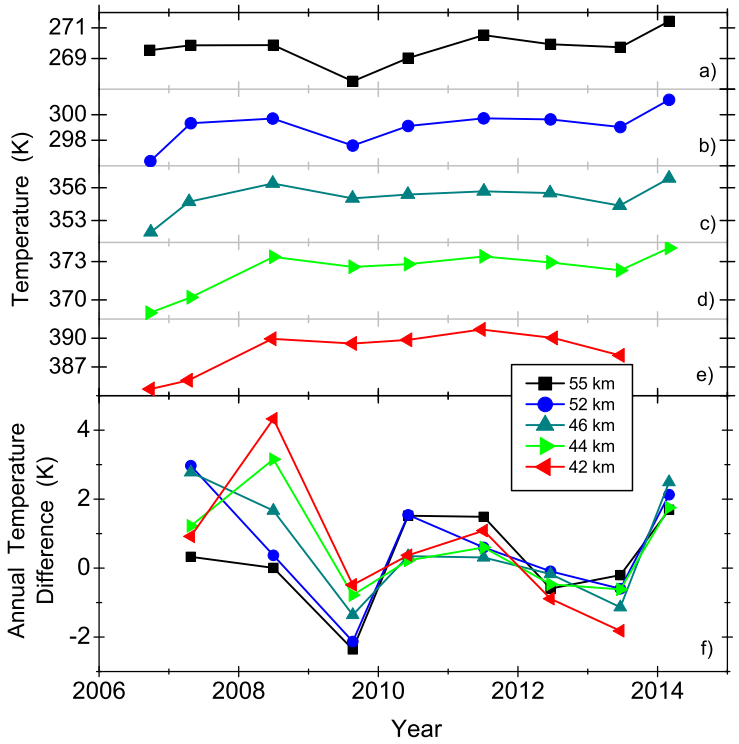

Figure 7.8: *Mean atmospheric temperature as a function of the year at altitudes levels between 55 and 42 km at the northern polar region (≥ 75°) (panel a) to e)) as well as its annual difference (panel f)) derived from VeRa's X-band radio occultation data.*

between the years 2006 and 2015. While the panels a) to e) show the mean temperature at altitude levels between 55 and 42 km, panel f) shows its annual difference. Two distinct periods can be distinguished:

i) **2006 - 2009**. A heating of the atmosphere is visible during this period of time. The comparison of the temperature evolution at different altitude levels (panels a) to e)) indicates, however, that the heating of the lower atmospheric region was delayed. This delay most probably affected the vertical temperature gradient and this way influenced the vertical SO_2 transport. This process could be mainly responsible for the rapid SO_2 enhancement which is visible in Figure 7.7.a).

The rapid increase of the temperature at 52 km altitude (panel b)) between the years 2006 and 2008 coincides with the enhancement of sulfur dioxide during this time period. It is also conceivable that the temperature increase may have affected the kinetics of the chemical sulfur cycle in this spatial region leading to the increased SO_2 abundance. The temperature dependence of the chemical

kinetics of sulfur gases in Venus' lower and middle atmosphere is discussed in detail for example by *Krasnopolsky* (2007) and *Zhang et al.* (2012).

ii) **2010 - 2014**. In contrast to the time-shifted temperature increase at different altitudes between the years 2006 and 2009, a simultaneous oscillation of the mean temperature at all considered altitude levels can be observed between 2010 and 2014. Atmospheric heating and cooling periods are visible around the years 2011 and 2013, respectively. An increase of the temperature is additionally visible around 2014 between 44 and 55 km altitude. Due to the simultaneous heating and cooling at all altitude levels, vertical temperature gradient variations were small between the years 2010 and 2014. As a consequence, variations of the vertical SO_2 transport were less intense, so that rapid abundance changes didn't occur.

Panel b) in Figure 7.7 reveals that an SO_2 long-term trend, similar to that observed at the polar latitudes, doesn't exist at the equatorial region. Here, sulfur dioxide values ranges between 0 and more than 200 ppm revealing an almost constant mean abundance of 90 ± 60 ppm. The latter is consistent with the mean sulfur dioxide values observed during the SO_2 low abundant periods at the polar region in the years 2006 and 2013. The missing long-term trend of SO_2 at equatorial latitudes indicates the absence of intense vertical transport variations near the cloud base.

Comparison with previous observations and other VEX measurements

The abundance of sulfur dioxide in the altitude range between 51 and 54 km is poorly known from previous measurements (section 2.2). Reliable results, ranging between 50 and 200 ppm, were particularly provided by the VEGA entry probes in the equatorial region. The Pioneer Venus large probe observed an increased value of less than 600 ppm. The SO_2 abundance values derived from VeRa's X-band absorptivity and H_2SO_4(g) data are comparable to those derived from the VEGA entry probe observations. Figure 7.9 shows the mean SO_2 values derived from VeRa's X-band data incorporated into Figure 2.4.a).

Obviously both, the equatorial and polar SO_2 values obtained from VeRa's observations matches that obtained by the VEGA landers in the corresponding altitude region. The distinct disagreement of both VEGA profiles at these altitudes is consistent with the measurement-to-measurement variability of the SO_2 values derived from VeRa's data (cf. Figure 7.7). Both observations emphasize the high variability of SO_2 near the cloud base. The high number of measurements obtained with VeRa, however, constrain

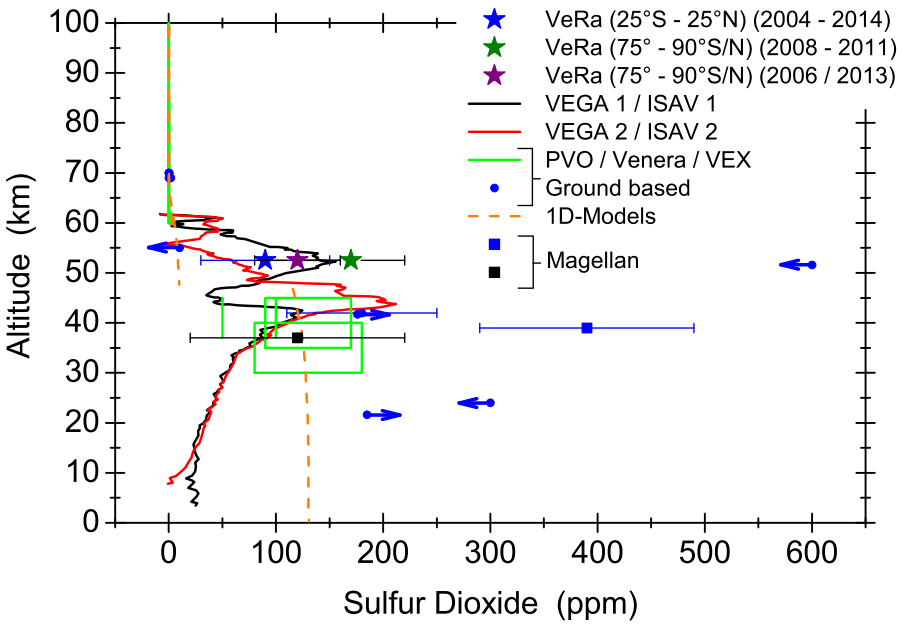

Figure 7.9: *Averaged abundance of SO_2 at the equatorial and polar region derived from VeRa's X-band absorptivity/H_2SO_4(g) data (cf. Figure 7.7) incorporated into Figure 2.4.*

the mean equatorial abundance to 90 ± 60 ppm. The latter is obviously higher than that predicted by one-dimensional photochemical models at these altitudes (dashed line in Figure 7.9). The mean SO_2 values derived from VeRa's data show that the vertical SO_2 gradient in the transition region between 50 and 60 km altitude is not as strong as suggested by the models.

Various observations of SO_2 within the upper clouds revealed a clear dependence on the local time (e.g. *Encrenaz et al.*, 2019; *Marcq et al.*, 2020). High photodissociation rates decrease the SO_2 abundance, so that lowest SO_2 values can be found between 10 h and 14 h local time. At higher solar zenith angles, the photochemical loss is lower. Significant photochemical dissociation of SO_2 occurs at wavelengths ≤ 350 nm (*Kumar*, 1982; *Manatt and Lane*, 1993; *Prahlad and Kumar*, 1997). The solar flux at these wavelengths strongly decreases in the main Venus clouds (e.g. *Tomasko et al.*, 1980; *Zhang et al.*, 2012). Photochemical loss of SO_2 plays therefore an important role at cloud top altitudes but is almost non existent near the cloud base. A local time dependance was therefore not found in the SO_2 abundance at the latter altitudes.

Among a clear dependence on the local time, a number of authors reported about distinct latitudinal and long-term variations of sulfur dioxide in the upper clouds (e.g.

Esposito et al., 1988; *Marcq et al.*, 2012, 2020). In the following these variations are compared with those near the cloud base derived from VeRa's radio occultation data.

Latitudinal variations

Figure 7.10.a) shows the latitudinal distribution of SO_2 at 70 km altitude derived by *Marcq et al.* (2020) from SPICAV-UV measurements. The comparison with the SO_2 abundance between 51 and 54 km altitude presented in Figure 7.6 reveals that similar to the latter values, those derived at cloud top altitudes also show an increased level of dispersion. Obviously the abundance of sulfur dioxide is highly variable at both altitude levels. The highest dispersions are located at the equatorial region which are most probably caused by short-term variations of the vertical SO_2 transport at these latitudes (*Marcq et al.*, 2020).

Panel b) in Figure 7.10 shows the latitudinal mean SO_2 distribution adopted from panel a) (blue) along with that adopted from Figure 7.6 between 51 and 54 km altitude. Both altitude regions reveal enhanced SO_2 abundance values at equatorial latitudes. The latter are likely caused by the upward directed transport at these latitudes. Around the equator, the upwelling branch of the Hadley circulation transports SO_2 from lower to higher altitudes leading to enhanced SO_2 values at both altitude levels. As upward transport is most probably missing at mid-latitudes (35° - 60°), the sulfur dioxide abundance in this spatial region is lower compared to that at the equa-

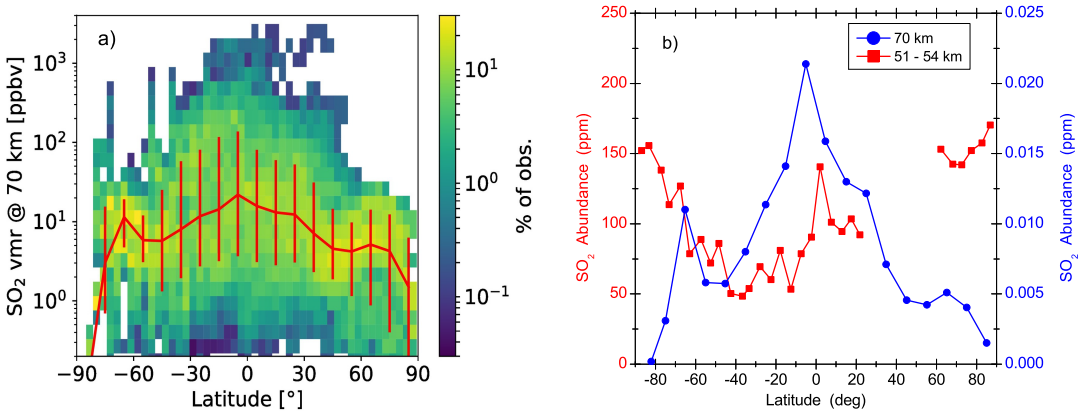

Figure 7.10: *Panel a): Latitudinal distribution of SO_2 at 70 km altitude as observed by Marcq et al. (2020) using SPICAV-UV data. Panel b): The mean SO_2 abundance adopted from panel a) (blue) along with that between 51 and 54 km altitude derived from radio occultation measurements (red) (cf. Figure 7.6).*

tor leading to a latitudinal SO_2 gradient. Furthermore, photodissociation at the upper region causes a significant decomposition of SO_2 while it is advected toward the polar latitudes. As a consequence, the SO_2 abundance distinctly decreases in the poleward direction (e.g. *Marcq et al.*, 2020). Since photochemical loss plays a minor role near the cloud bottom, the latitudinal SO_2 decrease between the equatorial and mid-latitudes is more pronounced at cloud top altitudes compared to that near the cloud base.

The most striking difference in the cloud top and the cloud bottom SO_2 abundance is visible at the polar regions. At these latitudes, a clear decrease of SO_2 can be seen at 70 km altitude, while the region near the cloud bottom reveals SO_2 values comparable to those found near the equator. The disagreement may be explained by considering the predominant transport mechanisms at the corresponding altitude regions. The altitude range between 51 and 54 km is steadily supplied with SO_2 from the deeper atmosphere by the polar vortices. The latter are most probably located below 65 km altitude (section 2.3), so that only small fractions of SO_2 reach the higher altitude levels. In contrast to the lower altitude range, the missing SO_2 transport toward the polar 70 km altitude region is most probably responsible for the low SO_2 abundance at this spatial region.

Long-term variations

The panels a) and b) in Figure 7.11 present the temporal evolution of the equatorial SO_2 abundance. Panel a) shows the mean abundance at 70 km altitude as observed by *Marcq et al.* (2020) in SPICAV-UV measurements (cf. Figure 2.4.b)). For comparison, panel b) shows the averaged abundance in the altitude range between 51 and 54 km altitude derived from VeRa's radio occultation data (cf. Figure 7.7.b)). The error bars represent the variability of the SO_2 abundance values observed in the corresponding years.

Distinctly increased SO_2 values at 70 km altitude are visible in the years 2007 and 2009. According to *Marcq et al.* (2020), those are caused by enhanced sulfur dioxide injections from lower altitudes. It is clearly visible from panel b), however, that significant enhancements of the equatorial SO_2 abundance near the cloud base are not present during these years. This disagreement may have various reasons, which are not mutually exclusive:

- Variations of the vertical transport which led to SO_2 injections from deeper to higher altitudes could be too weak to cause detectable SO_2 enhancements near the cloud base. According to *Encrenaz et al.* (2012) and references therein, injections of a small excess ($\sim 1\%$) would increase the SO_2 abundance at the upper cloud

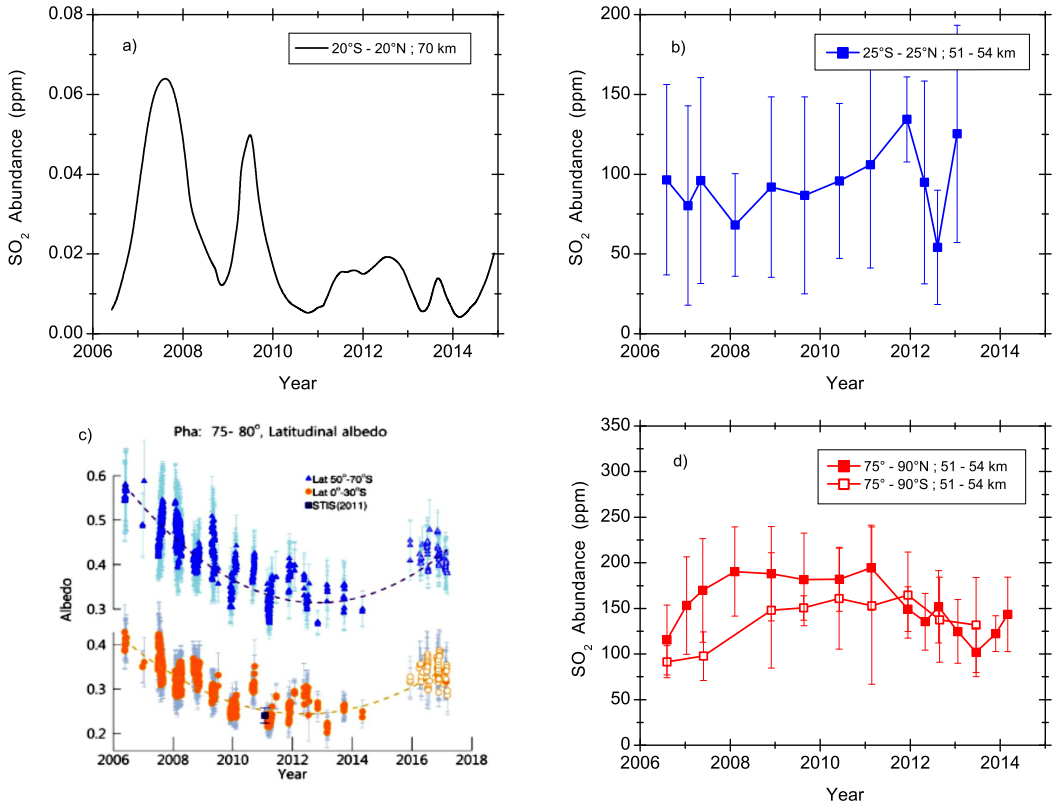

Figure 7.11: *Long-term evolution of SO_2 in the equatorial region at 70 km altitude (panel a)) extracted from Figure 2.4.b) as well as between 51 and 54 km altitude (panel b)) extracted from Figure 7.7.b). Panel c) shows the long-term trend in Venus' 365 nm albedo observed by Lee et al. (2019) at equatorial and mid-latitudes. Panel d) represents the temporal SO_2 evolution between 51 and 54 km altitude at both polar regions extracted from Figure 7.7.a). Error bars in the panels b) and d) represent the variability of the SO_2 abundance values observed in the corresponding years.*

region by a few tens ppb. The enhanced dispersion of the SO_2 values visible in panel b) may therefore superimpose those variations near the cloud bottom.

- Enhanced vertical transport variations were probably limited to the upper cloud region ($\geq$ 55 km). Furthermore, dynamical processes at these altitudes may be decoupled from those at the lower clouds as schematically indicated in Figure 2.7. As already discussed in the context of the polar SO_2 long-term trend, transport variations represent a dynamical response to temperature gradient variations. The latter can be studied by means of VeRa's radio occultation data as was done for the polar region between 42 and 55 km altitude (cf. Figure 7.8). In contrast

to the polar latitudes, however, a similar study at the equatorial upper cloud region is complicated. VeRa's radio occultation data from this spatial region must be corrected for *multipath effects* before any conclusions can be drawn (see Appendix B). Additionally, an extended study on thermal tides in the upper cloud region is necessary to separate those from a possible long-term variation (e.g. *Walterscheid et al.*, 1985; *Tellmann et al.*, 2009; *Takagi et al.*, 2018).

- SO_2 variations observed at the cloud top level may be additionally influenced by variations of the solar flux. As already mentioned, the latter strongly decreases in the main Venus clouds, so that its influence could be visible at cloud top altitudes rather than near the cloud base. *Lee et al.* (2019) found indications for a correlation between the neutron cosmic rays/Ly-α flux and the long-term trend in Venus' 365 nm albedo between the years 2006 and 2018. While the neutron cosmic ray flux increased / Ly-α flux decreased, the observed albedo revealed a gradual decrease between the years 2006 and 2012. The latter can be seen in panel c) of Figure 7.11 for the equatorial and mid-latitudes. The gas species responsible for the enhanced absorption of the incident solar flux is not identified so far. Sulfur dioxide is thought to be a promising candidate as a precursor for this unknown UV absorber (*Mills et al.*, 2018), which is believed to be located mainly in the upper cloud region. The enhancement of SO_2 observed by *Marcq et al.* (2020) would therefore increase the abundance of the UV absorber, leading to a decrease of the 365 nm albedo observed by *Lee et al.* (2019). Whether or not solar flux variations can cause significant SO_2 abundance variations at upper cloud levels can not be clarified in this context and must therefore be analyzed in further studies based on observations and photochemical models.

In addition to the aforementioned equatorial and mid-latitudinal long-term trend in Venus' 365 nm albedo, *Lee et al.* (2015) reported about a similar trend at the polar latitudes. According to *Lee et al.* (2019), a decrease of the albedo should cause a considerable heating of the atmosphere. It is likely that the increased absorption of solar radiation in Venus' polar atmosphere, which was observed as a long-term decrease of the albedo, caused the observed variations of the temperature presented in Figure 7.8. The resulting variations of the vertical transport most probably led to the long-term trend in the SO_2 abundance presented in panel d) of Figure 7.11.

7.3 H_2SO_4(g) profiles derived from VeRa's X-band data from the entire Venus Express mission

In addition to the correction of VeRa's X-band absorptivity data for the CO_2 and N_2 contributions (cf. equation (4.20a)), the sulfur dioxide abundance values derived in the previous section were used to remove the SO_2 contribution (cf. equations (4.20e) and (4.21)). A constant sulfur dioxide content was assumed for the altitude region below 55 km. It can be assumed that the residual absorption was caused by H_2SO_4(g), only, which was used to determine its abundance. In the following, sulfuric acid vapor profiles in the altitude range below 55 km as well as their variation derived from VeRa's X-band radio absorptivity data are presented.

7.3.1 Global H_2SO_4(g) distribution

About 800 radio occultation measurements from the years 2006 to 2014 were used in this section to compute the absorptivity and H_2SO_4(g) abundance profiles. The number of profiles used here is higher than that used to derive the SO_2 abundance in the previous section. Only profiles whose deepest altitudes are located at least at 51 km were considered for the SO_2 calculations. In contrast to this, the shorter profiles were also used for the present analysis of the global H_2SO_4(g) distribution.

The lower panel in Figure 7.12 shows the zonally and time-averaged H_2SO_4(g) distribution in Venus' atmosphere between 40 and 55 km altitude at the southern and northern hemispheres between the years 2006 and 2014. Both hemispheres were subdivided into equal latitudinal bins of 5° each. H_2SO_4(g) profiles located within each bin were averaged to one profile. The number of data samples used for averaging is presented in the upper panel of Figure 7.12. It shows that the majority of available measurements is located at the northern polar latitudes. In contrast to this a lack of measurements is visible at the northern mid-latitudes between 20° and 60°, which is a consequence of the orbit geometry of Venus Express. Southward of the latitude of 20°N the number of H_2SO_4(g) profiles used for averaging ranges between 10 and 30.

As was mentioned in section 7.1 the number of profiles used for averaging influences the error bars of the mean H_2SO_4(g) profiles (cf. Figures 7.2 and 7.3). The higher the number of profiles the lower the uncertainty. The lowest uncertainties in the global H_2SO_4(g) distribution presented in Figure 7.12 can therefore be found at the northern polar latitudes. The error bars don't exceed 0.5 ppm. The other latitudinal regions show uncertainties ranging between 0.2 and 1.0 ppm, sometimes increasing to more than 2.0 ppm.

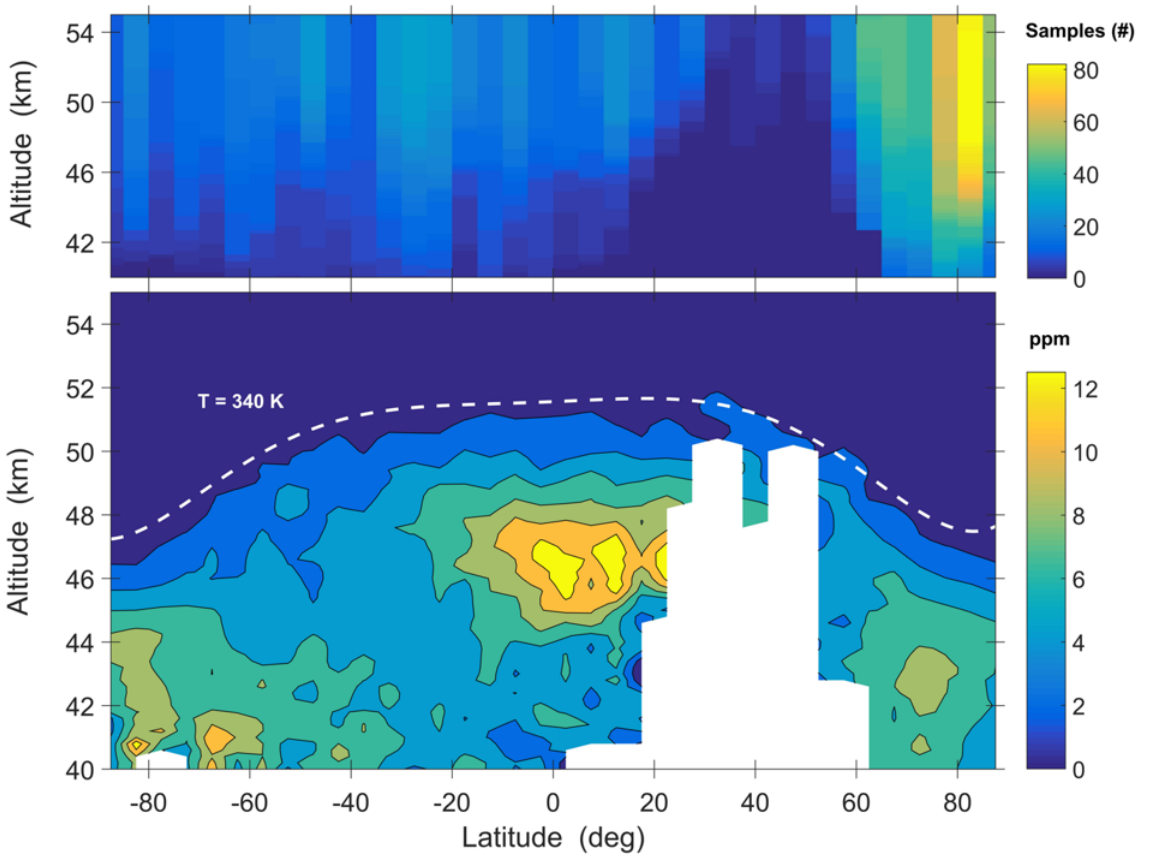

Figure 7.12: *Zonally and time-averaged H_2SO_4(g) distribution in Venus' lower atmosphere at the southern and northern hemispheres derived from VeRa's radio occultation data from the years 2006 to 2014 (lower panel). The hemispheres were subdivided into equal latitudinal bins of 5° each. H_2SO_4(g) profiles located within each bin were averaged to one sulfuric acid vapor profile. The number of data samples used for averaging is shown in the upper panel. The white dashed line in the lower panel shows the isotherm of T = 340 K derived from VeRa's X-band radio occultation data from the same period of time.*

Two prominent features can be clearly seen in the lower panel of Figure 7.12:

1. *A latitudinal H_2SO_4(g) gradient* visible in the altitude region between about 47 and 51 km at both hemispheres. It is clearly visible that the topside of the H_2SO_4(g) layer is located distinctly above 50 km altitude in the latitudinal region between about 40°S and 40°N. Poleward of this latitudinal region the topside decreases to altitudes between 46 and 48 km at polar latitudes. This latitudinal gradient is caused by the global temperature distribution within this altitude region, which is visible in panel a) of Figure 2.1. As an example, the isotherm of T = 340 K was plotted over the H_2SO_4(g) contour map (white dashed line).

It can be clearly seen that the isotherm almost perfectly matches the latitudinal distribution of the topside of the H_2SO_4 haze layer. At lower temperatures (higher altitudes) the abundance of gaseous sulfuric acid was not high enough to be detected by VeRa. Liquid sulfuric acid existing in this altitude region is almost transparent for radio waves at S-and X-band (section 4.1.3) and was therefore not detected by VeRa as well. At lower altitudes the temperature was high enough to evaporate enough liquid sulfuric acid to be detected by VeRa. The evaporation depends strongly on the environmental temperature. The observed latitudinal temperature gradient presented in Figure 7.12 is therefore the reason for the observed latitudinal gradient of the topside of the H_2SO_4(g) haze layer.

2. *An accumulation of sulfuric acid vapor* between about 44 and 49 km altitude at equatorial latitudes (25°S - 25°N) as well as below 45 km altitude at polar latitudes ($\geq$ 60°S/N). Increased values of more than 12 ppm can be observed in the first mentioned region, while highest values of 8 to 10 ppm are visible at both polar latitudes. The enhanced accumulations are most probably a consequence of the predominant atmospheric dynamics at these spatial regions. The study of the wind dynamics at these regions along with the comparison of the here derived global H_2SO_4(g) distribution is presented in chapter 8.

The comparison of the upper with the lower panel of Figure 7.12 shows the influence of the global H_2SO_4(g) distribution on the depth of the achieved profiles. For example, the increased accumulation of H_2SO_4(g) at the equatorial latitudes is obviously a strong barrier for radio waves at X-band. The radio waves passed this barrier once when the altitude region between 44 and 49 km was sounded. Due to the spherical shape of Venus, however, the waves passed the barrier twice when the region below 44 km altitude was sounded leading to a stronger absorption. In many measurements a carrier signal could therefore not be detected anymore at the tracking station when the lower altitude region was sounded. The deepest altitude of the most H_2SO_4(g) profiles achieved from these latitudes is therefore located between 44 and 46 km (see upper panel in Figure 7.12). In contrast to this, such a barrier is not present in the latitudinal region between 20°S and 40°S. The number of H_2SO_4(g) profiles showing the altitude region below 44 km is therefore distinctly higher compared to the equatorial region. At the southern polar latitudes, the increased H_2SO_4(g) abundance at the lower altitudes limits the depth of the H_2SO_4(g) profiles. Due to the lower refractive loss at the northern polar latitudes (cf. Figure 6.4) the power of the X-band radio signal was strong enough to withstand the absorption caused by the increased H_2SO_4(g) abundance at the lower altitudes. The number of profiles showing altitudes around 40 km is therefore highest at these latitudes.

7.3.2 H_2SO_4(g) abundance variations

The global distribution of H_2SO_4(g) shown in Figure 7.12 is in general the same on both, the dayside and the nightside of the planet. However, significant abundance variations of the H_2SO_4(g) accumulated regions at the equatorial and polar latitudes could be observed. Similar to the SO_2 long-term variation observed at both polar regions (cf. Figure 7.7.a)), the H_2SO_4(g) mixing ratio reveals a clear long-term trend at the northern polar latitudes in the same period of time. The equatorial H_2SO_4(g) content shows no such variation, which is in agreement with the observed SO_2 abundance in this latitudinal region. In contrast to the SO_2 abundance, however, the equatorial H_2SO_4(g) values show indications for a local time dependance. In the following, the variations of the enhanced H_2SO_4(g) accumulations at both latitudinal regions are discussed. For this purpose, the column density of H_2SO_4(g) was computed between 42 and 47 km altitude at the northern polar region ($\geq 75°$) and between 46 and 50 km at the equatorial latitudes (25°S - 25°N). It is visible from the upper panel of Figure 7.12 that the number of available H_2SO_4(g) data decreases with decreasing altitude. The number of H_2SO_4(g) profiles covering the above mentioned altitudes is lower than that covering the altitude range from 51 to 54 km in which SO_2 variations were analyzed. Therefore, the analysis of the SO_2 variations presented in section 7.2 comprises a larger number of profiles than the analysis of the H_2SO_4(g) variations.

Long-term variation at northern polar latitudes

In contrast to the study of the SO_2 long-term variation between 51 and 54 km altitude which was carried out at both polar regions (cf. Figure 7.7.a)), that of H_2SO_4(g) is limited to the north pole. It can be seen from the lower panel of Figure 7.12 that enhanced H_2SO_4(g) values at the polar regions are located below 47 km altitude. From the upper panel it can be seen that the number of H_2SO_4(g) profiles reaching these altitudes at the southern polar region is small compared to that at the north pole. The study of abundance variations at the southern polar latitudes would therefore be of limited informative value.

The upper panel in Figure 7.13 shows the temporal evolution of the H_2SO_4(g) column density between the years 2006 and 2013 in the altitude range from 42 to 47 km at the northern polar latitudes. While the lowest column densities can be found in the year 2007 with a mean value of $0.51 \cdot 10^{30}$ km^{-2}, a clear increase is visible between 2007 and 2008. From the end of 2008 onwards, distinctly enhanced values can be seen compared to those in 2006 and 2007. A mean value of $1.38 \cdot 10^{30}$ km^{-2} was calculated for this H_2SO_4(g) high abundant period.

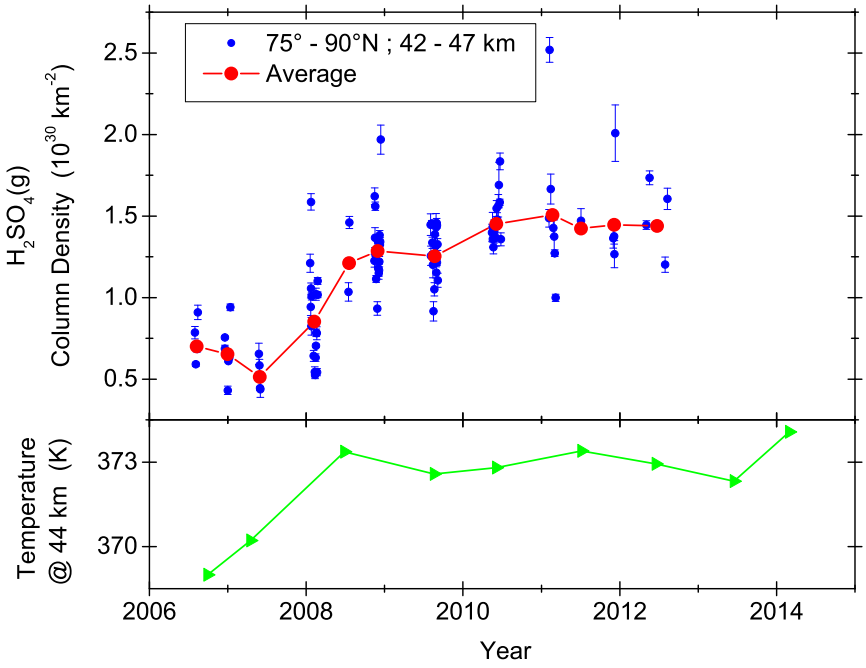

Figure 7.13: *Upper panel: H_2SO_4(g) column density computed between 42 and 47 km altitude in the northern polar region (75° - 90°) between 2006 and 2013. Red data represent averaged values computed from measurements obtained from different occultation seasons. Error bars (0.01 - 0.2·10^{30} km^{-2}) were calculated using the standard error propagation; Lower panel: Temporal evolution of the mean temperature at 44 km altitude in the northern polar region (75° - 90°) between 2006 and 2014. The lower panel was adopted from Figure 7.8.d).*

Figure 7.14 shows the corresponding mean sulfuric acid vapor abundance profiles from the H_2SO_4(g) low (panel a)) and high (panel b)) abundant periods. The profile from the earlier years show an almost constant mean H_2SO_4 abundance of about 4 ppm in the altitude range between 40 and 46 km. The dispersion of the observed values, which emphasizes the variability of the H_2SO_4(g) abundance, is in the order of 2 ppm, increasing to 4 ppm around 41 km altitude. In contrast to this, the profile from the high abundant period shows increased H_2SO_4(g) values below 46 km altitude with the highest abundance of 10 ppm around 43 km. Here, the variability reaches values of up to 12 ppm. Obviously, the enhanced abundance is accompanied by an increased level of dispersion. However, the higher dispersion during the H_2SO_4(g) high abundant period may be a consequence of the larger number of profiles available from the later years compared to the number of profiles from the earlier years. Below 43 km altitude, a gradual decrease of the mean H_2SO_4(g) abundance is visible to lowest values ranging between 6 and 8 ppm around 38 km altitude. Here, the profiles from both, the H_2SO_4(g) low and high abundant periods show similar values.

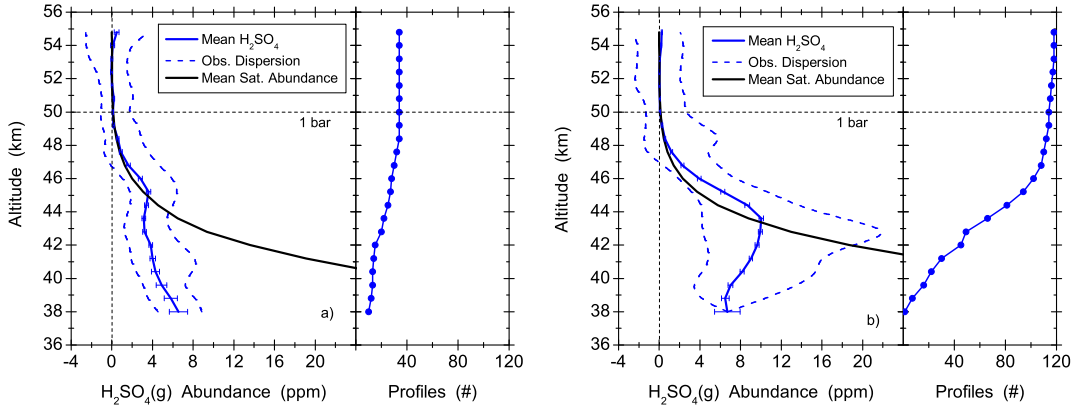

Figure 7.14: *Mean H_2SO_4(g) profiles (blue straight line) and observed variation (blue dashed lines) at the northern polar latitudes between the years 2006 and 2007 (panel a)) as well as between end of 2008 and 2013 (panel b)). Error bars were calculated using the standard error propagation. The mean saturation abundance (black straight line) was computed using equation (5.13). Narrow figures attached to the mean H_2SO_4(g) profiles represent the number of data used for averaging.*

Similar to the long-term trend of the polar SO_2 abundance visible in Figure 7.7.a), that of H_2SO_4(g) is probably caused by the temperature variations presented in Figure 7.8. It is likely that the latter particularly affected the vertical transport in this spatial region and this way increased the abundance of H_2SO_4(g) as well as that of SO_2 in the earlier years of VeRa's observations.

A second reason for the increase of the H_2SO_4(g) abundance before 2010 may be an enhanced production rate of sulfuric acid in the upper cloud region (section 2.2). This can be a consequence of the increased SO_2 content observed at cloud top altitudes in the earlier years (cf. Figure 7.11.a)). The increased production rate may consequently led to enhanced amounts of H_2SO_4 which were transported from higher to lower atmospheric regions by means of downward directed winds at latitudes poleward of 60°.

Additionally, the increase of the temperature in these years may had an direct influence on the H_2SO_4(g) abundance. As an example, the lower panel of Figure 7.13 shows the temporal evolution of the one-year averaged temperature at 44 km altitude adopted from Figure 7.8.d). It is clearly visible that the increase of the H_2SO_4(g) column density around the year 2008 coincides with that of the temperature. The latter led to an increase of the H_2SO_4 saturation vapor pressure (cf. Figure 7.14) so that consequently an enhanced amount of H_2SO_4(g) existed at these altitudes.

The comparison of the long-term trend of H_2SO_4(g) with that of SO_2 reveals that the enhancement of both species between 2006 and 2009 is time-shifted. This is a consequence of the time-shifted temperature increase at different altitudes during this period of time (cf. Figure 7.8).

Local time dependance at equatorial latitudes

The upper panel in Figure 7.15 shows the column density of H_2SO_4(g) in the altitude range between 46 and 50 km at equatorial latitudes as a function of the local time. It can be seen that the values on the nightside of the planet, between 0 h and 3 h, are lower compared to those on the dayside. A mean value of $0.69 \pm 0.02 \cdot 10^{30}$ km^{-2} was derived for the nightside values. In contrast to this, a mean value of $1.03 \pm 0.04 \cdot 10^{30}$ km^{-2} was computed for the dayside column density between 6 h and 10 h local time. The column densities between 18 h and 24 h show a large dispersion, with values similar to those derived for the previous time periods.

Figure 7.16 shows the corresponding mean sulfuric acid vapor abundance profiles. While panel a) represents that obtained from the nightside (0 h - 3 h), panel b) shows the profile from the dayside of the planet between 6 h and 10 h local time. In general, both profiles agree with each other above about 49 km altitude as well as between about 40 and 43 km. A mean value of 4 ppm can be observed around the 1 bar pressure level. Values between 4 and 6 ppm can be seen between 40 and 43 km altitude. Below 40 km altitude, a clear divergence of both profiles is visible with a minimal value of 2 ppm on the dayside and a maximal value of more than 7 ppm on the nightside. In this altitude region, however, the number of H_2SO_4(g) profiles is small so that the divergence may be a consequence of the measurement-to-measurement variability. As can be already seen in Figure 7.12, the highest H_2SO_4(g) abundance can be found in the altitude range between 44 and 49 km. In this altitude region, the largest difference in both profiles can be observed, which leads to the different column density values on the day-and nightside of the planet. Here, maximal values of 8 ppm are visible on the nightside of the planet, while on the dayside about 12 ppm can be seen. Further it is visible that similar to the polar region, the enhanced H_2SO_4(g) values at the equatorial latitudes, are accompanied by an increased level of dispersion. A variation of up to 6 ppm on the nightside and up to 12 ppm on the dayside can be observed. The smaller dispersion on the nightside, however, may be a consequence of the smaller number of profiles from this period of time compared to the number of profiles from the dayside. Similar to the H_2SO_4(g) variation at the northern polar region, that at the equatorial latitudes is most probably caused by variations of the vertical transport which is a consequence of temperature variations in this spatial region.

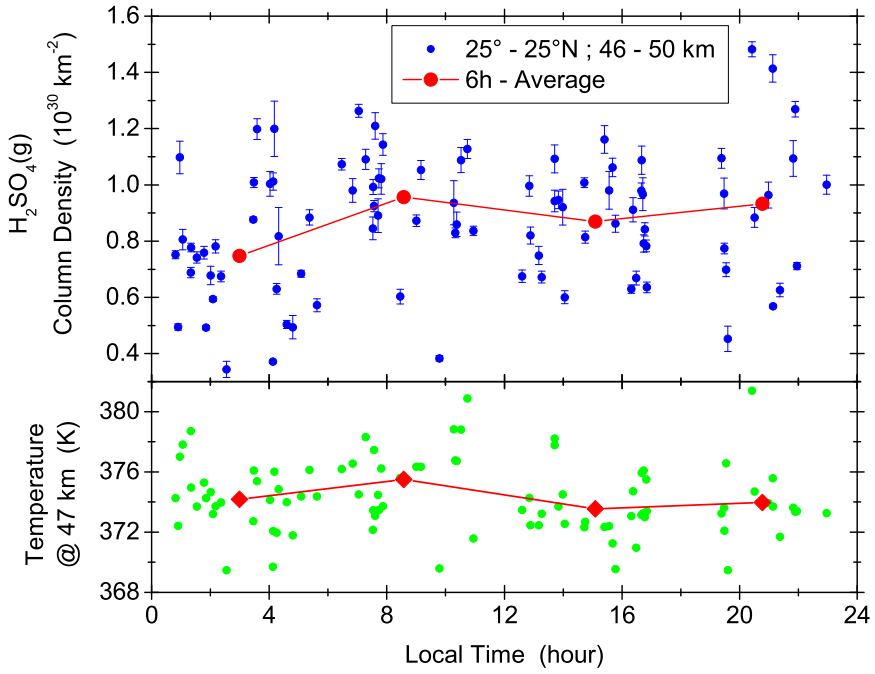

Figure 7.15: *Upper panel: H_2SO_4(g) column density computed between 46 and 50 km altitude in the equatorial region (25°S - 25°N) between the years 2006 and 2014. Error bars, in the order of 0.01 - 0.1·10^{30} km^{-2}, were calculated using the standard error propagation; Lower panel: Temperature at 47 km altitude in the same latitudinal region derived from VeRa's radio occultation data from the years 2006 to 2014. Red data represent mean values resulting from averaging over a time period of 6 hours.*

The lower panel in Figure 7.15 shows the temperature in the equatorial region at 47 km altitude as a function of the local time[2)]. A weak wavelike structure is visible with maximums located between 8 h and 10 h local time and between 20 h and 22 h. The minimums are located between 2 h and 4 h local time and between 14 h and 16 h. The oscillation is emphasized by the red data points which represent mean temperatures resulting from averaging of values located in bins of 6 hours each. It is likely that this oscillation is a global-scale atmospheric wave excited by solar heating, i.e., a thermal tide. The observed period of 12 hours indicates a semidiurnal tide whose influence is strongest at low latitudes (e.g. *Kouyama et al.*, 2019). A clear oscillation with a period of about 12 hours is also visible in the H_2SO_4(g) column density values visible in the

[2)] The temperature at 47 km altitude is shown here representatively for the region between 44 and 49 km, as the largest difference in the day and night H_2SO_4(g) profiles can be observed at this altitude (cf. Figure 7.16).

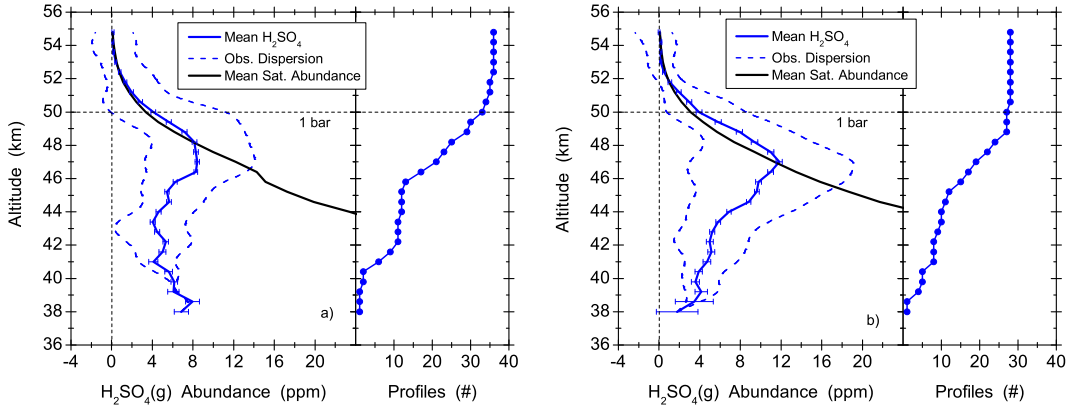

Figure 7.16: *Mean H_2SO_4(g) profiles (blue straight line) and observed variation (blue dashed lines) between 0 and 3 h local time (panel a)) as well as between 6 and 10 h local time (panel b)). Error bars were calculated using the standard error propagation. The mean saturation abundance (black straight line) was computed using equation (5.13). Narrow figures attached to the mean H_2SO_4(g) profiles represent the number of data used for averaging.*

upper panel of Figure 7.15. Similar to the lower panel, it is emphasized by the red data points which represent mean column densities resulting from averaging of values located in bins of 6 hours each.

The oscillations of both, the H_2SO_4(g) column density and that of the temperature are in-phase. The wavelike structure in the H_2SO_4(g) column density values is therefore most probably a manifestation of a tidal influence. The heating of the atmosphere on the dayside of the planet causes an expansion of the air. This process may enhance the vertical transport in the upward directed branch of the Hadley cell at equatorial latitudes. The amount of upward transported H_2SO_4(g) is therefore higher on the dayside than on the nightside of the planet.

In contrast to the polar latitudes, the temperature variation at equatorial latitudes visible in the lower panel of Figure 7.15 was too small to influence the H_2SO_4 saturation vapor pressure (cf. Figure 7.16). It is therefore likely that the variation of the H_2SO_4(g) abundance presented in the upper panel of Figure 7.15 is caused by transport variations, only.

In contrast to H_2SO_4(g), a tidal influence could not be observed in the equatorial SO_2 abundance presented in section 7.2. This is most probably a consequence of the small sensitivity of the X-band radio signals to sulfur dioxide. The increased error bars of the SO_2 values (cf. Figure 7.7.b)) may superimpose any tidal variations.

Comparison with previous observations

Absorptivity and sulfuric acid vapor profiles were previously obtained from Mariner, PVO and Magellan radio occultation measurements (see section 4.2). In the following those are compared with the H_2SO_4(g) abundance derived from VeRa's observations between the years 2006 and 2014.

The red and black profiles in Figure 7.17.a) show the H_2SO_4(g) abundance at equatorial latitudes derived from Mariner V observations at the planet's nightside and dayside, respectively, adopted from Figure 4.2. Equation (4.20c) was used to transfer S-band absorptivity profiles published by the *Mariner Stanford Group* (1967) as well as by *Fjeldbo et al.* (1971) into H_2SO_4(g) profiles. The green profile in Figure 7.17.a) show the equatorial sulfuric acid vapor abundance derived by *Kolodner and Steffes* (1998) from Mariner 10 radio occultation data. For comparison, the mean H_2SO_4(g) profiles derived from VeRa's measurements between the years 2006 and 2014 at the equatorial day- and nightside shown in Figure 7.16 were averaged to one profile. While the latter is presented by the straight blue profile in Figure 7.17.a), the dashed blue profiles show its observed variation.

Although with a few minor exceptions the mean H_2SO_4(g) profile derived from VeRa's observations show higher abundance values than the Mariner profiles, a gen-

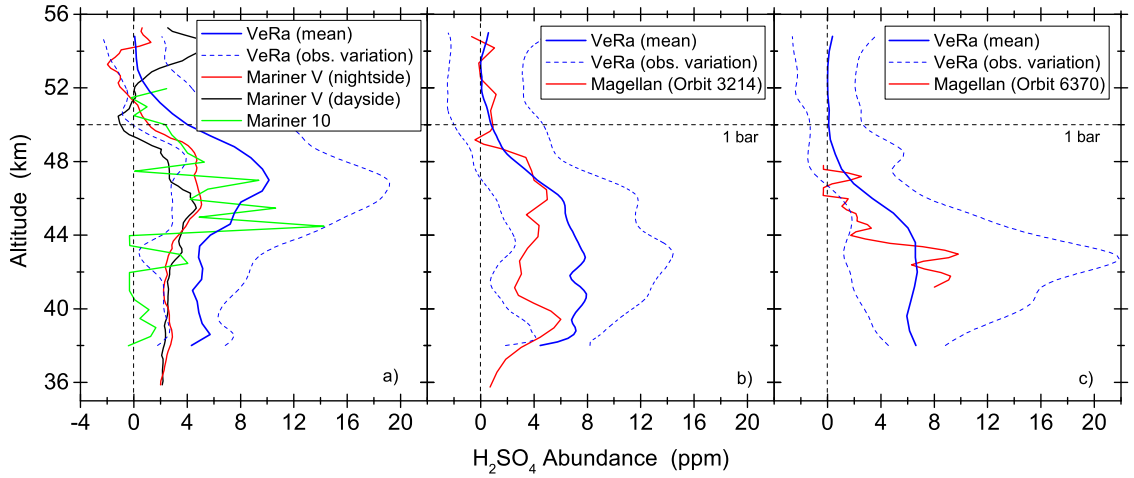

Figure 7.17: *Sulfuric acid vapor abundance profiles obtained from Mariner, Magellan and Venus Express radio occultation measurements at different latitudinal regions: a) equatorial latitudes, b) 65 - 70°S/N, c) polar region. Profiles from the Mariner observations were adopted from Figure 4.2 and Figure 4.3. While the Magellan profile in panel b) was adopted from Figure 4.5, that in panel c) was adopted from Kolodner and Steffes (1998).*

eral agreement is visible within the observed variation of the VeRa profiles (dashed blue lines). All profiles show the highest H_2SO_4(g) abundance values in the altitude range between 44 and 50 km as well as a gradual decrease below that altitude region. Below 42 km altitude, the profile derived from the Mariner 10 measurement show the lowest H_2SO_4(g) values which barely exceed 2 ppm. Such low values at these altitudes were neither observed by the Mariner V nor by the Venus Express spacecraft. This shows that the variation of the H_2SO_4(g) abundance exceeds that observed by VeRa between the years 2006 and 2014. The enhanced oscillations visible in the Mariner V and Mariner 10 H_2SO_4(g) profiles above about 50 km altitude are most probably caused by noise and/or atmospheric turbulence rather than by variation in the sulfuric acid vapor abundance.

In the panels b) and c) of Figure 7.17 mean H_2SO_4(g) abundance profiles obtained from VeRa's measurements are compared with those obtained from the Magellan spacecraft. The red profile in panel b) shows the H_2SO_4(g) abundance derived from Magellan's X-band absorptivity data at the *cold collar* latitudes adopted from Figure 4.5. Equation (4.20b) was used to transfer Magellan's absorptivity data into sulfuric acid vapor abundance profiles. The straight blue profile shows the mean H_2SO_4(g) abundance derived from VeRa's measurements, while the dashed lines represent its variation. Data obtained from the years between 2006 and 2014 from the latitudes between 65 - 70°S/N were used. Panel c) shows the mean H_2SO_4(g) abundance and its variation at the northern polar latitudes derived from VeRa's measurements from the years 2006 to 2014 (blue profiles) along with a southern polar H_2SO_4(g) profile derived by *Kolodner and Steffes* (1998) from Magellan's S-band absorptivity data. The blue profile represents the mean H_2SO_4(g) abundance computed from the profiles shown in Figure 7.14.

It is clearly visible that the H_2SO_4(g) profiles derived from Magellan's and VeRa's absorptivity data are consistent with each other within VeRa's H_2SO_4(g) variation range (dashed blue lines) at both latitudinal regions. Both profiles show enhanced abundance values below about 48 km altitude as well as relatively low values above that region.

The comparison of abundance profiles derived from Mariner's occultation measurements with those derived from Magellan's data indicates a latitudinal dependance of H_2SO_4(g) similar to that found in VeRa's observations (cf. Figure 7.12). A clear latitudinal variation was observed by *Cimino* (1982) as well as by *Jenkins and Steffes* (1991) in the S-band radio absorptivity derived from Pioneer Venus radio occultation measurements. Those are presented in Figure 4.4. They detected an increased absorption of the S-band radio signal just below the cloud bottom ($\sim$ 50 km) at equatorial latitudes indicating enhanced H_2SO_4(g) abundance values in this spatial region. *Cimino*

(1982) additionally observed a decrease of the absorption with decreasing altitude, so that in general the vertical distribution of the S-band absorption at the lower latitudes is similar to the equatorial H_2SO_4(g) abundance presented in the Figures 7.12, 7.16 and 7.17.a).

Increased S-band absorption at latitudes $\geq 70°$ was detected at lower altitudes compared to the equatorial region. This is consistent with the polar vertical H_2SO_4(g) distribution derived from VeRa's data (cf. Figures 7.12, 7.14 and 7.17.c)). *Jenkins and Steffes* (1991) additionally observed that the S-band absorption between about 43 and 48 km altitude at northern latitudes between 72° - 80° is higher compared to that at latitudes $\geq 85°$N in the same altitude region (cf. Figure 4.4.e)). This is consistent with the polar H_2SO_4(g) distribution derived from VeRa's measurements presented in Figure 7.12. It is clearly visible that the highest H_2SO_4(g) abundance at the northern polar latitudes is located between about 70° and 80°. This distribution of H_2SO_4(g) may be a consequence of the transport mechanisms within the polar region.

The comparison of the S-band absorptivity profiles obtained by *Cimino* (1982) from the *cold collar* latitudes (panel c) in Figure 4.4) with those achieved by *Jenkins and Steffes* (1991) (panel e) in Figure 4.4) from the same latitudinal region reveals a clear difference. The first mentioned profiles, obtained during the years 1978/1979, show distinctly higher absorptivity values than the second mentioned profiles which were achieved in the years 1986/1987. The distinct lower absorption values observed during the latter period indicates a decrease of H_2SO_4(g) between the years 1978/1979 and 1986/1987 in this spatial region as previously mentioned by *Jenkins and Steffes* (1991).

This long-term variation at higher latitudes is similar to that in the H_2SO_4(g) abundance observed at the northern polar latitudes ($\geq 75°$) between the years 2006 and 2013 (cf. Figures 7.13 and 7.14). The latter was most probably caused by an increased production rate of H_2SO_4 at higher altitudes and/or long-term variations of the temperature shown in Figure 7.8. As mentioned in the context of the SO_2 long term variation in section 7.2 (Figure 7.11), the significant temperature increase observed before the year 2010 may be a consequence of the decrease of Venus' 365 nm albedo. The latter was observed by *Lee et al.* (2015) as well as by *Lee et al.* (2019) at all latitudinal regions. The albedo decrease was preceded by an increase of the unknown UV absorbing gas species, whose precursor is thought to be sulfur dioxide (e.g. *Mills et al.*, 2018). Enhanced values of the latter were observed by *Marcq et al.* (2020) between the years 2006 and 2010 (cf. Figures 2.4.b) and 7.11.a)).

Similarly high SO_2 abundance values were reported by *Esposito et al.* (1988) at cloud top altitudes. They observed distinctly enhanced SO_2 values around the year

1978 and a gradual decrease in the later years. The increased SO_2 abundance could have increased the content of the unknown UV absorber so that a resultant increased absorption of the solar flux led to a heating of the atmosphere[3)]. The latter may have increased the amount of H_2SO_4(g) by affecting the vertical transport and the saturation vapor pressure of H_2SO_4. Additionally, as already mentioned in the context of the H_2SO_4(g) long-term variations observed in VeRa's data (cf. Figure 7.13), the enhanced SO_2 content in the upper clouds may have increased the production rate of sulfuric acid in this altitude region. This way an increased amount of H_2SO_4 may have been transported to lower altitudes. Consequently, an enhanced absorption of PVO's S-band radio signal was observed when the latitudinal region between 70° and 80° was sounded during this period of time.

The occurrence of enhanced SO_2 abundance values at cloud top altitudes and increased absorption/H_2SO_4(g) values in the lower atmosphere observed in the years 1978/1979 is similar to that observed between the years 2007 and 2009 (cf. Figure 7.11.a) and 7.13). It is therefore likely that the events occurred at both time periods are triggered by similar mechanisms. Volcanic forcing as well as periodic changes in atmospheric dynamics were proposed by various authors as reasons for the observed rapid increase in SO_2 at cloud top altitudes (e.g. *Esposito et al.*, 1988; *Marcq et al.*, 2012).

[3)] Neither *Cimino* (1982), nor *Jenkins and Steffes* (1991) provided any corresponding temperature profiles. A study of its temporal evolution, similar to that presented in Figure 7.8, is therefore not possible on the basis of PVO's data.

Chapter 8

Model results and comparison with observations and previous simulations

The zonally averaged H_2SO_4(g) distribution presented in Figure 7.12 shall be reproduced by using the transport model described in chapter 5. This way conclusions about the formation processes of the H_2SO_4(g) high abundant regions can be drawn. For this purpose, a total number of seven main simulation runs are conducted, each with different model settings. At each run the model is checked for its ability to reproduce the H_2SO_4(g) accumulated regions at equatorial and high latitudes.

In *Test 0*, the influence of the global temperature distribution in combination with sedimentation and diffusion is studied. For this purpose, the wind transport in equation (5.14) is neglected and two model runs are performed: *a)* The observed temperature distribution shown in Figure 2.1a) is used in the background atmosphere of the model; *b)* The latitudinal temperature gradient is removed so that the background atmosphere of the model consists of the equatorial vertical temperature distribution, only. In *Test 1*, wind transport is considered by including the two convection cells presented in section 5.1 into the model and the simulation is performed using the observed temperature gradient. The significance of the individual Hadley and polar convection cells is studied in *Test 2* and *Test 3*. Similar to the simulation run *Test 0*, two simulation runs, i.e., *a)* and *b)*, shall be performed. Table 8.1 summarizes the model settings for all executed simulation runs.

Section 8.1 presents the global H_2SO_4(g) distributions obtained from the simulation runs *Test 0* to *Test 3* (section 8.1.1) as well as the comparison with VeRa's observations (section 8.1.2). The global distribution of the Venus clouds and that of water vapor obtained from the simulations are presented in section 8.2. A comparison with previous observations as well as with other model results is given in section 8.3.

Simulation run	Convection cells		Temperature distribution
	Hadley	Polar	
Test 0	No	No	*a)* observed *b)* $\mathrm{d}T/\mathrm{d}\phi = 0$
Test 1	Yes	Yes	*a)* observed
Test 2	Yes	No	*a)* observed *b)* $\mathrm{d}T/\mathrm{d}\phi = 0$
Test 3	No	Yes	*a)* observed *b)* $\mathrm{d}T/\mathrm{d}\phi = 0$

Table 8.1: *Summary of conducted simulation runs. A total number of 7 runs are performed (Test 0 a), b),..., Test 3 a), b)) in order to study the influence of the transport mechanisms and that of the latitudinal temperature distribution on the computed zonally averaged H_2SO_4(g) abundance. The expressions 'Yes' and 'No' stand for 'implemented' and 'not implemented', respectively. The latitudinal temperature distribution used in the background atmosphere of the model is presented by a) and b). Test 1b) is not necessary, since this case is included in Test 2b) and Test 3b).*

8.1 Model results and comparison with VeRa

All simulation runs are performed until a steady state is achieved for the global distributions of n_l^{gas} and n_l^{liq}. The following settings are used in all simulation runs:

$$dz = 0.5 \text{ km}$$
$$d\phi = 1^\circ$$
$$dt = 6 \text{ hours}.$$

8.1.1 Modeled H_2SO_4(g) distribution

Comparison of results obtained from Test 0 and Test 1

Three simulation runs are performed here. The influence of the latitudinal temperature gradient on the global H_2SO_4(g) distribution is studied in *Test 0a)* and in *Test 0b)*. The mass transport is controlled solely by sedimentation and eddy diffusion. Wind transport is neglected. The influence of the latter is additionally considered in

Test 1, where the observed temperature distribution is used (*Test 1a)* in Table 8.1). Figure 8.1 shows the results.

The upper and middle panels in Figure 8.1 show the H_2SO_4(g) distributions obtained from the simulation runs *Test 0a)* and *Test 0b)*. A clear difference in the abundances and distributions can be seen. In general, the upper panel shows distinctly higher sulfuric acid vapor values compared to those in the middle panel. Additionally, the H_2SO_4(g) distribution obtained from *Test 0a)* reveals an enhanced accumulation located at polar latitudes which is missing in *Test 0b)*. Both features are consequences of the respective global temperature distributions (cf. Figure 2.1a)).

Gaseous sulfuric acid is produced in the upper cloud region around 66 km altitude where it rapidly condensates into droplets due to the low temperatures. In the model run *Test 0a)*, the condensation rate increased with latitude as a consequence of the latitudinal temperature gradient. The increased condensation rate enhanced the amount of H_2SO_4-H_2O droplets at high latitudes. The latter was constantly higher than the equatorial droplet amount, despite the fact that the H_2SO_4(g) production was highest at lower latitudes (cf. equation (5.21)). Consequently, the downward transport by sedimentation and diffusion as well as the subsequent evaporation at lower altitudes led to the enhanced H_2SO_4(g) accumulation at high latitudes visible in the upper panel. Values of up to 20 ppm can be found poleward of 75° around 41 km altitude. In the deeper atmosphere, thermal decomposition (cf. equations (2.2), (2.3), (5.22)) led to a loss of H_2SO_4(g) so that a decrease of the gas abundance is visible below that altitude. In the equatorward direction, the gas abundance decreases gradually as a consequence of the weaker H_2SO_4 supply from higher altitudes. Maximal values of 8 to 11 ppm can be found at low and mid-latitudes. Those are located at higher altitudes compared to the highest values in the polar region as indicated by the white dashed line in Figure 8.1. Obviously, the altitude of the maximal H_2SO_4(g) abundance follows the latitudinal temperature gradient. The latter caused a latitudinal variation of the evaporation rate of the downward transported droplets. This is also the reason for the latitudinal trend of the H_2SO_4(g) haze layer's topside.

As the latitudinal temperature gradient was removed in *Test 0b)*, the condensation rate in the clouds was constantly highest at the equatorial latitudes. This is a consequence of the solar zenith angle dependance of the H_2SO_4(g) production. Therefore, in contrast to the increased amount of H_2SO_4-H_2O cloud droplets at high latitudes in *Test 0a)*, the droplet amount in *Test 0b)* was highest in the equatorial region. The general supply of liquid H_2SO_4 from the upper clouds, however, was lower compared to that at high latitudes in *Test 0a)*. Additionally, eddy diffusion distributed the gaseous and liquid particles in the vertical direction so that only small H_2SO_4(g) amounts are visible

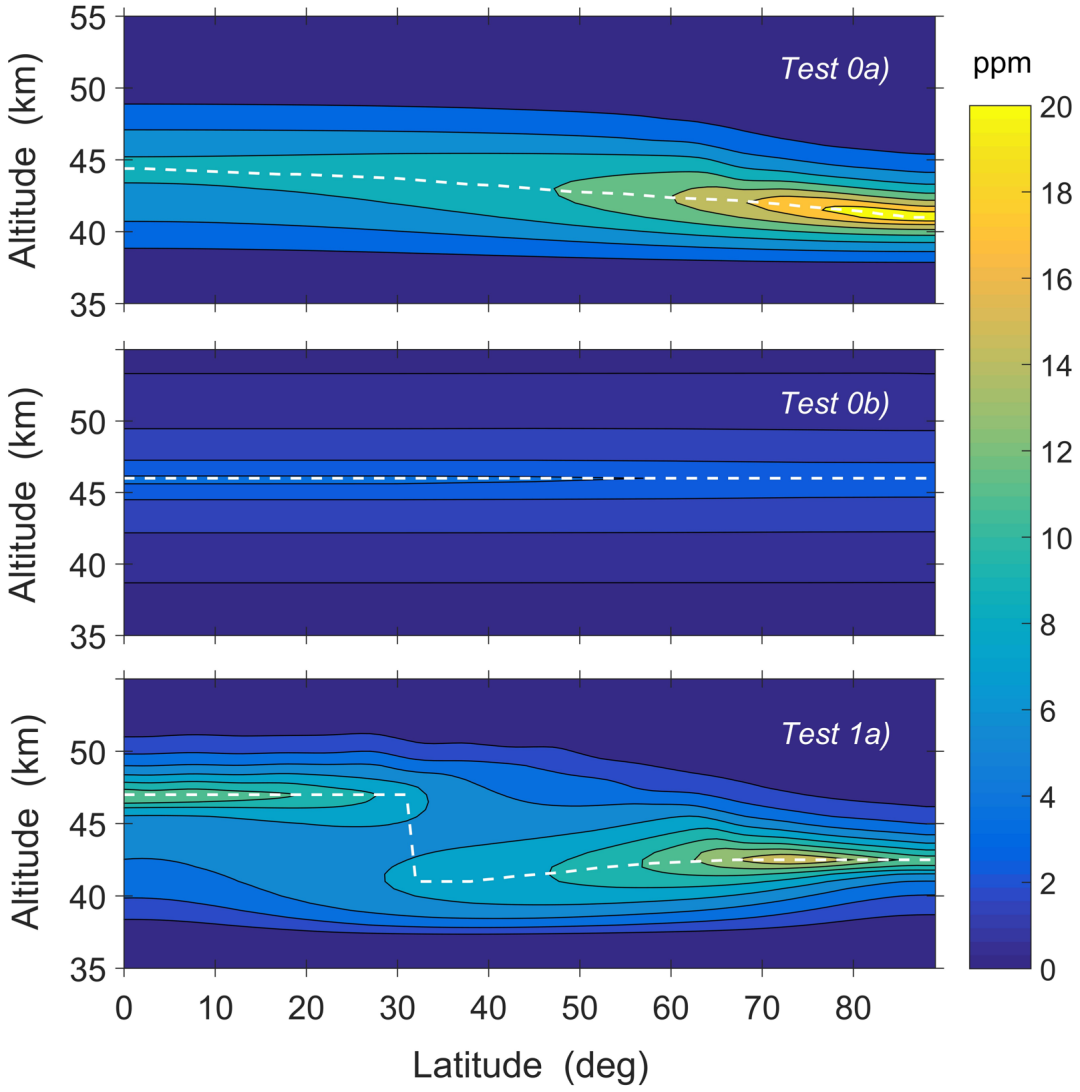

Figure 8.1: *$H_2SO_4(g)$ distribution in Venus' northern hemisphere obtained from the simulation runs Test 0a), Test 0b) and Test 1a). The white dashed lines mark the altitude of the highest $H_2SO_4(g)$ abundance.*

in the haze layer below about 50 km altitude. Maximal values of less than 3 ppm can be found around 46 km at the equatorial latitudes. The gas content barely decreases towards the polar region and maximal H_2SO_4(g) values are constantly located around 46 km altitude (white dashed line) which is a consequence of the missing temperature gradient. The latter is also responsible for the absence of the latitudinal trend of the topside of the haze layer.

The lower panel in Figure 8.1 shows the H_2SO_4(g) distribution obtained from the simulation run *Test 1a)*. In addition to sedimentation and eddy diffusion, the mass transport by wind was considered here and the background atmosphere contained the observed global temperature distribution visible in Figure 2.1a). In the following, the H_2SO_4(g) distributions obtained from *Test 1a)* and *Test 0a)* are compared. The influence of wind transport is obvious so that distinct differences are visible.

The global H_2SO_4(g) abundance obtained from *Test 1a)* is lower compared to that obtained from *Test 0a)*. This is mainly a consequence of the additional vertical transport by wind: 1) The descending branches of the Hadley and polar cells transported increased contents of H_2SO_4(g) into the altitude region between 35 and 40 km where it was horizontally distributed and thermally decomposed. A bulge has formed at the bottom of the H_2SO_4(g) haze layer as a result of the enhanced supply. 2) The ascending branches of both circulation cells transported H_2SO_4(g) from the haze layer to upper altitudes. Here, the gas condensed into droplets due to lower temperatures and this way decreased the haze abundance and increased the content of the clouds. The obtained global distribution of the latter is discussed in section 8.2.

The H_2SO_4(g) distribution obtained from *Test 1a)* reveals a clear accumulation at the equatorial region instead of an almost uniform haze layer at low and mid-latitudes as was obtained from *Test 0a)*. The associated formation process was previously described for example by *Knollenberg and Hunten* (1980) as well as by *Imamura and Hashimoto* (1998). H_2SO_4(g) was transported within the upwelling branch of the Hadley cell from lower to higher altitudes. Due to the low temperatures in this region, the gas condensed into droplets and fell back to lower altitudes. This opposite directed mass transport is therefore responsible for the H_2SO_4(g) accumulation visible at equatorial latitudes in the lower panel. Here peak values of about 12 ppm were reached around 47 km altitude. An additional simulation run with a circulation velocity decreased by 50% led to a lowering of that altitude by about 2 km. Moreover, the maximal H_2SO_4(g) abundance increased to more than 20 ppm due to the higher saturation vapor pressure at lower altitudes. Panel a) in Figure 8.2 shows the corresponding vertical H_2SO_4(g) profiles. It is obvious that the altitude of the maximum H_2SO_4(g) abundance depends on the velocity of the vertical wind.

The descending branches of the circulation cells located at mid-latitudes, transported increased H_2SO_4(g) amounts into the lower region. As a consequence, the highest H_2SO_4(g) values at mid-latitudes are located deeper when compared to those in the upper panel (cf. white dashed lines in Figure 8.1). Abundances of 7 to 8 ppm can be seen between 30° and 40° around 41 km altitude. From here, a gradual increase of the values towards the polar region is visible with highest abundances of about 16

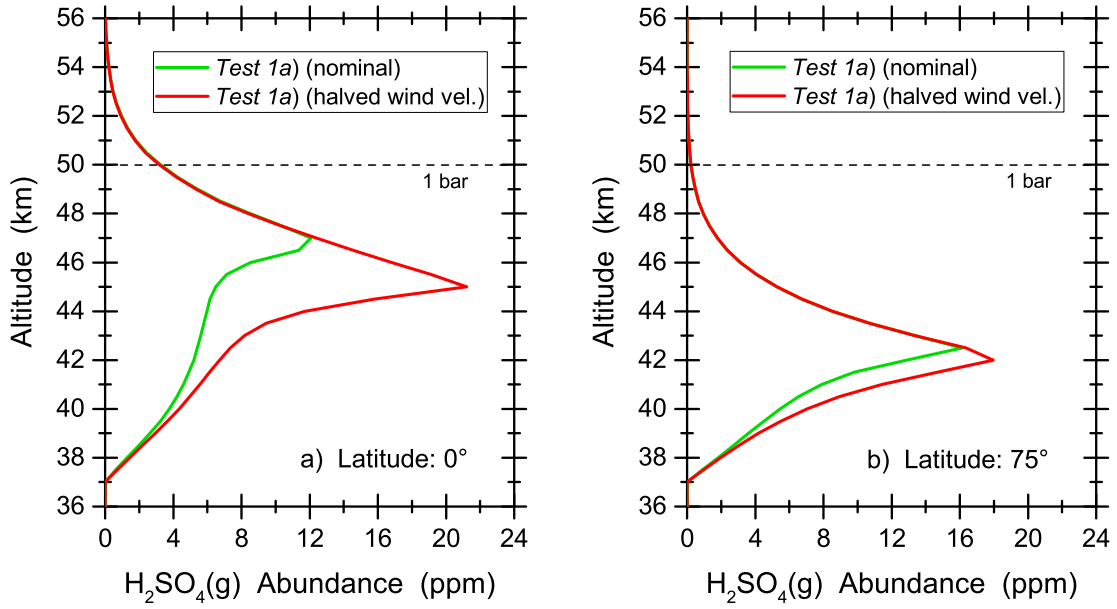

Figure 8.2: *Vertical profiles of H_2SO_4(g) in Venus' equatorial and polar atmosphere (panel a) and b), respectively) obtained from the simulation run Test 1a) performed with different circulation velocities of the Hadley and polar cells. The horizontal dashed lines show the approximate altitude of the 1 bar pressure level.*

ppm located between 70° and 75° at 42.5 km altitude.

The ascending branch of the polar cell, located poleward of 75°, transported sulfuric acid vapor to higher altitudes, where it condensed into droplets. This way, the enhanced content of the haze was reduced at these latitudes, while the density of the clouds increased. The process is similar to that caused by the Hadley cell at equatorial latitudes. The altitude of the peak H_2SO_4(g) abundance also depends on the strength of the upward directed wind of the circulation cell. It was lowered to 42 km in an additional simulation run where the circulation velocity was reduced by 50%. The maximum H_2SO_4(g) abundance increased to more than 18 ppm due to the higher saturation vapor pressure at lower altitudes. The corresponding vertical H_2SO_4(g) profiles can be seen in panel b) of Figure 8.2.

The comparison of both panels in Figure 8.2 reveals that the influence of the circulation cells is more pronounced at the equatorial latitudes. Their impact on the global H_2SO_4(g) distribution is studied in the simulation runs *Test 2* and *Test 3*.

Comparison of results obtained from Test 2 and Test 3

Four simulation runs are performed to study the individual influences of the respective cells. In each run, one circulation cell is removed and the simulation is performed twice, *a)* with and *b)* without the observed latitudinal temperature gradient in the background atmosphere. *Test 2* was performed using the Hadley cell and in *Test 3* the polar cell was present (cf. Table 8.1). Figure 8.3 shows the results.

Obviously, the enhanced H_2SO_4(g) accumulation at equatorial latitudes has only formed when the Hadley cell was present. As it can be seen from the simulation runs

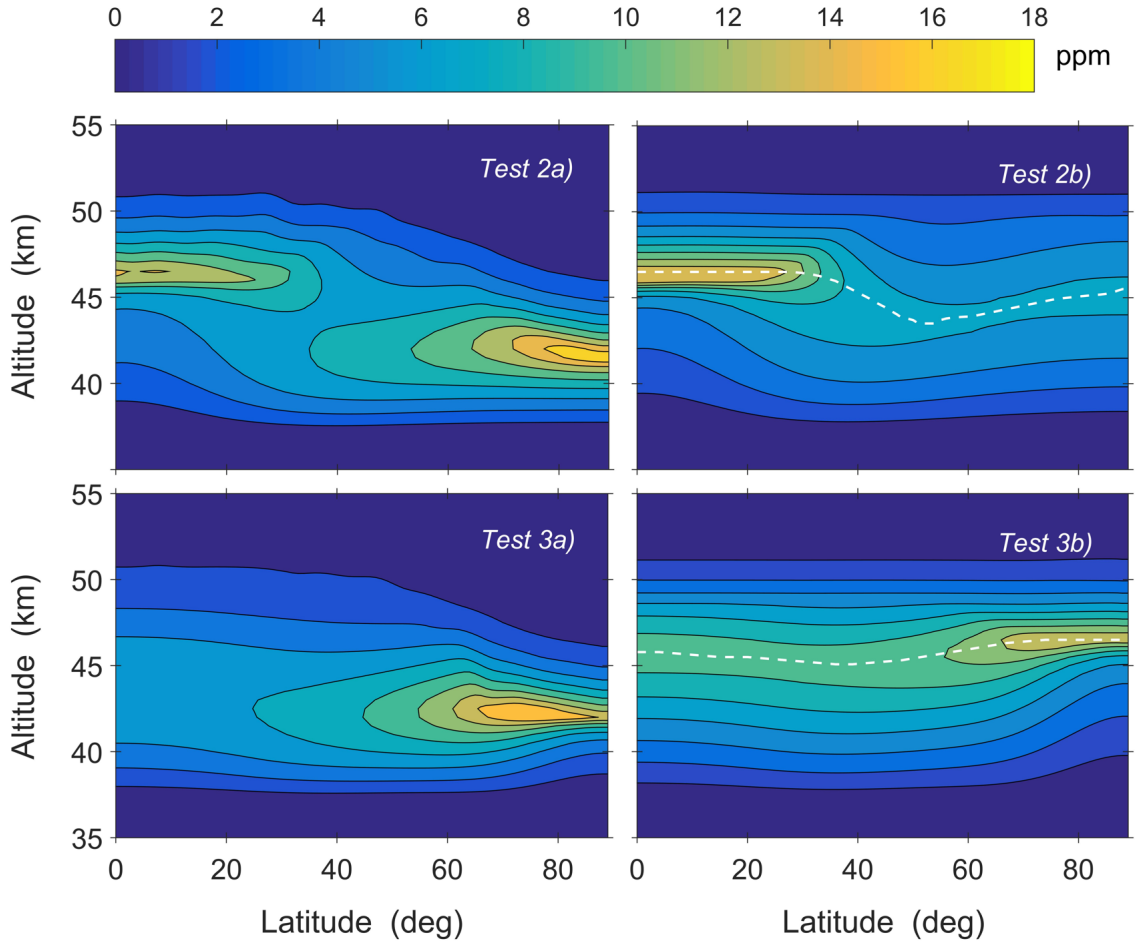

Figure 8.3: *H_2SO_4(g) distribution in Venus' northern hemisphere obtained from the simulation runs Test 2a) and b) as well as from Test 3a) and b). The white dashed lines in Test 2b) and Test 3b) mark the altitude of the highest H_2SO_4(g) abundance.*

Test 2a) and *Test 2b)*, the occurrence of the increased values obviously did not depend on the global temperature distribution. Rather the interaction of upward directed winds and sedimentation was the driving mechanism for its formation.

The low temperatures at higher latitudes in *Test 2a)*, however, increased the density of the cloud droplets in this spatial region compared to *Test 2b)*. The downward transport and evaporation of the latter led to the formation of the enhanced H_2SO_4(g) accumulation below about 45 km altitude located at the mid- and high latitudes. This effect was already demonstrated in the simulation run *Test 0a)* (Figure 8.1). The influence of the polar cell on this formation process was obviously small. For this reason, the global distribution of H_2SO_4(g) obtained from *Test 2a)* (polar cell not included) is similar to that obtained from *Test 1a)* (polar cell included). Upward winds located poleward of 75°, however, may constantly remove haze into higher altitudes so that highest H_2SO_4(g) values are located at lower latitudes when a polar cell is present.

The small impact of the polar cell was confirmed by the simulation run *Test 3a)*. Here, the Hadley cell was removed and the polar cell was responsible for the wind transport. As expected, its influence is visible at the highest latitudes, where the upward winds lifted the bottom of the H_2SO_4(g) haze layer to higher altitudes and reduced the H_2SO_4(g) content by constantly removing the gas into the clouds.

As the latitudinal temperature gradient was removed in *Test 3b)*, a region of enhanced H_2SO_4 vapor has formed between 45 and 48 km altitude. This is the consequence of the interaction of upward directed winds of the polar cell and sedimentation. The formation process is identical to that caused by the Hadley cell at equatorial latitudes. The polar cell in *Test 3b)* was not capable of forming an enhanced H_2SO_4(g) accumulation below about 45 km altitude.

The influence of the Hadley and polar cells was not limited to the corresponding latitudinal regions. This becomes most clear when the H_2SO_4(g) distributions obtained from *Test 2b)* and *Test 3b)* are compared with that obtained from *Test 0b)* (Figure 8.1). Obviously, the H_2SO_4(g) abundance increased globally when at least one circulation cell was present. Apart from the regions of enhanced accumulations, the highest values increased from less than 3 ppm in *Test 0b)* to 7 - 10 ppm in *Test 2b)* and *Test 3b)*. The altitude of the maximal H_2SO_4(g) abundance is marked by the white dashed lines in the corresponding figures.

The results of the simulation runs *Test 0a)* to *Test 3b)* are summarized in table 8.2. The region of enhanced H_2SO_4(g) accumulation at equatorial latitudes has only formed when the Hadley cell was present. No influence of the global temperature

Simulation run	Convection cells		Temperature distribution	H_2SO_4(g) accumulation	
	Hadley	Polar		Equatorial	Polar
Test 0	No	No	*a)* observed	✗	✓
			b) $dT/d\phi = 0$	✗	✗
Test 1	Yes	Yes	*a)* observed	✓	✓
Test 2	Yes	No	*a)* observed	✓	✓
			b) $dT/d\phi = 0$	✓	✗
Test 3	No	Yes	*a)* observed	✗	✓
			b) $dT/d\phi = 0$	✗	✗

Table 8.2: *Summary of the results derived from the conducted simulation runs (cf. table 8.1).*

distribution was found. The increased H_2SO_4(g) content below about 45 km at mid- and polar latitudes was formed by the downward transport of an increased number of cloud droplets at these latitudes. The enhanced droplet densities were favored by the low temperatures at high latitudes. The influence of the polar cell was small.

8.1.2 Comparison with VeRa

The global distribution of H_2SO_4(g) as observed by VeRa could be successfully reproduced by the simulation runs *Test 1a)* and *Test 2a)*. While the Hadley circulation was included in both runs, the polar cell was only present in *Test 1a)*. Due to the small influence of the latter on the formation process of the H_2SO_4(g) accumulation at mid- and high latitudes, both simulation runs provided similar results.

In the following, those are compared with observations obtained from VeRa's radio occultation experiment. The focus is put on small differences between the observed and the modeled results.

The upper and middle panels of Figure 8.4 show the global H_2SO_4(g) distributions obtained from both successful simulations runs *Test 1a)* and *Test 2a)*. The zonally and temporal averaged H_2SO_4(g) distribution obtained from VeRa is presented in the lower panel for comparison. It is clearly visible that the regions of enhanced H_2SO_4(g) ob-

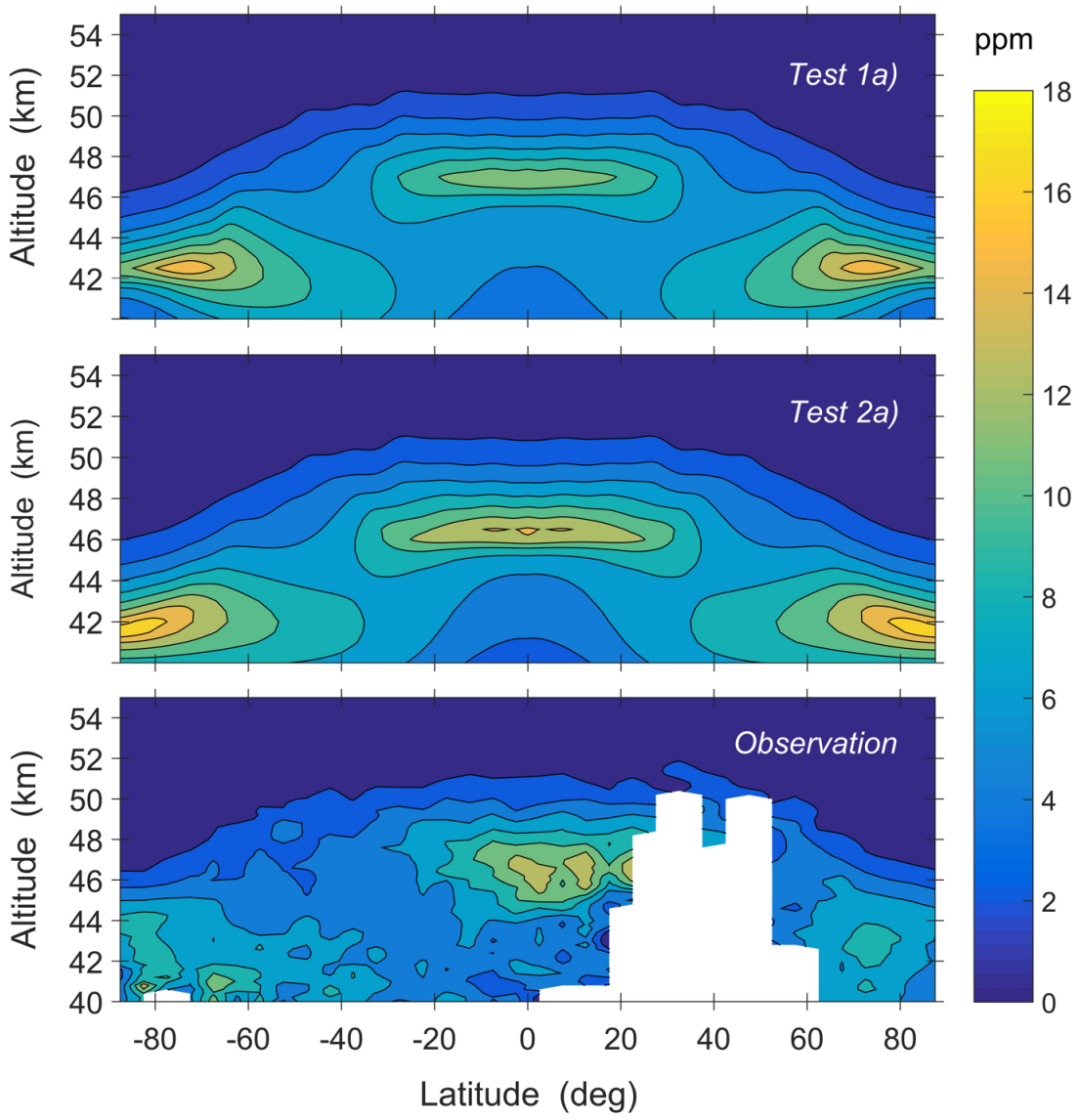

Figure 8.4: *$H_2SO_4(g)$ distribution in Venus' atmosphere obtained from the simulation runs Test 1a) (upper panel), Test 2a) (middle panel) as well as derived from VeRa's radio occultation observations (lower panel) adopted from Figure 7.12.*

tained from observations and simulations are in excellent global agreement. However, small differences in the abundances can be seen at the equatorial and the mid-/polar latitudes.

Equatorial latitudes

The H_2SO_4(g) accumulated region at the equatorial latitudes has formed in both simulation runs as a consequence of the interaction of sedimentation and upward directed winds within the ascending branch of the Hadley cell. It is clearly visible from Figure 8.4 that the location of the modeled H_2SO_4(g) accumulation at these latitudes in general agree with that observed by VeRa. Moreover, the H_2SO_4(g) abundances of the modeled regions (peak values of 12 - 15 ppm) agree well with the observed ones ($\sim$ 13).

However, small differences can be seen below the locations of the highest H_2SO_4(g) abundances in the altitude range between about 44 and 47 km. Here, the decrease of H_2SO_4(g) is more pronounced in the model results compared to the observed decrease. This can be clearly seen in Figure 8.5a). In contrast to the mean H_2SO_4(g) profile observed by VEX, the profiles obtained from *Test 1*a) and *Test 2*a) show a rapid decline of the haze between about 44 and 47 km altitude. The difference may have several reasons:

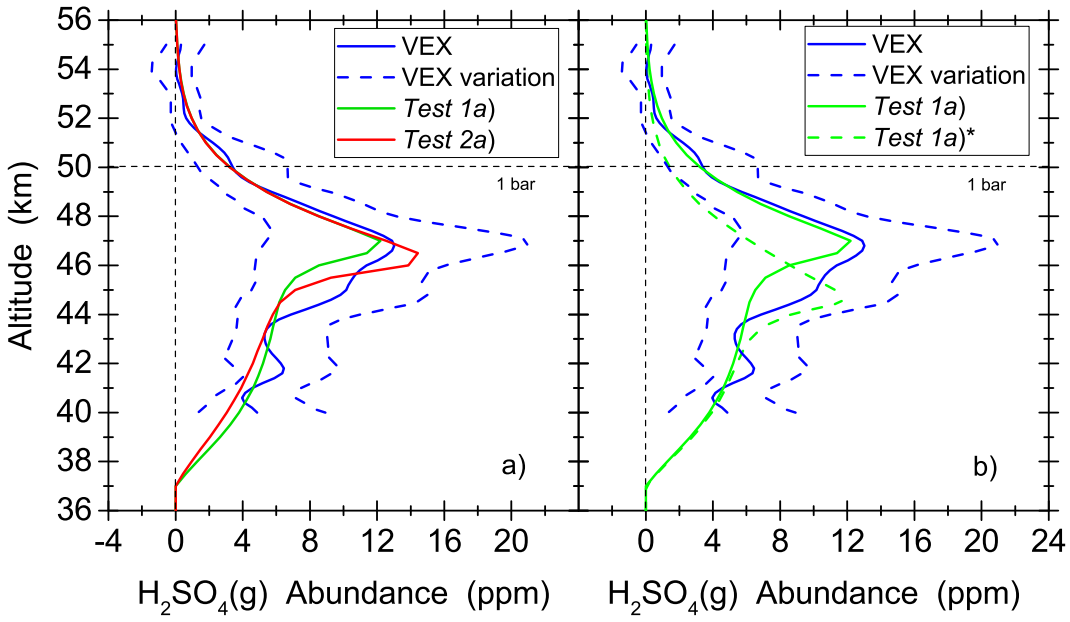

Figure 8.5: *Vertical profiles of H_2SO_4(g) at equatorial latitudes obtained from VeRa's observations as well as from the simulation runs Test 1a) and Test 2a). For the run Test 1a)* the global temperature was decreased by 10 K. Test The horizontal dashed lines show the approximate altitude of the 1 bar pressure level.*

i) The comparison of the profile obtained from *Test 1*a) with that obtained from *Test 2*a) shows that variations of the polar cell may affect the H_2SO_4(g) abundance at the equatorial latitudes. Obviously, the absence of the polar cell in *Test 2*a) led to higher haze contents at equatorial latitudes. Moreover, the location of the H_2SO_4(g) peak value moved to lower altitudes. The influence of both circulation cells on the global H_2SO_4(g) distribution can also be seen in Figure 8.3.

ii) The difference may also be associated with vertical wind velocity variations in this spatial region. Their occurrence is most likely in Venus' atmosphere but they were not included in the simulation runs. Instead, constant upward winds were applied in the model, whose vertical velocities are presented in Figure 5.2. Figure 8.2a) shows that the altitude of the peak abundance can move to lower altitudes when the wind velocity is reduced by 50%.

iii) Wind velocity variations can be caused by temperature variations. The latter may also impact the cloud density and this way influence the amount of downward transported H_2SO_4-H_2O droplets into the deeper atmosphere where liquid H_2SO_4 evaporates into gas. This may affect the altitude of the maximal H_2SO_4(g) abundance. In an additional simulation run, a decrease of the global temperature by 10 K lowered the location of the peak abundance by about 2 km. The corresponding profile is presented in panel b) of Figure 8.5.

iv) Temperature variations can also have a significant influence on the saturation vapor pressure of sulfuric acid and may therefore affect the abundance of H_2SO_4(g) as well as the location of the maximal value.

The above mentioned factors may contribute to a significant variation of the abundance and location of the H_2SO_4(g) peak values at equatorial latitudes. They are not mutually exclusive. Rather they act interdependently and this way most probably affect the vertical extension of the H_2SO_4(g) accumulation in this spatial region.

Mid- and high latitudes

The H_2SO_4(g) accumulated region at mid- and high latitudes below about 45 km altitude has formed in both simulation runs as a consequence of the increased evaporation of an enlarged number of cloud droplets. The presence of the latter was the result of the low temperatures in this spatial region. The contribution of the polar cell to the formation process of the H_2SO_4(g) accumulation was minor. Its influence is most visible at the highest latitudes, $\geq 70°$, where upward directed winds transported the gas into the clouds. This way the H_2SO_4(g) abundance below about 42 km altitude was

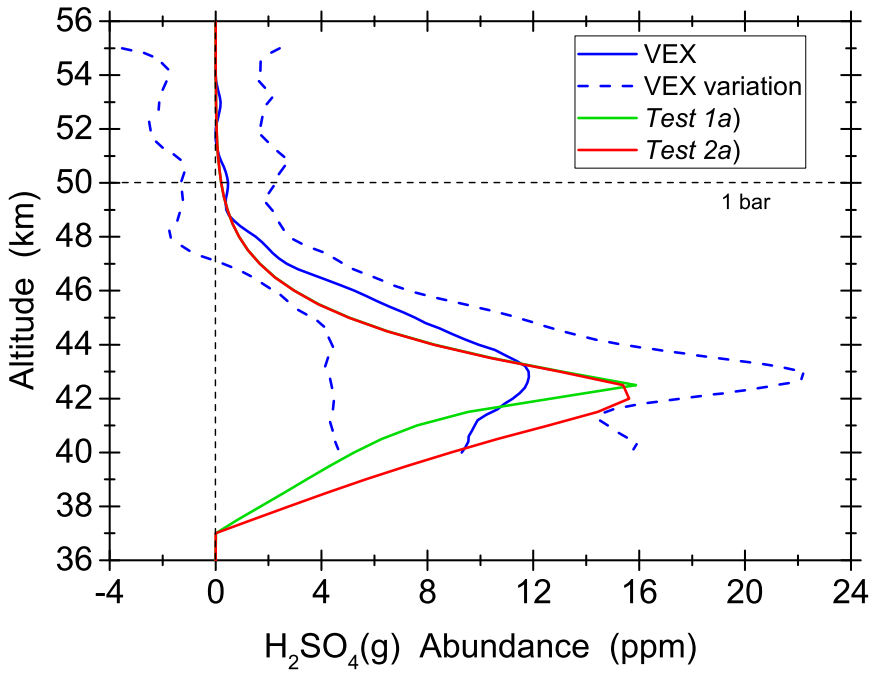

Figure 8.6: *Vertical profiles of $H_2SO_4(g)$ in Venus' northern polar atmosphere obtained from the simulation runs Test 1a) and Test 2a) as well as obtained from VeRa's observations. The horizontal dashed line show the approximate altitude of the 1 bar pressure level.*

reduced at these latitudes. A reduction of the gas content can also be seen in VeRa's observation at the northern polar latitudes indicating the presence of upward winds in this spatial region.

It is visible from Figure 8.4 that the modeled location of the H_2SO_4(g) high accumulated regions in general matches the location observed by VeRa. This indicates that the formation process in the model may serve as a possible explanation for the observed gas accumulation in Venus' atmosphere at these latitudes.

Modeled and observed abundances reveal similar values of 7 to 9 ppm at mid-latitudes. Differences can be seen at higher regions. Here, the modeled H_2SO_4(g) accumulations reveal peak abundances of 16 ppm (*Test 1a)*) to 18 ppm (*Test 2a)*) at latitudes $\geq$70°. The observation shows maximal mean values of almost 10 ppm around 75°N and about 14 ppm around 80°S. The southern abundance, however, is only confirmed by a small number of measurements (cf. upper panel in Figure 7.12) while the northern values contain the influence of the long-term trend of H_2SO_4(g) in this spatial region (cf. upper panel in Figure 7.13).

Figure 8.6 shows the modeled and observed vertical profiles of H_2SO_4(g) around 75°N. The latter was corrected for the above mentioned long-term trend. Obviously, the modeled profile agrees with the observed values within their variation range. However, the vertical extension of the observed H_2SO_4(g) accumulation, with peak values around 43 km altitude, is larger compared to the vertical extension of the modeled region. The disagreement is similar to that visible at the equatorial latitudes and the factors i) to iv) may also serve as possible explanations for the disagreement at the polar latitudes.

The H_2SO_4(g) high abundant regions at the equatorial and high latitudes observed by VeRa are clearly separated by a region of less gas content. Due to the orbit geometry of Venus Express, this spatial region could only be observed in the southern hemisphere. The separation is also visible in the modeled results. Values of 5 ppm to more than 7 ppm can be found in both, the observed and the modeled H_2SO_4(g) distributions. In the model calculations the separation was caused by the descending branches of the circulation cells (cf. Figure 5.1). The latter constantly transported H_2SO_4(g) to lowest altitudes where the gas was thermally decomposed. The downward transport at mid-latitudes consequently reduced the H_2SO_4(g) abundance between about 40 and 50 km altitude. The similarity of the modeled and the observed gas distributions indicates that such a downward transport may indeed exist in Venus' atmosphere where it is responsible for the clear separation of the H_2SO_4(g) high abundant regions observed by VeRa.

The presence of downward directed winds in Venus' mid-latitudinal region is supported by the observed latitudinal distribution of SO_2 between 51 and 54 km altitude. The latter was derived from VeRa's X-band data. Figure 8.7 shows the mass stream function ψ adopted from Figure 5.1 with superimposed mean SO_2 values adopted from Figure 7.6. Values from the southern hemisphere were transferred to the corresponding northern latitudes.

It is visible that regions of increased SO_2 values coincide with the upwelling branches of the circulation cells. Upward directed winds at equatorial and polar latitudes may have transported sulfur dioxide from lower to higher altitudes. Lowest SO_2 values were observed at mid-latitudes. Their location coincides with that of the downwelling branches of the circulation cells. The latter may have transported sulfur dioxide from higher to lower altitudes and this way reduced the amount of SO_2 at mid-latitudes around the cloud base level.

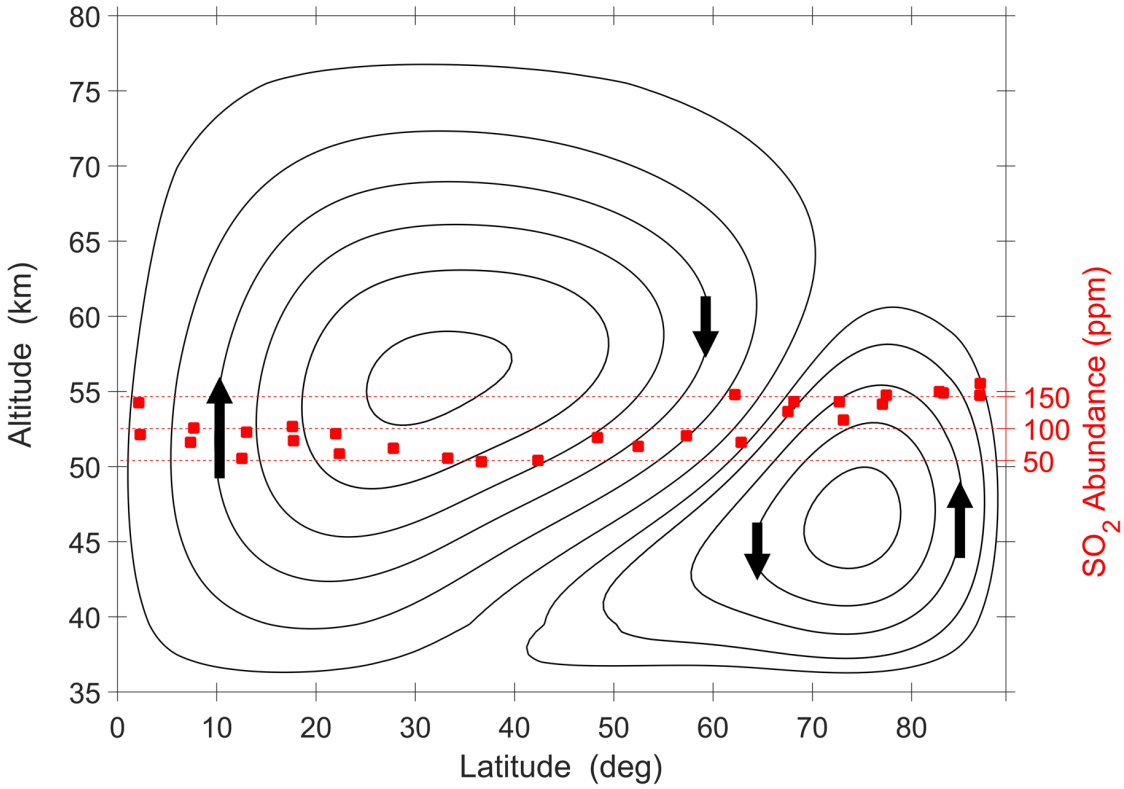

Figure 8.7: *Mean SO_2 abundance in the altitude region between 51 and 54 km derived from VeRa's X-band data between the years 2006 and 2015 (data from the southern and northern hemisphere were adopted from Figure 7.6) superimposed on the mass stream function ψ in the northern hemisphere used in the simulation run Test 1 (adopted from Figure 5.1).*

8.2 Modeled distributions of the clouds and water vapor

In the previous section the influence of both circulation cells on the H_2SO_4(g) distribution in the lower atmosphere was studied. The comparison of modeled results with those obtained from VeRa's H_2SO_4(g) and SO_2 observations supports the presence of upward directed winds at equatorial and polar latitudes as well as downward directed winds at mid-latitudes. In the present section their impact on the clouds, consisting of H_2SO_4-H_2O droplets, as well as on water vapor is discussed.

H_2SO_4-H_2O droplets

Figure 8.8 shows the spatial distribution of the Venus clouds bulk density obtained from the simulation run *Test 1a)* in the northern hemisphere. It is clearly visible from the upper panel that the bulk of the cloud material is located between about 45 and 65 km altitude. Herein, distinct latitudinal differences can be seen.

At altitudes above about 55 km, highest cloud density values of more than 16 mg/m^3 are visible at high latitudes. This is a consequence of the poleward directed mass transport in the upper branch of the Hadley cell and the upward directed mass transport by the polar cell towards this spatial region. The sum of both processes led to the accumulation of cloud material visible in Figure 8.8. The cloud density at these altitudes is additionally influenced by the lower temperatures compared to those at the equatorial region. The low temperature increased the condensation rate so that enhanced number densities of H_2SO_4-H_2O droplets can be found in this region.

Below about 55 km altitude, increased cloud densities are visible at the equatorial and polar latitudes. Values of more than 45 mg/m^3 can be found at the equatorial region between 48 and 49 km altitude. The enhanced density at the clouds bottom is a consequence of opposite directed mass transport in this altitude region, i.e., upward winds, diffusion and sedimentation. Condensation of upward transported gas increased the number density of cloud droplets while the downward transport of these particles and the subsequent evaporation led to the enhanced H_2SO_4(g) accumulation below 48 km altitude (cf. Figure 8.1). The formation process was previously suggested for example by *Knollenberg and Hunten* (1980) as well as by *Imamura and Hashimoto* (1998). The same process is responsible for the enhanced cloud density and increased H_2SO_4(g) abundance at polar latitudes. Here, cloud density values of more than 85 mg/m^3 can be found at 45 km altitude. Due to the latitudinal temperature gradient, the region of enhanced cloud density at polar latitudes is located at deeper altitudes compared to the corresponding equatorial region.

In the simulation runs *Test 0a)* to *Test 3a)*, the maximal cloud density values at the equatorial and polar regions varied as a consequence of vertical wind variations. For example, the absence of the polar cell in *Test 2a)* caused a decrease of the cloud density at high latitudes to values of about 37 mg/m^3 at 43 km altitude. At the same time, the cloud density at the equatorial region increased to values of more than 65 mg/m^3.

As in the model calculations downward transport has dominated at mid-latitudes, no accumulation of cloud droplets has formed in this region. Additionally, it can be

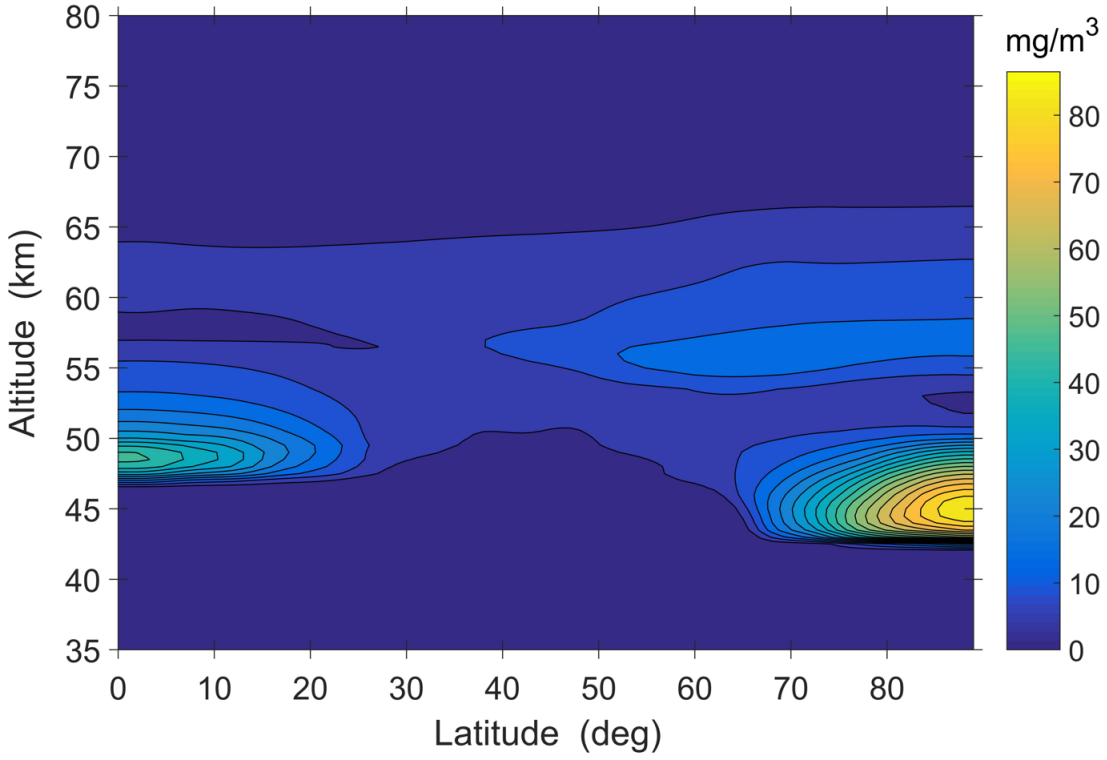

Figure 8.8: *Bulk density of the Venus clouds consisting of H_2SO_4-H_2O droplets obtained from the simulation run Test 1a) in the northern hemisphere.*

seen from Figure 8.8 that the cloud base is located at higher altitudes compared to its location at equatorial and polar latitudes. This shows that predominating vertical winds may influence the location of the cloud base which in general is controlled by the vertical temperature distribution at the corresponding latitudinal regions.

In the deeper atmosphere, the highest H_2SO_4(g) values can be found below 43 km altitude in this latitudinal region as can be seen in the lower panel of Figure 8.1. A comparison of vertical profiles of H_2SO_4(g) with those of cloud droplet density can be seen in Figure 8.9. Here, panel a) shows the vertical profiles obtained in the equatorial region while the panels b) and c) present those obtained from the mid- and polar latitudes, respectively. The influence of the predominant vertical wind direction at the corresponding regions is obvious.

It is clearly visible from panel b) that the decrease of the clouds density below about 57 km altitude at mid-latitudes is accompanied by an increase of the H_2SO_4(g) abundance. As mentioned above, droplets were mainly transported downwards at these latitudes. As a consequence of the high temperatures and the resulting increased evap-

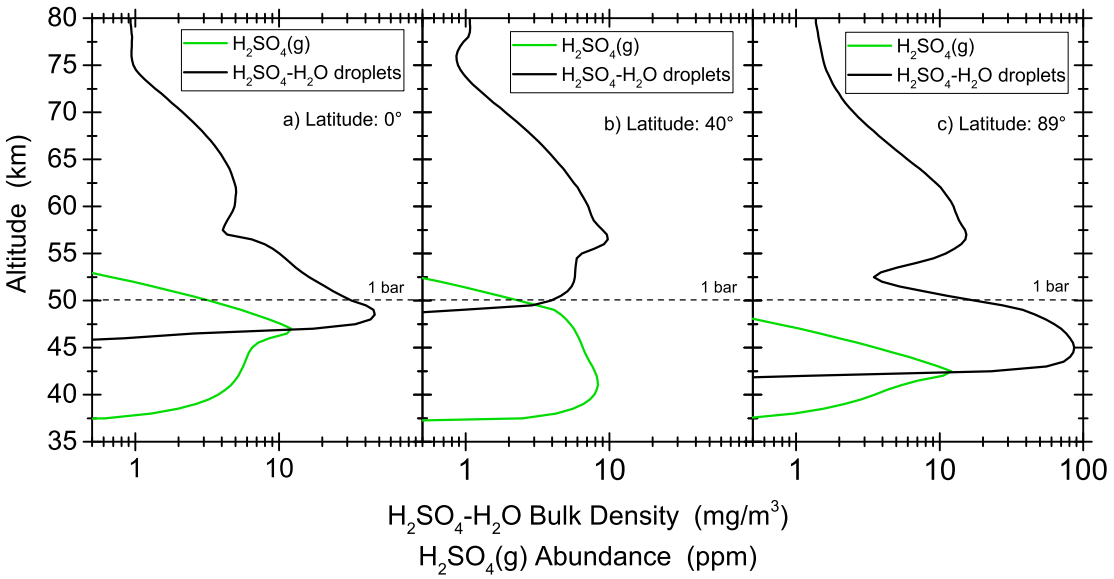

Figure 8.9: *Vertical profiles of $H_2SO_4(g)$ and H_2SO_4-H_2O cloud droplets at equatorial (panel a)), mid- (panel b)), and polar (panel c)) latitudes obtained from the simulation run Test 1a). The horizontal dashed line shows the approximate altitude of the 1 bar pressure level.*

oration rate at lower altitudes, the number density of droplets decreased while the gas amount increased. Highest cloud density values can be found around 57 km altitude and maximal H_2SO_4(g) abundance values are located about 15 km deeper.

In contrast to this, the regions of increased cloud density at equatorial and polar latitudes are accompanied by regions of enhanced H_2SO_4(g) accumulation (panels a) and c)). Due to the opposite directed mass transport as well as condensation and evaporation processes, the vertical locations of the corresponding peak values are only about 2 km apart.

Water vapor

Figure 8.10 presents the global distribution of water vapor in Venus' northern hemisphere obtained from the simulation run *Test 1a)*. Values between 1 and 30 ppm can be seen in the considered altitude range between 35 and 80 km, where the abundance increases with decreasing altitude. Influences of the global temperature distribution as well as of the vertical wind transport are clearly visible.

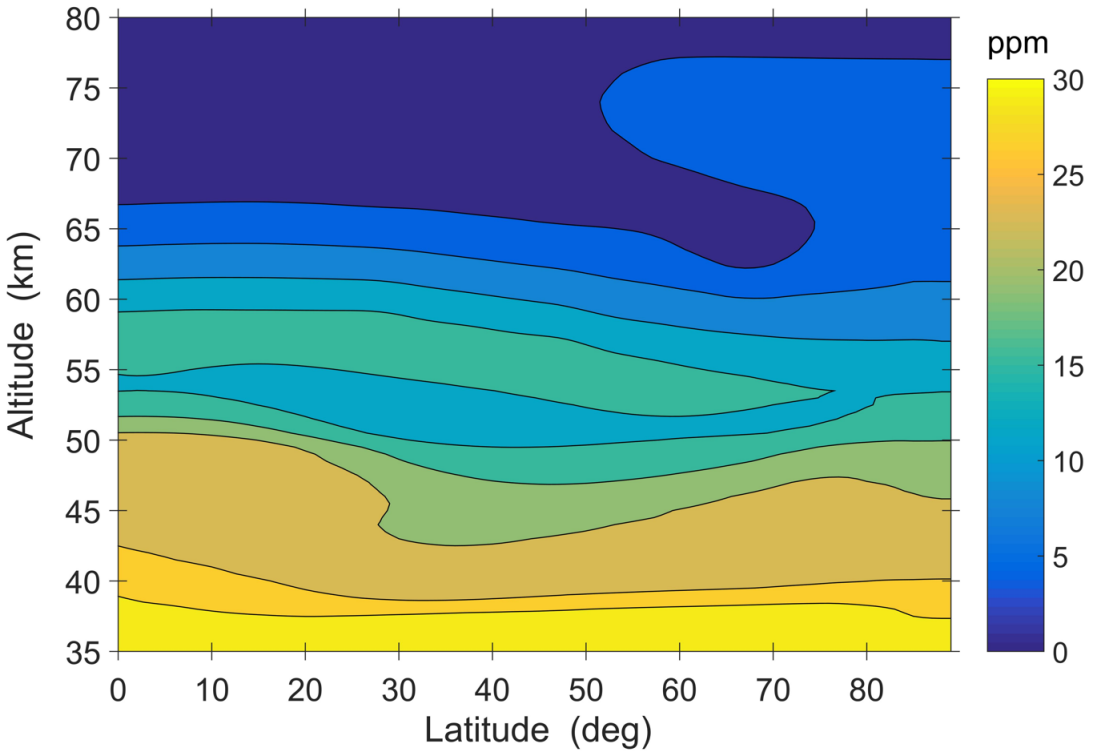

Figure 8.10: *Spatial distribution of water vapor obtained from the simulation run Test 1a) in the northern hemisphere.*

At the highest altitude levels ($\geq$70 km), the influence of the global temperature distribution on the latitudinal distribution of water vapor is obvious. While H_2O(g) abundances of 1 to 2 ppm can be found at the equatorial region, enhanced amounts of more than 6 ppm are located at high latitudes. This is a consequence of the increased temperature and the resulting enhanced saturation vapor pressure at high latitudes compared to that at the equatorial region (cf. Figure 2.1a)).

An exception to this is the cold collar region, located around 65 km altitude between 60° and 70°. The cold temperatures in this spatial region reduce the saturation vapor pressure of water so that an increased number density of cloud droplets can be found here. The abundance of water vapor is lower than 2 ppm.

At lower altitudes, the influence of vertical winds becomes increasingly obvious. Upward winds at the equatorial and polar latitudes transport water vapor from lower to higher altitudes, while downward winds at mid-latitudes transport the gas from higher to lower altitudes. The impact of the predominant vertical wind direction is mostly visible in the altitude range between about 45 and 50 km. Here, the highest

values can be found at the low and high latitudes. Mean values of about 25 ppm and 22 ppm were obtained at the equatorial (0° - 20°) and the polar (70° - 89°) regions, respectively. At mid-latitudes (35° - 55°), a mean value of about 18 ppm was obtained. In the lowest altitude region (≤40 km), the influence of the vertical winds was small.

8.3 Comparison with other model results and previous observations

In the following section the global distributions of H_2SO_4(g), the cloud density and H_2O(g) obtained from the simulation run *Test 1a)* are compared with previous simulations. Especially, results achieved from two- and three-dimensional mass transport models (*Imamura and Hashimoto*, 1998; *Ando et al.*, 2020) are considered for a comparison of the latitudinal distributions. Moreover, results obtained from microphysical, chemical kinetic and photochemical models (e.g. *Imamura and Hashimoto*, 2001; *Krasnopolsky*, 2007, 2012; *Parkinson et al.*, 2015; *McGouldrick*, 2017) which were used to compute equatorial and polar profiles of H_2SO_4(g), the clouds and H_2O(g) are considered. Additionally, the cloud density and water vapor distributions are compared with results obtained from previous observations.

Sulfuric acid vapor

The global distribution of H_2SO_4(g) was previously modeled by *Imamura and Hashimoto* (1998) as well as by *Ando et al.* (2020) using 2D and 3D mass transport models, respectively. Their results are presented in Figure 8.11 along with that obtained from the simulation run *Test 1a)* for comparison.

It is clearly visible that the spatial distribution of the haze layer obtained by *Imamura and Hashimoto* (1998) (panel b)) reveals an enhancement of H_2SO_4(g) at latitudes <40°. Peak values of about 8 ppm can be found in the altitude range between 46 and 48 km around 30°. The formation of the accumulation is attributed to opposite directed mass transport as well as condensation and evaporation processes in this spatial region. It is similar to the process that formed the H_2SO_4(g) accumulation at equatorial latitudes in the simulation run *Test 1a)* visible in panel a).

The spatial distribution of H_2SO_4(g) at equatorial latitudes as well as its abundance obtained from the present model calculations (*Test 1a) & Test 2a)*) in general agree with the distribution and abundance obtained by *Imamura and Hashimoto* (1998) in this spatial region. This is a consequence of similar transport mechanisms present at

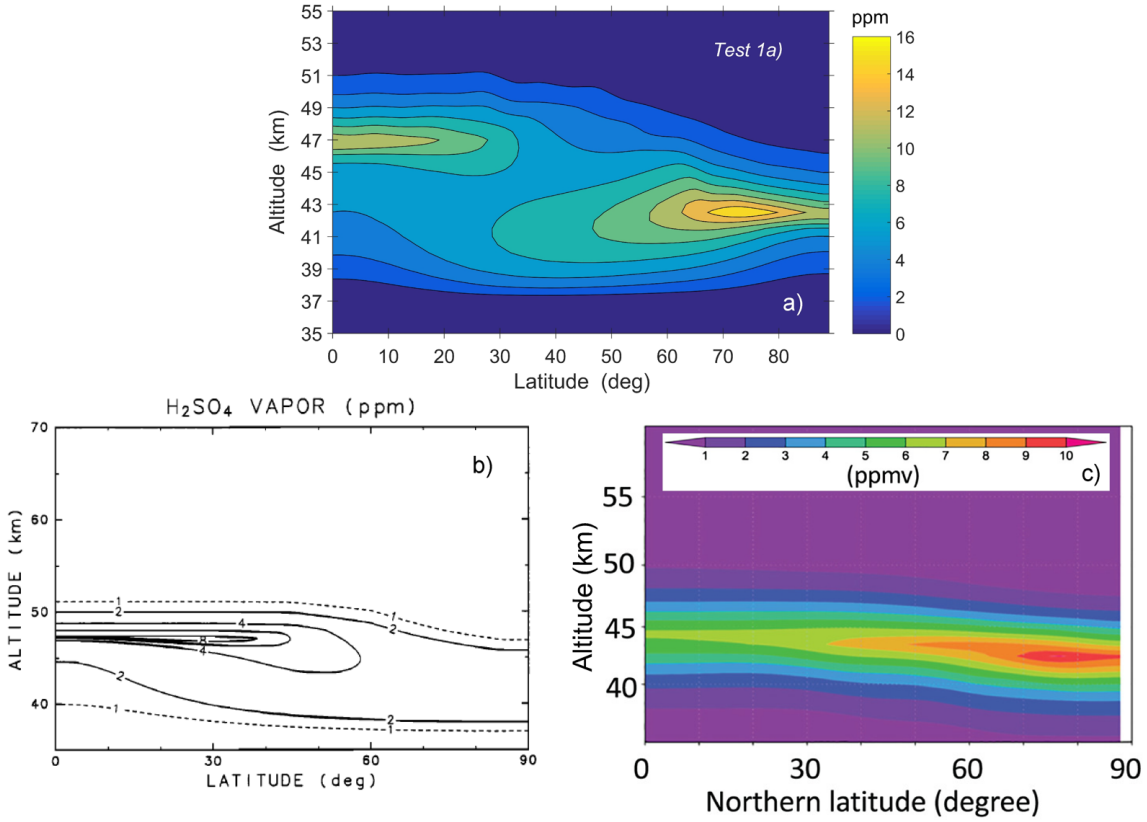

Figure 8.11: *Spatial distribution of sulfuric acid vapor obtained from the simulation run Test 1a) (panel a)) as well as obtained by Imamura and Hashimoto (1998) from a 2D model (panel b)) and by Ando et al. (2020) from a 3D model (panel c)).*

these latitudes in both models. Small differences in the structure and abundances must be attributed to differences in the model input parameters (vertical/meridional wind velocities, vertical/horizontal eddy diffusion).

However, both models provide different results at mid- and polar latitudes. Here, distinctly increased H_2SO_4(g) values were obtained from the simulation run *Test 1a)* (panel a)), while no accumulation of sulfuric acid vapor is visible in Figure 8.11b). As described in section 8.1.1, the enhanced H_2SO_4(g) content in this spatial region is mainly formed by the evaporation of an increased number of downward transported H_2SO_4-H_2O droplets. The latter is a consequence of the low temperatures at high latitudes. An additional simulation run has revealed that H_2SO_4(g) does not accumulate at mid- and polar latitudes when one single circulation cell is present in the model, similar to that used by *Imamura and Hashimoto* (1998) in their simulation (cf. Figure 2.8c)). The sinking branch of the Hadley cell along with equatorward gas transport

at polar latitudes prevent the accumulation of sulfuric acid in this spatial region. It is likely that for this reason no enhancement of H_2SO_4(g) is visible at mid- and polar latitudes in the results provided by *Imamura and Hashimoto* (1998).

Increased H_2SO_4(g) abundances in this spatial region can be seen in the results provided by *Ando et al.* (2020). Highest values of 10 - 11 ppm are visible around 43 km altitude poleward of 70°. While the location of the H_2SO_4(g) accumulation agrees with that obtained from the simulation run *Test 1a)*, the spatial distribution of the gas at lower latitudes disagrees in both models. Rather, the latitudinal distribution of H_2SO_4(g) provided by *Ando et al.* (2020) is similar to that obtained from the simulation run *Test 0a)* (cf. Figure 8.1). Here, the mass transport by the Hadley and polar cell was removed so that mass transport was solely associated with sedimentation and eddy diffusion. *Ando et al.* (2020) used a General Circulation Model (GCM) to calculate the H_2SO_4(g) distribution in Venus' lower atmosphere, whose meridional wind structure revealed a diurnal variation (e.g. *Takagi et al.*, 2018; *Ando et al.*, 2020). The similarity of their results and the H_2SO_4(g) distribution obtained from *Test 0a)* indicates that the wind transport at equatorial and mid- latitudes used by *Ando et al.* (2020) was probably underestimated.

While two- and three-dimensional models are used to investigate the global wind circulation in Venus' atmosphere, the main focus of one-dimensional microphysical and photochemical models is on the study of chemical kinetics, evaporation and condensation processes. Most of those models provide vertical distributions of gaseous species as well as of the cloud density in the equatorial and polar region. Meridional wind plays a minor role at these latitudes so that only the vertical mass flux must be considered. Most of the H_2SO_4(g) profiles provided by 1D models agree with those obtained from the simulation runs *Test 1a)* and *Test 2a)* at the topside of the H_2SO_4(g) haze layer. This is because the sulfuric acid vapor abundance in this altitude region is controlled by its saturation vapor pressure that is similar in both, the present two-dimensional model and the one-dimensional models. Panel a) in Figure 8.12 shows the H_2SO_4(g) profile obtained from the simulation run *Test 1a)* at the equatorial region (cf. Figure 8.2). For comparison, the panels b) and c) present two examples of equatorial H_2SO_4(g) profiles calculated by *Imamura and Hashimoto* (2001) (panel b)) as well as by *Parkinson et al.* (2015) (panel c)) using 1D models. It can be clearly seen that in all three cases the H_2SO_4(g) amount at the topside of the haze layer follows the saturation vapor abundance.

Differences between H_2SO_4(g) profiles obtained from multidimensional models and those obtained from one-dimensional models occur at lower altitudes. Here, the gas amount is controlled by the vertical transport as well as by chemical kinetics at the

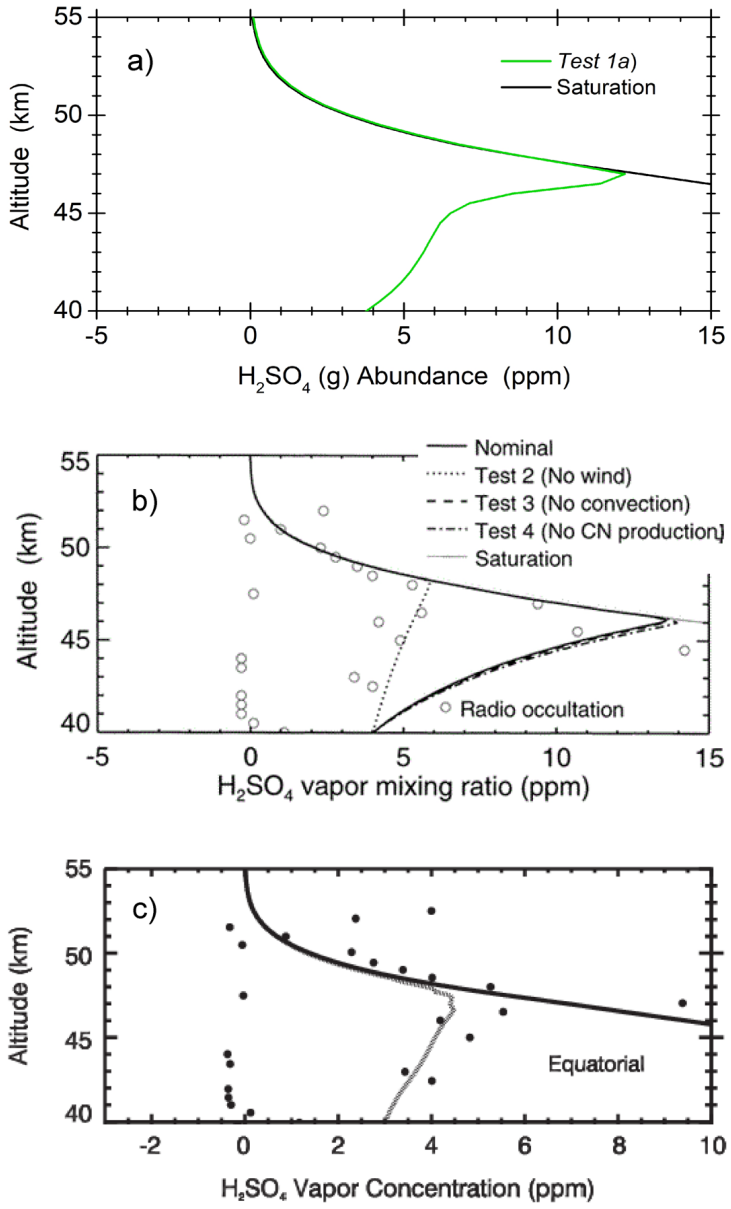

Figure 8.12: *Sulfuric acid vapor profiles in the equatorial region obtained from the simulation run Test 1a) (panel a) as well as calculated by Imamura and Hashimoto (2001) (panel b) and by Parkinson et al. (2015) (panel c) using 1D models. Explanation of the legend in panel b) can be found in Imamura and Hashimoto (2001). Black dots in panel c) represent $H_2SO_4(g)$ values derived by Kolodner and Steffes (1998) from Mariner 10 radio occultation data.*

lowest altitudes. Moreover, boundary conditions for H_2SO_4(g) may have a strong influence on the gas abundance in 1D models. While upward winds were incorporated in the present simulation *Test 1a)* (panel a) and in the 1D model of *Imamura and Hashimoto* (2001) (panel b), those were not considered in the 1D model of *Parkinson et al.* (2015) (panel c). The effect is obvious below the locations of the peak values of the corresponding H_2SO_4(g) profiles. While the profiles presented in the panels a) and b) (except for Test 2 in panel b)) in general agree at these altitudes, both disagree with that presented in panel c). The latter reveals a distinctly low peak value of less than 5 ppm around 47 km altitude as well as an almost constant H_2SO_4(g) abundance in the lower region. The disagreement is most probably a consequence of underestimated upward transport in panel c). This is supported by the similarity of the profile to that obtained by *Imamura and Hashimoto* (2001) in 'Test 2'. Here, wind transport was neglected which led to maximal values of less than 6 ppm around 48 km altitude and an almost constant abundance in the lower region.

H_2SO_4-H_2O droplets

Measurements of the Venus cloud density have been reported by *Knollenberg and Hunten* (1980). Figure 8.13 shows the vertical distribution of the clouds bulk density derived from PVO's particle size spectrometer measurements along with that obtained from the simulation run *Test 1a)*.

It is clearly visible that the latter roughly agrees with PVO's observations below about 55 km altitude. Although the bottom of the modeled cloud deck is located at lower altitudes compared to that observed by PVO, the observed enhanced cloud density between about 47 and 50 km altitude was in general successfully reproduced by the present model. Both profiles show a decrease of the cloud density above that altitude range with distinct structures visible in the observed profile. Those are most probably a consequence of microphysical processes which is a subject to one-dimensional models (e.g. *Imamura and Hashimoto*, 2001; *Parkinson et al.*, 2015; *McGouldrick*, 2017). As those processes are not considered in the present transport model, the simulated profile shows a smooth, gradual decrease. Above about 57 km, both profiles reveal a clear disagreement that increases with altitude. This might indicate an overestimated vertical transport at these altitudes in the present model.

Similar to the spatial distribution of H_2SO_4(g) (cf. Figure 8.11), that of the cloud density calculated by *Imamura and Hashimoto* (1998) as well as by *Ando et al.* (2020) is compared with the cloud density obtained from the present model. Figure 8.14 shows the corresponding results. While panel a) presents the cloud density obtained from the

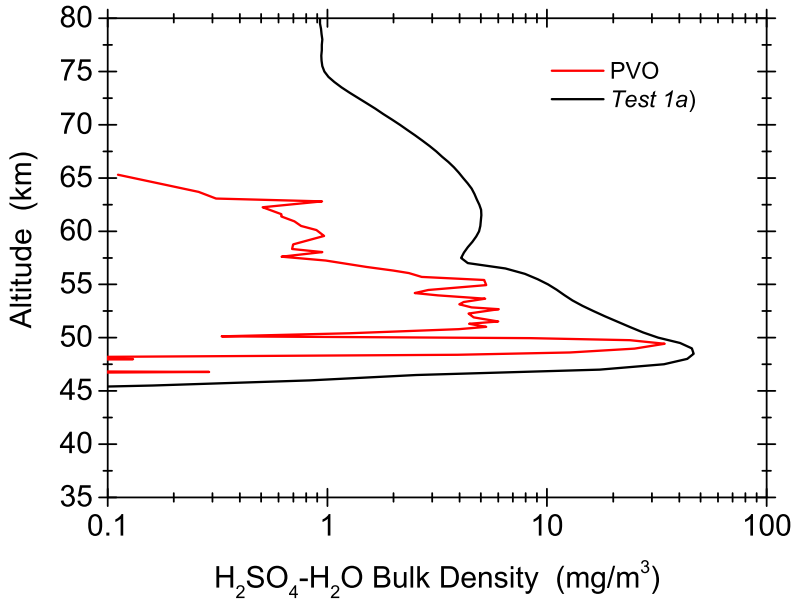

Figure 8.13: *Vertical profiles of the Venus clouds bulk density observed by Knollenberg and Hunten (1980) (cf. Figure 2.2b)) as well as obtained from the simulation run Test 1a).*

simulation run *Test 1a)*, the panels b) and c) show that calculated by *Imamura and Hashimoto* (1998) as well as by *Ando et al.* (2020), respectively.

The panels a) and b) show increased cloud densities between about 55 and 65 km altitude poleward of 40°. The formation process in the present model was discussed in section 8.2 and is similar to that in *Imamura and Hashimoto* (1998). In panel b), a clear decrease of the cloud top is visible at latitudes $> 60°$, which is consistent with observations (e.g. *Ignatiev et al.*, 2009; *Titov et al.*, 2012) and inconsistent with the cloud density obtained from *Test 1a)*. The decrease of the cloud top in panel b) was caused by downward winds in the sinking branch of the Hadley cell located at polar latitudes. In contrast to this, in *Test 1a)* a polar cell was incorporated in this spatial region with upward winds poleward of about 75°. It is therefore likely that the upward transport in *Test 1a)* was overestimated at altitudes > 60 km in the polar region.

Panel c) shows a clear depletion of the cloud top at about 65 km altitude around 60°. It was probably caused by intense downdrafts in this spatial region. Poleward of 60°, panel c) reveals a clear increase of the cloud density in the altitude range between about 40 and 65 km. The highest accumulation of droplets is located around 45 km altitude. The location is consistent with the region of increased cloud density values obtained from *Test 1a)* (panel a)).

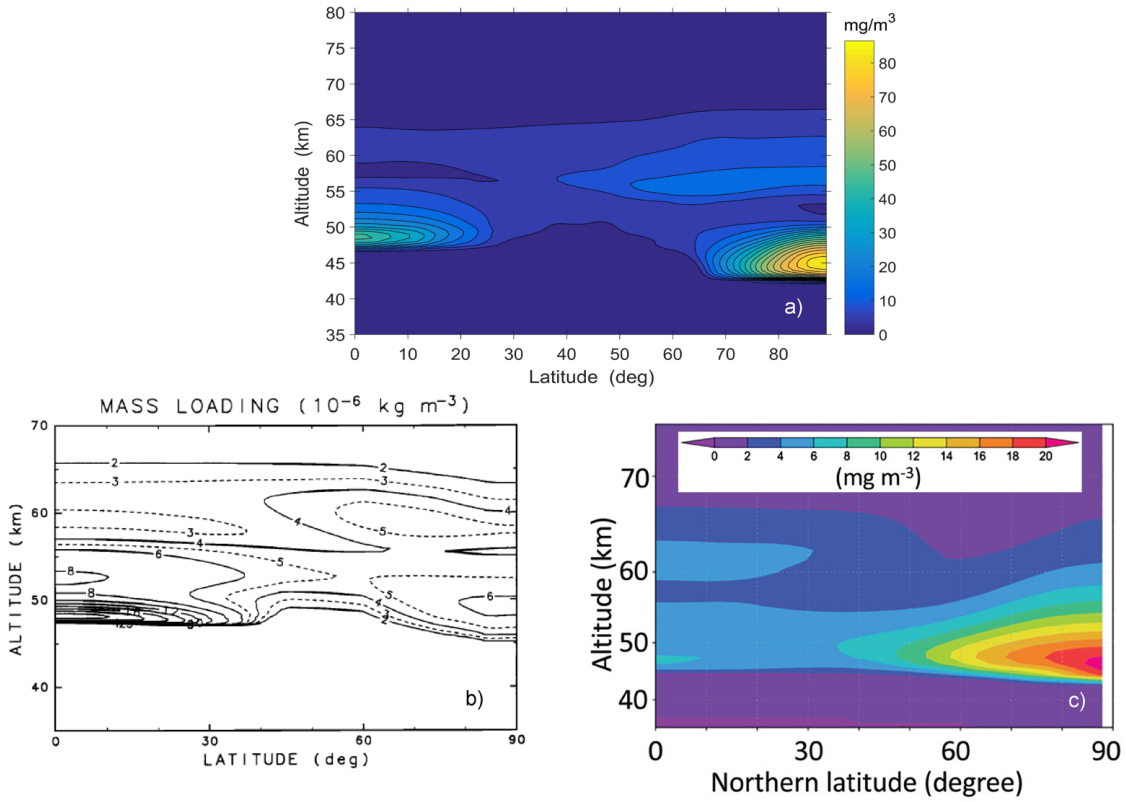

Figure 8.14: *Spatial distribution of the cloud density obtained from the simulation run Test 1a) (panel a)) as well as obtained by Imamura and Hashimoto (1998) from a 2D model (panel b)) and by Ando et al. (2020) from a 3D model (panel c)).*

In the equatorward direction, the spatial distribution of the cloud density in panel a) is similar to that in panel b). A clear accumulation of droplets can be seen near the cloud base at equatorial latitudes, which is consistent with observations (cf. Figure 2.2). In contrast to this, panel c) shows just a moderate droplet accumulation between 45 and 50 km altitude. Similar to the missing H_2SO_4(g) accumulation in this spatial region (cf. Figure 8.11), this might be a consequence of underestimated vertical transport at these latitudes.

The mid-latitudinal region in the panels a) and b) is characterized by a higher located cloud bottom compared to its location at the equatorial and polar latitudes. As explained in section 8.2, downward directed winds in the sinking branches of the Hadley and polar cells dominated the vertical mass transport at theses latitudes in the present model (panel a)). Therefore, cloud droplets could not accumulate near the cloud base. Although in panel c) the cloud bottom is located slightly higher compared

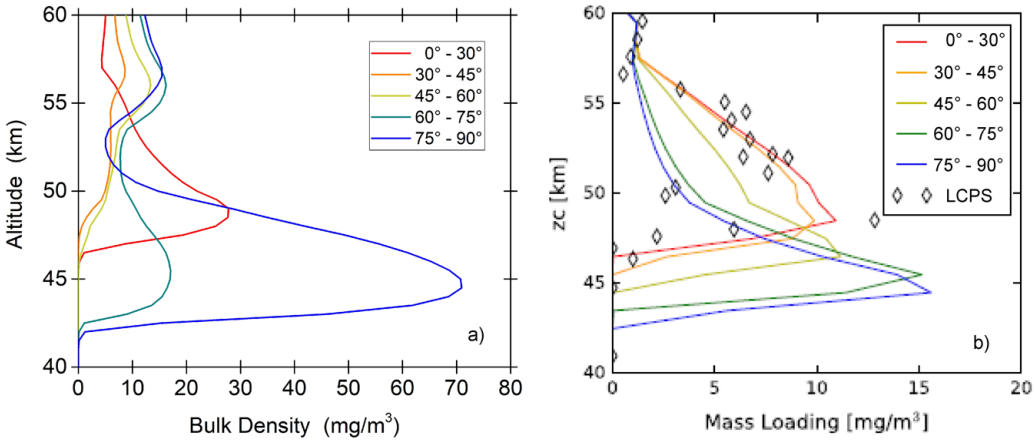

Figure 8.15: *Profiles of the cloud density at different latitudinal regions obtained from the simulation run Test 1a) (panel a)) as well as obtained by McGouldrick (2017) from a 1D model (panel b)). LCPS data in panel b) represent measurements from the Pioneer Venus Large probe Cloud Particle size Spectrometer. The legend in panel b) was adjusted according to the caption in McGouldrick (2017).*

to its location at low and high latitudes, the latitudinal variation of the cloud bottom is more pronounced in the panels a) and b). The difference can be most probably attributed to differences in the transport mechanisms in this spatial region as well as their intensities in the corresponding models.

A latitudinal trend in the cloud bottom location was also observed in 1D model calculations conducted for example by *Hashimoto and Abe* (2001), *Parkinson et al.* (2015) and *McGouldrick* (2017). It was caused by the latitudinal temperature gradient in this spatial region. As an example, panel b) of Figure 8.15 shows vertical profiles of the cloud density at different latitudes calculated by *McGouldrick* (2017) using a one-dimensional microphysical model. For comparison, panel a) shows averaged cloud density profiles from the same latitudinal regions obtained from the present model *Test 1a)*.

It can be clearly seen that the location of the cloud bottom in panel b) decreases with increasing latitude. A distinct layer of enhanced cloud density is visible at all latitudinal regions. It is the so-called *lower cloud layer* that is believed to form the lowest part of the main clouds (cf. Table 2.1). No such layer is visible at mid-latitudes (30° - 60°) in panel a). The formation is prevented in the present model by the intense downward winds in this spatial region. Instead, the highest cloud density values can be found above 55 km altitude.

Water vapor

As mentioned in section 2.2, water vapor could be observed in the entire middle and lower atmosphere of Venus. A summary of selected measurements along with results obtained from one-dimensional model calculations is presented in Figure 2.3. The figure is adopted here for a comparison with water vapor profiles obtained from the present model calculations at the equatorial and polar regions. This is presented in Figure 8.16.

It can be clearly seen that both profiles obtained from *Test 1a)* in general agree with observations and 1D model calculations. A mixing ratio of 30 ppm was set at the models lower boundary. No latitudinal variations were considered which is consistent with previous observations (e.g. *Marcq et al.*, 2008). The decrease of H_2O(g) above 35 km altitude matches the decrease provided by one-dimensional model calculations in this spatial region. In this altitude range, the water vapor mixing ratio obtained from *Test 1a)* at equatorial latitudes is constantly higher than that obtained from the polar latitudes. This is mainly a consequence of the vertical transport which was more efficient at lower latitudes compared to that at the polar region. Above about 65 km altitude this latitudinal trend is reversed. Owing to increased temperatures at

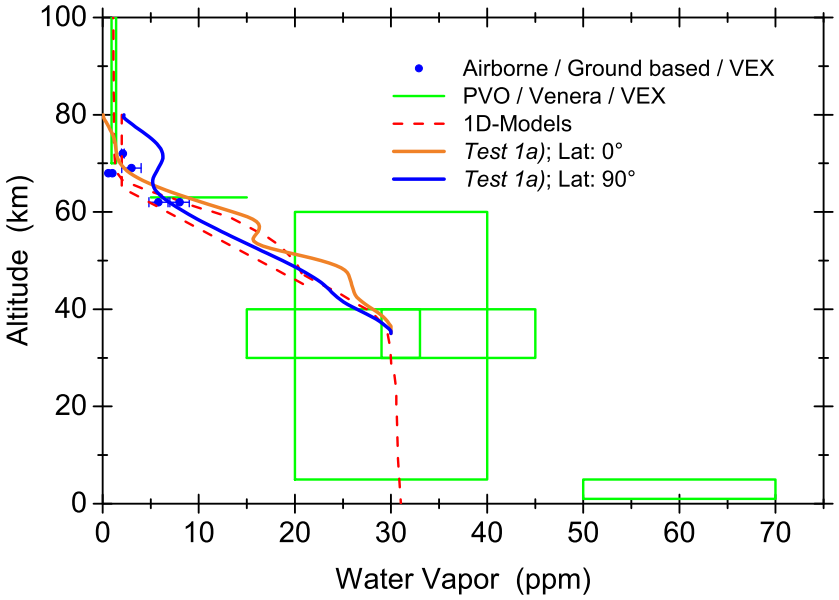

Figure 8.16: *Water vapor concentration in Venus' middle and lower atmosphere obtained from observations and model calculations adopted from Figure 2.3 along with H_2O(g) profiles at the equatorial and polar latitudes obtained from the simulation run Test 1a).*

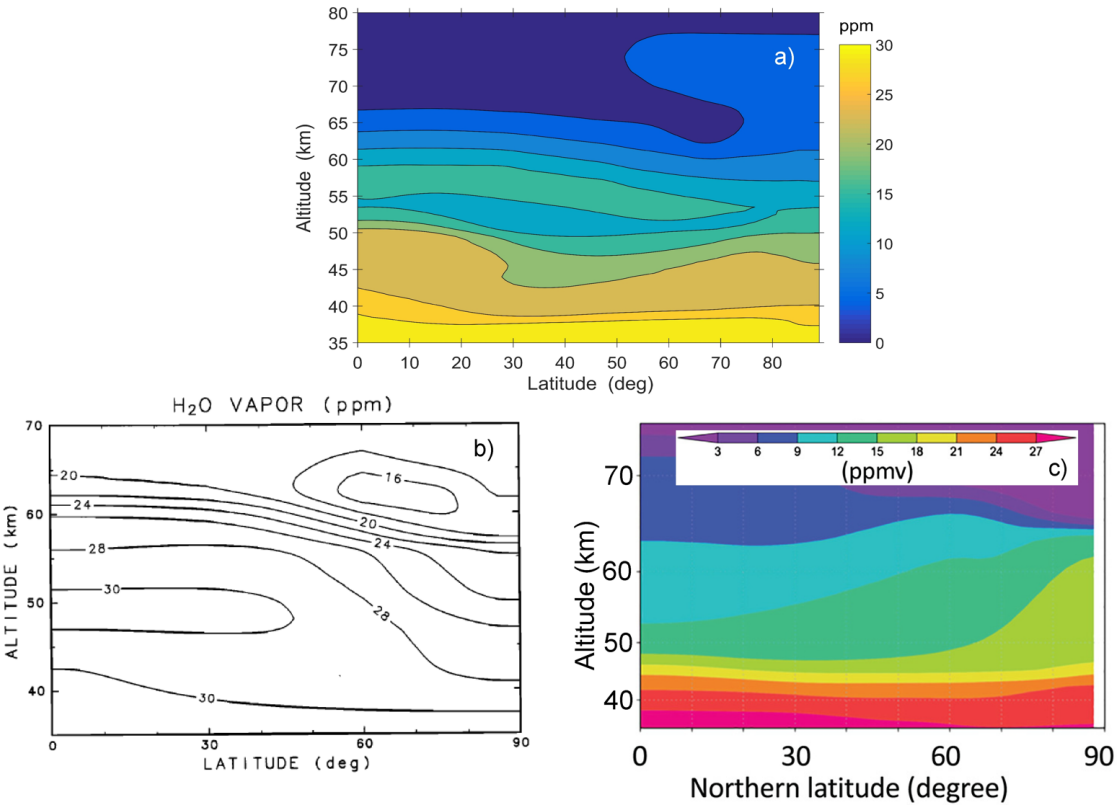

Figure 8.17: *Spatial distribution of water vapor obtained from the simulation run Test 1a) (panel a)) as well as obtained by Imamura and Hashimoto (1998) from a 2D model (panel b)) and by Ando et al. (2020) from a 3D model (panel c)).*

the polar latitudes (cf. Figure 2.1), highest H_2O(g) values of more than 6 ppm can be found in this spatial region, while mixing ratios of less than 2 ppm are visible at low latitudes. A similar latitudinal variation was observed by *Cottini et al.* (2012) and *Fedorova et al.* (2016). They found H_2O(g) values of about 5 - 7 ppm at the polar region and 3 - 5 ppm at the equatorial and mid-latitudes. Here too, increased temperatures at polar latitudes may be responsible for the observed latitudinal trend. Another explanation is provided by enhanced upward winds, which transport H_2O(g) from the lower atmospheric region to cloud altitudes.

Those were responsible for enhanced H_2O(g) values above 60 km altitude at high latitudes obtained by *Ando et al.* (2020) from their 3D model calculations. Their results are presented in Figure 8.17. Here, for comparison panel a) shows the spatial distribution of H_2O(g) obtained from the present model. The panels b) and c) present the latitude-height distributions of water vapor obtained from *Imamura and Hashimoto* (1998) as well as from *Ando et al.* (2020).

A clear increase in the H_2O(g) abundance is visible above about 50 km altitude in the polar region in panel c). Values of 12 ppm can be seen at 63 km altitude. This altitude region marks the location of the cloud top at polar latitudes. Its location increases equatorward to altitudes of about 71 - 75 km (e.g. *Titov et al.*, 2008; *Ignatiev et al.*, 2009). Here, values of about 6 ppm can be seen in panel c). This latitudinal trend in the H_2O(g) abundance at cloud top altitudes seems to be missing in panel b). It is possible that the intense downward transport of water in the sinking branch of the Hadley cell located at high latitudes led to decreased H_2O(g) values in the polar region. Additionally, the influence of the *cold collar* (60° - 70°, 60 - 70 km) decreased the H_2O(g) abundance. The low temperatures in this spatial region enhanced the condensation rate and decreased this way the water vapor abundance. While the influence of the *cold collar* is also visible in panel a), it is missing in the results provided by *Ando et al.* (2020) (panel c)).

In the altitude region below about 50 km, the panels a) and b) reveal influences of the corresponding descending branches of the circulation cells. Those are visible at mid- and polar latitudes. In contrast to this, the water vapor abundance in panel c) reveals an almost constant distribution between the equatorial and polar latitudes. This is most probably a result of less intense wind transport compared to that in the panels a) and b) in this spatial region.

Chapter 9

Summary and future prospects

Radio occultation measurements conducted by the Radio Science experiment VeRa on board Venus Express were used to derive the global distributions of H_2SO_4(g) and SO_2 as well as their variations between 40 and 55 km altitude in Venus' atmosphere. The global distributions of these trace gases provide information on Venus' meridional wind pattern which plays a crucial role in the evolution and maintenance of the Venusian atmospheric superrotation. A two-dimensional mass transport model was developed in the present work in order to interpret VeRa's observations and to draw conclusions about the meridional wind dynamics in Venus' atmosphere. In the following chapter, the spatial distributions of H_2SO_4(g) and SO_2 derived from VeRa as well as the global distribution of H_2SO_4(g) obtained from the model calculations presented in the chapters 6 to 8 are summarized. Section 9.1 repeats the key statements about the sulfuric acid vapor and sulfur dioxide observations. Section 9.2 summarizes the results of the model calculations. Section 9.3 presents implications for future studies.

9.1 Observation

Data base

A total number of 805 data sets obtained in the years 2006 to 2014 from the radio science experiment VeRa on board Venus Express were used for the present work. VeRa's X- and S-band radio signals were recorded at ESA and NASA ground stations in the CL and OL receiving mode (cf. section 3.2.1). For the present analysis, OL data were used. The advantage of the latter over CL data lies in the possibility of post-recording analysis of the radio signals so that the signals amplitude and frequency could be retrieved even when Venus' deep atmosphere was sounded (cf. Figure 6.1). Moreover, the orbit geometry of Venus Express allowed to sound Venus' atmosphere over a wide range of latitudes, longitudes and local times. As a result, for the first

time a global picture of the Venusian H_2SO_4(g) haze layer was obtained in the altitude range between 40 and 55 km altitude.

Uncertainties

The main error source in the derived SO_2 and H_2SO_4(g) abundances are small scale fluctuations in the derived amplitude and frequency of the X- and S-band radio signals. The frequency was used to derive radio ray parameters, like the bending angle and the impact parameter (cf. section 3.2.2), so that fluctuations were also present in these parameters. These small scale fluctuations have been eliminated to a large extent from the data by applying downsampling and filtering tools in the process of absorptivity and H_2SO_4(g) calculations. However, a residual noise remained. It increased with decreasing altitude leading to higher error bars of the H_2SO_4(g) profiles at lower altitudes (cf. Figures 7.1 and 7.2). Those are larger on the S-band profiles as a consequence of the weaker S-band signal compared to the X-band signal (5-W S-band; 65-W X-band) (S-band: 1.0 - 4.0 ppm, sometimes increasing to more than 6.0 ppm; X-band: 0.5 - 2.0 ppm, sometimes increasing to more than 5.0 ppm).

The large number of available X-band profiles, however, decreased the mean error of the zonally and and time-averaged H_2SO_4(g) distribution presented in Figure 7.12. Here, the highest uncertainties don't exceed 2.5 ppm. Those can be found in the southern polar region as a consequence of the relatively low number of measurements at these latitudes (cf. upper panel in Figure 7.12).

The error bars of the H_2SO_4(g) profiles were used to estimate the uncertainty of the SO_2 values derived in the altitude range between 51 and 54 km altitude. Due to the weak sensitivity of X-band radio waves to sulfur dioxide (cf. equation (4.20e)), the error bars of the latter values are quite large (cf. Figure 7.6).

Results

Signal attenuation

The abundance of H_2SO_4(g) was derived from the determined absorption of the X- and S-band radio signals in Venus' atmosphere. In addition to absorption, pointing inaccuracies of the S/C antenna as well as refractive defocussing of the radio beam were responsible for the attenuation of the radio signals. The latter two factors had to

be removed from the total signal attenuation so that signal absorption remains which was mainly caused by H_2SO_4(g), SO_2 and CO_2.

Thanks to predetermined slew maneuvers of the S/C, significant degradations of the signal amplitude due to **mispointing** could be avoided when the HGA1 was used for measurements (cf. Figure 6.5a)). However, no slew maneuvers were performed when the smaller second HGA2 was used. In this case a severe signal degradation occurred (cf. Figure 6.5b)) so that correction calculations must have been applied based on derived radio ray parameters (cf. section 3.2.2) as well as on spacecraft attitude information and ephemeris data for the celestial bodies provided by ESA. This way an overestimation of the radio signal absorption and the derived H_2SO_4(g) abundance could be avoided.

As can be seen from Figure 6.3, **refractive defocussing** was the main reason for the observed signal attenuation below about 100 km altitude. Additionally, Figure 6.4 shows that the contribution of refractive defocussing to the total signal attenuation increases with the S/C to Venus distance. The latter was largest when Venus' southern hemisphere was sounded leading to highest attenuation values of about 25 dB at the south pole. Due to the strong attenuation, a smaller number of usable measurements was obtained from the southern polar region compared to that obtained from the northern polar latitudes. Here, the attenuation due to refractive defocussing was about 10 dB less than at the south pole.

After removing the contributions of antenna mispointing and that of refractive defocussing from the total signal attenuation, the remaining attenuation could be attributed to **signal absorption**. Figure 6.3 shows that significant absorption of the X-band radio signals occurred when the altitude region below about 55 km was sounded. The observed S-band radio signal absorption in this altitude region was weaker (cf. Figure 7.2). The absorption of both, the X- and S-band radio signals was mainly caused by CO_2, SO_2 and H_2SO_4(g) in Venus' atmosphere. The contribution of CO_2 was removed by using equation (4.20a) and the remained absorption by SO_2 and H_2SO_4(g) was used to derive the corresponding abundances.

SO_2 and H_2SO_4(g) abundances

Thanks to the frequency-squared dependency of the SO_2 radio signal absorptivity (cf. equation (4.20e)), a comparison of the H_2SO_4(g) profiles derived from the X-band radio signals with those derived from the S-band radio signals allows to infer increased abundances of SO_2 ($\gg$ 200 ppm). As VeRa's S-band radio signal was only available

in the year 2006, the comparison could be made for a small number of measurements, only. No significant differences in the derived H_2SO_4(g) profiles were observed (cf. Figures 7.1 and 7.3). This indicates that no enhanced SO_2 abundances occurred at the time of the measurements.

According to the saturation vapor pressure of H_2SO_4 (cf. equation 5.13), significant abundances of sulfuric acid vapor are located below about 51 km altitude. Increased signal absorption observed above that altitude level is therefore attributed to SO_2. The absorption at theses altitudes was therefore used to determine the abundance of SO_2 between 51 and 55 km using the X-band radio signals. The inferred abundance was also used to remove the absorption contribution of SO_2 at lower altitudes. The remaining absorption could then be attributed solely to H_2SO_4(g) so that its abundance could be determined.

The derived SO_2 and H_2SO_4(g) abundance values agree well with those derived from previous observations (cf. Figures 7.9 and 7.17, respectively). Mean SO_2 mixing ratios of 90 - 170 ppm were estimated in the altitude region between 51 and 54 km, while the derived H_2SO_4(g) abundance reached maximal values of about 12 ppm. Both, the derived abundance of SO_2 and that of H_2SO_4(g) revealed clear latitudinal and long-term variations. Moreover the H_2SO_4(g) content at equatorial latitudes shows indications for a local time variation.

SO_2 and H_2SO_4(g) abundances - latitudinal variations

It was shown for the first time that the SO_2 abundance near the cloud base exhibits a clear latitudinal variation. Highest values were found at both polar regions as well as at the equatorial latitudes. The lowest SO_2 content was observed at the mid- southern latitudes (cf. Figure 7.6). It is possible that the latitudinal variation is a consequence of the predominant vertical wind transport (upward / downward) in the corresponding regions as indicated in Figure 8.7. Upward winds at low and high latitudes transport SO_2 rich air from lower to higher altitudes, while downward winds at mid-latitudes push the gas to lower altitudes.

A similar latitudinal variation was observed by *Marcq et al.* (2020) in the SO_2 abundance around 70 km altitude using SPICAV-UV measurements. However, a clear difference exists in the polar regions. As can be seen in Figure 7.10, they observed a clear decrease of SO_2 at these latitudes while the SO_2 content between 51 and 54 km altitude increases at both polar regions. As indicated in Figure 8.7, the decrease around 70 km altitude might be a consequence of missing SO_2 supply from lower altitudes as

well as from lower latitudes. In contrast to this, the altitude region between 51 and 54 km is steadily supplied with SO_2 from the lower atmospheric regions.

A latitudinal variation of H_2SO_4(g) below 55 km altitude was indicated in the S-band radio absorptivity data derived by *Cimino* (1982) as well as by *Jenkins and Steffes* (1991) from Pioneer Venus radio occultation measurements. *Oschlisniok et al.* (2012) have observed a clear latitudinal variation of H_2SO_4(g) around 50 km altitude using VeRa's CL data. In the context of the present work, for the first time a global picture of the zonally and time-averaged H_2SO_4(g) content between 40 and 55 km altitude was obtained. The latter is presented in Figure 7.12. It shows a clear latitudinal variation of the topside of the H_2SO_4(g) haze layer. The latter was caused by the latitudinal temperature gradient in this spatial region (cf. Figure 2.1). Additionally, regions of distinctly enhanced H_2SO_4(g) abundance exist in the equatorial as well as at mid- and polar latitudes. As was shown in model calculations made for example by *Imamura and Hashimoto* (1998), *Ando et al.* (2020) and in the present work, those are a consequence of wind transport and the global temperature distribution.

SO_2 and H_2SO_4(g) abundances - long-term variations

Long-term variations of SO_2 were observed for example by *Esposito* (1984), *Marcq et al.* (2013) and *Marcq et al.* (2020) at equatorial cloud top altitudes. In the present work, for the first time a distinct variation of SO_2 in the lower cloud region could be derived (cf. Figure 7.7). The variation was observed at both polar regions with highest SO_2 values around the year 2010 and lowest abundances around 2006 and 2013. It is possible that at least the variation at the northern polar region was caused by the long-term variation of the temperature observed at these latitudes (Figure 7.8). The temperature variation may have influenced the vertical transport mechanisms as well as the sulfur chemistry in this region and could have affected the mixing ratio of SO_2.

It is possible that the long-term trend in the temperature is a consequence of the long-term trend in Venus' 365 nm albedo. The latter was observed by *Lee et al.* (2015) at the polar region and by *Lee et al.* (2019) at equatorial and mid-latitudes. A decrease (increase) of the albedo would lead to a heating (cooling) of the atmosphere so that significant temperature variations were conceivable. The observed long-term trend in Venus' 365 nm albedo is attributed to a yet unidentified gas. SO_2 is believed to be a promising candidate as a precursor for this unknown absorber (e.g. *Mills et al.*, 2018). Therefore, the above mentioned long-term trend in SO_2 observed at the equatorial cloud top altitudes could have caused a variation in the abundance of the unknown gas which then led to the long-term trend in Venus' 365 nm albedo.

Indications for a long-term variation of H_2SO_4(g) were observed by *Cimino* (1982) as well as by *Jenkins and Steffes* (1991) in Pioneer Venus radio occultation measurements (cf. Figure 4.4). They have detected a decrease of the S-band radio signal absorption at the *cold collar* latitudes between the years 1978/1979 and 1986/1987 which indicates a decrease of H_2SO_4(g). In the context of the present work, for the first time a distinct appearance of a long-term trend in the H_2SO_4(g) abundance at northern polar latitudes could be derived (cf. Figure 7.13). The lowest H_2SO_4(g) amount was observed in the year 2007 which increased between 2007 and 2008. From the end of 2008 onwards, distinctly increased values were detected. Similar to the long-term trend of SO_2, that of H_2SO_4(g) is most probably a result of the long-term variation of the temperature observed at these latitudes. As mentioned above, the latter may have influenced the vertical transport mechanisms as well as the sulfur chemistry in this region.

H_2SO_4(g) abundance - local time variation

In contrast to the H_2SO_4(g) long-term trend observed at polar latitudes, the equatorial H_2SO_4(g) abundance shows no such variation. Instead, a weak tidal influence could be found in the latter region. The calculated H_2SO_4(g) column density at these latitudes shows an oscillation with a period of 12 hours indicating the influence of a semidiurnal tide (cf. Figure 7.15). Among wind circulation cells, thermal tides are thought to play a crucial role in the maintenance of Venus' superrotating atmosphere (e.g. *Newman and Leovy*, 1992). The influence of thermal tides was previously detected in temperature measurements and wind velocity observations at cloud top altitudes (e.g. *Taylor et al.*, 1980; *Horinouchi et al.*, 2018). In the present study, for the first time the influence of thermal tides was observed in the H_2SO_4(g) abundance below 50 km altitude.

9.2 Modeling

In order to study the main processes which formed the observed global H_2SO_4(g) distribution presented in Figure 7.12, a two-dimensional transport model was developed. Among simplified chemical, condensation and evaporation processes, the mass transport by eddy diffusion, sedimentation and wind was incorporated (cf. section 5.1). The latter transport consisted of two circulation cells, i.e., a Hadley and a polar cell. A background atmosphere consisting of temperature, pressure and number density was incorporated. Those values were available from VeRa's measurements (cf. section 3.2.2) as well as from the *Venus International Reference Atmosphere* (VIRA). In a total number of seven simulation runs the number densities of H_2SO_4(g), H_2O(g) and

that of the main clouds consisting entirely of H_2SO_4-H_2O droplets were calculated until a steady state distribution was reached.

Limits of the model

The vertical and horizontal eddy diffusion coefficients were chosen according to previous atmospheric models. Those were kept constant in all simulation runs (cf. Figure 5.3). Increased vertical and horizontal variations of both, K_{zz} and K_{yy}, can affect the spatial distribution of the gases and that of the cloud density. A similar influence is conceivable by the convection layer located between about 50 and 60 km altitude in Venus' atmosphere (cf. Figure 2.1b)). It was simulated in the present model calculations by increasing K_{zz} in this altitude region (cf. Figure 5.3a)). A variation of K_{zz} in this altitude range may affect the number densities of H_2SO_4(g), H_2O(g) and that of the droplets (e.g. *Imamura and Hashimoto*, 1998).

The wind pattern in Venus' atmosphere was in the present model simulated by the circulation cells presented in Figure 5.1. Their geometry and circulation velocity was not changed in the simulation runs. Observations in Venus' atmosphere have indicated that the meridional wind pattern below about 100 km altitude is more complicated than that assumed in the present model (cf. Figure 2.7). The circulation cells used in the present model provide therefore the dominating large scale wind structure. It can not be excluded, that additional smaller circulation cells exist in Venus' atmosphere. Furthermore, observations revealed that particularly the polar vortices are highly irregular features which continuously change their shapes from a single pole over an S-form to a dipole (e.g. *Luz et al.*, 2011; *Garate-Lopez et al.*, 2013). Consequently, upward as well as downward winds were observed at polar latitudes.

In the present model, the assumed cloud particles consist entirely of H_2SO_4-H_2O droplets whose concentration varies vertically and is constant in the horizontal direction. A latitudinal variation is possible (e.g. *Krasnopolsky*, 2015). It was assumed that the size of the droplets varies with height while a latitudinal variation was not considered. Such a variation is conceivable for the Venus' atmosphere (e.g. *Parkinson et al.*, 2015; *McGouldrick*, 2017).

Results

The various simulation runs were used to study the role of the circulation cells and that of the global temperature distribution in the formation process of both H_2SO_4(g)

accumulated regions, i.e., that at low latitudes above 45 km altitude and that at mid- and polar latitudes below 45 km (cf. Figure 7.12).

Both regions could be successfully reproduced by two simulation runs (cf. Figure 8.4). The locations of the H_2SO_4(g) accumulated regions at low and mid-/high latitudes obtained from the model calculations agree generally with those obtained from VeRa. Moreover, the modeled abundances agree well with the VeRa measurements within the observed variation range (cf. Figures 8.5 and 8.6). Differences between the modeled and observed values can be most probably attributed to wind velocity variations which likely occur in Venus' atmosphere. Those may significantly influence the global distribution of H_2SO_4(g). Additionally, temperature variations may largely affect the sulfuric acid vapor content. Both effects were shown in the simulation runs.

The present simulation calculations have shown that the enhanced H_2SO_4(g) content at equatorial latitudes was formed by opposite directed mass transport. Condensation of upward transported H_2SO_4(g) and H_2O(g) increased the number density of the cloud droplets while the downward transport of these particles and the subsequent evaporation enhanced the H_2SO_4(g) accumulation at lower altitudes. This way, a region of enhanced H_2SO_4(g) was formed around 47 km altitude and a region of increased cloud density was created between 48 and 49 km altitude (cf. Figure 8.9). It turned out that the Hadley cell plays a crucial role in this formation process. These findings agree with those presented for example by *Knollenberg and Hunten* (1980) as well as by *Imamura and Hashimoto* (1998).

The H_2SO_4(g) accumulation at mid- and polar latitudes, however, could not be reproduced by these authors. An additional simulation run performed in the context of the present work has revealed that H_2SO_4(g) does not accumulate at mid- and polar latitudes when one single circulation cell is used, which is similar to that applied by *Imamura and Hashimoto* (1998) (cf. Figure 2.8c)). In contrast to this, this region of increased H_2SO_4(g) content was successfully reproduced in various simulation runs of the present model (cf. table 8.2). It was mainly formed by sedimentation and subsequent evaporation of sulfuric acid droplets. The number density of the latter was constantly highest at high latitudes which was a consequence of the low temperatures in this region. The polar cell played a minor role in this formation process. As the upper and lower panels in Figure 8.1 show, polar winds, however, may significantly affect the abundance and structure of the H_2SO_4(g) accumulated region. Upward winds transported haze into higher altitudes where the gas condensed into droplets due to the lower temperatures. This way, the haze content was decreased and the cloud density was increased in this region. Highest values of H_2SO_4(g) were formed around 43 km altitude, while the maximum cloud densities are located around 45 km.

The formation process of the H_2SO_4(g) accumulated region at mid- and high latitudes is similar to that described by *Ando et al.* (2020). The global H_2SO_4(g) distribution presented by these authors, however, is comparable to that obtained from the simulation run *Test 0*a) (cf. Figure 8.1). In this simulation run, the wind circulation was deactivated and the mass transport was solely calculated by sedimentation and eddy diffusion. As a result, the distribution of the H_2SO_4(g) accumulation at the mid- and polar region follows the latitudinal temperature gradient and no H_2SO_4(g) accumulation was formed at equatorial latitudes. This was not observed by VeRa (cf. Figure 7.12). The similarity of the H_2SO_4(g) distribution obtained from *Test 0*a) and that presented by *Ando et al.* (2020) indicates that the transport mechanisms below about 50 km altitude were underestimated in the model used by *Ando et al.* (2020).

VeRa measurements revealed that both H_2SO_4(g) accumulated regions (equatorial and mid-/polar) are distinctly separated (cf. Figure 7.12). In the present model, this separation was successfully reproduced by the descending branches of the circulation cells at mid-latitudes (cf. Figure 5.1). The latter transported H_2SO_4(g) to low altitudes so that the simulated gas distribution at mid-latitudes is similar to that observed by VeRa (cf. Figure 8.4). The similarity is a strong indication for the existence of downward winds in this spatial region of Venus' atmosphere. Downward winds at mid-latitudes may also serve as an explanation for the low SO_2 abundance between 51 and 54 km altitude at these latitudes (cf. Figure 8.7). The amount of SO_2 is distinctly higher at the equatorial and polar latitudes which is most probably a result of upward winds in these regions. A further consequence of the dominating downward transport at mid-latitudes in the present model is the absence of a cloud droplet accumulation at these latitudes so that the cloud bottom is located at higher altitudes compared to that at the equatorial and polar regions (cf. Figure 8.8). The absence of a *lower cloud layer* (cf. Table 2.1) at mid-latitudes is inconsistent with previous 1D model calculations (e.g. *McGouldrick*, 2017) and consistent with the 2D transport model presented by *Imamura and Hashimoto* (1998) (cf. Figure 8.14).

The global distribution of water vapor obtained from the present model shows a gradual decrease from lower to higher altitudes (30 ppm to $<$ 10 ppm), which is consistent with observations (cf. Figure 8.16). The influence of vertical wind transport in the model is mainly visible between about 45 and 50 km altitude as can be seen from Figure 8.10. Here, the equatorial and the polar regions reveal higher H_2O(g) contents compared to that at mid-latitudes. At the *cold collar* region, the low temperatures decreased the amount of water vapor and increased that of the cloud droplets. An increased cloud density in this spatial region is also visible in the model of *Imamura and Hashimoto* (1998) (cf. Figure 8.17). Above about 70 km altitude, a clear latitudinal dependance has been formed in the present model with increased H_2O(g) values at polar

latitudes and lower mixing ratios at the equatorial region. This is a consequence of the latitudinal temperature distribution at these altitudes (cf. Figure 2.1a)). A latitudinal trend in the H_2O(g) abundance at the higher altitudes is consistent with observations (e.g. *Cottini et al.*, 2012; *Fedorova et al.*, 2016).

9.3 Outlook

The global distributions of H_2SO_4(g) and SO_2 derived from VeRa's radio occultation measurements presented in chapter 7 as well as the two-dimensional transport model developed and applied in the present work (chapters 5 and 8) provide approaches for further radio science measurements on Venus as well as for additional simulation studies. The following requirements and scientific goals should be aimed in future observations and model calculations:

Observation

- In order to withstand the strong signal absorption in Venus deep atmosphere, the operating spacecraft used for radio occultation measurements at Venus should be equipped with an EIRP value which exceeds that of Venus Express (cf. table 3.1). It can be seen from Figure 7.12 that the number of data samples decreased rapidly as VeRa's radio rays traversed Venus's atmosphere below about 50 km altitude. A high EIRP value ensures a measurable carrier signal at the ground station on Earth even when Venus' deep atmosphere is sounded. This way the number of data samples retrieved from this atmospheric region can be increased which enhances the reliability of the derived H_2SO_4(g) abundance in this altitude region.

- A strong carrier signal can also be ensured by reducing the S/C to Venus distance during the radio occultation measurements. The contribution of refractive defocussing to the total signal attenuation increases with the S/C to Venus distance. As can be seen from Figure 6.4, the large distance of VEX at the southern polar and sub-polar region was responsible for a relatively high signal attenuation at these latitudes so that only a few data samples were retrieved from the deeper atmosphere. A reduction of the S/C to Venus distance would reduce the signal attenuation and increase the number of data samples from the lower altitudes.

- The usage of three frequencies in radio occultation measurements would allow to distinguish between the absorptivity contributions of SO_2, H_2SO_4(g) and that of the cloud droplets. S- and X-band measurements can be used to derive a global picture of the SO_2 and H_2SO_4(g) abundance in Venus' atmosphere below about

55 km altitude (cf. section 7.1). The additional usage of a higher frequency (Ka-band) would provide the density of the cloud droplets at cloud bottom altitudes (cf. Figure 8.8) which is not feasible with S- and X-band radio signals.

- VeRa's radio occultation measurements for the first time allowed to derive a global picture of the H_2SO_4(g) abundance between 40 and 55 km altitude. Due to the orbit geometry, however, a coverage of the northern mid-latitudinal region was not possible (cf. Figure 7.12). The orbit of future spacecrafts should ensure a uniform coverage of all spatial regions. Those measurements would either confirm or disprove the atmospheric symmetry of both hemispheres.

- In order to extend/complement the study of long-term variations of trace gases in Venus' atmosphere (cf. Figures 7.7 and 7.13), the duration of future missions should not be shorter than the period of Venus Express. Those measurements would help to investigate the connection of the observed long-term variations of H_2SO_4(g), SO_2, 365-nm albedo, temperature and the unknown UV absorbing gas (cf. Figures 7.11 and 7.13).

- The study of short-term variations and that of local time dependencies as observed with VeRa at equatorial latitudes (cf. Figure 7.15) provide insights into atmospheric changes on short time scales. The latter contain key information about maintenance mechanisms of the superrotating atmosphere. The study can be supported by an increased number of occultation measurements per Earth day.

Modeling

- The profiles of the vertical and horizontal eddy diffusion coefficients K_{zz} and K_{yy}, respectively, were chosen in accordance with previous models (cf. Figure 5.3). The variation of these parameters may influence the calculated number densities of H_2SO_4(g), H_2O(g) and that of the cloud droplets (e.g. *Hashimoto and Abe*, 2001). The variation of the convection layer located between about 50 and 60 km altitude, which was simulated by increased values of K_{zz}, may also affect the calculated spatial distributions of the number densities (e.g. *Imamura and Hashimoto*, 1998). The study of the influence of K_{zz} and K_{yy} on H_2SO_4 and H_2O(g) should therefore be considered in future simulation runs.

- The saturation vapor pressures of H_2SO_4(g) and H_2O(g) depend on the concentration of the H_2SO_4-H_2O solution (e.g. *Zeleznik*, 1991). A latitudinal variation of the latter is likely in Venus' atmosphere (e.g. *Krasnopolsky*, 2015). It may affect the condensation and evaporation processes and therefore affect the spatial

distributions of the calculated number densities. The condensation and evaporation processes should therefore be calculated with a higher grade of detail in future modeling work.

- As can be seen from Figure 8.13, the number density of the cloud droplets obtained from the present model calculations disagrees with the observations above about 57 km altitude. This is most probably a consequence of overestimated vertical transport mechanisms at higher altitudes. The latter should be adjusted for future simulation runs.

- The developed mass transport model can be easily connected to a one-dimensional photochemical model. This way, in addition to the number densities of H_2SO_4(g), H_2O(g) and of the cloud droplets, the global distribution of SO_2 can be simulated. The simulation of SO_2 requires additionally the calculation of the photochemical reactions of SO_2 which are responsible for the depletion of the gas at upper cloud altitudes (cf. section 2.2).

- Furthermore, the long-term variations as well as the local time dependencies of SO_2 and H_2SO_4(g) presented in the Figures 7.7 and 7.13 can be studied by using the developed mass transport model. The investigations can help to understand the nature of these variations and this way provide information about the significance of the transport mechanisms. The latter is of high importance for the study of the maintenance of the superrotating atmosphere.

- Moreover, the developed mass transport model provides an excellent tool which allows to extend the study of the global wind pattern in Venus' atmosphere. In the present work, a system of two circulation cells was applied, i.e. Hadley and polar cell. The number of circulation cells, their geometry and their circulation velocity can easily be varied. The variation may provide information on the existence of small scale circulation cells and this way provide possible explanations for the wind velocity observations presented in Figure 2.7.

Appendix A

Radio signal attenuation in the Earth atmosphere

Attenuation of radio waves in the Earth atmosphere is mainly caused by oxygen, water vapor, rain as well as clouds and fog. In the following, the attenuation due to these factors is shortly discussed.

Oxygen and water vapor attenuation

The mixing ratio of oxygen is stable in the atmosphere, so that global variations of radio attenuation caused by O_2 are small. In contrast, the water vapor mixing ratio shows a large global variation. Radio signal attenuation due to water vapor depends therefore strongly on the location of the G/S. Attenuation calculations for oxygen and water vapor based on empirical modelling can be found in e.g. *Ho et al.* (2004) or *ITU-R Recommendation* (2013). The specific attenuation due to oxygen in units of dB/km is

$$\alpha_{O_2} = \left(\frac{7.2 r_t^{2.8}}{f^2 + 0.34 r_p^2 r_t^{1.6}} + \frac{0.62 \xi_3}{(54 - f)^{1.16\xi_1} + 0.83\xi_2} \right) \cdot f^2 r_p^2 \cdot 10^{-3}, \tag{A.1}$$

with

$$\xi_1 = \varphi\left(r_p, r_t, 0.0717, -1.8132, 0.0156, -1.6515\right) \tag{A.1a}$$
$$\xi_2 = \varphi\left(r_p, r_t, 0.5146, -4.6368, -0.1921, -5.7416\right) \tag{A.1b}$$
$$\xi_3 = \varphi\left(r_p, r_t, 0.3414, -6.5851, 0.2130, -8.5854\right) \tag{A.1c}$$

where

$$\varphi\left(r_p, r_t, a, b, c, d\right) = r_p^a r_t^b e^{c(1-r_p)+d(1-r_t)} \tag{A.1d}$$

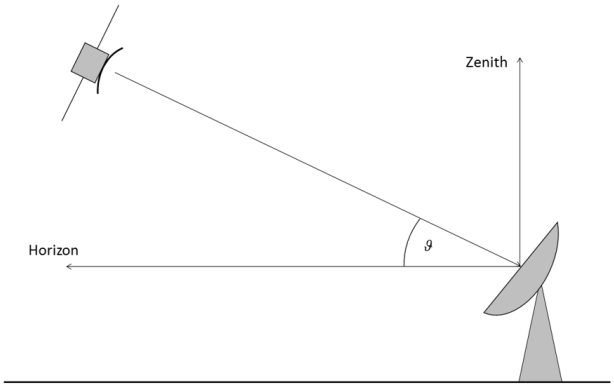

Figure A.1: *Receiving antenna pointing angle distribution. The elevation angle is represented by ϑ.*

and

$$r_p = \frac{p}{1013} \qquad \text{and} \qquad r_t = \frac{288}{273 + T}. \tag{A.1e}$$

The units of the frequency f (for $f \leq 54$ GHz), pressure p and temperature T are GHz, hPa and °C, respectively.

The specific attenuation due to water vapor in units of dB/km is

$$\alpha_{\mathrm{H_2O}} = A_{\mathrm{H_2O}} \cdot f^2 \cdot \rho \cdot 10^{-4}, \tag{A.2}$$

where

$$A_{\mathrm{H_2O}} = \left(0.067 + \frac{3}{(f - 22.3)^2 + 7.3} + \frac{9}{(f - 183.3)^2 + 6} + \frac{4.3}{(f - 323.8)^2 + 10}\right) \tag{A.2a}$$

and ρ in g/m^3 is the water vapor density. In order to compute the path attenuation τ in units of dB, the specific attenuation α along the radio ray path within Earth's atmosphere must be considered. The attenuation increases with increasing path length. As can be seen in Figure A.1, the latter increases with decreasing elevation angle ϑ. The path attenuation for elevation angles between 5° and 90° can be computed by

$$\tau_{\mathrm{O_2,H_2O}} = \frac{h_p \left(\alpha_{\mathrm{O_2}} + \alpha_{\mathrm{H_2O}}\right)}{\sin \vartheta}, \tag{A.3}$$

where the path length is denoted by h_p. As an example, Figure A.2 shows the path attenuation $\tau_{\mathrm{O_2}}$ and $\tau_{\mathrm{H_2O}}$ in the frequency range between 1 and 40 GHz for the elevation angles 5° and 90°. Here, the vertical distribution of the pressure and water vapor

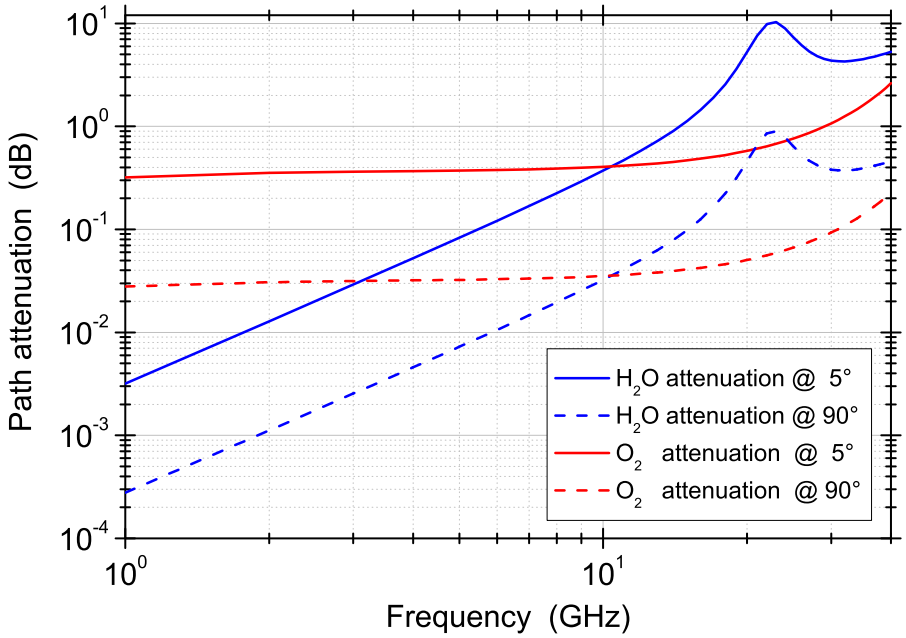

Figure A.2: *Path attenuation in the Earth atmosphere due to oxygen and water vapor for the elevation angles $\vartheta = 5°$ and $\vartheta = 90°$.*

density between 0 and 15 km altitude were modeled by means of the barometric formula

$$p(z) = p_0 e^{\frac{(z-z_0)}{H_p}} \tag{A.4}$$

$$\rho(z) = \rho_0 e^{\frac{(z-z_0)}{H_{\mathrm{H2O}}}}. \tag{A.5}$$

The pressure and water vapor density at sea level were set to $p_0 = 980$ hPa and $\rho_0 = 15$ g/m^3. The pressure and water vapor scale heights were chosen to be constant, with $H_p = 8$ km and $H_{\mathrm{H_2O}} = 2.5$ km. The temperature at sea level was chosen to be $T = 23°$C, decreasing monotonically to $T = -55°$C between 12 and 15 km altitude. The altitude range between 0 and 15 km was subdivided into equal 0.5 km thick layers. Mean temperature, pressure and water vapor density values were computed within each layer. Subsequently, the path attenuation in each layer was calculated using equation (A.3). The sum gives the total path attenuation visible in Figure A.2.

It is clearly visible, that the radio attenuation increases with decreasing elevation angle. The absorption at 5° is approx. ten times greater than that at 90° for both, oxygen and water vapor. While below approx. 10 GHz the absorption is dominated by oxygen, above approx. 10 GHz the absorption due to water vapor is stronger. It reaches maximal values around 22.235 GHz due to the rotational absorption of H_2O

at this frequency. Maximal attenuation values of almost 1 dB can occur for a zenith radio ray path and increase to values around 10 dB for an elevation angle of 5°. The strong increase of the oxygen absorption visible at $f > 30$ GHz is attributed to the O_2 absorption line at 60 GHz. In contrast to the higher frequencies, the attenuation of X- and S-band radio signals due to oxygen and water vapor in Earth's atmosphere is negligible small. Highest values of $10^{-2} - 10^{-1}$ dB for the X-band and $10^{-3} - 10^{-2}$ dB for the S-band are visible.

It turned out that the attenuation of radio waves in Earth's atmosphere occurs mainly below the altitude of about 10 - 15 km. An increase of the upper boundary to altitudes above 15 km has no significant effect on the attenuation values presented in Figure (A.2).

Cloud and fog attenuation

Earth's cloud particles reveal sizes smaller than 100 µm. Therefore, similar to the case of Venus, the attenuation of radio waves (with $f \leq 100$ GHz) due to Earth's cloud particles can be calculated by applying the *Rayleigh approximation* (cf. section 4.1.3). The specific absorption in units of dB/km can be written as (cf. equation (4.18))

$$\alpha_c = K \cdot M, \tag{A.6}$$

where M is the liquid water density in the cloud or fog in units of g/m^3. Based on empirical modelling, the coefficient K can be calculated by (*ITU-R Recommendation*, 2017*a*)

$$K = \frac{0.819 \cdot f}{\epsilon'' (1 + \eta)}, \tag{A.6a}$$

with

$$\eta = \frac{2 + \epsilon'}{\epsilon''} \tag{A.6b}$$

$$\epsilon' = \frac{\epsilon_0 - \epsilon_1}{1 + \left(\frac{f}{f_p}\right)^2} + \frac{\epsilon_1 - \epsilon_2}{1 + \left(\frac{f}{f_s}\right)^2} + \epsilon_2 \tag{A.6c}$$

$$\epsilon'' = \frac{f\,(\epsilon_0 - \epsilon_1)}{f_p \left(1 + \left(\frac{f}{f_p}\right)^2\right)} + \frac{f\,(\epsilon_1 - \epsilon_2)}{f_s \left(1 + \left(\frac{f}{f_s}\right)^2\right)} \tag{A.6d}$$

and

$$\epsilon_0 = 77.66 + 103.3(\varsigma - 1) \tag{A.6e}$$

$$\epsilon_1 = 0.0671 \cdot \epsilon_0 \tag{A.6f}$$

$$\epsilon_2 = 3.52 \tag{A.6g}$$

$$\varsigma = \frac{300}{T}, \tag{A.6h}$$

where T is the liquid water temperature in units of K. The principal and secondary relaxation frequencies in units of GHz are

$$f_p = 20.2 - 146(\varsigma - 1) + 316(\varsigma - 1)^2 \tag{A.6i}$$

$$f_s = 39.8 \cdot f_p. \tag{A.6j}$$

The path attenuation τ_c is obtained by multiplying the specific attenuation α_c by the traversed path of the radio wave within the cloud or fog. It can be easily seen from equation (A.6) that τ_c can then be written as

$$\tau_c = \frac{K \cdot L_c}{\sin \vartheta}, \tag{A.7}$$

where L_c is the columnar content of the cloud liquid water in units of kg/m^2 or, equivalently, mm. Values of L_c are available at the website of the *International Telecommunication Union* [1)]. Path attenuation due to clouds/fog in the frequency range between 1 and 40 GHz for the elevation angles $\vartheta = 5°$ and $\vartheta = 90°$ is presented in Figure A.3. Here, a columnar content of 2 kg/m^2 was used for an exceedance probability of 0.1%. The attenuation increases from lower to higher frequencies, reaching maximal values of approx. 2 dB and 20 dB for elevation angles of 90° and 5°, respectively. The attenuation of VeRa's radio signals reaches maximal values of more than 2 dB for the X-band for $\vartheta = 5°$.

Rain attenuation

The size of rain drops may be of the order of a few millimeters. In this case, *Rayleigh approximation* is not applicable for radio frequencies greater than approx. 3 GHz. Attenuation must then be calculated from the complete Mie theory. It was found that the specific radio signal attenuation due to rain α_r in units of dB/km can be expressed as a function of the precipitation rate R in units of mm/h (*Battan*, 1973)

$$\alpha_r = K_r \cdot R^{w_r}. \tag{A.8}$$

[1)] https://www.itu.int/rec/R-REC-P.840-7-201712-I

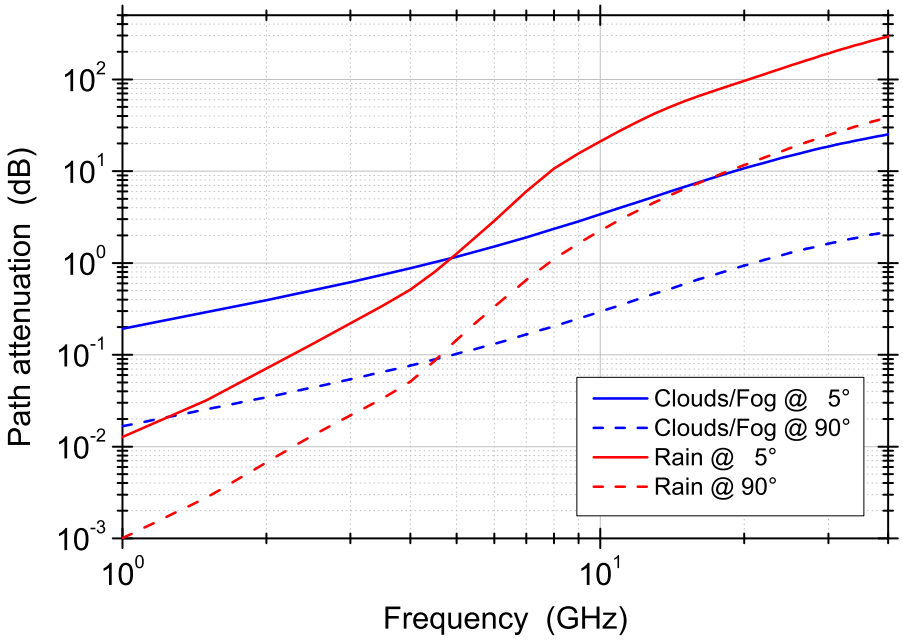

Figure A.3: *Path attenuation in the Earth atmosphere due to clouds/fog and rain for the elevation angles $\vartheta = 5°$ and $\vartheta = 90°$. For the cloud/fog attenuation it was set: $L_c = 2$ kg/m^2; exceedance probability: 0.1%. For the rain attenuation it was set: $R = 25$ mm/h; exceedance probability: 0.01%; rain height: 3.9 km.*

Values for the coefficients K_r and w_r can be calculated using equations provided in *ITU-R Recommendation* (2005)

$$K_r = \frac{K_{r,H} + K_{r,V} + (K_{r,H} - K_{r,V}) \cos^2 \vartheta \cos 2\chi}{2} \tag{A.8a}$$

$$w_r = \frac{K_{r,H} w_{r,H} + K_{r,V} w_{r,V} + (K_{r,H} w_{r,H} - K_{r,V} w_{r,V}) \cos^2 \vartheta \cos 2\chi}{2K_r}. \tag{A.8b}$$

Here, χ represents the polarization tilt angle relative to the horizontal polarization. It is $\chi = 45°$ for circular and $\chi = 90°$ for linear polarization. Values for the coefficients $K_{r,H,V}$ and $w_{r,H,V}$ can be obtained from *ITU-R Recommendation* (2005), either for horizontal or vertical polarizations.

Similar to water vapor, the precipitation rate R shows a high global variation. The radio attenuation in the Earth atmosphere due to rainfall depends therefore strongly on the location of the G/S receiver. Figure A.3 shows the path attenuation τ_R due to rain in the frequency range between 1 and 40 GHz for the location of the New Norcia G/S. Following the algorithm presented in *ITU-R Recommendation* (2017*c*), τ_R was

computed for the elevation angles 5° and 90°. The precipitation rate R, here 25 mm/h for an exceedance probability of 0.01%, was obtained from *ITU-R Recommendation* (2017*b*). The rain height value was set to 3.9 km.

It is clearly visible that the attenuation due to rainfall can be quite strong, particularly at high frequencies. Values between approx. 1 and 10 dB can be observed for the X-band radio signal, increasing with increasing frequency. In contrast, the attenuation of the S-band signal ranges between 10^{-2} and 10^{-1} dB. It is obvious, that rain attenuation is weaker than the attenuation due to clouds/fog below approx. 5 GHz. For f $>$ 5 GHz, however, rain attenuation shows the highest values when compared with cloud/fog as well as with O_2 and H_2O attenuation (cf. Figure A.2).

Appendix B

Multipath propagation effects occurring in Venus Express radio occultation experiments

For the analysis of radio occultation data the Fast Fourier Transform (FFT) is applied to the received radio signals in order to determine the sky frequency and amplitude (section 3.2). Enhanced temperature inversions, however, manifested in variations of the refractive index, may lead to a complicated structure of the received radio signals. Several different radio rays may arrive at the receiver simultaneously when sounding those atmospheric regions. Figure B.1 shows the geometry for the case of *multipath propagation*.

CL-receivers, which track the incoming radio signals by using phase-locked loops (cf. section 3.2), provide incorrect phase/frequency and amplitude information. In the OL-technique, used for Venus Express radio occultation measurements, the incoming radio signals were down-converted to base band and its complex form was stored for later processing. The Fast Fourier Transform was then applied to determine the sky frequency and amplitude of the signals. In Venus' *multipath* region, however, the FFT-based analysis sometimes provided incorrect results. The simultaneous occurrence of three radio rays at the receiver, as depicted in Figure B.1, made an unambiguous detection of the carrier signal difficult.

Figure B.2 shows the power spectra of VeRa's X-band radio signals when Venus' *multipath* region was sounded during two *ingress* measurements in the year 2006. The radio signals were down converted to base-band and corrected for the Doppler shift induced by the relative motion between the S/C and G/S. Additionally, a predicted atmospheric Doppler shift was removed. The band width of the residual signals was less than 50 Hz. While panel a) shows the latitudinal region around 73°S, panel b)

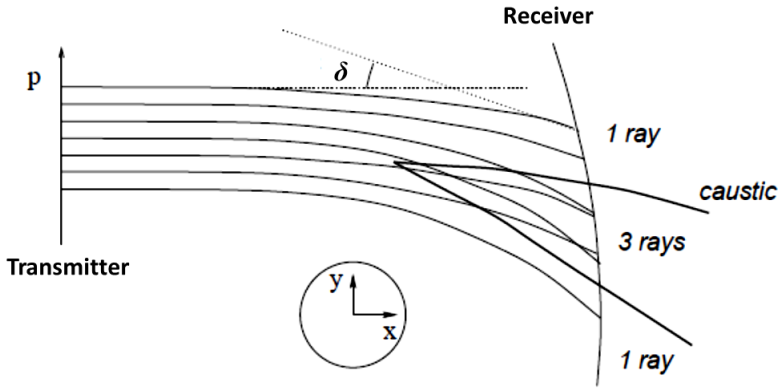

Figure B.1: *Sketch of multipath propagation in the atmosphere. Radio rays, emitted by the transmitter, traverse the atmospheric region where inhomogeneities of the refractive index occur. The refractive index doesn't increase monotonically with depth and causes therefore a variation of the radio ray refraction in a narrow altitude range. This implies that several different radio rays arrive at the receiver at the same time. The sketch of the multipath geometry was adopted from Lauritsen and Lohmann (2004) who depicted the occurrence of multipath propagation in radio occultation measurements conducted on the Earth atmosphere.*

shows the region around 65°S. Both latitudes are located in the *cold collar* region (60° - 75°).

The structure of the power spectra represented as a function of time shows the typical frequency behavior in the *multipath* region. Three carrier signals are visible at the same time separated by frequency values ranging from a few Hertz to several tens of Hertz. The FFT-based algorithm, which was developed for the analysis of VeRa's OL data, extracts the frequency and amplitude of the strongest carrier signal. The result is presented by the black dots. In the presence of multiple radio rays an unambiguous detection of the correct carrier signal is difficult. It can be seen that in the time range between 219 seconds and 233 seconds after beginning of the measurement, the almost linear decreasing part of the power spectra is 'ignored'. Consequently, the standard FFT-based algorithm provides an incorrect time series of the frequency and amplitude accompanied by jumps in the data.

It is clearly visible from Figure B.2 that the affected time range is variable. While the latter has a length of approx. 14 seconds in panel a), only 2 seconds of the time series are affected in panel b). The corresponding altitude ranges are 3.7 km in panel a) and 1.2 km in panel b). It should be noted that the altitudes depicted in both

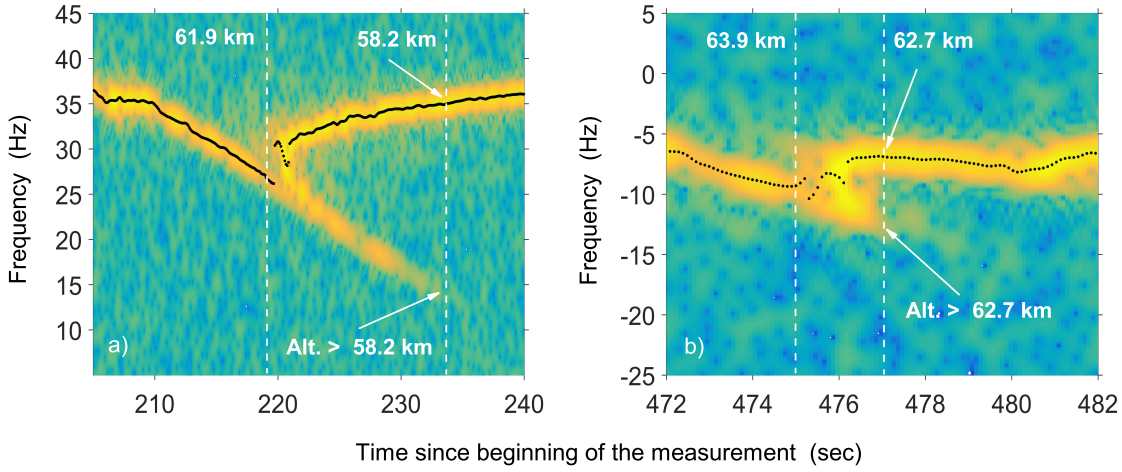

Figure B.2: *Power spectra of VeRa's X-band radio signals computed when the multipath region in Venus' atmosphere was sounded. The signals were down converted to base-band. The Doppler shift induced by the relative motion between the S/C and G/S was removed. Additionally a predicted atmospheric Doppler shift was removed. The down mixing of the base-band signal by using the predicted Doppler shift results either in positive or in negative frequencies of the residual signal. The black dots show the residual frequency f_{res} computed by using the standard FFT-based algorithm outlined in section 3.2.1. Panel a) shows the latitudinal region around 73°S, panel b) shows the region around 65°S. The white dashed lines represent the sounded altitude corresponding to the ground station received time visible on the abscissa.*

panels are derived from the Doppler shift computed using the FFT-based algorithm (black dots). The lowest frequency values of the 'ignored' parts of the power spectra in both panels correspond therefore to altitudes above 58.2 km and 62.7 km, respectively. Atmospheric profiles derived in later processing steps (section 3.2.2) contain therefore incorrect values between 61.9 km and 58.2 km (panel a)) as well as between 63.9 km and 62.7 km altitude (panel b)).

The shape of the *multipath* structure (length of the time range and frequency difference of multiple carrier signals) visible in the power spectra is mainly controlled by the depth and thickness of the inversion layer in Venus' atmosphere. The strongest *multipath effects* can be observed in measurements performed at the *cold collar* regions (S. Tellmann, personal communication). *Hinson et al.* (1998) have shown that the shape of the *multipath* structure also depends on the spacecrafts velocity, the signal frequency and the distance D (see Figure 3.2). Figure B.3.a) shows the X-band measurement, adopted from Figure B.2.a), along with the corresponding S-band measurement (panel

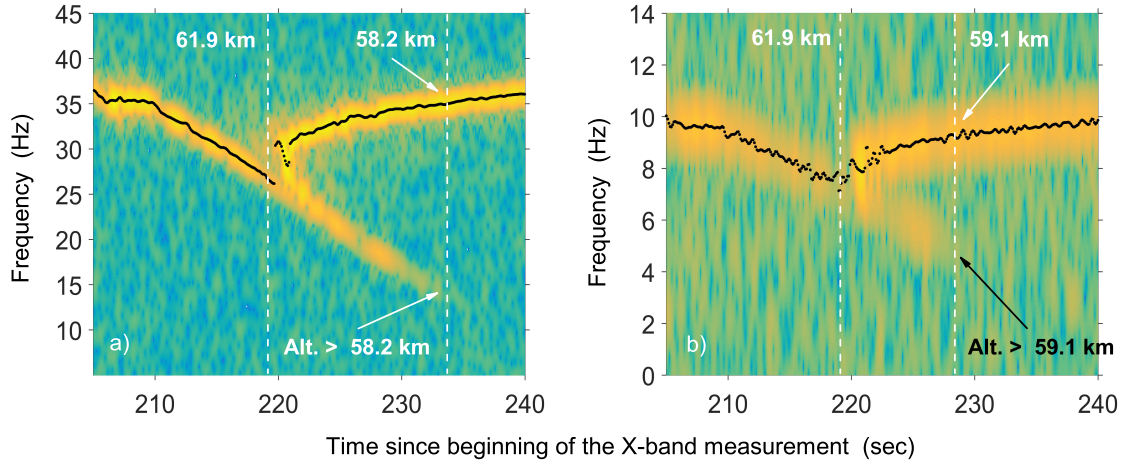

Figure B.3: *Panel a): Power spectra of VeRa's X-band radio signal adopted from Figure B.2.a). Panel b): Power spectra of VeRa's S-band radio signal from the same measurement as presented in panel a).*

b). Similar to the X-band measurement, the time series of the frequency of the S-band radio signal is not correct computed by the standard FFT-based algorithm (black dots) within the *multipath* region. However, the affected time range is shorter compared to the X-band signal. It is approx. 10 seconds at S-band versus 14 seconds at X-band. The corresponding altitude range is 2.8 km for the S-band radio signal. Atmospheric profiles derived from the S-band data contain incorrect values between 61.9 km and 59.1 km altitude.

In order to correct for *multipath effects* in radio occultation experiments, high resolution methods must be applied for the detection of the correct carrier signal. Only this way a correct time series of the frequency and amplitude can be obtained, so that an unambiguous assignment of the frequency and radio ray parameters (section 3.2.2) can be made.

A large number of methods (e.g. back-propagation (e.g. *Ao et al.*, 2003), canonical transform (e.g. *Gorbunov*, 2002), full spectrum inversion (e.g. *Jensen et al.*, 2003)) have been developed inspired by the occurrence of *multipath effects* in planetary radio occultation measurements and GPS supported radio occultation experiments performed at the Earth atmosphere.

Appendix C

Coefficients for the mass transport equation

For the substitution of the first order spatial derivatives in equation (5.14) with difference quotients it is important to distinguish between various mass flow directions. If the flow direction is from left to right ($v_\phi \geq 0$), the left-handed difference quotient must be used, otherwise ($v_\phi < 0$) the right-handed difference quotient is used. This must also be considered for upward ($v_h \geq 0$) and downward ($v_h < 0$) directed mass flows. In the following, the coefficients for the equation (5.16) are presented by considering the mass flow direction.

$\underline{v_\phi \geq 0 \; ; \; v_h \geq 0}$

$$
\begin{aligned}
C_1 &= \frac{\Delta t}{r\Delta\phi}\left(v_\phi + \tan\phi\frac{K_\phi}{r} + 2\frac{K_\phi}{r\Delta\phi}\right) \\
&\quad + \frac{\Delta t}{\Delta h}\left(2\frac{K_h}{\Delta h} - v_{sed} - v_h\right) \\
&\quad - \tan\phi\frac{v_\phi}{r}\Delta t + 1 \\
C_2 &= -\frac{\Delta t}{r\Delta\phi}\left(v_\phi + \tan\phi\frac{K_\phi}{r} + \frac{K_\phi}{r\Delta\phi}\right) \\
C_3 &= -\frac{K_\phi}{r^2}\frac{\Delta t}{\Delta\phi^2} \\
C_4 &= -K_h\frac{\Delta t}{\Delta h^2} \\
C_5 &= \frac{\Delta t}{\Delta h}\left(v_{sed} + v_h - \frac{K_h}{\Delta h}\right)
\end{aligned}
\tag{C.1}
$$

$\underline{v_\phi < 0 \ ; \ v_h < 0}$

$$
\begin{aligned}
C_1 &= \frac{\Delta t}{r\Delta\phi}\left(\tan\phi\frac{K_\phi}{r} + 2\frac{K_\phi}{r\Delta\phi} - v_\phi\right) \\
&\quad + \frac{\Delta t}{\Delta h}\left(2\frac{K_h}{\Delta h} - v_{sed} - v_h\right) \\
&\quad - \tan\phi\frac{v_\phi}{r}\Delta t + 1 \\
C_2 &= -\frac{K_\phi}{r^2}\frac{\Delta t}{\Delta\phi}\left(\tan\phi + \frac{1}{\Delta\phi}\right) \\
C_3 &= \frac{\Delta t}{r\Delta\phi}\left(v_\phi - \frac{K_\phi}{r\Delta\phi}\right) \\
C_4 &= -K_h\frac{\Delta t}{\Delta h^2} \\
C_5 &= \frac{\Delta t}{\Delta h}\left(v_{sed} + v_h - \frac{K_h}{\Delta h}\right)
\end{aligned}
\tag{C.2}
$$

$\underline{v_\phi \geq 0 \ ; \ v_h < 0}$

$$
\begin{aligned}
C_1 &= \frac{\Delta t}{r\Delta\phi}\left(v_\phi + \tan\phi\frac{K_\phi}{r} + 2\frac{K_\phi}{r\Delta\phi}\right) \\
&\quad + \frac{\Delta t}{\Delta h}\left(2\frac{K_h}{\Delta h} - v_{sed} - v_h\right) \\
&\quad - \tan\phi\frac{v_\phi}{r}\Delta t + 1 \\
C_2 &= -\frac{\Delta t}{r\Delta\phi}\left(v_\phi + \tan\phi\frac{K_\phi}{r} + \frac{K_\phi}{r\Delta\phi}\right) \\
C_3 &= -\frac{K_\phi}{r^2}\frac{\Delta t}{\Delta\phi^2} \\
C_4 &= -K_h\frac{\Delta t}{\Delta h^2} \\
C_5 &= \frac{\Delta t}{\Delta h}\left(v_{sed} + v_h - \frac{K_h}{\Delta h}\right)
\end{aligned}
\tag{C.3}
$$

$\underline{v_\phi < 0 \ ; \ v_h \geq 0}$

$$
\begin{aligned}
C_1 &= \frac{\Delta t}{r\Delta\phi}\left(\tan\phi\frac{K_\phi}{r} + 2\frac{K_\phi}{r\Delta\phi} - v_\phi\right) \\
&\quad + \frac{\Delta t}{\Delta h}\left(v_h + 2\frac{K_h}{\Delta h} - v_{sed}\right) \\
&\quad - \tan\phi\frac{v_\phi}{r}\Delta t + 1 \\
C_2 &= -\frac{K_\phi}{r^2}\frac{\Delta t}{\Delta\phi}\left(\tan\phi + \frac{1}{\Delta\phi}\right) \\
C_3 &= \frac{\Delta t}{r\Delta\phi}\left(v_\phi - \frac{K_\phi}{r\Delta\phi}\right) \\
C_4 &= -\frac{\Delta t}{\Delta h}\left(v_h + \frac{K_h}{\Delta h}\right) \\
C_5 &= \frac{\Delta t}{\Delta h}\left(v_{sed} - \frac{K_h}{\Delta h}\right)
\end{aligned}
\tag{C.4}
$$

Appendix D

The effect of the antenna mispointing on the Venus Express S-band radio signal

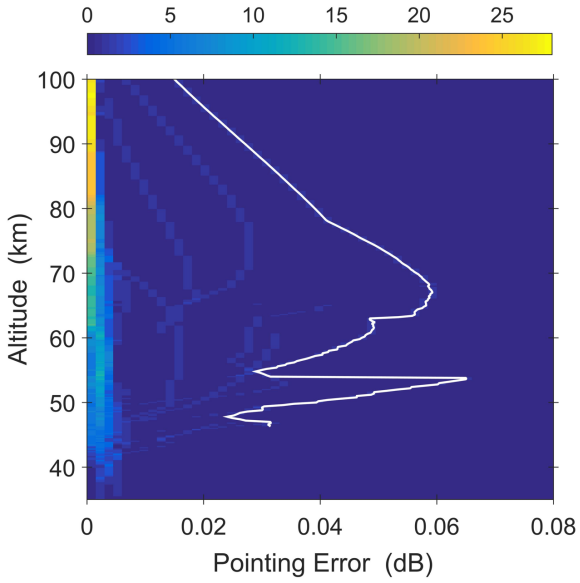

Figure D.1: *The effect of pointing inaccuracies on Venus Express' S-Band radio signals occurred during the occultation measurements in the year 2006 as a function of the sounded altitude. The horizontal axes were subdivided into equal bins of 0.0015 dB each and measurements located within each bin were counted. The color code gives the number of measurements located within each bin. The white profile represents maximal pointing inaccuracies occurred in 2006.*

Due to a large half power beam width value of $\vartheta_{3\mathrm{dB}}^{\text{S-band}} \approx 6^{\circ}$ for the HGA1 the effect of mispointing on VeRa' S-band radio signals was smaller than that on the X-band signals. Figure D.1 shows the effect of mispointing on the S-band radio signals during measurements carried out with the HGA1 in the year 2006. The horizontal axes were subdivided into equal bins of 0.0015 dB each and measurements located within each bin were counted. The color code gives the number of measurements located within each bin. The white profile represents maximal observed pointing inaccuracy values.

Appendix E

H_2SO_4(g) profiles derived from VeRa's X- and S-band radio absorptivity in the year 2006.

The Figures E.1 and E.2 show vertical profiles of the H_2SO_4(g) abundance in Venus atmosphere at the northern cold collar and polar latitudes, respectively. The profiles were derived from VeRa's X- and S-band radio absorption measurements carried out between 2006-07-19 and 2006-08-21 in the year 2006. The profiles along with those

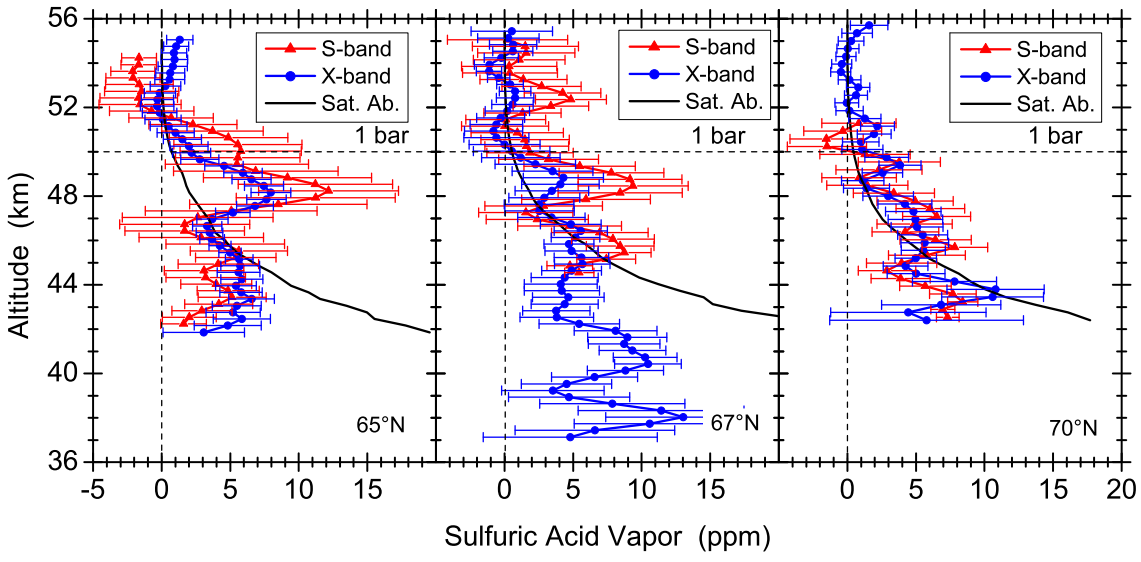

Figure E.1: *Sulfuric acid vapor profiles at the northern cold collar latitudes in Venus atmosphere derived from VeRa's X- and S-band radio signal absorption in the year 2006.*

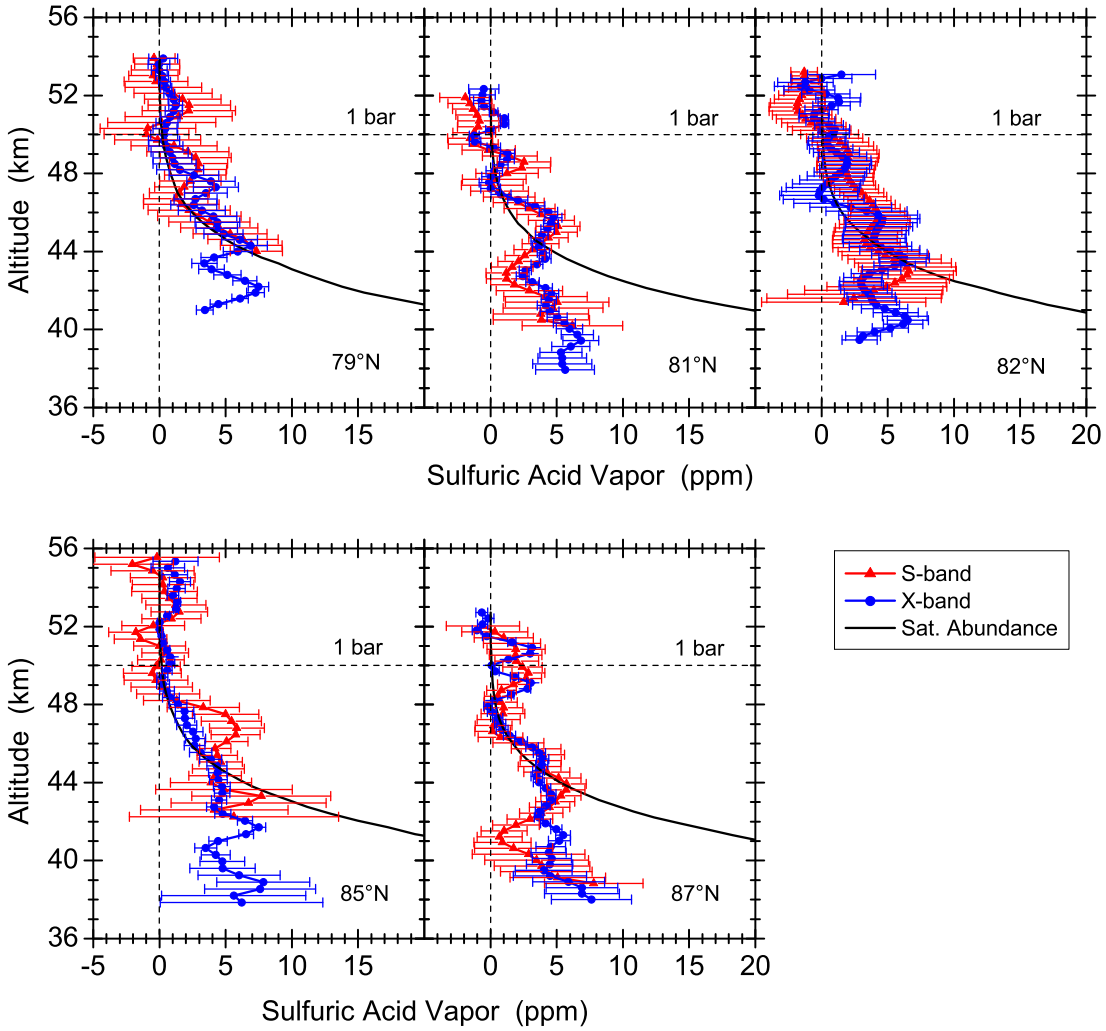

Figure E.2: *Sulfuric acid vapor profiles at the northern polar region in Venus atmosphere derived from VeRa's X- and S-band radio signal absorption in the year 2006.*

visible in the Figure 7.1 were used to calculate the mean sulfuric acid vapor abundance presented in Figure 7.3.

Bibliography

Abello, R., Rsi ifms specification: Grst-nno-ifms-sp-1001-tosgss, *ESA*, 2003.

Adams, W. S. and T. J. Dunham, Absorption bands in the infra-red spectrum of venus, *Astronomical Society of the Pacific*, *44*, (260), 243–245, 1932.

Adel, A., Note on the temperature of venus, *Astronomical Journal*, *86*, 337–339, 1937.

Ahmad, B., *Accuracy and resolution of atmospheric profiles obtained from radio occultation measurements*, Ph.d. thesis, Stanford University, Stanford, 1998.

Alegre Pérez, J. P., S. Celma Pueyo and B. Calvo López, *Automatic gain control: Techniques and architectures for RF receivers*, Analog circuits and signal processing, Springer, New York, 2011.

Ando, H., T. Imamura, T. Tsuda, S. Tellmann, M. Pätzold and B. Häusler, Vertical wavenumber spectra of gravity waves in the venus atmosphere obtained from venus express radio occultation data: Evidence for saturation, *J. Atmos. Sci.*, *72*, (6), 2318–2329, 2015.

Ando, H., M. Takagi, N. Sugimoto, H. Sagawa and Y. Matsuda, Venusian cloud distribution simulated by a general circulation model, *Journal of Geophysical Research: Planets*, *125*, (7), 484, 2020.

Ao, C. O., G. A. Hajj, T. K. Meehan, S. S. Leroy, E. R. Kursinski, de la Juárez, Manuel Torre, B. A. Iijima and A. J. Mannucci, Backpropagation processing of gps radio occultation data, in *First CHAMP Mission Results for Gravity, Magnetic and Atmospheric Studies*, herausgegeben von C. Reigber, H. Lühr, and P. Schwintzer, 415–422, Springer Berlin Heidelberg, Berlin, Heidelberg, 2003.

Avduevsky, V. S., M. Y. Marov, M. K. Rozhdestvensky, N. F. Borodin and V. V. Kerzhanovich, Soft landing of venera 7 on the venus surface and preliminary results of investigations of the venus atmosphere, *Journal of the Atmospheric Sciences*, *28*, (2), 263–269, 1971.

Ayers, G. P., R. W. Gillett and J. L. Gras, On the vapor pressure of sulfuric acid, *Geophysical Research Letters*, *7*, (6), 433–436, 1980.

Baker, R. D., G. Schubert and P. W. Jones, Convectively generated internal gravity waves in the lower atmosphere of venus. part i: No wind shear, *J. Atmos. Sci.*, *57*, (2), 184–199, 2000*a*.

Baker, R. D., G. Schubert and P. W. Jones, Convectively generated internal gravity waves in the lower atmosphere of venus. part ii: Mean wind shear and wave–mean flow interaction, *J. Atmos. Sci.*, *57*, (2), 200–215, 2000*b*.

Barabash, S., J.-A. Sauvaud, H. Gunell, H. Andersson, A. Grigoriev, K. Brinkfeldt, M. Holmström, R. Lundin, M. Yamauchi, K. Asamura, W. Baumjohann, T. L. Zhang, A. J. Coates, D. R. Linder, D. O. Kataria, C. C. Curtis, K. C. Hsieh, B. R. Sandel, A. Fedorov, C. Mazelle, J.-J. Thocaven, M. Grande, H. E. Koskinen, E. Kallio, T. Säles, P. Riihela, J. Kozyra, N. Krupp, J. Woch, J. Luhmann, S. McKenna-Lawlor, S. Orsini, R. Cerulli-Irelli, M. Mura, M. Milillo, M. Maggi, E. Roelof, P. Brandt, C. T. Russell, K. Szego, J. D. Winningham, R. A. Frahm, J. Scherrer, J. R. Sharber, P. Wurz and P. Bochsler, The analyser of space plasmas and energetic atoms (aspera-4) for the venus express mission, *Planetary and Space Science*, *55*, (12), 1772–1792, 2007.

Barin, I. and F. Sauert, *Thermochemical data of pure substances*, VCH, Weinheim, 1989.

Barker, E. S., Detection of so 2 in the uv spectrum of venus, *Geophysical Research Letters*, *6*, (2), 117–120, 1979.

Batchelor, G. K., *An Introduction to Fluid Dynamics*, Cambridge University Press, 2012.

Battan, L. J., *Radar observation of the atmosphere*, University of Chicago Press, Chicago, 1973.

Bell, J. F., D. Crisp, P. G. Lucey, T. A. Ozoroski, W. M. Sinton, S. C. Willis and B. A. Campbell, Spectroscopic observations of bright and dark emission features on the night side of venus, *Science (New York, N.Y.)*, *252*, (5010), 1293–1296, 1991.

Belyaev, D. A., F. Montmessin, J.-L. Bertaux, A. Mahieux, A. A. Fedorova, O. I. Korablev, E. Marcq, Y. L. Yung and X. Zhang, Vertical profiling of so2 and so above venus' clouds by spicav/soir solar occultations, *Icarus*, *217*, (2), 740–751, 2012.

L. Bengtsson, R.-M. Bonnet, D. Grinspoon, S. Koumoutsaris, S. Lebonnois, and D. Titov (Hrsg.), *Towards Understanding the Climate of Venus: Applications of Terrestrial Models to Our Sister Planet*, Springer New York, New York, NY, 2013.

Bergh, C. d., B. Bézard, D. Crisp, J. P. Maillard, T. Owen, J. Pollack and D. Grinspoon, Water in the deep atmosphere of venus from high-resolution spectra of the night side, *Advances in Space Research*, *15*, (4), 79–88, 1995.

Bertaux, J.-L., T. Widemann, A. Hauchecorne, V. I. Moroz and A. P. Ekonomov, Vega 1 and vega 2 entry probes: An investigation of local uv absorption (220-400 nm) in the atmosphere of venus (so 2 aerosols, cloud structure), *Journal of Geophysical Research: Planets*, *101*, (E5), 12709–12745, 1996.

Bertaux, J.-L., D. Nevejans, O. Korablev, E. Villard, E. Quémerais, E. Neefs, F. Montmessin, F. Leblanc, J. P. Dubois, E. Dimarellis, A. Hauchecorne, F. Lefèvre, P. Rannou, J. Y. Chaufray, M. Cabane, G. Cernogora, G. Souchon, F. Semelin, A. Reberac, E. van Ransbeek, S. Berkenbosch, R. Clairquin, C. Muller, F. Forget, F. Hourdin, O. Talagrand, A. Rodin, A. Fedorova, A. Stepanov, I. Vinogradov, A. Kiselev, Y. Kalinnikov, G. Durry, B. Sandel, A. Stern and J. C. Gérard, Spicav on venus express: Three spectrometers to study the global structure and composition of the venus atmosphere, *Planetary and Space Science*, *55*, (12), 1673–1700, 2007.

Best, R. E., *Phase-locked loops: Design, simulation, and applications*, McGraw-Hill's AccessEngineering, McGraw-Hill, [Place of publication not identified], 6th ed. Auflage, 2011.

Bézard, B., C. d. Bergh, D. Crisp and J.-P. Maillard, The deep atmosphere of venus revealed by high-resolution nightside spectra, *Nature*, *345*, (6275), 508–511, 1990.

Bézard, B., C. d. Bergh, B. Fegley, J.-P. Maillard, D. Crisp, T. Owen, J. B. Pollack and D. Grinspoon, The abundance of sulfur dioxide below the clouds of venus, *Geophysical Research Letters*, *20*, (15), 1587–1590, 1993.

Bird, M. K., H. Volland, M. Pätzold, P. Edenhofer, S. W. Asmar and J. P. Brenkle, The coronal electron density distribution determined from dual-frequency ranging measurements during the 1991 solar conjunction of the ulysses spacecraft, *The Astronomical Journal*, *426*, (1), 373–381, 1994.

Bjoraker, G. L., H. P. Larson, M. J. Mumma, R. Timmermann and J. L. Montani, Airborne observations of the gas composition of venus above the cloud tops: Measurements of h2o, hdo, hf, and the d/h and 18o/16o, 1992.

Born, M., E. Wolf and E. Hecht, Principles of optics: Electromagnetic theory of propagation, interference and diffraction of light, *Physics Today*, *53*, (10), 77–78, 2000.

Boyer, C. and H. Camichel, Observations photographiques de la planète vénus, *Annales d'Astrophysique*, *24*, 531–535, 1961.

Brzeziński, D. W. and P. Ostalczyk, High-accuracy numerical integration methods for fractional order derivatives and integrals computations, *Bulletin of the Polish Academy of Sciences Technical Sciences*, *62*, (4), 723–733, 2014.

Carlson, R. W., K. H. Baines, T. Encrenaz, F. W. Taylor, P. Drossart, L. W. Kamp, J. B. Pollack, E. Lellouch, A. D. Collard, S. B. Calcutt, D. Grinspoon, P. R. Weissman, W. D. Smythe, A. C. Ocampo, G. E. Danielson, F. P. Fanale, T. V. Johnson, H. H. Kieffer, D. L. Matson, T. B. McCord and L. A. Soderblom, Galileo infrared imaging spectroscopy measurements at venus, *Science (New York, N.Y.)*, *253*, (5027), 1541–1548, 1991.

Cimino, J., The composition and vertical structure of the lower cloud deck on venus, *Icarus*, *51*, (2), 334–357, 1982.

Clancy, R. T. and D. O. Muhleman, Diurnal co variations in the venus mesophere from co microwave spectra, *Icarus*, *64*, (2), 157–182, 1985.

Clancy, R. T., B. J. Sandor and G. H. Moriarty-Schieven, Observational definition of the venus mesopause: Vertical structure, diurnal variation, and temporal instability, *Icarus*, *161*, (1), 1–16, 2003.

Colin, L. and C. F. Hall, The pioneer venus program, *Space Science Reviews*, *20*, (3), 283–306, 1977.

Cottini, V., N. I. Ignatiev, G. Piccioni, P. Drossart, D. Grassi and W. J. Markiewicz, Water vapor near the cloud tops of venus from venus express/virtis dayside data, *Icarus*, *217*, (2), 561–569, 2012.

Counselman, C. C., S. A. Gourevitch, R. W. King, G. B. Loriot and E. S. Ginsberg, Zonal and meridional circulation of the lower atmosphere of venus determined by radio interferometry, *Journal of Geophysical Research*, *85*, (A13), 8026, 1980.

Crisp, D., D. A. Allen, D. H. Grinspoon and J. B. Pollack, The dark side of venus: near-infrared images and spectra from the anglo-australian observatory, *Science (New York, N.Y.)*, *253*, 1263–1266, 1991.

Donahue, T. M. and R. R. Hodges, Past and present water budget of venus, *Journal of Geophysical Research*, *97*, (E4), 6083, 1992.

Drossart, P., G. Piccioni, A. Adriani, F. Angrilli, G. Arnold, K. H. Baines, G. Bellucci, J. Benkhoff, B. Bézard, J.-P. Bibring, A. Blanco, M. I. Blecka, R. W. Carlson, A. Coradini, A. Di Lellis, T. Encrenaz, S. Erard, S. Fonti, V. Formisano, T. Fouchet, R. Garcia, R. Haus, J. Helbert, N. I. Ignatiev, P. Irwin, Y. Langevin, S. Lebonnois, M. A. Lopez-Valverde, D. Luz, L. Marinangeli, V. Orofino, A. V. Rodin, M. C. Roos-Serote, B. Saggin, A. Sanchez-Lavega, D. M. Stam, F. W. Taylor, D. Titov, G. Visconti, M. Zambelli, R. Hueso, C. Tsang, C. F. Wilson and T. Z. Afanasenko, Scientific goals for the observation of venus by virtis on esa/venus express mission, *Planetary and Space Science*, *55*, (12), 1653–1672, 2007.

Dubinin, E., M. Fraenz, T. L. Zhang, J. Woch, Y. Wei, A. Fedorov, S. Barabash and R. Lundin, Plasma in the near venus tail: Venus express observations, *Journal of Geophysical Research: Space Physics*, *118*, (12), 7624–7634, 2013.

Encrenaz, T., T. K. Greathouse, H. Roe, M. Richter, J. Lacy, B. Bézard, T. Fouchet and T. Widemann, Hdo and so 2 thermal mapping on venus: Evidence for strong so 2 variability, *Astronomy & Astrophysics*, *543*, A153, 2012.

Encrenaz, T., T. K. Greathouse, M. J. Richter, C. DeWitt, T. Widemann, B. Bézard, T. Fouchet, S. K. Atreya and H. Sagawa, Hdo and so 2 thermal mapping on venus: Iii. short-term and long-term variations between 2012 and 2016, *Astronomy & Astrophysics*, *595*, A74, 2016.

Encrenaz, T., T. K. Greathouse, E. Marcq, H. Sagawa, T. Widemann, B. Bézard, T. Fouchet, F. Lefèvre, S. Lebonnois, S. K. Atreya, Y. J. Lee, R. Giles and S. Watanabe, Hdo and so 2 thermal mapping on venus: Iv. statistical analysis of the so2 plumes, *Astronomy & Astrophysics*, *623*, A70, 2019.

Eshleman, V. R., The radio occultation method for the study of planetary atmospheres, *Planetary and Space Science*, *21*, (9), 1521–1531, 1973.

Eshleman, V. R., G. L. Tyler and W. T. Freeman, Deep radio occultations and "evolute flashes"; their characteristics and utility for planetary studies, *Icarus*, *37*, (3), 612–626, 1979.

Eshleman, V. R., D. O. Muhleman, P. D. Nicholson and P. G. Steffes, Comment on absorbing regions in the atmosphere of venus as measured by radio occultation, *Icarus*, *44*, (3), 793–803, 1980.

Esposito, L. W., Sulfur dioxide: Episodic injection shows evidence for active venus volcanism, *Science*, *223*, (4640), 1072–1074, 1984.

Esposito, L. W., R. G. Knollenberg, M. I. Marov, O. B. Toon and R. P. Turco, The clouds and hazes of venus., in *Venus*, 484–564, Univ. of Ariz. Press, Tucson, 1983.

Esposito, L. W., C. M. Eckert, L. Gates, A. I. F. Stewart and H. Worden, Sulfur dioxide at the venus cloud tops, 1978-1986, *Journal of Geophysical Research*, *93*, 5267–5276, 1988.

E. T. Karayel and D. P. Hinson, Sub-fresnel-scale vertical resolution in atmospheric profiles from radio occultation, *Radio Science*, *32*, (2), 411–423, 1997.

Etling, D., *Theoretische Meteorologie: Eine Einführung*, Vieweg+Teubner Verlag, 2013.

Fahd, A. K. and P. G. Steffes, Laboratory measurements of the microwave and millimeter-wave opacity of gaseous sulfur dioxide (so2) under simulated conditions for the venus atmosphere, *Icarus*, *97*, (2), 200–210, 1992.

Fedorova, A., O. Korablev, A.-C. Vandaele, J.-L. Bertaux, D. Belyaev, A. Mahieux, E. Neefs, W. V. Wilquet, R. Drummond, F. Montmessin and E. Villard, Hdo and h 2 o vertical distributions and isotopic ratio in the venus mesosphere by solar occultation at infrared spectrometer on board venus express, *Journal of Geophysical Research*, *113*, (E12), 1772, 2008.

Fedorova, A., E. Marcq, M. Luginin, O. Korablev, J.-L. Bertaux and F. Montmessin, Variations of water vapor and cloud top altitude in the venus' mesosphere from spicav/vex observations, *Icarus*, *275*, 143–162, 2016.

Feynman, R. P., R. B. Leighton and M. L. Sands, *Mainly electromagnetism and matter*, Bd. / Richard P. Feynman; Robert B. Leighton; Matthew Sands ; 2 von *Addison-Wesley world student series*, Addison-Wesley, Reading/Mass., [nachdr.] Auflage, 1964.

Feynman, R. P., R. B. Leighton and M. Sands, *Feynman Lectures on Physics, Vol. I: The New Millennium Edition: Mainly Mechanics, Radiation, and Heat*, Perseus (Hachette), New York, 2011.

Fink, U., H. P. Larson, G. P. Kuiper and R. F. Poppen, Water vapor in the atmosphere of venus, *Icarus*, *17*, (3), 617–631, 1972.

Fjeldbo, G. and V. R. Eshleman, The atmosphere of mars analyzed by integral inversion of the mariner iv occultation data, *Planetary and Space Science*, *16*, (8), 1035–1059, 1968.

Fjeldbo, G. and V. R. Eshleman, Atmosphere of venus as studied with the mariner 5 dual radio-frequency occultation experiment, *Radio Science*, *4*, (10), 879–897, 1969.

Fjeldbo, G., A. J. Kliore and V. R. Eshleman, The neutral atmosphere of venus as studied with the mariner v radio occultation experiments, *Astronomical Journal*, *76*, 123–140, 1971.

Formisano, V., F. Angrilli, G. Arnold, S. Atreya, K. H. Baines, G. Bellucci, B. Bezard, F. Billebaud, D. Biondi, M. I. Blecka, L. Colangeli, L. Comolli, D. Crisp, M. D'Amore, T. Encrenaz, A. Ekonomov, F. Esposito, C. Fiorenza, S. Fonti, M. Giuranna, D. Grassi, B. Grieger, A. Grigoriev, J. Helbert, H. Hirsch, N. Ignatiev, A. Jurewicz, I. Khatuntsev, S. Lebonnois, E. Lellouch, A. Mattana, A. Maturilli, E. Mencarelli, M. Michalska, J. Lopez Moreno, B. Moshkin, F. Nespoli, Y. Nikolsky, F. Nuccilli, P. Orleanski, E. Palomba, G. Piccioni, M. Rataj, G. Rinaldi, M. Rossi, B. Saggin, D. Stam, D. Titov, G. Visconti and L. Zasova, The planetary fourier spectrometer (pfs) onboard the european venus express mission, *Planetary and Space Science*, *54*, (13-14), 1298–1314, 2006.

Garate-Lopez, I., R. Hueso, A. Sanchez-Lavega, J. Peralta, G. Piccioni and P. Drossart, A chaotic long-lived vortex at the southern pole of venus, *Nature Geoscience*, *6*, 254–257, 2013.

Geiger, B., Venus express spacecraft housekeeping data products available for instrument teams, *ESA*, *1*, 2011.

Gerya, T. V., *Introduction to numerical geodynamic modelling*, Cambridge University Press, second edition Auflage, 2019.

Gilli, G., M. A. López-Valverde, J. Peralta, S. Bougher, A. Brecht, P. Drossart and G. Piccioni, Carbon monoxide and temperature in the upper atmosphere of venus from virtis/venus express non-lte limb measurements, *Icarus*, *248*, 478–498, 2015.

Goldblatt, C. and A. J. Watson, The runaway greenhouse: implications for future climate change, geoengineering and planetary atmospheres, *Philosophical transactions. Series A, Mathematical, physical, and engineering sciences*, *370*, (1974), 4197–4216, 2012.

Goldhammer, L. J., J. S. Powe and M. Smith, Flight performance of the pioneer venus orbiter solar array, 1987.

Gonçalves, R., P. Machado, T. Widemann, J. Peralta, S. Watanabe, A. Yamazaki, T. Satoh, M. Takagi, K. Ogohara, Y.-J. Lee, A. Harutyunyan and J. Silva, Venus' cloud top wind study: Coordinated akatsuki/uvi with cloud tracking and tng/harps-n with doppler velocimetry observations, *Icarus*, *335*, 113418, 2020.

Gorbunov, M. E., Canonical transform method for processing radio occultation data in the lower troposphere, *Radio Science*, *37*, (5), 9–1–9–10, 2002.

Grassi, D., P. Drossart, G. Piccioni, N. I. Ignatiev, L. V. Zasova, A. Adriani, M. L. Moriconi, P. G. J. Irwin, A. Negrão and A. Migliorini, Retrieval of air temperature profiles in the venusian mesosphere from virtis-m data: Description and validation of algorithms, *Journal of Geophysical Research*, *113*, (2), 391, 2008.

Grassi, D., A. Migliorini, L. Montabone, S. Lebonnois, A. Cardesìn-Moinelo, G. Piccioni, P. Drossart and L. V. Zasova, Thermal structure of venusian nighttime mesosphere as observed by virtis-venus express, *Journal of Geophysical Research*, *115*, (E9), 1673, 2010.

Gringauz, K. I., M. I. Verigin, T. K. Breus and T. Gombosi, The interaction of electrons in the optical umbra of venus with the planetary atmosphere—the origin of the nighttime ionosphere, *Journal of Geophysical Research*, *84*, (A5), 2123, 1979.

Grinspoon, D. H., Implications of the high d/h ratio for the sources of water in venus' atmosphere, *Nature*, *363*, (6428), 428–431, 1993.

Gubenko, V. N., O. I. Yakovlev and S. S. Matyugov, Radio occultation measurements of the radio wave absorption and the sulfuric acid vapor content in the atmosphere of venus, *Cosmic Research*, *39*, (5), 439–445, 2001.

Gubenko, V. N., V. E. Andreev and A. G. Pavelyev, Detection of layering in the upper cloud layer of venus northern polar atmosphere observed from radio occultation data, *Journal of Geophysical Research*, *113*, (E3), 200, 2008.

Gunn, K. L. S. and T. W. R. East, The microwave properties of precipitation particles, *Quarterly Journal of the Royal Meteorological Society*, *80*, (346), 522–545, 1954.

Hahn, M., *Großskalige Variationen der Sonnenkorona in 2004 und 2006*, Diploma thesis, Universität zu Köln, Cologne, Germany, 2008.

Hairer, E. and G. Wanner, *Solving Ordinary Differential Equations II: Stiff and Differential-Algebraic Problems*, Bd. 14 von *Springer Series in Computational Mathematics*, Springer-Verlag Berlin Heidelberg, Berlin, Heidelberg, 2., rev. ed. Auflage, 2010.

Hansen, J. E. and J. W. Hovenier, Interpretation of the polarization of venus, *Journal of the Atmospheric Sciences*, *31*, (4), 1137–1160, 1974.

Hantel, M., *Einführung Theoretische Meteorologie*, Springer Berlin Heidelberg, Berlin, Heidelberg, 2013.

Hantel, M. and D. Mayer, *Skriptum Theoretische Meteorologie I*, Bd. 5 von *Wiener Meteorologische Schriften*, Facultas, Wien, 2006.

Hashimoto, G. L. and Y. Abe, Predictions of a simple cloud model for water vapor cloud albedo feedback on venus, *Journal of Geophysical Research: Planets*, *106*, (E7), 14675–14690, 2001.

Häusler, B., W. Eidel, D. Hagl, S. Remus, J. Selle and M. Pätzold, Venus express radio science experiment vera, reference systems and techniques used for the simulation and prediction of atmospheric and ionospheric sounding measurements at planet venus, *Forschungsbericht LRT-WE-9-FB-4, Universität der Bundeswehr München*, 2003.

Häusler, B., M. Pätzold, G. L. Tyler, R. A. Simpson, M. K. Bird, V. Dehant, J.-P. Barriot, W. Eidel, R. Mattei, S. Remus, J. Selle, S. Tellmann and T. Imamura, Radio science investigations by vera onboard the venus express spacecraft, *Planetary and Space Science*, *54*, (13-14), 1315–1335, 2006.

Haußer, F. and Y. Luchko, *Mathematische Modellierung mit MATLAB: Eine praxisorientierte Einführung*, Spektrum Akademischer Verlag, Heidelberg, 2011.

Herzberg, G., The atmospheres of the planets, *Journal of the Royal Astronomical Society of Canada*, *45*, 100–123, 1951.

Hinson, D. P. and J. M. Jenkins, Magellan radio occultation measurements of atmospheric waves on venus, *Icarus*, *114*, (2), 310–327, 1995.

Hinson, D. P., J. D. Twicken and E. T. Karayel, Jupiter's ionosphere: New results from voyager 2 radio occultation measurements, *Journal of Geophysical Research: Space Physics*, *103*, (A5), 9505–9520, 1998.

Hinson, D. P., R. A. Simpson, J. D. Twicken, G. L. Tyler and F. M. Flasar, Initial results from radio occultation measurements with mars global surveyor, *Journal of Geophysical Research*, *104*, (E11), 26997–27012, 1999.

Ho, W., I. A. Kaufman and P. Thaddeus, Laboratory measurement of microwave absorption in models of the atmosphere of venus, *Journal of Geophysical Research*, *71*, (21), 5091–5108, 1966.

Ho, C. M., C. Wang, K. Angkasa and K. Gritton, Estimation of microwave power margin losses due to earth's atmosphere and weather in the frequency range of 3 - 30 ghz: Prepared for the united states air force spectrum efficient technologies for test and evaluation advanced range telemetry edwards air force base, *JPL*, *2004*, (JPL), D–27879, 2004.

Hoffman, J. H., R. R. Hodges, T. M. Donahue and M. B. McElroy, Composition of the venus lower atmosphere from the pioneer venus mass spectrometer, *Journal of Geophysical Research*, *85*, (A13), 7882, 1980.

Hong, Y. and B. Fegley, Formation of carbonyl sulfide (ocs) from carbon monoxide and sulfur vapor and applications to venus, *Icarus*, *130*, (2), 495–504, 1997.

Horinouchi, T., S.-y. Murakami, T. Satoh, J. Peralta, K. Ogohara, T. Kouyama, T. Imamura, H. Kashimura, S. S. Limaye, K. McGouldrick, M. Nakamura, T. M. Sato, K.-i. Sugiyama, M. Takagi, S. Watanabe, M. Yamada, A. Yamazaki and E. F. Young, Equatorial jet in the lower to middle cloud layer of venus revealed by akatsuki, *Nature Geoscience*, *10*, 646 EP –, 2017.

Horinouchi, T., T. Kouyama, Y. J. Lee, S.-y. Murakami, K. Ogohara, M. Takagi, T. Imamura, K. Nakajima, J. Peralta, A. Yamazaki, M. Yamada and S. Watanabe, Mean winds at the cloud top of venus obtained from two-wavelength uv imaging by akatsuki, *Earth, Planets and Space*, *70*, (1), 10, 2018.

Howard, H. T., G. L. Tyler, G. Fjeldbo, A. J. Kliore, G. S. Levy, D. L. Brunn, R. Dickinson, R. E. Edelson, W. L. Martin, R. B. Postal, B. Seidel, T. T. Sesplaukis, D. L. Shirley, C. T. Stelzried, D. N. Sweetnam, A. I. Zygielbaum, P. B. Esposito, J. D. Anderson, I. I. Shapiro and R. D. Reasenberg, Venus: mass, gravity field, atmosphere, and ionosphere as measured by the mariner 10 dual-frequency radio system, *Science*, *183*, (4131), 1297–1301, 1974.

Hueso, R., J. Peralta and A. Sánchez-Lavega, Assessing the long-term variability of venus winds at cloud level from virtis–venus express, *Icarus*, *217*, (2), 585–598, 2012.

Ignatiev, N. I., V. I. Moroz, B. E. Moshkin, A. P. Ekonomov, V. I. Gnedykh, A. V. Grigoriev and I. V. Khatuntsev, Water vapour in the lower atmosphere

of venus: A new analysis of optical spectra measured by entry probes, *Planetary and Space Science*, *45*, (4), 427–438, 1997.

Ignatiev, N., V. Moroz, L. V. Zasova and I. Khatuntsev, Water vapour in the middle atmosphere of venus, *Planetary and Space Science*, *47*, (8-9), 1061–1075, 1999.

Ignatiev, N. I., D. V. Titov, G. Piccioni, P. Drossart, W. J. Markiewicz, V. Cottini, T. Roatsch, M. Almeida and N. Manoel, Altimetry of the venus cloud tops from the venus express observations, *Journal of Geophysical Research*, *114*, (E5), 5029, 2009.

Imamura, T. and G. L. Hashimoto, Venus cloud formation in the meridional circulation, *Journal of Geophysical Research: Planets*, *103*, (E13), 31349–31366, 1998.

Imamura, T. and G. L. Hashimoto, Microphysics of venusian clouds in rising tropical air, *Journal of the Atmospheric Sciences*, *58*, (23), 3597–3612, 2001.

Imamura, T., T. Toda, A. Tomiki, D. Hirahara, T. Hayashiyama, N. Mochizuki, Z.-i. Yamamoto, T. Abe, T. Iwata, H. Noda, Y. Futaana, H. Ando, B. Häusler, M. Pätzold and A. Nabatov, Radio occultation experiment of the venus atmosphere and ionosphere with the venus orbiter akatsuki, *Earth, Planets and Space*, *63*, (6), 493–501, 2011.

Imamura, T., T. Higuchi, Y. Maejima, M. Takagi, N. Sugimoto, K. Ikeda and H. Ando, Inverse insolation dependence of venus' cloud-level convection, *Icarus*, *228*, 181–188, 2014.

Imamura, T., M. Miyamoto, H. Ando, B. Häusler, M. Pätzold, S. Tellmann, T. Tsuda, Y. Aoyama, Y. Murata, H. Takeuchi, A. Yamazaki, T. Toda and A. Tomiki, Fine vertical structures at the cloud heights of venus revealed by radio holographic analysis of venus express and akatsuki radio occultation data, *Journal of Geophysical Research: Planets*, *6*, (1), 2318, 2018.

Imbriale, W. A., *Spaceborne antennas for planetary exploration*, Deep-space communications and navigation series, Wiley-Interscience, Hoboken, N.J, 2006.

Ingersoll, A. P., The runaway greenhouse: A history of water on venus, *Journal of the Atmospheric Sciences*, *26*, (6), 1191–1198, 1969.

Irwin, P. G. J., R. d. Kok, A. Negrão, C. C. C. Tsang, C. F. Wilson, P. Drossart, G. Piccioni, D. Grassi and F. W. Taylor, Spatial variability of carbon monoxide in venus' mesosphere from venus express/visible and infrared thermal imaging spectrometer measurements, *Journal of Geophysical Research*, *113*, 646, 2008.

ITU-R Recommendation, Specific attenuation model for rain for use in prediction methods, *International Telecommunication Union*, P. 838–3, 2005.

ITU-R Recommendation, Attenuation by atmospheric gases, *International Telecommunication Union*, P. 676–10, 2013.

ITU-R Recommendation, Attenuation due to clouds and fog: Radiowave propagation, *International Telecommunication Union*, P. 840–7, 2017*a*.

ITU-R Recommendation, Characteristics of precipitation for propagation modelling: Radiowave propagation, *International Telecommunication Union*, P. 837–7, 2017*b*.

ITU-R Recommendation, Propagation data and prediction methods required for the design of earth-space telecommunication systems: Radiowave propagation, *International Telecommunication Union*, P. 618–13, 2017*c*.

Jakovlev, O. I., *Space radio science*, Bd. 8 von *Earth Space Institute book series*, Taylor & Francis, London, 2002.

James, E. P., O. B. Toon and G. Schubert, A numerical microphysical model of the condensational venus cloud, *Icarus*, *129*, (1), 147–171, 1997.

Jenkins, J. M. and P. G. Steffes, Results for 13-cm absorptivity and h2so4 abundance profiles from the season 10 (1986) pioneer venus orbiter radio occultation experiment, *Icarus*, *90*, (1), 129–138, 1991.

Jenkins, J., P. Steffes, D. P. Hinson, J. D. Twicken and G. L. Tyler, Radio occultation studies of the venus atmosphere with the magellan spacecraft 2. results from the october 1991 experiments, *Icarus*, *110*, (1), 79–94, 1994.

Jenkins, J., M. A. Kolodner, B. J. Butler, S. H. Suleiman and P. G. Steffes, Microwave remote sensing of the temperature and distribution of sulfur compounds in the lower atmosphere of venus, *Icarus*, *158*, (2), 312–328, 2002.

Jensen, A. S., M. S. Lohmann, H.-H. Benzon and A. S. Nielsen, Full spectrum inversion of radio occultation signals, *Radio Science*, *38*, (3), n/a–n/a, 2003.

Jessup, K. L., E. Marcq, F. Mills, A. Mahieux, S. Limaye, C. Wilson, M. Allen, J.-L. Bertaux, W. Markiewicz, T. Roman, A.-C. Vandaele, V. Wilquet and Y. Yung, Coordinated hubble space telescope and venus express observations of venus' upper cloud deck, *Icarus*, *258*, 309–336, 2015.

Kasting, J. F., Runaway and moist greenhouse atmospheres and the evolution of earth and venus, *Icarus*, *74*, (3), 472–494, 1988.

Kasting, J. F. and J. B. Pollack, Loss of water from venus. i. hydrodynamic escape of hydrogen, *Icarus*, *53*, (3), 479–508, 1983.

Kawabata, K., D. L. Coffeen, J. E. Hansen, W. A. Lane, M. Sato and L. D. Travis, Cloud and haze properties from pioneer venus polarimetry, *Journal of Geophysical Research*, *85*, (A13), 8129, 1980.

Keating, G. M., J. Y. Nicholson and L. R. Lake, Venus upper atmosphere structure, *Journal of Geophysical Research*, *85*, (A13), 7941, 1980.

Keldysh, M. V., Venus exploration with the venera 9 and venera 10 spacecraft, *Icarus*, *30*, (4), 605–625, 1977.

Kerzhanovich, V. V., M. Marov and M. K. Rozhdestvensky, Data on dynamics of the subcloud venus atmosphere from venera spaceprobe measurements, *Icarus*, *17*, (3), 659–674, 1972.

Khatuntsev, I. V., M. V. Patsaeva, D. V. Titov, N. I. Ignatiev, A. V. Turin, S. S. Limaye, W. J. Markiewicz, M. Almeida, T. Roatsch and R. Moissl, Cloud level winds from the venus express monitoring camera imaging, *Icarus*, *226*, (1), 140–158, 2013.

Khatuntsev, I. V., M. V. Patsaeva, D. V. Titov, N. I. Ignatiev, A. V. Turin, A. A. Fedorova and W. J. Markiewicz, Winds in the middle cloud deck from the near-ir imaging by the venus monitoring camera onboard venus express, *Journal of Geophysical Research: Planets*, *122*, (11), 2312–2327, 2017.

Kliore, A. J. and I. R. Patel, Vertical structure of the atmosphere of venus from pioneer venus orbiter radio occultations, *Journal of Geophysical Research*, *85*, (A13), 7957, 1980.

Kliore, A. J. and I. R. Patel, Thermal structure of the atmosphere of venus from pioneer venus radio occultations, *Icarus*, *52*, (2), 320–334, 1982.

Kliore, A., D. L. Cain, G. S. Levy, V. R. Eshleman, G. Fjeldbo and F. D. Drake, Occultation experiment: Results of the first direct measurement of mars's atmosphere and ionosphere, *Science*, *149*, (3689), 1243, 1965.

Kliore, A., G. S. Levy, D. L. Cain, G. Fjeldbo and S. I. Rasool, Atmosphere and ionosphere of venus from the mariner v s-band radio occultation measurement, *Science*, *158*, (3809), 1683, 1967.

Knollenberg, R. G. and D. M. Hunten, The microphysics of the clouds of venus: Results of the pioneer venus particle size spectrometer experiment, *Journal of Geophysical Research: Space Physics*, *85*, (A13), 8039–8058, 1980.

Kolodner, M. A. and P. G. Steffes, The microwave absorption and abundance of sulfuric acid vapor in the venus atmosphere based on new laboratory measurements, *Icarus*, *132*, (1), 151–169, 1998.

Kouyama, T., T. Imamura, M. Nakamura, T. Satoh and Y. Futaana, Long-term variation in the cloud-tracked zonal velocities at the cloud top of venus deduced from venus express vmc images, *Journal of Geophysical Research: Planets*, *118*, (1), 37–46, 2013.

Kouyama, T., M. Taguchi, T. Fukuhara, T. Imamura, T. Horinouchi, T. M. Sato, S. Murakami, G. L. Hashimoto, Y. J. Lee, M. Futaguchi, T. Yamada, M. Akiba, T. Satoh and M. Nakamura, Global structure of thermal tides in the upper cloud layer of venus revealed by lir on board akatsuki, *Geophysical Research Letters*, *46*, (16), 9457–9465, 2019.

Krasnopolsky, V. A., Chemical kinetic model for the lower atmosphere of venus, *Icarus*, *191*, (1), 25–37, 2007.

Krasnopolsky, V. A., A photochemical model for the venus atmosphere at 47–112km, *Icarus*, *218*, (1), 230–246, 2012.

Krasnopolsky, V. A., Vertical profiles of h2o, h2so4, and sulfuric acid concentration at 45–75km on venus, *Icarus*, *252*, 327–333, 2015.

Krasnopolsky, V. A. and J. B. Pollack, H2o-h2so4 system in venus' clouds and ocs, co, and h2so4 profiles in venus' troposphere, *Icarus*, *109*, (1), 58–78, 1994.

Krüger, C., *Numerische Bestimmung der inversen Abeltransformation zur Bestimmung der Dämpfung in der Venusatmosphäre*, Diploma thesis, Universität der Bundeswehr München, München, 2008.

Kulmala, M. and A. Laaksonen, Binary nucleation of water–sulfuric acid system: Comparison of classical theories with different h 2 so 4 saturation vapor pressures, *The Journal of Chemical Physics*, *93*, (1), 696–701, 1990.

Kumar, S., Photochemistry of so 2 in the atmosphere of io and implications on atmospheric escape, *Journal of Geophysical Research: Space Physics*, *87*, (A3), 1677–1684, 1982.

Lambert, J. D., *Numerical methods for ordinary differential systems: The initial value problem*, Wiley, Chichester, reprint Auflage, 1997.

Lane, W. A. and R. Opstbaum, High altitude venus haze from pioneer venus limb scans, *Icarus*, *54*, (1), 48–58, 1983.

Lauritsen, K. B. and M. S. Lohmann, Unfolding of radio occultation multipath behavior using phase models, in *Occultations for Probing Atmosphere and Climate*, herausgegeben von G. Kirchengast, U. Foelsche, and A. K. Steiner, 69–76, Springer Berlin Heidelberg, Berlin, Heidelberg, 2004.

Lee, Y. J., T. Imamura, S. E. Schröder and E. Marcq, Long-term variations of the uv contrast on venus observed by the venus monitoring camera on board venus express, *Icarus*, *253*, 1–15, 2015.

Lee, Y. J., K.-L. Jessup, S. Perez-Hoyos, D. V. Titov, S. Lebonnois, J. Peralta, T. Horinouchi, T. Imamura, S. Limaye, E. Marcq, M. Takagi, A. Yamazaki, M. Yamada, S. Watanabe, S.-y. Murakami, K. Ogohara, W. M. McClintock, G. Holsclaw and A. Roman, Long-term variations of venus's 365 nm albedo observed by venus express, akatsuki, messenger, and the hubble space telescope, *The Astronomical Journal*, *158*, (3), 126, 2019.

Leftwich, T. E., R. R. B. Frese, H. R. Kim, H. C. Noltimier, L. V. Potts, D. R. Roman and L. Tan, Crustal analysis of venus from magellan satellite observations at atalanta planitia, beta regio, and thetis regio, *Journal of Geophysical Research*, *104*, (E4), 8441–8462, 1999.

Leroy, S. S. and A. P. Ingersoll, Radio scintillations in venus's atmosphere: Application of a theory of gravity wave generation, *J. Atmos. Sci.*, *53*, (7), 1018–1028, 1996.

L Essen and K D Froome, The refractive indices and dielectric constants of air and its principal constituents at 24,000 mc/s, *Proceedings of the Physical Society. Section B*, *64*, (10), 862, 1951.

Limaye, S. S. and M. Rengel, Atmospheric circulation and dynamics, in *Towards Understanding the Climate of Venus: Applications of Terrestrial Models to Our Sister Planet*, herausgegeben von L. Bengtsson, R.-M. Bonnet, D. Grinspoon, S. Koumoutsaris, S. Lebonnois, and D. Titov, 55–70, Springer New York, New York, NY, 2013.

Limaye, S. S. and V. E. Suomi, Cloud motions on venus: Global structure and organization, *Journal of the Atmospheric Sciences*, *38*, (6), 1220–1235, 1981.

Limaye, S. S., D. Grassi, A. Mahieux, A. Migliorini, S. Tellmann and D. Titov, Venus atmospheric thermal structure and radiative balance, *Space Science Reviews*, *214*, (5), 222, 2018.

Lindal, G. F., The atmosphere of neptune - an analysis of radio occultation data acquired with voyager 2, *Astronomical Journal*, *103*, 967–982, 1992.

Lindal, G. F., G. E. Wood, G. S. Levy, J. D. Anderson, D. N. Sweetnam, H. B. Hotz, B. J. Buckles, D. P. Holmes, P. E. Doms, V. R. Eshleman, G. L. Tyler and T. A. Croft, The atmosphere of jupiter: An analysis of the voyager radio occultation measurements, *Journal of Geophysical Research*, *86*, (A10), 8721–8727, 1981.

Lindal, G. F., D. N. Sweetnam and V. R. Eshleman, The atmosphere of saturn - an analysis of the voyager radio occultation measurements, *Astronomical Journal*, *90*, 1136–1146, 1985.

Lindal, G. F., J. R. Lyons, D. N. Sweetnam, V. R. Eshleman, D. P. Hinson and G. L. Tyler, The atmosphere of uranus: Results of radio occultation measurements with voyager 2, *Journal of Geophysical Research*, *92*, (A13), 14987, 1987.

Lipa, B. and G. L. Tyler, Statistical and computational uncertainties in atmospheric profiles from radio occultation: Mariner 10 at venus, *Icarus*, *39*, (2), 192–208, 1979.

Lorentz, H. A., *The theory of electrons and its applications to the phenomena of light and radiant heat*, Dover Publications, New York, 2. ed. Auflage, 2011.

Luz, D., D. L. Berry, G. Piccioni, P. Drossart, R. Politi, C. F. Wilson, S. Erard and F. Nuccilli, Venus's southern polar vortex reveals precessing circulation, *Science (New York, N.Y.)*, *332*, (6029), 577–580, 2011.

Mahieux, A., A. C. Vandaele, E. Neefs, S. Robert, V. Wilquet, R. Drummond, A. Federova and J. L. Bertaux, Densities and temperatures in the venus mesosphere and lower thermosphere retrieved from soir on board venus express: Retrieval technique, *Journal of Geophysical Research*, *115*, (E12), 499, 2010.

Mahieux, A., A. C. Vandaele, S. Robert, V. Wilquet, R. Drummond, F. Montmessin and J. L. Bertaux, Densities and temperatures in the venus mesosphere and lower thermosphere retrieved from soir on board venus express: Carbon dioxide measurements at the venus terminator, *Journal of Geophysical Research*, *117*, (E7), 2012.

Manatt, S. L. and A. L. Lane, A compilation of the absorption cross-sections of so2 from 106 to 403 nm, *Journal of Quantitative Spectroscopy and Radiative Transfer*, *50*, (3), 267–276, 1993.

Maral, G. and M. Bousquet, *Satellite communications systems: Systems, techniques and technology*, Wiley, Chichester, 5. ed., [3. nachdr.] Auflage, 2011.

Marcq, E., B. Bezard, T. Encrenaz and M. BIRLAN, Latitudinal variations of co and ocs in the lower atmosphere of venus from near-infrared nightside spectroimaging, *Icarus*, *179*, (2), 375–386, 2005.

Marcq, E., T. Encrenaz, B. Bézard and M. BIRLAN, Remote sensing of venus' lower atmosphere from ground-based ir spectroscopy: Latitudinal and vertical distribution of minor species, *Planetary and Space Science*, *54*, (13-14), 1360–1370, 2006.

Marcq, E., B. Bézard, P. Drossart, G. Piccioni, J. M. Reess and F. Henry, A latitudinal survey of co, ocs, h 2 o, and so 2 in the lower atmosphere of venus: Spectroscopic studies using virtis-h, *Journal of Geophysical Research*, *113*, 222, 2008.

Marcq, E., J.-L. Bertaux, F. Montmessin and D. Belyaev, Variations of sulphur dioxide at the cloud top of venus's dynamic atmosphere, *Nature Geoscience*, *6*, 25 EP –, 2012.

Marcq, E., J.-L. Bertaux, F. Montmessin and D. Belyaev, Variations of sulphur dioxide at the cloud top of venus's dynamic atmosphere, *Nature Geoscience*, *6*, (1), 25–28, 2013.

Marcq, E., K. Lea Jessup, L. Baggio, T. Encrenaz, Y. J. Lee, F. Montmessin, D. Belyaev, O. Korablev and J.-L. Bertaux, Climatology of so2 and uv absorber at venus' cloud top from spicav-uv nadir dataset, *Icarus*, *335*, 113368, 2020.

Mariner Stanford Group, Venus: Ionosphere and atmosphere as measured by dual-frequency radio occultation of mariner v, *Science*, *158*, (3809), 1678–1683, 1967.

Markiewicz, W. J., D. V. Titov, N. Ignatiev, H. U. Keller, D. Crisp, S. S. Limaye, R. Jaumann, R. Moissl, N. Thomas, L. Esposito, S. Watanabe, B. Fiethe, T. Behnke, I. Szemerey, H. Michalik, H. Perplies, M. Wedemeier, I. Sebastian, W. Boogaerts, S. F. Hviid, C. Dierker, B. Osterloh, W. Böker, M. Koch, H. Michaelis, D. Belyaev, A. Dannenberg, M. Tschimmel, P. Russo, T. Roatsch and K. D. Matz, Venus monitoring camera for venus express, *Planetary and Space Science*, *55*, (12), 1701–1711, 2007.

Mattei, R., *Radio Science Experiment Data Analysis in the framework of the ESA Missions "Venus Express" and "Rosetta"*, Phd thesis, Universität der Bundeswehr München, Neubiberg, Germany, 2011.

Mattei, R. and B. Häusler, Venus express radio science experiment vera: Radio science "open-loop" occultation data processing software package software design specifications, *VeRa Radio Science Team*, *2*, 1–36, 2011.

McGouldrick, K., Effects of variation in coagulation and photochemistry parameters on the particle size distributions in the venus clouds, *Earth, planets, and space : EPS*, *69*, (1), 161, 2017.

Meadows, V. S. and D. Crisp, Ground-based near-infrared observations of the venus nightside: The thermal structure and water abundance near the surface, *Journal of Geophysical Research: Planets*, *101*, (E2), 4595–4622, 1996.

Mie, G., Beiträge zur optik trüber medien, speziell kolloidaler metallösungen, *Annalen der Physik*, *330*, (3), 377–445, 1908.

F. Mills, K. L. Jessup, Y. Yung, and J. Petrass (Hrsg.), *Simulations of vertical profiles of sulfur monoxide and sulfur dioxide in Venus' mesosphere*, Bd. 42, 2018.

Moissl, R., I. Khatuntsev, S. S. Limaye, D. V. Titov, W. J. Markiewicz, N. I. Ignatiev, T. Roatsch, K.-D. Matz, R. Jaumann, M. Almeida, G. Portyankina, T. Behnke and S. F. Hviid, Venus cloud top winds from tracking uv features in venus monitoring camera images, *Journal of Geophysical Research*, *114*, (9), 1531, 2009.

Molaverdikhani, K., K. McGouldrick and L. W. Esposito, The abundance and vertical distribution of the unknown ultraviolet absorber in the venusian atmosphere from analysis of venus monitoring camera images, *Icarus*, *217*, (2), 648–660, 2012.

Moore, C. B., J. R. Smith and A. Gaalswyk, On the use of constant-level balloons to measure horizontal motions in the atmosphere, *J. Meteor.*, *11*, (3), 167–172, 1954.

NAIF, An overview of reference framesand coordinate systems in the spice context, 2020.

Newman, M. and C. Leovy, Maintenance of strong rotational winds in venus' middle atmosphere by thermal tides, *Science (New York, N.Y.)*, *257*, (5070), 647–650, 1992.

Nicholson, P. D. and D. O. Muhleman, Independent radio-occultation studies of venus' atmosphere, *Icarus*, *33*, (1), 89–101, 1978.

Oschlisniok, J., *Absorption und Ausbreitungseffekte von Radiowellen in der Venusatmosphäre beobachtet vom Venus Express Radio Science Experiment*, Diploma thesis, Universität zu Köln, Köln, 2010.

Oschlisniok, J., B. Häusler, M. Pätzold, G. L. Tyler, M. K. Bird, S. Tellmann, S. Remus and T. Andert, Microwave absorptivity by sulfuric acid in the venus atmosphere: First results from the venus express radio science experiment vera, *Icarus*, *221*, (2), 940–948, 2012.

Oyama, V. I., G. C. Carle, F. Woeller, J. B. Pollack, R. T. Reynolds and R. A. Craig, Pioneer venus gas chromatography of the lower atmosphere of venus, *Journal of Geophysical Research*, *85*, (A13), 7891, 1980.

Palmer, K. F. and D. Williams, Optical constants of sulfuric acid; application to the clouds of venus?, *Applied optics*, *14*, (1), 208–219, 1975.

Parisot, J. P., P. Rigaud and D. Huguenin, Balloon observations of venus from 200 to 320 nm, *Astronomy and Astrophysics (ISSN 0004-6361), vol. 166, no. 1-2, Sept. 1986, p. 333-336.*, *166*, 333–336, 1986.

Parkinson, C. D., P. Gao, R. Schulte, S. W. Bougher, Y. L. Yung, C. G. Bardeen, V. Wilquet, A. C. Vandaele, A. Mahieux, S. Tellmann and M. Pätzold, Distribution of sulphuric acid aerosols in the clouds and upper haze of venus using venus express vast and vera temperature profiles, *Planetary and Space Science*, *113-114*, 205–218, 2015.

Pater, I. d. and J. J. Lissauer, *Planetary sciences*, Cambridge University Press, Cambridge, second edition Auflage, 2015.

Pätzold, M., B. Häusler, M. K. Bird, S. Tellmann, R. Mattei, S. W. Asmar, V. Dehant, W. Eidel, T. Imamura, R. A. Simpson and G. L. Tyler, The structure of venus' middle atmosphere and ionosphere, *Nature*, *450*, 657–660, 2007.

Peralta, J., R. Hueso and A. Sánchez-Lavega, Cloud brightness distribution and turbulence in venus using galileo violet images, *Icarus*, *188*, (2), 305–314, 2007.

Peter, K., M. Pätzold, G. Molina-Cuberos, O. Witasse, F. González-Galindo, P. Withers, M. K. Bird, B. Häusler, D. P. Hinson, S. Tellmann and G. L. Tyler, The dayside ionospheres of mars and venus: Comparing a one-dimensional photochemical model with mars (mars express) and vera (venus express) observations, *Icarus*, *233*, 66–82, 2014.

Pettengill, G. H., P. G. Ford and R. A. Simpson, Electrical properties of the venus surface from bistatic radar observations, *Science*, *272*, (5268), 1628–1631, 1996.

Piccialli, A., F. Montmessin, D. Belyaev, A. Mahieux, A. Fedorova, E. Marcq, J.-L. Bertaux, S. Tellmann, A. C. Vandaele and O. Korablev, Thermal structure of venus nightside upper atmosphere measured by stellar occultations with spicav/venus express, *Planetary and Space Science*, *113-114*, 321–335, 2015.

Pollack, J. B., J. Dalton, D. Grinspoon, R. B. Wattson, R. Freedman, D. Crisp, D. A. Allen, B. Bezard, C. DeBergh, L. P. Giver, Q. Ma and

R. Tipping, Near-infrared light from venus' nightside: A spectroscopic analysis, *Icarus*, *103*, (1), 1–42, 1993.

Prahlad, V. and V. Kumar, Temperature dependence of photoabsorption cross-sections of sulfur dioxide at 188–220 nm, *Journal of Quantitative Spectroscopy and Radiative Transfer*, *57*, (5), 719–723, 1997.

Prinn, R. G., Venus: Chemistry of the lower atmosphere prior to the pioneer venus mission, *Geophysical Research Letters*, *5*, (11), 973–976, 1978.

Prölss, G. W., *Physik des erdnahen Weltraums: Eine Einführung*, Springer Berlin Heidelberg, Berlin, Heidelberg, 2001.

Rappaport, N. J., A. S. Konopliv, A. B. Kucinskas and P. G. Ford, An improved 360 degree and order model of venus topography, *Icarus*, *139*, (1), 19–31, 1999.

Rausch, R., W. Schäfer and C. Wagner, *Einführung in die Transportmodellierung im Grundwasser: Mit 9 Tabellen im Text*, Borntraeger, Berlin, 2002.

Reese, D. E. and P. R. Swan, Venera 4 probes atmosphere of venus, *Science*, *159*, (3820), 1228–1230, 1968.

Remus, S., *Untersuchungen zur Durchführung von satellitengestützten Radio Science Experimenten im interplanetaren Raum*, Phd thesis, Universität der Bundeswehr München, Neubiberg, Germany, 2004.

Rossow, W. B., A. D. Del Genio, S. S. Limaye, L. D. Travis and P. H. Stone, Cloud morphology and motions from pioneer venus images, *Journal of Geophysical Research: Space Physics*, *85*, (A13), 8107–8128, 1980.

Rossow, W. B., A. D. Del Genio and T. Eichler, Cloud-tracked winds from pioneer venus ocpp images, *J. Atmos. Sci.*, *47*, (17), 2053–2084, 1989.

Sagan, C., Structure of the lower atmosphere of venus, *Icarus*, *1*, (1-6), 151–169, 1962.

Sánchez-Lavega, A., R. Hueso, G. Piccioni, P. Drossart, J. Peralta, S. Pérez-Hoyos, C. F. Wilson, F. W. Taylor, K. H. Baines, D. Luz, S. Erard and S. Lebonnois, Variable winds on venus mapped in three dimensions, *Geophysical Research Letters*, *35*, (13), 1531, 2008.

Savich, N. A., Comparative analysis of venusian ionosphere dual-frequency radio soundings with the satellites venera-9, 10 and pioneer-venus, *Advances in Space Research*, *1*, (9), 17–25, 1981.

Schaa, R., *Abel-Inversion von Radio-Okkultationen*, Diploma thesis, Universität zu Köln, Cologne, Germany, 2005.

Schmidt, T., J. Wickert, G. Beyerle and S. Heise, Global tropopause height trends estimated from gps radio occultation data, *Geophysical Research Letters*, *35*, (11), 49, 2008.

Schofield, J. T. and D. J. Diner, Rotation of venus's polar dipole, *Nature*, *305*, (5930), 116–119, 1983.

Schubert, G., C. Covey, A. D. Genio, L. S. ELSON, G. Keating, A. Seiff, R. E. YOUNG, J. Apt, C. C. Counselman, A. J. Kliore, S. S. Limaye, H. E. Revercomb, L. A. Sromovsky, V. E. Suomi, F. Taylor, R. Woo and U. v. ZAHN, Structure and circulation of the venus atmosphere, *Journal of Geophysical Research*, *85*, (A13), 8007, 1980.

Seiff, A., J. T. Schofield, A. J. Kliore, F. W. Taylor, S. S. Limaye, H. E. Revercomb, L. A. Sromovsky, V. V. Kerzhanovich, V. I. Moroz and M. Marov, Models of the structure of the atmosphere of venus from the surface to 100 kilometers altitude, *Advances in Space Research*, *5*, (11), 3–58, 1985.

Selle, J., *Planung und Simulation von Radio-Science-Experimenten interplanetarer Raumflugmissionen*, Ph.d. thesis, Universität der Bundeswehr München, Neubiberg, Germany, 2005.

Shampine, L. F. and M. W. Reichelt, The matlab ode suite, *SIAM Journal on Scientific Computing*, *18*, 1–22, 1997.

Shia, R. L., Y. L. Yung, M. Allen, R. W. Zurek and D. Crisp, Sensitivity study of advection and diffusion coefficients in a two-dimensional stratospheric model using excess carbon 14 data, *Journal of geophysical research*, *94*, (D15), 18467–18484, 1989.

Simpson, R. A., G. L. Tyler, B. Häusler, R. Mattei and M. Pätzold, Venus express bistatic radar: High-elevation anomalous reflectivity, *Journal of Geophysical Research*, *114*, 22695, 2009.

Sivac, P. and T. Schirmann, The venus express spacecraft system design, *ESA*, 1–22, 2007.

Smith, B. A., Rotation of venus: continuing contradictions, *Science (New York, N.Y.)*, *158*, (3797), 114–116, 1967.

Smithsonian, *Smithsonian Meteorological Tables: Based on guyot's meteorological and physical tables ... (classic reprint)*, Forgotten Books, 2015.

Smolarkiewicz, P. K., A simple positive definite advection scheme with small implicit diffusion, *Monthly Weather Review*, *111*, (3), 479–486, 1983.

Smolarkiewicz, P. K., A fully multidimensional positive definite advection transport algorithm with small implicit diffusion, *Journal of Computational Physics*, *54*, (2), 325–362, 1984.

Smolarkiewicz, P. K. and T. L. Clark, The multidimensional positive definite advection transport algorithm: Further development and applications, *Journal of Computational Physics*, *67*, (2), 396–438, 1986.

Smolarkiewicz, P. K. and W. W. Grabowski, The multidimensional positive definite advection transport algorithm: Nonoscillatory option, *Journal of Computational Physics*, *86*, (2), 355–375, 1990.

Steffes, P. G., Laboratory measurements of the microwave opacity and vapor pressure of sulfuric acid vapor under simulated conditions for the middle atmosphere of venus, *Icarus*, *64*, (3), 576–585, 1985.

Steffes, P. G. and V. R. Eshleman, Sulfur dioxide and other cloud-related gases as the source of the microwave opacity of the middle atmosphere of venus, *Icarus*, *46*, (1), 127–131, 1981.

Steffes, P. G. and V. R. Eshleman, Sulfuric acid vapor and other cloud-related gases in the venus atmosphere: Abundances inferred from observed radio opacity, *Icarus*, *51*, (2), 322–333, 1982.

Steffes, P., J. Jenkins, R. S. Austin, S. W. Asmar, D. T. Lyons, E. Seale and G. L. Tyler, Radio occultation studies of the venus atmosphere with the magellan spacecraft 1. experimental description and performance, *Icarus*, *110*, (1), 71–78, 1994.

Suleiman, S. H., M. A. Kolodner and P. G. Steffes, Laboratory measurement of the temperature dependence of gaseous sulfur dioxide (so 2) microwave absorption with application to the venus atmosphere, *Journal of Geophysical Research*, *101*, (E2), 4623–4635, 1996.

Svedhem, H., D. V. Titov, F. W. Taylor and O. Witasse, Venus as a more earth-like planet, *Nature*, *450*, 629 EP –, 2007.

Svedhem, H., D. Titov, F. Taylor and O. Witasse, Venus express mission, *Journal of Geophysical Research*, *114*, 222, 2009.

Takagi, M., N. Sugimoto, H. Ando and Y. Matsuda, Three-dimensional structures of thermal tides simulated by a venus gcm, *Journal of Geophysical Research: Planets*, *123*, (2), 335–352, 2018.

Taylor, F. W., Remote sensing of venus atmospheric dynamics, *Advances in Space Research*, *12*, (9), 57–71, 1992.

Taylor, F. W., Venus before venus express, *Planetary and Space Science*, *54*, (13-14), 1249–1262, 2006.

Taylor, F. W., R. Beer, M. T. Chahine, D. J. Diner, L. S. ELSON, R. D. Haskins, D. J. McCleese, J. V. Martonchik, P. E. Reichley, S. P. Bradley, J. Delderfield, J. T. Schofield, C. B. Farmer, L. Froidevaux, J. Leung, M. T. Coffey and J. C. Gille, Structure and meteorology of the middle atmosphere of venus: Infrared remote sensing from the pioneer orbiter, *Journal of Geophysical Research*, *85*, (A13), 7963, 1980.

Tellmann, S., M. Pätzold, B. Häusler, M. K. Bird and G. L. Tyler, Structure of the venus neutral atmosphere as observed by the radio science experiment vera on venus express, *Journal of Geophysical Research*, *114*, (9), 129, 2009.

Tellmann, S., B. Häusler, D. P. Hinson, G. L. Tyler, T. P. Andert, M. K. Bird, T. Imamura, M. Pätzold and S. Remus, Small-scale temperature fluctuations seen by the vera radio science experiment on venus express, *Icarus*, *221*, (2), 471–480, 2012.

Titov, D. V., H. Svedhem, D. McCoy, J.-P. Lebreton, S. Barabash, J.-L. Bertaux, P. Drossart, V. Formisano, B. Haeusler, O. I. Korablev, W. Markiewicz, D. Neveance, M. Petzold, G. Piccioni, T. L. Zhang, F. W. Taylor, E. Lellouch, D. Koschny, O. Witasse, M. Warhaut, A. Acomazzo, J. Rodrigues-Cannabal, J. Fabrega, T. Schirmann, A. Clochet and M. Coradini, Venus express: Scientific goals, instrumentation, and scenario of the mission, *Cosmic Research*, *44*, (4), 334–348, 2006.

Titov, D. V., F. W. Taylor, H. Svedhem, N. I. Ignatiev, W. J. Markiewicz, G. Piccioni and P. Drossart, Atmospheric structure and dynamics as the cause of ultraviolet markings in the clouds of venus, *Nature*, *456*, 620 EP –, 2008.

Titov, D. V., W. J. Markiewicz, N. I. Ignatiev, L. Song, S. S. Limaye, A. Sanchez-Lavega, J. Hesemann, M. Almeida, T. Roatsch, K.-D. Matz, F. Scholten, D. Crisp, L. W. Esposito, S. F. Hviid, R. Jaumann, H. U. Keller and R. Moissl, Morphology of the cloud tops as observed by the venus express monitoring camera, *Icarus*, *217*, (2), 682–701, 2012.

Tomasko, M. G., L. R. Doose, P. H. Smith and A. P. Odell, Measurements of the flux of sunlight in the atmosphere of venus, *Journal of Geophysical Research*, *85*, (A13), 8167, 1980.

Toon, O. B., B. Ragent, D. Colburn, J. Blamont and C. Cot, Large, solid particles in the clouds of venus: Do they exist?, *Icarus*, *57*, (2), 143–160, 1984.

Tyler, G. L., J. P. Brenkle, T. A. Komarek and A. I. Zygielbaum, The viking solar corona experiment, *Journal of Geophysical Research*, *82*, (28), 4335–4340, 1977.

Vandaele, A. C., O. Korablev, D. Belyaev, S. Chamberlain, D. Evdokimova, T. Encrenaz, L. Esposito, K. L. Jessup, F. Lefèvre, S. Limaye, A. Mahieux, E. Marcq, F. P. Mills, F. Montmessin, C. D. Parkinson, S. Robert, T. Roman, B. Sandor, A. Stolzenbach, C. Wilson and V. Wilquet, Sulfur dioxide in the venus atmosphere: Ii. spatial and temporal variability, *Icarus*, *295*, 1–15, 2017.

van Vleck, J. H., The absorption of microwaves by oxygen, *Physical Review*, *71*, (7), 413–424, 1947.

van Vleck, J. H. and V. F. Weisskopf, On the shape of collision-broadened lines, *Reviews of Modern Physics*, *17*, (2-3), 227–236, 1945.

Wagner, W. and A. Pruß, The iapws formulation 1995 for the thermodynamic properties of ordinary water substance for general and scientific use, *Journal of Physical and Chemical Reference Data*, *31*, (2), 387–535, 2002.

Walterscheid, R. L., G. Schubert, M. Newman and A. J. Kliore, Zonal winds and the angular momentum balance of venus' atmosphere within and above the clouds, *Journal of the Atmospheric Sciences*, *42*, (19), 1982–1990, 1985.

White, F. M., *Fluid mechanics*, McGraw-Hill, New York, NY, 8. ed. Auflage, 2016.

Whittaker, I., G. Guymer, M. Grande, B. Pintér, S. Barabash, A. Federov, C. Mazelle, J. A. Sauvaud, R. Lundin, C. T. Russell, Y. Futaana, M. Fränz, T. L. Zhang, H. Andersson, A. Grigoriev, M. Holmström, M. Yamauchi, K. Asamura, W. Baumjohann, H. Lammer, A. J. Coates, D. O. Kataria, D. R. Linder, C. C. Curtis, K. C. Hsieh, H. E. J. Koskinen, E. Kallio, P. Riihelä, W. Schmidt, J. Kozyra, S. McKenna-Lawlor, J. J. Thocaven, S. Orsini, R. Cerulli-Irelli, A. Mura, M. Milillo, M. Maggi, E. Roelof, P. Brandt, R. A. Frahm, J. R. Sharber, P. Wurz and P. Bochsler, Venusian bow shock as seen by the aspera-4 ion instrument on venus express, *Journal of Geophysical Research*, *115*, (A9), n/a–n/a, 2010.

Wickert, J., C. Reigber, G. Beyerle, R. König, C. Marquardt, T. Schmidt, L. Grunwaldt, R. Galas, T. K. Meehan, W. G. Melbourne and K. Hocke, Atmosphere sounding by gps radio occultation: First results from champ, *Geophysical Research Letters*, *28*, (17), 3263–3266, 2001.

Wickert, J., G. Michalak, T. Schmidt, G. Beyerle, C.-Z. Cheng, S. B. Healy, S. Heise, C.-Y. Huang, N. Jakowski, W. Köhler, C. Mayer, D. Offiler, E. Ozawa, A. G. Pavelyev, M. Rothacher, B. Tapley and C. Köhler, Gps radio occultation: Results from champ, grace and formosat-3/cosmic, *Terrestrial, Atmospheric and Oceanic Sciences*, *20*, (1), 35, 2009.

Woo, R. and A. Ishimaru, Eddy diffusion coefficient for the atmosphere of venus from radio scintillation measurements, *Nature*, *289*, 383–384, 1981.

Woo, R., J. W. Armstrong and A. J. Kliore, Small-scale turbulence in the atmosphere of venus, *Icarus*, *52*, (2), 335–345, 1982.

Yakovlev, O. I., S. S. Matyugov and V. N. Gubenko, Venera-15 and -16 middle atmosphere profiles from radio occultations: Polar and near-polar atmosphere of venus, *Icarus*, *94*, (2), 493–510, 1991.

Yamamoto, M. and M. Takahashi, Superrotation maintained by meridional circulation and waves in a venus-like agcm, *Journal of the Atmospheric Sciences*, *63*, (12), 3296–3314, 2006.

Yamamoto, M. and H. Tanaka, Formation and maintenance of the 4-day circulation in the venus middle atmosphere, *Journal of the Atmospheric Sciences*, *54*, (11), 1472–1489, 1997.

Young, L., High resolution spectra of venus—a review, *Icarus*, *17*, (3), 632–658, 1972.

Young, A. T., Are the clouds of venus sulfuric acid?, *Icarus*, *18*, (4), 564–582, 1973.

Yung, Y. L. and W. B. Demore, Photochemistry of the stratosphere of venus: Implications for atmospheric evolution, *Icarus*, *51*, (2), 199–247, 1982.

Zasova, L. V., V. I. Moroz, L. W. Esposito and C. Y. Na, So2 in the middle atmosphere of venus: Ir measurements from venera-15 and comparison to uv data, *Icarus*, *105*, (1), 92–109, 1993.

Zeleznik, F. J., Thermodynamic properties of the aqueous sulfuric acid system to 350 k, *Journal of Physical and Chemical Reference Data*, *20*, (6), 1157–1200, 1991.

R. Zellner (Hrsg.), *Chemie über den Wolken: ... und darunter*, Sachbuch, Wiley-VCH Verlag GmbH & Co. KGaA, Weinheim, 1. auflage Auflage, 2011.

Zhang, T. L., W. Baumjohann, M. Delva, H.-U. Auster, A. Balogh, C. T. Russell, S. Barabash, M. Balikhin, G. Berghofer, H. K. Biernat, H. Lammer, H. Lichtenegger, W. Magnes, R. Nakamura, T. Penz, K. Schwingenschuh, Z. Vörös, W. Zambelli, K.-H. Fornacon, K.-H. Glassmeier, I. Richter, C. Carr, K. Kudela, J. K. Shi, H. Zhao, U. Motschmann and J.-P. Lebreton, Magnetic field investigation of the venus plasma environment: Expected new results from venus express, *Planetary and Space Science*, *54*, (13-14), 1336–1343, 2006.

Zhang, X., M.-C. Liang, F. Montmessin, J.-L. Bertaux, C. Parkinson and Y. L. Yung, Photolysis of sulphuric acid as the source of sulphur oxides in the mesosphere of venus, *Nature Geoscience*, *3*, 834 EP –, 2010.

Zhang, X., M. C. Liang, F. P. Mills, D. A. Belyaev and Y. L. Yung, Sulfur chemistry in the middle atmosphere of venus, *Icarus*, *217*, (2), 714–739, 2012.

Danksagung

Mein Dank gilt zunächst meinem Doktorvater Priv. Doz. Dr. Martin Pätzold der mit seinem Interesse und seinen Anregungen diese Arbeit stark gefördert hat. Desweitern möchte ich mich beim Prof. Dr. rer. nat. Bernd Häusler bedanken, der mir mit kompetenten Ratschlägen immer zur Seite stand. Ich bedanke mich ebenfalls bei Dr. Silvia Tellmann und Dr. Kerstin Peter, die diese Arbeit trotz hoher Arbeitsbelastung mit vielen wissenschaftlichen Diskussionen inspiriert haben. Ich bedanke mich auch bei meinen Kollegen, die mir bei Fragen sachlich und humorvoll zur Seite standen. Mein weterer Dank gilt den MaRS, VeRa und RSI Teams, für die vielen Gespräche, Ratschläge und Diskussionen die diese Arbeit ebenfalls beeinflusst haben.
Bei meiner Freundin Anja bedanke ich mich vor allem für ihre Geduld und ihr Verständniss. Für die moralische Unterstützung bedanke ich mich ebenfalls bei meiner Familie, allen Freunden und Bekannten.

Ich versichere, dass ich die von mir vorgelegte Dissertation selbständig angefertigt, die benutzten Quellen und Hilfsmittel vollständig angegeben und die Stellen der Arbeit - einschließlich Tabellen, Karten und Abbildungen -, die anderen Werken im Wortlaut oder dem Sinn nach entnommen sind, in jedem Einzelfall als Entlehnung kenntlich gemacht habe; dass diese Dissertation noch keiner anderen Fakultät oder Universität zur Prüfung vorgelegen hat; dass sie - abgesehen von unten angegebenen Teilpublikationen - noch nicht veröffentlicht worden ist, sowie, dass ich eine solche Veröffentlichung vor Abschluss des Promotionsverfahrens nicht vornehmen werde.
Die Bestimmungen der Promotionsordnung sind mir bekannt. Die von mir vorgelegte Dissertation ist von Priv. Doz. Dr. Martin Pätzold betreut worden.

Teilpublikationen:
-

Köln, den 10.08.2020